A thesis for the degree of Doctor of Philosophy

Data-driven assessment and modelling of extended endplate connections

by

Zizhou Ding

ORCiD: 0009-0002-0573-8146

DOI: https://doi.org/10.5258/SOTON/PG/T119

Infrastructure Research Group

Department of Civil, Maritime and Environmental Engineering

Faculty of Engineering and Physical Sciences

School of Engineering

University of Southampton
Southampton, UK
April 2026

University of Southampton

Abstract

Faculty of Engineering and Physical Sciences
School of Engineering

Doctor of Philosophy

Data-Driven Assessment and Modelling of Extended Endplate Connections

by Zizhou Ding

Extended endplate connections (EEPCs) are widely used in construction practice to resist gravity, wind, earthquakes, progressive collapse, as well as other hazards. EEPCs can be designed as either fully- or semi-rigid achieving wide ranges of rotational stiffness, moment resistance, and ductility. As demonstrated in past research, accurately predicting EEPCs' behaviour can be challenging, particularly for semi-rigid ones where plastic deformations may occur in any of the connection components, individually or simultaneously. This has been the case because of simplified assumptions and limited datasets.

In this thesis, data-driven approaches are used to develop robust empirical methodologies for assessing and modelling semi-rigid EEPCs. This is achieved by mobilizing the extensive body of experimental research available in the literature. A major effort is made towards collating, digitising, and curating all available data. The data are used to assess all types of existing predictive models and confirming their limitations. The data is further supplemented by parametric finite element simulations, with emphasis on ductility quantification, i.e., bolt tensile rupture. Traditional regression and machine learning algorithms are then used to develop robust predictive models to capture semi-rigid EEPCs' moment-rotation response and governing deformation mode. The new models' novelty lies in their generality (larger applicability range), consideration of uncertainty, characterization of ductility, post-failure behaviour, and hysteretic response. The proposed models are detrimental in probabilistic and performance-based approaches to design, assess, and retrofit steel frame structures. They can effectively help the industry deliver economical designs with less material consumption, which is critical to achieve the goal of the net-zero strategy by 2050.

Declaration of Authorship

I declare that this thesis and the work presented in it are my own and have been generated by me as the result of my own original research.

I confirm that:

1. This work was done wholly or mainly while in candidature for a research degree at this University;
2. Where any part of this thesis has previously been submitted for a degree or any other qualification at this University or any other institution, this has been clearly stated;
3. Where I have consulted the published work of others, this is always clearly attributed;
4. Where I have quoted from the work of others, the source is always given. With the exception of such quotations, this thesis is entirely my own work;
5. I have acknowledged all the main sources of help;
6. Where the thesis is based on work done myself jointly with others, I have made clear exactly what was done by others and what I have contributed myself;
7. Parts of this work have been published as:

   Journal Papers:

   - Ding Z. and Elkady A. (2026), "Deformation mode classification in extended endplate connections and implications on hysteretic response", *Engineering Structures*. 346.
   - Ding Z. and Elkady A. (2025), "Backbone moment-rotation models for partial-strength steel endplate connections", *Engineering Structures*: 345.
   - Ding Z. and Elkady A. (2025), "Generalized spring model for steel bolts in tension considering uncertainty and loading speed", *Journal of Constructional Steel Research*: 231.
   - Ding Z. and Elkady A. (2023), "Semirigid bolted endplate moment connections: Review and experimental-based assessment of available predictive models. *ASCE Journal of Structural Engineering*.:149(9).

   Conference Papers:

   - Ding Z. and Elkady A. (2025), "Characterizing the hysteretic response of extended endplate connections based on deformation mode classification", *The 9th International Conference on Structural Engineering, Mechanics and Computation (SEMC2025)*, Cape Town, South Africa.
   - Ding Z. and Elkady A. (2025), "Experimental quantification of high-strength bolt fracture uncertainty under varying loading rates", *The International Colloquium on Stability and Ductility of Steel Structures (SDSS2025)*, Barcelona, Spain.

- Ding Z. and Elkady A. (2024), "An empirical spring model for simulating bolt fracture incorporating uncertainty", *The 11th International Conference on Behaviour of Steel Structures in Seismic Areas (STESSA)*, Salerno, Italy.
- Xu H., Ding Z., and Elkady A. (2024), "Traditional and machine-learning numerical models for partial-strength extended endplate connections", *The 11th International Conference on Behaviour of Steel Structures in Seismic Areas (STESSA)*, Salerno, Italy.
- Ding Z. and Elkady A. (2023), "Accuracy assessment of predictive models for semirigid extended end-plate connections", *The 10th European Conference on Steel Structures (EUROSTEEL2023)*, Amsterdam, Netherlands.

Signature: ……Date: ……...

Publication list

Journal Papers:

- **Ding Z.** and Elkady A. (2025), "Deformation mode classification in extended endplate connections and implications on hysteretic response", *Engineering Structures*: 346. DOI: https://doi.org/10.1016/j.engstruct.2025.121709.
- **Ding Z.** and Elkady A. (2025), "Backbone moment-rotation models for partial-strength steel endplate connections", *Engineering Structures*: 345. DOI: https://doi.org/10.1016/j.engstruct.2025.121465.
- **Ding Z.** and Elkady A. (2025), "Generalized spring model for steel bolts in tension considering uncertainty and loading speed", *Journal of Constructional Steel Research*: 231, DOI: https://doi.org/10.1016/j.jcsr.2025.109574.
- **Ding Z.** and Elkady A. (2023), "Semirigid bolted endplate moment connections: Review and experimental-based assessment of available predictive models. *ASCE Journal of Structural Engineering*.:149(9). DOI: https://doi.org/10.1061/JSENDH.STENG-11797.

Conference Papers:

- **Ding Z.** and Elkady A. (2025), "Characterizing the hysteretic response of extended endplate connections based on deformation mode classification", *The 9th International Conference on Structural Engineering, Mechanics and Computation (SEMC2025)*, September 1-3, 2025, Cape Town, South Africa. DOI: https://doi.org/10.1201/9781003677895.
- **Ding Z.** and Elkady A. (2025), "Experimental quantification of high-strength bolt fracture uncertainty under varying loading rates", *The International Colloquium on Stability and Ductility of Steel Structures (SDSS2025)*, September 8-10, Barcelona, Spain. DOI: http://doi.org/10.1002/cepa.70130.
- **Ding Z.** and Elkady A. (2024), "An empirical spring model for simulating bolt fracture incorporating uncertainty", *The 11th International Conference on Behaviour of Steel Structures in Seismic Areas (STESSA)*. July 8-10, 2024, Salerno, Italy. DOI: https://doi.org/10.1007/978-3-031-62884-9_46.
- Xu H., **Ding Z.**, and Elkady A. (2024), "Traditional and machine-learning numerical models for partial-strength extended endplate connections", *The 11th International Conference on Behaviour of Steel Structures in Seismic Areas (STESSA)*. July 8-10, 2024, Salerno, Italy. DOI: https://doi.org/10.1007/978-3-031-62884-9_47.
- **Ding Z.** and Elkady A. (2023), "Accuracy assessment of predictive models for semirigid extended end-plate connections", *The 10th European Conference on Steel Structures (EUROSTEEL2023)*, September 12-14, 2023, Amsterdam, Netherlands. DOI: https://doi.org/10.1002/cepa.2242.

Acknowledgements

The journey of a PhD over the past four years is profoundly meaningful., it is a great pleasure to have the opportunity to express my gratitude to all the people who have supported and guided me throughout this period.

Firstly, I would like to express my sincerest gratitude to my supervisor, Prof. Ahmed Elkady, for his guidance and supervision throughout my PhD studies and research. His knowledge, feedback, and mentorship are the cornerstone of the successful completion of this work. I am especially grateful for his patience in mentoring me from the very basics. At the beginning of my studies, I was even unable to write a single line of code, but I can now develop sophisticated programs to support my work under his excellent supervision. Beyond the technical skills I developed, he also taught me how to think and act as a good structural engineer. This will remain valuable throughout my future career.

I would also like to thank my second supervisor Dr. Marco Baiguera. We firstly met each other at a lecture during my MSc study. His knowledge and expertise about advanced structural engineering impressed me. This became one of the reasons I decided to continue my academic journey and pursue a PhD degree.

Special thanks to my colleagues, Dr. Rebecca Presswood, Dr. Hamish Moodley, Mr Aran Naserpour, and Mr. Weiran Li. Whenever I struggled to solve the academic problems, they always offered their support and helpful suggestions without any hesitation. It's not only about the academic support, but also about the memories we shared. I will never forget the countless late-night McDonald's dinners with Weiran in the office, or the laughter our research group shared over pints at the pub. Those moments of friendship are among my most treasured from this journey. I also extend my strongest encouragement to Weiran and Aran. I have every confidence that they will successfully cross the finish line.

I would like to acknowledge the University of Southampton for providing access to the Iridis5 High-Performance Computer. The ability to run large-scale parametric finite element simulations was indispensable to this research and formed one of the cornerstones of my PhD work.

I am also grateful to Dr. Andy Robinson and Dr. Stuart Findlow of the Test and Structure Research Laboratory at the University of Southampton. Their technical guidance and professional skill were instrumental in enabling the experimental aspects of this research.

Last but certainly not least, my deepest gratitude goes to my family and my girlfriend – Tong Liu (Alice). Their unwavering support, endless encouragement, and selflessness have been the constant pillar of my strength and motivation throughout the most challenging, yet most significant, period of my life!

Contents

TABLE OF FIGURES

LIST OF TABLES

LIST OF NOTATIONS

Abbreviations

ANN	Artificial neural network model
BA	Bolt anchorage failure
Balanced	Endplate bending mode plus either beam buckling or column web shear
BE	Bolt elongation
BFY	Beam flange yielding
BR	Bolt rupture/Bayesian regulation
BS	Bolt stripping
BWB	Beam web buckling
BWY	Beam web yielding
BZP	Bright zinc plated bolt
CC	Concrete cracking
CFB	Column flange yielding / tube wall buckling
CFE	Continuum finite element simulation
CS	Concrete spalling
CWB	Column web buckling
CWS	Column panel zone in shear
CWY	Column web yielding
DB	Experimental database
DD	Metal deck detachment
DIC	Digital image correlation camera
DT	Decision tree model
ED	Excessive deformation
EEPC(s)	Extended endplate connection(s)
EPB	Endplate excessive/visible bending
EPY	Endplate yielding
ES	Equal strength
FR	Fully rigid
FT	Fully threaded bolt
GLV	Galvanised plated bolt
GUI	Graphic user interface
HC	Cracking of HSS corner
HV	‘Hochfest Vorgespannt’ bolts
IMK	Ibarra-Medina-Krawinkler deterioration model

KNN	*K*-nearest neighbour model
LB	Loss of rebar-concrete bond / Lower bound prediction interval
Load/Joint	Symmetry of the applied load
LVDT	Linear displacement potentiometer
MF	Mesh fracture
MIMO	Multiple inputs and multiple outputs ANN model
MISO	Multiple inputs and single output ANN model
MVLR	Multivariate linear regression model
PBD	Performance-based design
PI	Prediction interval
PS	Partial-strength
PT	Partially threaded bolt
RF	Rebar fracture / Random forest model
RY	Rebar yielding
SB	Plate stiffener buckling
SC	Presence of column web stiffeners
SHAP	Shapley value
SR	Semi-rigid
SVM	Support vector machine model
UB	Upper bound prediction interval
UDL	Uniformly distributed load
VIF	Variance inflation factor
WF	Weld fracture

Latin symbols

A_{fracture}	Area of the fracture cross section
A_{s}	Shear area of bolts
b_{bf}	Width of the beam flange
b_{cf}	Width of the column flange
b_{ep}	Width of the endplate
c	Distance between inner outside and inner inside tension bolt rows
C_1	Strain parameter under shear
C_2	Strain parameter under tension
C_{pr}	Overstrength factor
D	Damage variable
d_{b}	Bolt diameter

$d_{b,head}$	Bolt head diameter
$d_{b,req\_ductile}$	Required bolt diameter to satisfy the ductility requirement
$d_{b,shank}$	Bolt shank diameter
$d_{b,thread}$	Bolt thread diameter
d_e	The vertical distance between the centre of extreme bolt row in tension and edge of endplate
D_{max}	Maximum value of the damage variable
d_w	Diameter of the bolt washer
E	Young's modulus
E_b	Beam modulus of elasticity
E_{bolt}	Bolt modulus of elasticity
e_c	The endplate extension at the compression side
E_c	Concrete modulus of elasticity
E_{cl}	Column modulus of elasticity
E_{ep}	Extended endplate modulus of elasticity
E_{mod}	Modified modulus of elasticity
e_{rc}	The vertical distance between centre of extreme bolt row in compression and edge of endplate
E_{rebar}	Rebar modulus of elasticity
e_{rt}	The vertical distance between centre of extreme bolt row in tension and edge of endplate
e_{sc}	Distance between first shear connector and column flange face
e_t	Endplate extension at the tension side
F	Applied force
f_{cm}	Concrete measured characteristic compressive strength
f_{ct}	Concrete measured characteristic tensile strength
$F_{frcature}$	Applied force at the fracture
$F_{t,b,Rd}$	Tensile resistance of bolts
$F_{t,Rd}$	Tensile resistance
$f_{u,b}$	Bolt measured ultimate stress
$f_{u,b}$	Bolt nominal ultimate stress
$f_{u,B}$	Beam measured ultimate stress
$f_{u,B}$	Beam nominal ultimate stress
$f_{u,C}$	Column measured ultimate stress
$f_{u,C}$	Column nominal ultimate stress
$f_{u,P}$	Endplate measured ultimate stress
$f_{u,P}$	Endplate nominal ultimate stress
$f_{y,b}$	Bolt measured yield stress
$f_{y,B}$	Beam measured yield stress

$F_{y,bolt}$	Yielding force of bolt
$f_{y,C}$	Column measured yield stress
$f_{y,P}$	Endplate measured yield stress
$f_{yn,b}$	Bolt nominal yield stress
$f_{yn,B}$	Beam nominal yield stress
$f_{yn,C}$	Column nominal yield stress
$f_{yn,desk}$	Steel deck nominal yield stress
$f_{yn,P}$	Endplate nominal yield stress
g	Bolt gauge (pitch between bolt columns)
G	Shear modulus
h_b	Beam height
h_c	Column height
h_{ep}	Endplate height
h_i / Z_i	Distance from centreline of the compression flange to a tension bolt row to the centreline of the i_{th} bolt row
h_{rib}	Steel deck rib height
h_{sc}	Height of shear connector
h_{slab}	Total height (thickness) of concrete slab
I_b	Beam's second moment of area
k_b	Normalised stiffness
$k_{b,1.5}$	Shift factor of the stiffness
K_e	Elastic stiffness
K_{inc}	Increment stiffness
k_r	Component stiffness factor
K_s	Post-yielding stiffness
$K_{s,incomp}$	Incompatible post-yield stiffness
$K_{s,tan}$	Tangent post-yield slope
$K_{s,true}$	True post-yield stiffness
K_{secant}	Secant stiffness
K_{trans}	Transition stiffness
L_a	Mesh element width
L_b	Beam length / Mesh element height / Bolt total length
L_c	Column length / Mesh characteristic length
$l_{eff,i}$	Equivalent T-stub effective length
L_g	Bolt grip length
L_{mesh}	Mesh element length
L_n	Bolt nut thickness

L_s	Bolt shank length
L_t	Bolt thread length
M	Moment
m_b	Normalised plastic resistance
$m_{b,1.5}$	Shift factor of the plastic resistance
M_{cap}	Capping moment
M_{cf}	Moment at the face of the column flange
M_{end}	End moment
M_{max}	Maximum moment
$M_{max,incomp}$	Incompatible maximum moment
$M_{max,true}$	True maximum moment
M_{np}	Moment caused by prying force
M_o	Reference moment
$M_{p,b}$	Plastic moment of the beam
$M_{p,Rd}$	Moment resistance of the joint
$M_{pl,cl}$	Plastic moment of the column flange
$M_{pl,p}$	Plastic moment of the endplate
M_{pr}	Plastic moment at the beam plastic hinge
m_x	Diagonal of the p_{fi} and the half of the g minus the t_{bw}
M_y	Yielding moment
M_{ye}	Effective yield moment
$M_{ye,incomp}$	Incompatible effective yield moment
$M_{ye,true}$	True effective yield moment
N_b	Axial beam load
n_C	Numbers of bolts below the beam neutral axis
N_c	Axial column load
n_T	Numbers of bolts above the beam neutral axis
n_{Total}	Total numbers of bolts
n_w	Number of bolt washers
p	Hydrostatic stress
p	Pitch between bolt rows in tension within the beam flanges
P_{20}	Possibility of the error within ±20%
P_{50}	Possibility of the error within ±50%
p_c	Pitch between bolt rows in compression above/below the beam flange
$PEEQ$	Equivalent plastic strain
p_{fi}	Distance from inside of the beam tension flange to the nearest inside bolt row
p_{fo}	Distance from outside of the beam tension flange to the nearest outside bolt row

p_i	Distance between the most interior bolt row in tension and the most interior bolt row in compression
p_{sc}	Pitch between shear connectors
p_t	Pitch between bolt rows in tension above/below the beam flange
P_t	Bolt pretension level
q	Von mises stress
s	Distance from the centreline of the most inside or most outside tension bolt row to the edge of the yield line pattern
S_h	Distance from the face of the column flange to the plastic hinge
$S_{j,ini}$	Initial elastic stiffness of the joint
t_{bf}	Thickness of the beam flange
T_{bolt}	Bolt tension force
t_{bw}	Thickness of the beam web
t_{cf}	Thickness of the column flange
t_{cw}	Thickness of the column web
t_{deck}	Steel deck thickness
t_{ep}	Thickness of the extended endplate
t_h	Bolt head thickness
t_{rib}	Steel deck rib thickness
$t_{stiff,P}$	Thickness of the rib plate stiffener
t_w	Bolt washer thickness
t_{weld}	Thickness of the fillet welding
u_f	Plastic displacement at fracture
V_{bolt}	Bolt shear force
$V_{gravity}$	Shear force caused by gravity
w_g	Load along the beam
W_{slab}	Width of concrete slab
X_{model}	Predicted value by models
X_n	Independent variables
X_{test}	Value of the test data
Y	Dependent variables
Y_c	Column flange yield line parameter
Y_p	Endplate yield line parameter
z_r	Lever arm of each bolt row to the centre of the beam bottom flange
$Z_{x,b}$	The plastic modulus of the beam cross-section about the strong-axis

Greek symbols

α	Strength coefficient
α_{index}	Material-specific toughness index
α_K / α_m	Angular coefficient
β	Stiffness coefficient / Bolt stiffness correlation factor
β_i / c_i	Coefficient of multi-variate linear regression models
β_K / β_m	The intercept of the linear function
δ	Vertical displacement
Δ	Bolt's axial elongation
$\Delta_{f,p}$	Plastic fracture displacement
Δ_u	Ultimate displacement
$\Delta_{u,p}$	Plastic ultimate displacement
Δ_y	Yield displacement
ϵ	Error metrics
$\varepsilon_{engineering}$	Engineering strain
ε_f	Fracture strain
$\varepsilon_{pl,0}$	Equivalent plastic strain at the onset of damage
$\varepsilon_{pl,f}$	Equivalent plastic strain at fracture
$\varepsilon_{true,fracture}$	True fracture strain
$\varepsilon_{true,hardening}$	True hardening strain
ε_u	Ultimate strain
η	Stress triaxiality / Shape factor
θ	Rotation
θ_b	Beam rotation
θ_{bolt}	Bolt rotation
θ_c	Column rotation/capping rotation
θ_{cl}	Column flange rotation
θ_{end}	Rotation at the end of the test
θ_{ep}	Endplate rotation
θ_j	Joint rotation
θ_{max}	Maximum rotation
θ_p	Plastic rotation
θ_{pz}	Panel zone rotation
θ_r	Reference rotation
θ_{total}	Total rotation
θ_y	Yield rotation

θ_{ye}	Effective yield rotation
κ_d	Pinching parameter defining the break point with respect to the maximum permanent deformation experienced in the direction of loading
κ_f	Pinching parameter defining the break point with respect to the maximum force experienced in the direction of loading
μ	Stiffness ratio
ν	Poisson ratio
ρ	Reinforcement ratio
$\sigma_{engineering}$	Engineering stress
$\sigma_{true,fracture}$	True fracture stress
$\sigma_{true,hardening}$	True hardening stress
ϕ_n	Safety factor of bolts

1

INTRODUCTION

1.1. EEPCs in steel frame construction

Steel connections between structural members (beam-to-beam and beam-to-column) play an important role in the design and analysis of steel-framed structures. Fig. 1-1 shows several bolted connection types that are widely used in practice worldwide; those are the T-stub, extended endplate, flush endplate, angle cleat, and shear tab connection. This is mainly attributed to their relatively lower cost and ease of on-site erection. Among those connections, the extended endplate connection (EEPC), as shown in Fig. 1-2, is a popular one in multi-storey moment frames. Beyond their simple layout, EEPCs provide the highest rigidity, moment resistance, and energy dissipation compared to other bolted connections [1]. This is critical for a frame to resist both gravity and lateral loads, such as earthquake and strong winds.

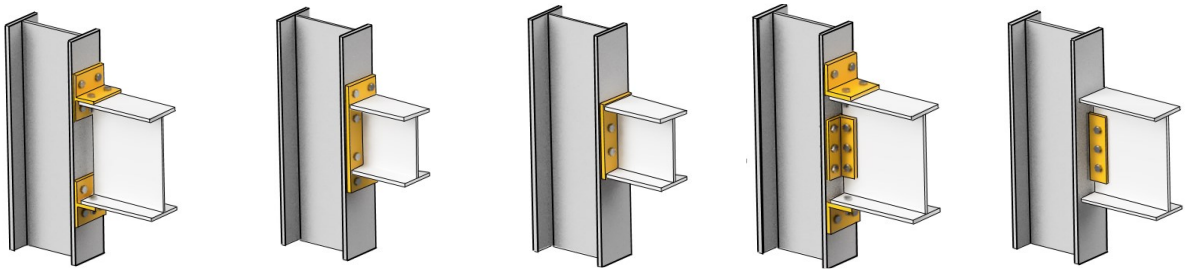

(a) T-stub (b) extended endplate (c) flush endplate (d) angle cleat (e) shear tab

Fig. 1-1 Main types of bolted connections.

(a) Source: islandmcr.co.uk (b) Source: engineerexcel.com (c) Source: weixiaosecondlife.blogspot.com

Fig. 1-2 EEPCs in construction practices.

Several EEPC layouts used in construction practice are illustrated in Fig. 1-3. Based on topology, EEPCs are classified by 1) the endplate extension, 2) the stiffening method, 3) the number of bolts, and 4) the presence of a concrete slab. In Fig. 1-3(a-b), EEPCs can be classified as single-sided or double-sided. Single-sided EEPCs are used to resist gravity load, where only a negative moment is exerted at the beam end. Double-sided EEPCs are used to resist cyclic loads triggered by strong winds or earthquakes. EEPCs can be stiffened at the endplate (i.e., rib stiffeners) or the column web (i.e., continuity plates) as illustrated in Fig. 1-3(c-d). This is an effective method to improve the moment resistance and rigidity instead of increasing the endplate thickness or beam size. The standard bolt arrangement configuration involves four

bolt rows with two bolts per row as described in Murray and Sumner [2] and commonly referred to as the eight-bolt EEPC. For a higher rigidity, EEPCs can also be designed with more than two bolts per row or with multiple bolt rows beyond the beam flanges, as shown in Fig. 1-3(e-f). Less commonly, EEPCs can be used to connect a beam to the column's weak axis (see Fig. 1-3(g)). In practical cases, a concrete slab, with or without a corrugated metal deck, can be used to act compositely with the steel beam to maintain strength and rigidity while reducing beam depth (see Fig. 1-3(h)).

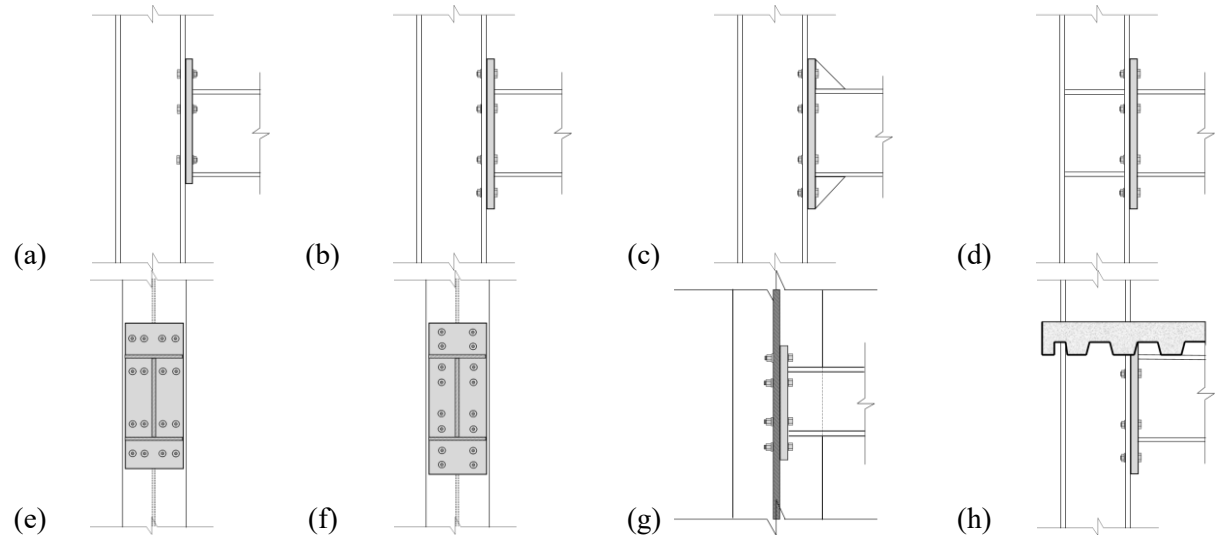

Fig. 1-3 Typical EEPCs classified by topology: (a) single-sided; (b) double-sided; (c) stiffened plate; (d) stiffened column web; (e) multiple bolts per row; (f) multiple bolt rows above the beam flange; (g) weak axis; (h) transverse steel deck.

1.2. Steel frame design and analysis

Steel frames are commonly designed using a conventional method where the members (i.e., beams and columns) are preliminarily sized based on the distributions of internal force and moment obtained from the structural global analysis (mostly elastic analysis). In this analysis, the connection behaviour is assumed as either pinned or rigid. Pinned connections (Fig. 1-4(a)), are designed to resist gravity loads with no moment being transferred at the beam ends. In contrast, rigid connections (Fig. 1-4(b)), transfer the entire moment from the beam to the column without any significant relative rotation. These connections are used in moment-resisting frames to resist both gravity and lateral loads. In the rigid connection case, the beam deflection under gravity load is significantly reduced due to the moment resistance at the beam ends. This means that a smaller beam size could potentially be used. The rigid assumption requires more material usage for the connection components as well as stiffeners to ensure full rigidity. The pinned assumption requires a deeper beam size and additional bracing systems to resist the gravity load and lateral loads, respectively. In reality, most connections behave more as semi-rigid (SR) with some degree of rotational

flexibility and moment resistance, due to the interacting elastic and plastic deformations of the different connection components (Fig. 1-4(c)). In practice, EEPCs are generally assumed as rigid. This is acceptable as they are mostly designed as fully rigid (FR), where the plastic hinges occur at the beam and the connection remains elastic. However, the rigid assumption may lead to an inaccurate result of global structural analysis. Therefore, the consideration of connection's true mechanical response is of high importance. Moreover, implementing semi-continuous design for EEPCs in both gravity and moment-resisting frames offers significant potential for material and cost savings. Steenhuis [3] reported a 9% cost saving in a braced frame achieved by using a shallower beam. Similarly, Tahir [4] demonstrated in a case study that semi-continuous design yields overall savings of 6% in cost and 8% in weight. Weynand et al [5] further corroborated these benefits, documenting material savings of up to 12% for frames utilising British hot-rolled sections. Most recently, by quantifying the utilisation ratio of beams and columns from 23 buildings in the UK, Moynihan and Allwood [6] found that a 36% reduction in material consumption and 214 million tonnes of carbon emissions per year could be achieved if the member sizes were optimised at the early design stage.

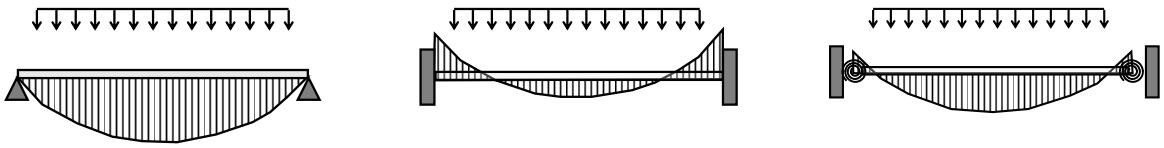

(a) pinned (b) rigid (c) semi-rigid

Fig. 1-4 Moment distribution under UDL for different idealised connections: (a) pinned, (b) rigid, and (c) semi-rigid.

Nowadays, with the wide availability of computational tools and resources, nonlinear global structural analysis is widely conducted. As part of nonlinear analysis, one must explicitly consider the connection's nonlinear elastic-plastic behaviour to investigate structural behaviour under serviceability and ultimate limit states. As demonstrated in Fig. 1-5, the structural members (i.e., beams and columns) are modelled as linear elastic elements, and lumped rotational springs with nonlinear models are assigned at the expected plastic hinge locations (such as the connections). Moreover, beyond the building codes' baseline performance objectives, the performance-based design (PBD) framework is used to achieve advanced performance objectives under a given loading scenario. PBD relies on the availability of robust numerical models that are able to predict the connection's damage fragility and its monotonic/cyclic response up to failure.

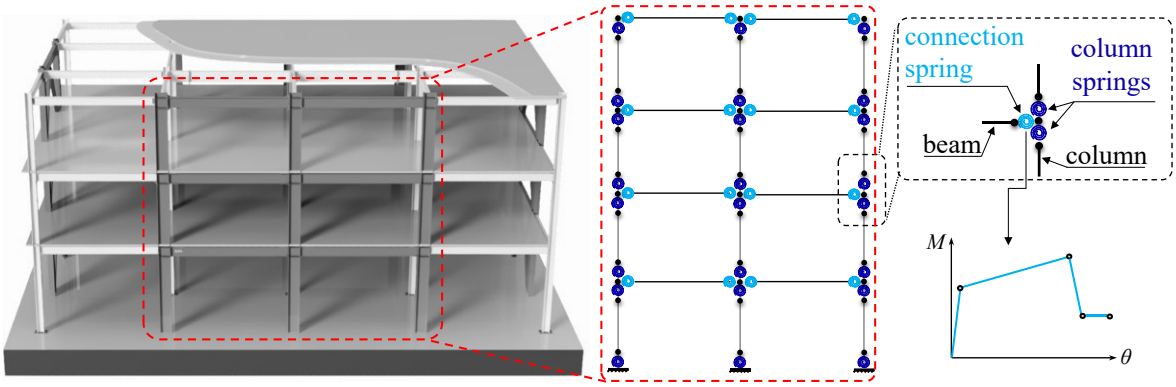

Fig. 1-5 Illustration of nonlinear frame analysis/PBD incorporating lumped springs.

1.3. Characteristics of EEPCs

Current standards by the European Commission and the American Institute of Steel Construction define classification boundaries for connections as show in Fig. 1-6. For the moment capacity, Eurocode 3 [7] states that partial-strength (PS) connections shall be able to transmit at least 25% of the beam's plastic moment resistance ($M_{p,b}$) but not exceed it. For the rotational stiffness, SR connections shall develop a stiffness larger than 0.5 times the beam elastic rigidity $(E_bI_b)/L_b$ but less than eight times of the beam's elastic stiffness (for unbraced frames) or 25 times of the beam's elastic stiffness (for braced frames), where E_b is the Young's modulus, I_b is the beam's moment-of-inertia, and L_b is the beam length. Similarly, in AISC 360-22 [8], partial-restrained (PR) connections shall develop a stiffness that is between 2 and 20 times the beam elastic rigidity. For the moment capacity, PR connections shall develop a strength larger than 20% of $M_{p,b}$. In this thesis, the terms SR and PS are considered synonymous in the context of joint classification.

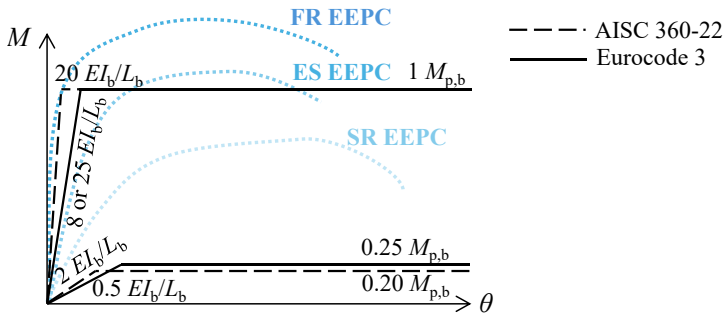

Fig. 1-6 Connection classifications in current design standards [7, 8].

EEPCs can be FR or SR/PS as illustrated in Fig. 1-6. Each type has a different pattern of connection deformation mode(s) and mechanical characteristic. FR EEPCs are designed by current codes [7, 8] to force the plastic deformations to occur in the beam (Fig. 1-7(a)). Those are primarily used in highly ductile steel frame systems in highly seismic regions. SR EEPCs can develop several deformation modes including

endplate bending, column flange bending, and column web/panel zone in shear (Fig. 1-7(b)). SR EEPCs can develop a large enough moment capacity that is close to $M_{p,b}$. which leads to beam yielding (Fig. 1-7(c)). This connection category is referred to as an equal strength (ES) connection [9].

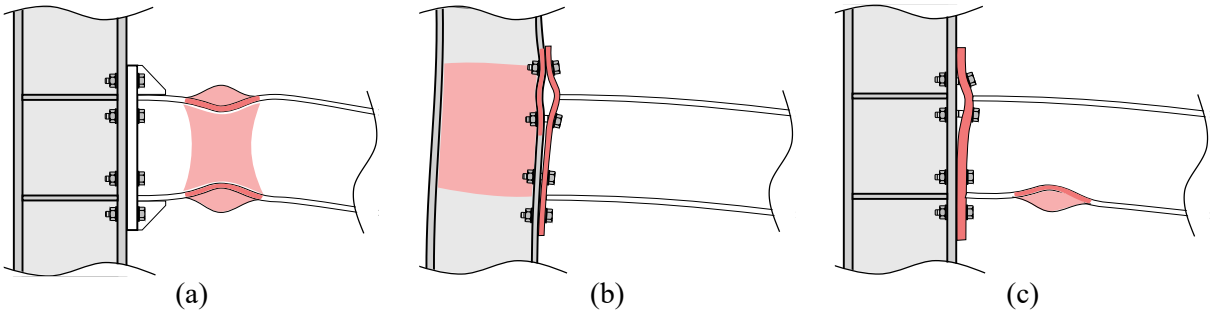

Fig. 1-7 EEPCs' deformation modes: (a) FR; (b) SR/PS; and (c) ES.

The mechanical behaviour of EEPCs is primarily governed by moment–rotation (M-θ) responses. For a FR EEPC under monotonic loading (Fig. 1-8(a)), the connection exhibits linear elastic behaviour up to the onset of beam yielding. Beyond this point, nonlinear strain hardening occurs until the maximum moment capacity is reached at the onset of local buckling in the beam. Following local buckling, the strength degrades until ductile tearing occurs. Under cyclic loading (Fig. 1-8(b)), FR EEPC demonstrates a stable and rounded hysteretic response prior to the onset of beam local buckling. Once buckling occurs, in-cycle degradation of both strength and stiffness develops, continuing until ductile tearing caused by low-cycle fatigue.

The behaviour of SR EEPCs, however, is more complex. This complexity arises from the fact that individual connection components can undergo plastic deformation either independently or simultaneously. Under monotonic loading (Fig. 1-8(c)), SR EEPC exhibits an initial linear elastic response up to the onset of component yielding. Beyond this point, the connection displays a nonlinear response resulting from plastic deformations in individual components, such as endplate bending, column flange bending, and/or panel zone shear. After reaching its maximum moment resistance, the connection typically experiences a sudden strength drop due to brittle failure, such as bolt rupture or weld fracture at the heat-affected zone.

Under cyclic loading (Fig. 1-8(d)), SR EEPC exhibits a similar elastic behaviour to that observed under monotonic loading. However, significant pinching is observed during the plastic stage, primarily due to the gap opening between the endplate and column flange. With respect to the M-θ response, there is no significant difference between the monotonic backbone curve and the cyclic envelope curve. This is attributed to the absence of in-cycle strength deterioration, which results from the stable plastic cyclic behaviour associated with endplate bending, column flange bending, and/or panel zone shear. In-cycle strength degradation only occurs in limited cases where beam yielding/buckling is part of the deformation

modes. In the absence of beam flange local buckling, the slight difference observed in moment rotation only relates to the cyclic material hardening properties. In that sense, SR EEPCs do not experience load history dependency as observed in other structural components that experience unrestrained web/flange buckling, such as wide-flange beam-columns [10, 11] and FR welded/bolted beam-to-column connections [12, 13]. It should be noted that ductility parameters, such as failure rotation, may be influenced by cyclic loading, as repeated load cycles can trigger unexpected weld failures.

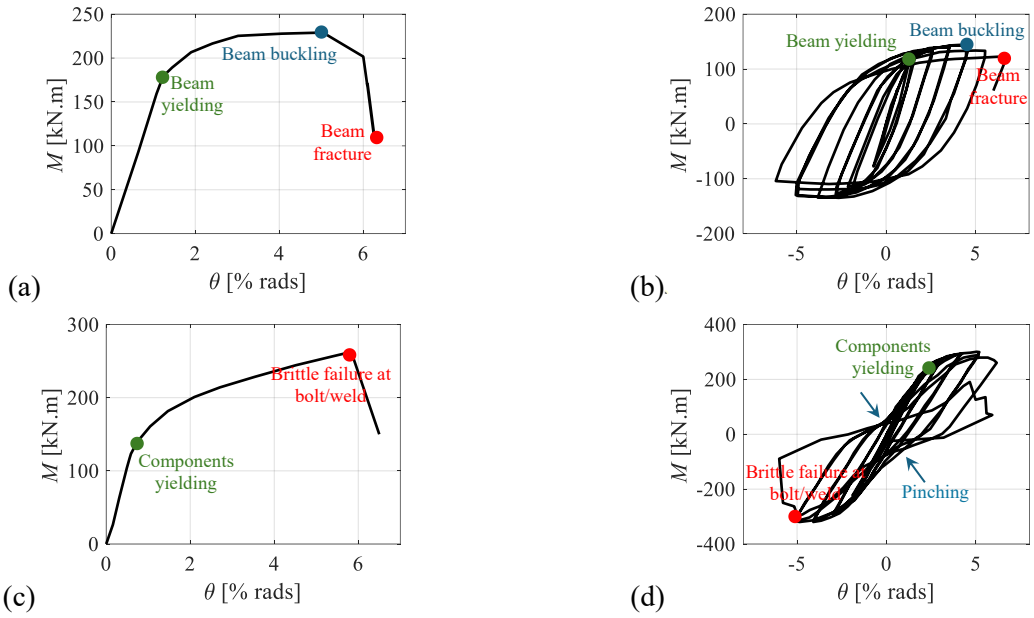

Fig. 1-8 Typical *M*-θ response of EEPCs: (a) FR under monotonic loading, (b) FR under cyclic loading, (c) SR under monotonic loading, and (d) SR under cyclic loading.

1.4. Semi-continuous design role in decarbonization

In multi-storey frames, the connection material weight accounts for less than 5% of the total frame weight, but the cost of connection fabrications accounts for over 30% of the total cost [14] . This means that even a small change in connection design can lead to significant cost savings, which is critical to the market and industry. Apart from the cost saving, efficient material usage leads to decarbonisation. According to the UK government report [15], around 40% of domestic carbon emissions are linked to construction activities. The construction sector also generates around 60% of the UK waste. Globally, up to 2010, around 30% of carbon emissions were attributed to steel manufacture and construction activities [16], and steel demand is expected to double in the coming decades [17]. The UK net-zero strategy aims to achieve a 100% reduction in the net UK carbon emissions by 2050, including the intermediate reduction targets of 68% by 2030 and 78% by 2035. The construction industry has already delivered a 20% reduction in absolute carbon emissions since 1990 [18]. However, it is still urgent to meet the net-zero environmental strategy by 2050. Royal

Academy of Engineering has pointed out that this target can be achieved by four steps, which are product outcome, design and specification, construction and reuse, and changes to procurement [19]. The design and specification aspect have a significant impact on carbon emissions. The roadmap in BCSA [18] estimates that a 17.5% reduction in carbon emissions is achievable by 2050 through smarter design, which maintains structural performance while using less steel. Therefore, rethinking design standards is essential to improve material efficiency and carbon performance.

1.5. Research problems

The nonlinear structural analysis and design of semi-continuous moment frames incorporating SR EEPCs face several key challenges.

First, robust and accurate predictive models for the M-θ backbone curves, deformation modes, and hysteretic responses of EEPCs are essential for reliable nonlinear structural analysis. Although numerous empirical, analytical, mechanical, and machine-learning models have been proposed since the 1960s, **they still fail short in predicting fundamental response parameters such as elastic stiffness and plastic strength (P1).** For example, the most recent empirical model developed by Eladly and Schafer [20] demonstrates errors of up to ±40% in estimating plastic strength and initial stiffness, while the Eurocode 3 mechanical-based component method has been shown to overestimate initial stiffness by up to 50% and underestimate plastic strength by up to 30% [21-23]. **Furthermore, most existing models neglect rotational ductility and post-capping behaviour due to insufficient data (P2)**, despite their critical role in ensuring structural robustness under extreme loading scenarios such as earthquakes, explosions, column loss, and fire.

SR EEPCs may exhibit several deformation modes that can develop individually or concurrently depending on the connection's geometry and the relative strength of its components. Therefore, accurately predicting the governing deformation mode is challenging. While code-based methods, including the component method [7] and the yield line analysis [8, 24] can be used to infer the deformation modes of EEPCs by identifying the weakest component, **these models suffer from procedural complexity and limited prediction accuracy, particularly when multiple modes interact (P3).** The deformation mode also governs the connection's hysteretic response which ranges from rounded loops to highly pinched ones; however**, no generalised guidance currently exists for defining the cyclic (pinching) parameters of SR EEPCs in phenomenological models (P4).**

Developing data-driven predictive models for EEPCs requires large and high-quality data. Although several databases for steel connections have been compiled since the 1980s, their scope is restricted, and the most

recent effort was undertaken in the 1990s. As a result, nearly three decades of experimental research remain uncollected, non-digital, and not organised for modern data-driven analysis. **There is therefore a pressing need for a comprehensive multi-attribute EEPC database to enable future advancements (P5).**

Despite extensive testing since the 1960s, available experimental data do not fully capture the geometric and material variability present in EEPC configurations. Given the high cost of full-scale testing, parametric numerical simulations are a practical means of addressing these gaps. **However, a systematic continuum finite-element (CFE) approach capable of accurately modelling bolted connection behaviour up to failure–across diverse geometries, material properties, and uncertainty sources–remains lacking (P6).** A large data pool that integrates a comprehensive experimental database with supplementary CFE-based parametric simulations is therefore essential for developing reliable predictive models of EEPC behaviour.

1.6. Research objectives

This research aims to develop robust predictive models for the M-θ responses, deformation modes, and hysteretic responses of EEPCs to support efficient structural design and robust structural analysis. To that end, the research's objectives are as follows:

- **Objective1:** Develop a comprehensive digital multi-attribute experimental database for SR EEPCs.
- **Objective2:** Assess the accuracy of existing predictive models and determine the influence of key predictors to inform the development of more robust models.
- **Objective3:** Develop a CFE modelling approach that captures bolt rupture and its uncertainty.
- **Objective4:** Develop accurate predictive models for predicting the full-range M-θ backbone curve, deformation modes, and hysteretic responses of EEPCs.

1.7. Research methodology

The thesis background, objectives, and methodology are outlined in Fig. 1-9. In summary, the methodology steps are as follows:

M1 for Objective1: Past EEPC experimental studies are collected through a rigorous literature search. Information is extracted from each reference and systematically tabulated and stored within EXCEL and MATLAB files. This database includes test information, configuration, geometrical parameters, material properties, and damage modes. Afterwards, the M-θ curves are digitised and stored in the data pool. The M-θ curve of each specimen is fitted with a systematic numerical method, and critical response parameters

are deduced. This compiled experimental database serves as the essential foundation for the development of robust predictive models.

M2 for Objective2: Existing predictive models are assessed by quantifying the relative error between the model prediction and collected data. The advantages and disadvantages of each model are summarised by the model's assumptions, formulas, and prediction performance. Afterwards, the correlation between the geometric and material parameters and the prediction error is conducted to investigate the applicability of each model. This assessment facilitates the subsequent development of new predictive models.

M3 for Objective3: A total 200 high-strength bolts with different grades and geometrical parameters are tested under varying loading speeds. Subsequently, a bolt database is compiled based on the experimental and collected data from past studies. This bolt database includes geometric parameters, material parameters, and damage mode(s). A bolt force-elongation model up to failure is proposed incorporating material uncertainty, which can be used as part of CFE simulations.

M4 for Objective3: An easy-to-use CFE simulation approach is developed for SR endplate connections, which the failure mode is controlled by bolt rupture. This includes the nonlinear material models, mesh, boundary conditions, interaction, and analysis solver. Furthermore, the critical parameters governing the ductile damage model for high-strength bolts are calibrated against experimental data. The developed CFE approach is first validated against experimental data from several test specimens and then used to conduct an extensive parametric simulation.

M5 for Objective3: A systematic investigation is conducted to identify gaps in the geometric and response parameters of the experimental database. Subsequently, a parametric study is designed to fulfil these gaps. A total of 1980 specimens are simulated, which provide a substantial variability on EEPCs' M-θ responses and deformation mode(s). A large-scale data pool encompassing the experimental test data and parametric simulations is then assembled, which is the source for developing more accurate and robust predictive models.

M6 for Objective4: Key response characteristics of EEPCs with respect to strength, stiffness, and ductility, are defined. A correlation analysis is first performed to identify the influence of geometric and material parameters on these characteristics. The most influential parameters are then selected as input features for predictive models. Robust predictive models are proposed using different numerical algorithms, such as multivariate linear regression (MVLR), artificial neural network (ANN), and random forest (RF), to quantify the full-range backbone M-θ response and deformation modes of EEPCs. Additionally, the critical pinching parameters in existing phenomenological models are calibrated to capture the characteristic of

EEPCs' hysteretic response. An empirical expression is subsequently derived to define these calibrated parameters as a function of key geometrical parameters.

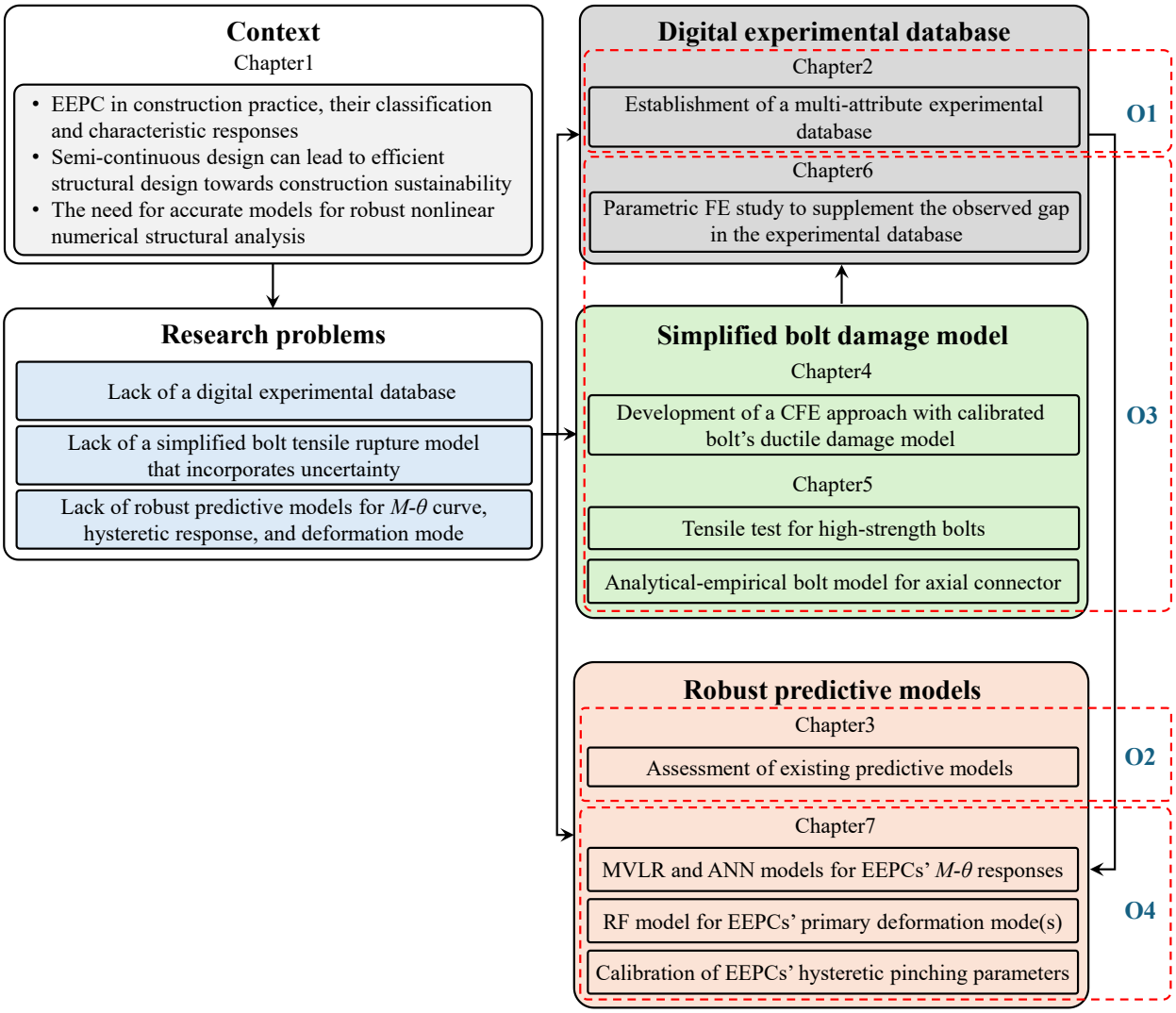

Fig. 1-9 Overview of the thesis background, research problems, objectives, and methodology.

2

DEVELOPMENT OF A DIGITAL EXPERIMENTAL DATABASE

2.1. Literature review of past experimental research

Since the 1960s, numerous experimental programs have been conducted to study the behaviour of bare steel and composite EEPCs with I-shaped sections under monotonic or cyclic loading conditions. Figure Fig. 2-1 shows the histogram of the number of tested specimens versus the year. Overall, a large number of specimens were tested after 1990.

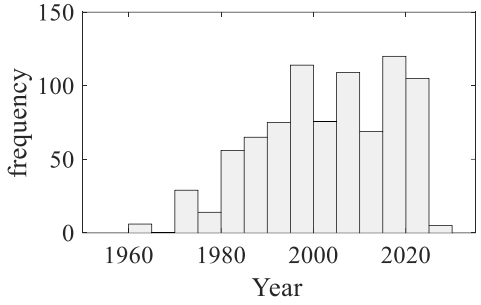

Fig. 2-1 Distribution of the number of tested specimens versus the year.

Sherbourne [25] was the first to study the monotonic behaviour of five interior joint specimens. Specimens were differentiated by the presence of column web stiffener, stiffener thickness, endplate thickness, and bolt diameter. These tests demonstrated that EEPCs could develop excessive plastic deformations simultaneously at the connection and beam. From the 1960s to the 1980s, several experimental tests were conducted in Europe and North America to study EEPCs under monotonic loading [26-30]. During this period, research primarily focused on understanding how key geometric parameters, such as beam and column sizes, endplate thickness, bolt diameter, bolt arrangement, and the presence of column stiffeners, affect connection behaviour.

The number of tested specimens increased exponentially over time, from approximately 100 in 1980 to more than 400 by 2000, with about 200 specimens tested between 1995 and 2000. During this period, researchers began to focus on the cyclic behaviour of connections, as well as the effects of bolt pretension and endplate rib stiffeners. Several experimental tests were conducted [1, 31-35], highlighting the role of bolt pretension in enhancing initial rotational stiffness, the contribution of endplate rib stiffeners in increasing connection strength, the excellent ductility and hysteretic energy dissipation capacity of EEPCs, and the potential applicability of SR EEPCs in seismic design.

From 2000 to 2020, the number of tested specimens increased constantly by 100 every five years. These researchers began to focusing on evaluating the accuracy of CEN [7] component method [22, 36-38]. Since 2010, research efforts have increasingly aimed at enhancing the performance of EEPCs. For instance, the European Equal-joints PLUS project [39] investigated the seismic behaviour of ES EEPCs using European

steel profiles and construction practices. Other studies explored the use of stainless-steel EEPCs to improve plastic rotational capacity [40-44].

Efforts to compile experimental databases for EEPCs emerged in the 1980s. Fig. 2-2 illustrates the existing databases for bolted connections. Initially, Jones et al [45] developed a database for eight types of SR connections. This database included a total of 255 beam-to-column specimens from 38 publications. Subsequently, Goverdhan [46] collected 266 experimental test data for five types of bolted connections from 22 publications. Chen and Kishi [47] developed a database of 303 beam-to-column specimens from 27 publications, which includes seven types of SR connections. Abdalla and Chen [48] developed a database of 46 beam-to-column EEPCs from 12 publications. Benterkia [49] developed perhaps the first relatively comprehensive database with 280 specimens of header-plate, flush endplate (FEPCs), and EEPCs. Since then, hundreds of specimens have been tested in the literature, yet no additional database for EEPCs has been found. Most recently, Mak and Elkady [50] developed an experimental database for bare-steel and composite flush endplate connections. This parametric database included several geometric and material parameters, and digitised *M-θ* curves. This motivated the effort undertaken here to compile a comprehensive digital experimental database for EEPCs.

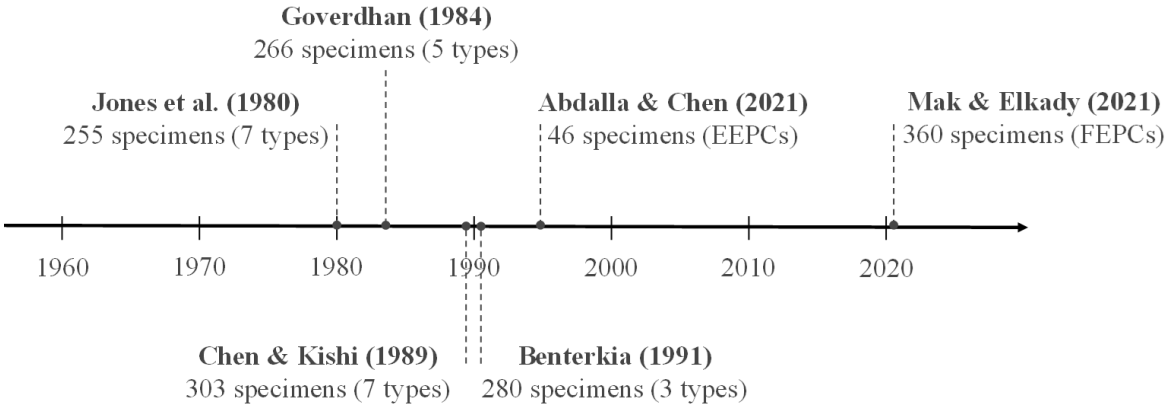

Fig. 2-2 Existing experimental databases over the years.

2.2. Overview of collected tests

The database comprises 849 specimens collected from 149 research sources, including journal papers, technical reports, and dissertations published between 1960 and 2025. Fig. 2-3 shows the research countries with respect to the number of tested specimens. It is observed that the majority of tests were conducted in Asia, Europe, and North America. The geometric and material characteristics of the collected tests are shown in Fig. 2-4. It is noticed that most research focuses on beam-to-column connections (i.e., cantilever or cruciform configurations). Only 12% of the studies focused on beam-to-beam connections (i.e., splice configurations), while over 95% of the specimens were tested about the major axis. The database contains an approximately equal number of double-sided and single-sided specimens. Most tests (67%) were

conducted under monotonic loading, with the remaining performed cyclically. Research on composite sections accounts for only 8% of the total, whereas 92% pertains to bare steel connections. Studies involving stiffened columns reported a 52% success rate, approximately 4% higher than that of unstiffened configurations. These fundamental parameters represent the key factors and scenarios to be considered in the development of predictive models.

Fig. 2-3 Distribution of the research country with respect to the number of tested specimens.

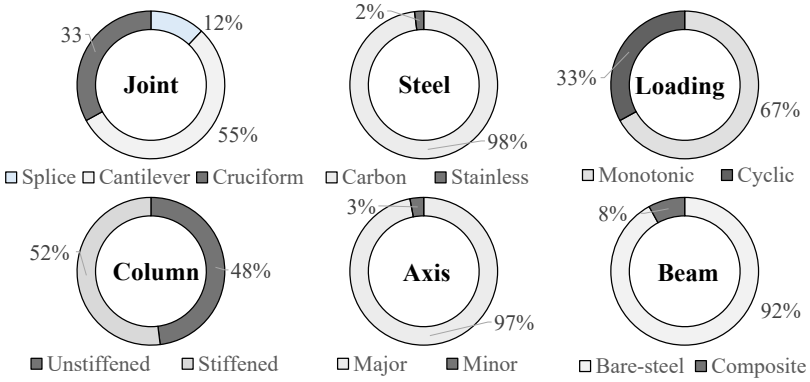

Fig. 2-4 Geometric and material characteristics of the collected tests.

2.3. Tabulated parameters

To accurately describe different specimens without redundancy, the collected parameters are categorised as the *'Research Information'*, *'Test Configuration'*, *'Specimen Configuration'*, *'Geometric Properties'*, *'Material Properties'*, *'Damage Mode'*, and *'Additional Notes'*. *'Research Information'* covers the research background, number of specimens, institution, and research focus. *'Test Configuration'* mainly includes types of setups, loading types, and column axis orientation. Note that eight types of test setups are considered, as shown in Fig. 2-5. *'Specimen Configuration'* mainly includes the presence of stiffeners, a concrete slab, and a composite beam. *'Geometric properties'* include the geometric details of column, beam, endplate, and bolt for bare steel specimens. Additional details for components ('*Slab*', '*Shear Connector*', and '*Reinforcement*') are also included for those composite specimens. *'Material properties'* mainly include the measured material strength and *Young's* modulus of column, beam, endplate, and bolt for bare steel specimens. Additionally, the strength and *Young's* modulus of concrete, rebars, and steel deck (if applicable)

are included for composite specimens. A comprehensive abbreviation list of damage modes has been tabulated in the Section 2.3.3, and the reported damage modes for each specimen are based on this list. The *'Additional Notes'* is used for some specimens about the additional information not tabulated in all these parameters. Based on the description in '*Notes*', some specimens are marked as '*Yes*' in '*Special Case*'. This means those specimens are different from the general EEPCs experimental procedure. A total 130 parameters were tabulated to describe the geometric characteristics and material uncertainty of each specimen.

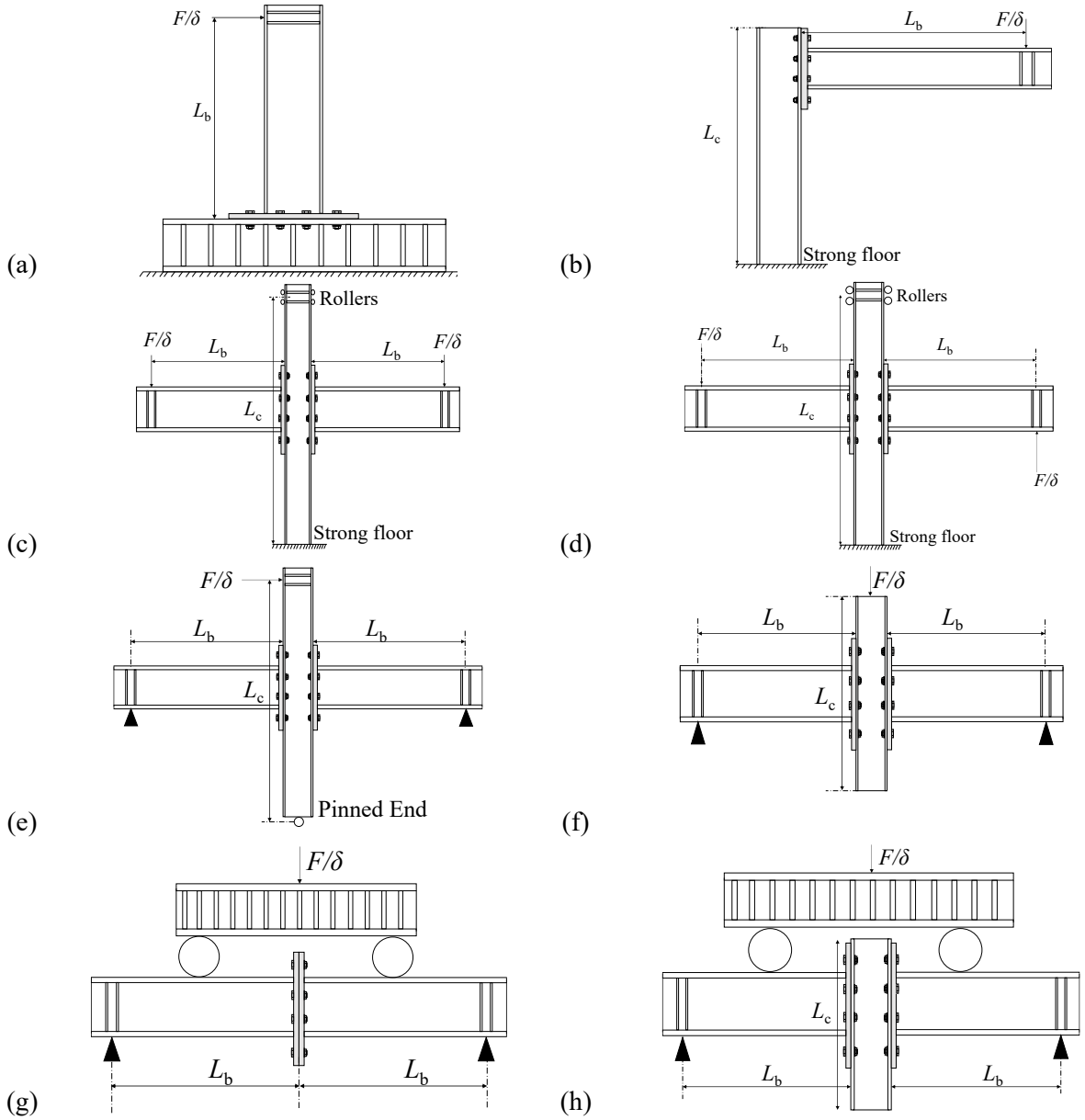

Fig. 2-5 Illustration of different test configurations: (a) T-B; (b) L-B; (c) C-B-Sym; (d) C-B-Asym; (e) C-C-Asym; (f) C-C-Sym; (g) S-BS-Sym; (h) C-BS-Sym.

2.3.1. Geometric and layout parameters

A total of 60 parameters were tabulated to describe the connection geometry and bolt layout. These parameters include the dimensions of the column, beam, endplate, bolts, and slab (where applicable). Fig. 2-6 shows the basic geometric and layout parameters for bare steel and composite connections. To describe the bolt layout accurately, parameters such as the number of bolts at the tensile side (n_T; i.e., above the beam neutral axis), the number of bolts at the compressive side (n_C; i.e., below the beam neutral axis), and the total number of bolts (n_{Total}) are recorded. Additional geometric parameters/flags are included to identify special layouts, such as the presence of multiple bolt rows above the beam flange and the number of bolt columns (in case more than 2).

Mechanical section properties, including the beam's second moment of inertia, plastic section modulus, bolt tensile stress area, and bolt pretension force, were incorporated directly into the database to enable rapid data extraction without the need for recalculation. For composite connections, the database also includes slab-related details, covering slab dimensions, metal deck type and dimensions (if applicable), shear connector size and type, and the number and spacing of both main and mesh reinforcement bars.

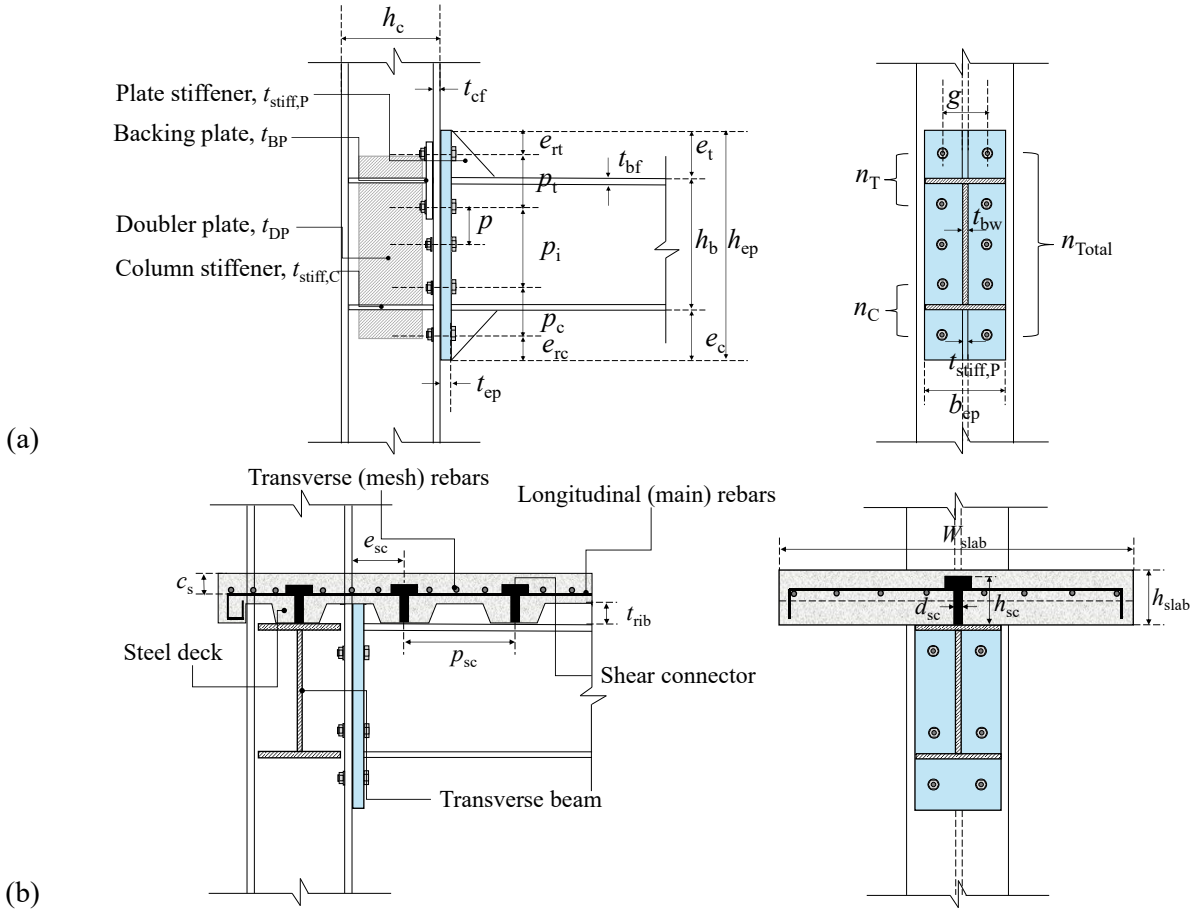

Fig. 2-6 Illustration of key geometric parameters in (a) bare steel EEPCs, and (b) composite EEPCs.

Fig. 2-7 shows the distribution of geometric parameters with mean, median, max, and min values. The beam height ranges from shallow sections (h_b ~ 110mm) to deep sections (h_b ~ 1500mm). These specimens with the deep beam are full-scale and used to investigate connection behaviour in the real structure. The endplate thickness ranges from thin (t_{ep} ~ 5mm) to thick (t_{ep} ~ 60mm). Most endplates are relatively thin (10mm – 20mm) to study plate behaviour, such as bending, yielding, and fracture. Some endplates are thick (over 40mm) and are used to study the behaviour of other components. Most specimens have four bolts at the tensile side and eight bolts in total, as shown in Fig. 2-6 (a). There is also limited research about the specimens with more than ten bolts, multiple bolt columns, or other non-standard layouts.

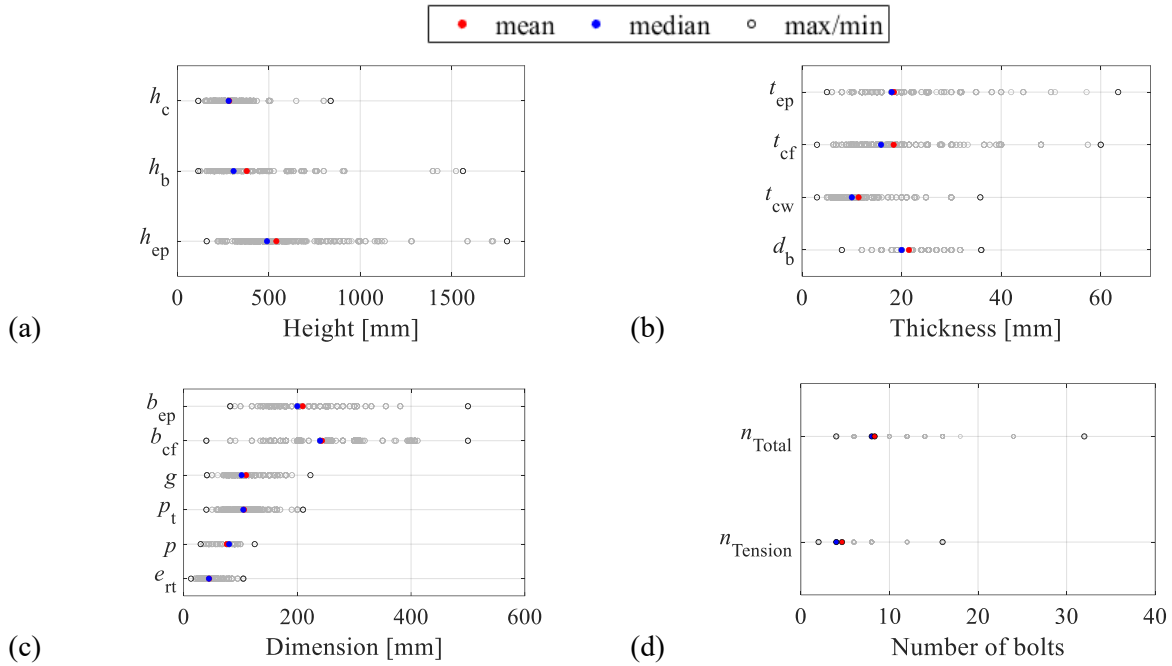

Fig. 2-7 Distribution of geometric parameters based on the collated experimental database for bare steel connections.

2.3.2. Material properties

The steel grade and the measured material properties for each of the connection components (i.e., column, beam, endplate, and bolt) were recorded. This included six parameters, which are the steel grade, nominal yield stress (f_{yn}), nominal ultimate stress (f_{un}), measured yield stress (f_{ym}), measured ultimate stress (f_{um}), and Young's modulus (E). Fig. 2-8 shows the typical strain–stress (f-ε) curves for conventional carbon steel and stainless steel. For the stainless steel, the 0.2% offset stress ($f_{y,0.2}$) was taken as the measured yield stress (f_{ym}). The nominal material values are based on those specified in the respective material standards. The researchers typically reported the measured material values based on coupon testing. In cases where the material properties are reported for both the flange and the web, the average value is tabulated. In cases where the material properties are not reported, the expected–to–nominal stress ratios (R_y and R_t) in AISC [51] were used to assume the measured values from the nominal ones.

Fig. 2-9 shows the distribution of the nominal material properties for the critical components (i.e., endplate, beam, and column). It is observed that S235, S275, and S355 are equally used in most of the endplates and beams, while S275 and S355 are mainly used for columns. Note that only 30 specimens are with high-strength steels (i.e., >S355). Additionally, two primary bolt grades are equally used in the collected specimens: Gr 8.8 and 10.9. Fig. 2-10 shows the distribution of the measured material properties. The measured yield and ultimate strengths for columns, beams, and plates are around 350 and 500 MPa, respectively. Limited specimens with the high-strength steel can reach over 800 and 1000 MPa, respectively.

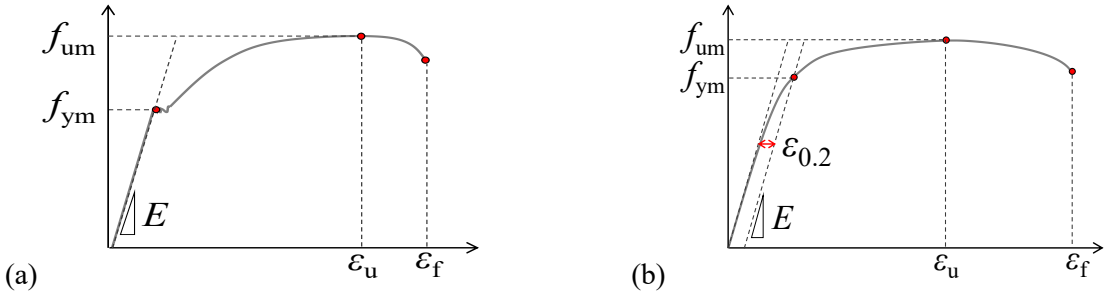

Fig. 2-8 Illustration of deduced material properties from typical engineering stress-strain curves of: (a) carbon steel; (b) stainless steel.

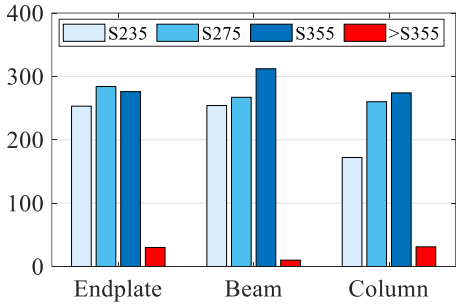

Fig. 2-9 Distribution of the nominal stress for different components in the experimental database.

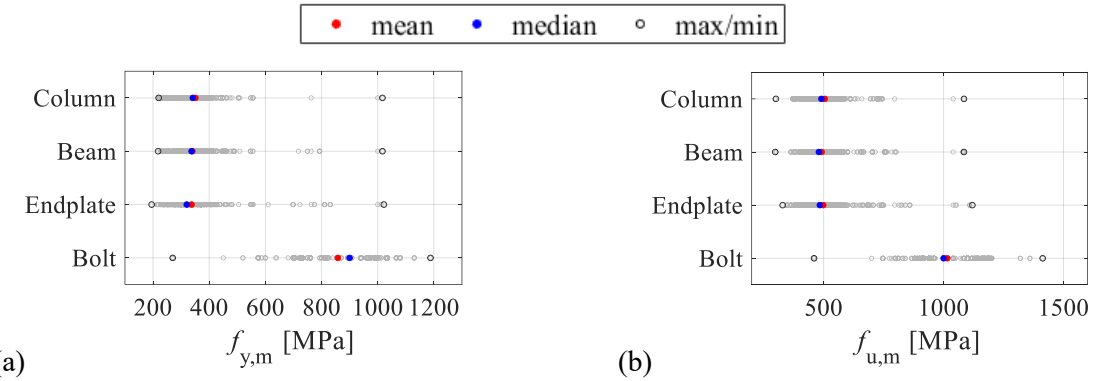

Fig. 2-10 Distribution of the measured stress values for the different connection components: (a) $f_{y,m}$ and (b) $f_{u,m}$.

For the composite specimens, the material properties of the concrete are recorded, including the grade, the measured compressive strength (f_c), the measured tensile strength (f_t), and Young's modulus (E). Generally,

the concrete compressive and tensile strengths measured on the day of testing are recorded. Otherwise, the reported 28-day compressive and tensile strengths were used. If the data is missing, the values are assumed to be the characteristic strength of concrete. Besides, the database also marks whether the strength is from the cube or the cylinder. The material properties of other components, such as the rebar and the steel deck strength, were also reported.

2.3.3. Damage modes

A total of 24 damage modes were identified, as described and illustrated in Table. 2-1. These modes are observed in the collected specimens, encompassing both plastic deformation and failure mechanisms. Fig. 2-11 shows the distribution of plastic connection deformation and failure observed in the collected tests. In general, the primary deformation mode for each specimen is reported in the original source. To ensure the accuracy and completeness of the damage mode classification, available test photographs were reviewed to verify and, if necessary, correct any misreported modes. The final, consolidated damage modes were then incorporated into the database. For specimens with no reported damage or failure modes, the CFE simulation approach described in Section 4 was used to determine the corresponding damage and failure modes. Fig. 2-12 illustrates typical plastic deformation and failure modes for both bare-steel and composite EEPCs documented in the literature.

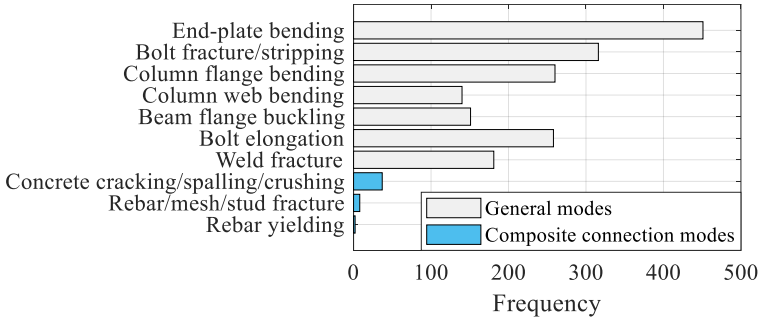

Fig. 2-11 Frequency of damage and failure modes.

Table. 2-1 Summary of the observed damage modes

Damage mode ID	Description	Category
BA	Bolt anchorage failure	Brittle
BE	Bolt elongation	Brittle
BFY	Beam flange yielding	Ductile
BR	Bolt fracture	Brittle
BS	Bolt stripping	Brittle
BWB	Beam web buckling	Ductile
BWY	Beam web yielding	Ductile
CC	Concrete cracking	Brittle
CFB	Column flange yielding / tube wall buckling	Ductile
CS	Concrete spalling	Brittle
CWB	Column web buckling	Ductile
CWS	Column panel zone in shear	Ductile
CWY	Column web yielding	Ductile
DD	Metal deck detachment	Brittle
ED	Excessive deformation	Ductile
EPB	Endplate excessive/visible bending	Ductile
EPY	Endplate yielding	Ductile
HC	Cracking of the HSS corner	Brittle
LB	Loss of rebar-concrete bond	Brittle
MF	Mesh fracture	Brittle
RF	Rebar fracture	Brittle
RY	Rebar yielding	Ductile
SB	Plate stiffener buckling	Ductile
WF	Weld fracture	Brittle

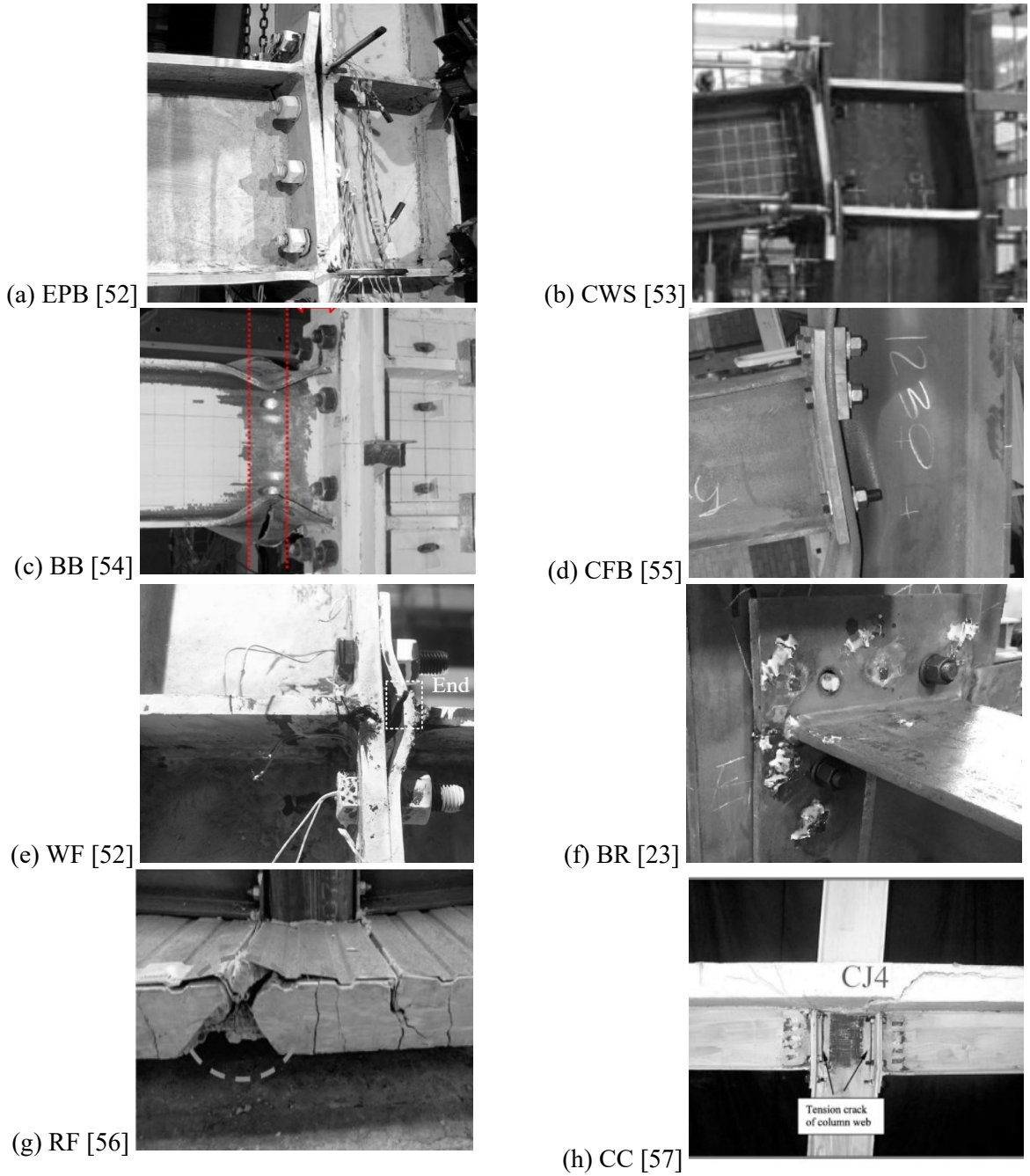

(a) EPB [52] (b) CWS [53]
(c) BB [54] (d) CFB [55]
(e) WF [52] (f) BR [23]
(g) RF [56] (h) CC [57]

Fig. 2-12 Typical plastic deformation and failure modes reported in the literature.

2.4. Digitised moment-rotation data

The most substantial part of the data-collection effort involved digitising the specimens' *M-θ* curves from the published plots. This was done manually using two tools, *Digitiser* by Lignos [58] and *WebPlotDigitiser* by Rohatgi [59]. Fig. 2-13 shows two examples of digitised *M-θ* curves (in grey dashed lines) under monotonic and cyclic loading. For the specimen under cyclic loading, the digitised curves include the positive envelope, the negative envelope, the overall envelope, and the full cyclic response, as shown in Fig.

2-13(b). The envelope represents the 1st-cycle envelope joining the peak points of the first cycle at each new rotation level.

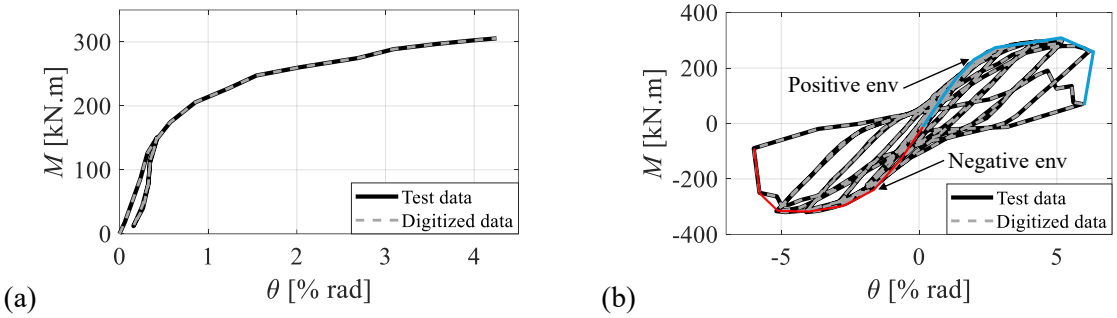

Fig. 2-13 Examples of digitised data: (a) monotonic curve; (b) cyclic curve.

It should be noted that the moment (M) reported in the vast majority of research is defined as the product of the force at the beam tip and the horizontal distance from the point of load application to the column flange surface. This definition is used here as well. The reported rotation mainly depends on the instrumentation used by the different researchers. In SR/PS connections, rotation results from the collective contributions of the different deforming components. In most published papers, the reported rotation is the joint rotation (θ_j), which includes the rotational contributions of endplate bending (θ_{ep}), bolt elongation (θ_{bolt}), column web shear distortion (θ_{pz}), and column flange bending (θ_{fl}). In a few studies, the reported rotation is based on the beam chord rotation (i.e., beam tip deflection divided by the distance from the beam tip to the column flange face). This is referred to as the total rotation (θ_{total}), which -by definition- includes the joint rotation (θ_j) in addition to the elastic rotational contributions of both the beam and column in shear/flexure (θ_b and θ_c, respectively). In these cases, θ_b and θ_c are computed based on the principles of joint/solid mechanics and then subtracted from the total rotation to obtain θ_j.

2.5. Data fitting and deduction of response parameters

Several key response parameters were deduced from the M-θ curve of each specimen using bilinear fitting. As demonstrated in Fig. 2-14(a), those parameters are the initial elastic rotational stiffness K_e, the post-yield (strain hardening) stiffness K_s, the yield moment M_y, the effective yield (plastic) moment M_{ye}, the capping moment M_c, and the corresponding rotations; i.e., the yield rotation θ_y, the plastic rotation θ_{ye}, and the capping rotation θ_c. Note that under cyclic loading, the response parameters were deduced for each of the positive and negative envelope curves, and the average value of the two is eventually recorded.

One should note that M_c represents the moment at which strength degradation (i.e., failure) occurs. Since failure did not always happen in all specimens, another parameter, M_{max}, is introduced herein to represent the maximum moment reached during the test, even though it is not necessarily the capping one. Similarly, the corresponding rotation parameter θ_{max} is introduced.

Bilinear fitting curves are among the most widely adopted models for representing connection behaviour in global structural analysis, as they effectively capture the key response parameters governing structural performance [60]. In addition, their relatively simple mathematical formulation enables efficient implementation in numerical models, resulting in enhanced computational efficiency without significant loss of accuracy. However, bilinear fitting curves may not accurately capture the nonlinear transition between the initial elastic stage and fully developed plastic stage. For this reason, a trilinear fitting curve, as shown in Fig. 2-14(b), is also employed with an additional transition stiffness (K_{trans}), which enables a more realistic representation of the gradual stiffness degradation and nonlinear response in the intermediate stage between elastic and plastic behaviour. This transition stiffness can be useful in design to accurately compute beam deflections beyond the serviceability limit states.

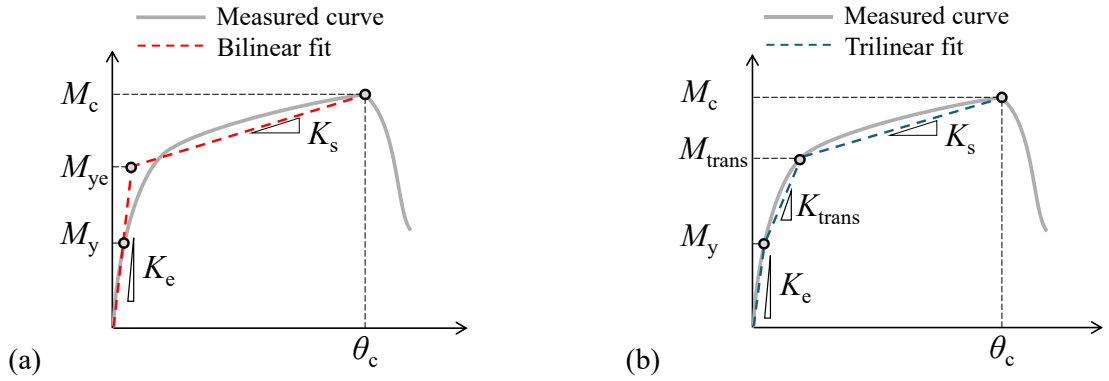

Fig. 2-14 Definition of key response parameters: (a) bilinear fitting curve; (b) trilinear fitting curve.

A systematic procedure was followed to deduce the response parameters in bilinear fitting curve using an automated MATLAB script, as demonstrated in Fig. 2-15. For each specimen, using linear interpolation, the digitised data was refined first by 100 points up to M_{max}. This is done to ensure consistency between specimens during the fitting procedure. The elastic stiffness (K_e) is the first parameter to be deduced. This can be challenging in some instances because the data curve may be noisy or highly nonlinear. Acknowledging the sensitivity involved in determining the initial stiffness slope, three numerical methods are used here to deduce K_e, as illustrated in Fig. 2-16. The median value of the three methods is then used. In the first method, Fig. 2-16(a), K_e is defined as the secant stiffness, joining the origin and the point at 1/3 M_{max}. This is because the yield moment is generally observed around this range. In the second method, Fig. 2-16(b) and Eq. 2-1, K_e is defined as the secant stiffness at point i where the difference between the secant stiffness (K^i_{secant}) and the average secant stiffness value of the previous points is larger than 20%. In the third method, based on Fig. 2-16(c) and Eq. 2-2, K_e is defined as the incremental stiffness between points i-1 and i when the difference of the incremental stiffness (K^i_{inc}) to the average stiffness of the previous increments is larger than 30%.

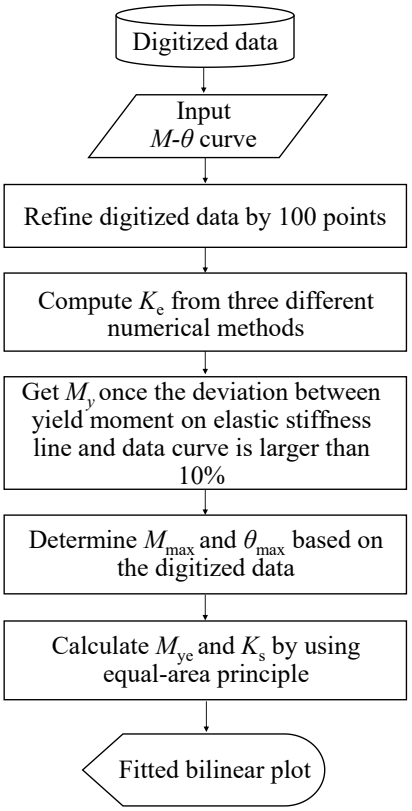

Fig. 2-15 Flowchart of the response parameters' deduction procedure.

Note that different K_e deduction methods may lead to a significantly different value. Several specimens deduced with three different methods for K_e are shown in Fig. 2-17. Generally, four types of curves are widely observed from the collected test data, which are: 1) smooth curve; 2) toothing curve; 3) straight elastic stage curve; and 4) nonlinear elastic stage curve. It is noticed that different deduction methods visually show a similar K_e. However, the difference in value can reach 55% to 60%, especially in cases 1 and 2. By comparing these three methods, Method 2 was chosen to deduce the K_e since this method adapts and provides a better effect for most specimens. For those specimens in which Method 2 cannot fit well, the elastic stiffness (K_e) was explicitly overwritten to adapt the M-θ curve or the envelop curves.

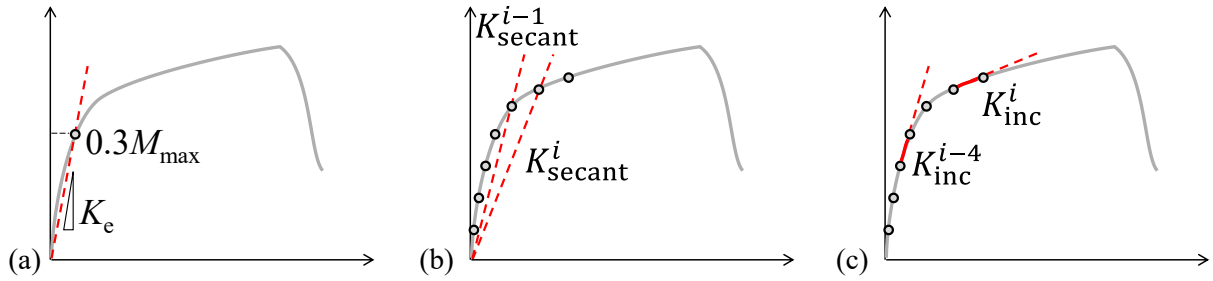

Fig. 2-16 Methods for deducing K_e based on: (a) 1/3 M_{max} secant stiffness, (b) average secant stiffness, and (c) average incremental stiffness.

$$K_e = \text{avg}\left(K_{\text{secant}}^{1\text{ to }i-1}\right) \text{ where, } \frac{K_{\text{secant}}^{i} - \text{avg}\left(K_{\text{secant}}^{1\text{ to }i-1}\right)}{\text{avg}\left(K_{\text{secant}}^{1\text{ to }i-1}\right)} \geq 0.2 \quad 2\text{-}1$$

$$K_e = \text{avg}\left(K_{\text{inc}}^{1\text{ to }i-1}\right) \text{ where, } \frac{K_{\text{inc}}^{i} - \text{avg}\left(K_{\text{inc}}^{1\text{ to }i-1}\right)}{\text{avg}\left(K_{\text{inc}}^{1\text{ to }i-1}\right)} \geq 0.3 \quad 2\text{-}2$$

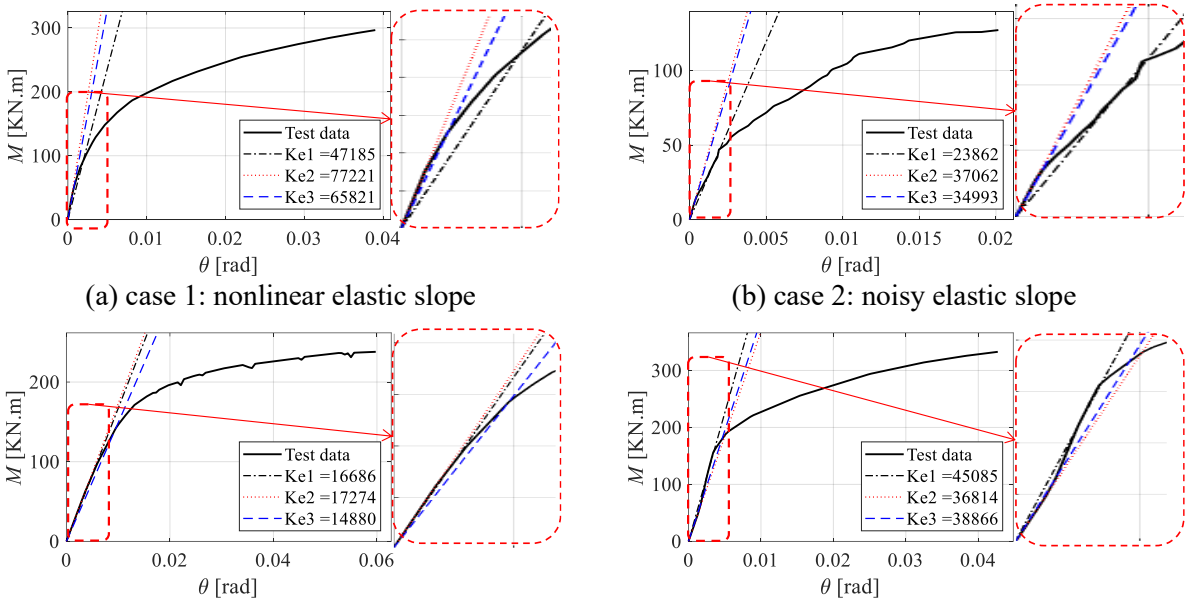

(a) case 1: nonlinear elastic slope (b) case 2: noisy elastic slope

(c) case 3: linear elastic slope (d) case 4: stiffening elastic slope

Fig. 2-17 Illustration of the K_e deduction methods based on different curve shapes.

Table. 2-2 Expected K_e variation for different cases based on sample specimens

Specimens	Case 1	Case 2	Case 3	Case 4
Variation [%]	60	55	25	22

The yield moment (M_y) was deduced as the first point at which the test curve deviates (with respect to rotation) from the K_e slope by more than 10%. The post-yield stiffness (K_s), which is the slope of the line joining the M_{max} and M_{ye} points, was then deduced. This was done based on the equal–area principle as demonstrated in Fig. 2-18(a). Essentially, K_s is the slope of the line originating from M_{max} at which the difference between area A (above the K_s line) and area B (below the K_s line) is minimum. The effective yield moment (M_{ye}) was deduced as the intersection point between K_e and K_s. For the trilinear fit, the transition stiffness K_{trans}, shown in Fig. 2-18(b), is deduced. This is done by first computing M_{trans} as the intersection point between the test curve and K_s. Following, K_{trans} is deduced as the line joining M_y and M_{trans}.

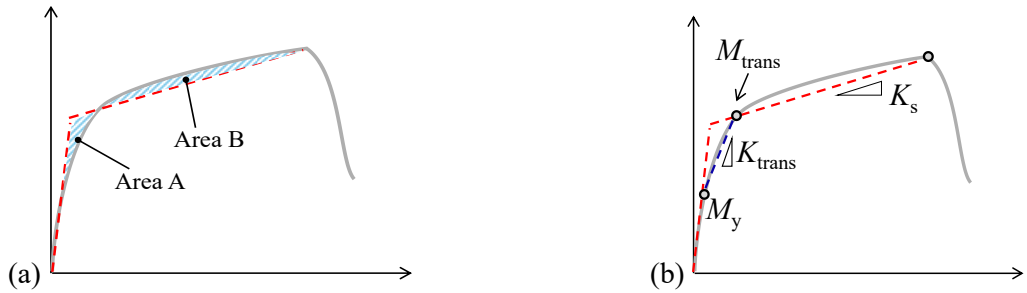

Fig. 2-18 Numerical method for deducing post-yield stiffness: (a) the equal-area method for deducing K_s in bilinear fitting; (b) the intersection method for deducing K_{trans} in trilinear fitting.

Fig. 2-19(a) shows an example of the bilinear fitting for a specimen that reached a maximum rotation of 4.2% rads. Fig. 2-19(b) shows the same specimen with the trilinear fitting. Note that not all specimens reached large rotations because failure occurred early without developing plastic deformations. Therefore, θ_{max} of 1.5% is used here as a cutoff for deducing the nonlinear response parameters. In such cases, only K_e and M_y can be deduced, which is linear fitting. This is demonstrated in Fig. 2-19(c).

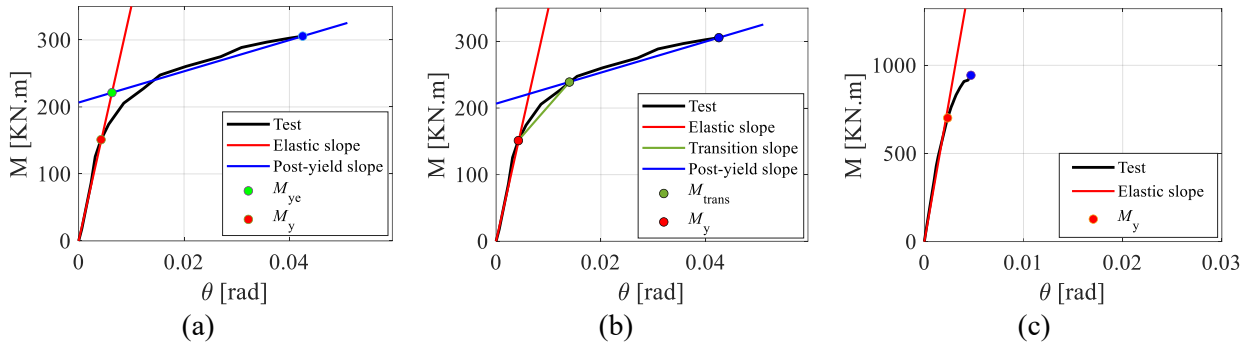

Fig. 2-19 Illustration of data fitting for specimens with (a) bilinear fitting: $\theta_{max} \geq 1.5\%$, (b) trilienar fitting: $\theta_{max} \geq 1.5\%$, and (c) linear fitting: $\theta_{max} < 1.5\%$.

Fig. 2-20 shows the distribution of the deduced key response parameters. It is observed that all response parameters have a substantial variability, which K_e, M_{ye}, and θ_{max} can reach up to 200000kN.m/rad, 1000kN.m, and 15% rads, respectively. This large-scale data can be used as the source for developing a more accurate and robust predictive model. However, the number of specimens developed K_e, M_{ye}, and θ_{max} over 80000kN.m/rad, 400kN.m, and 6% rads are limited, which is a data gap. This can be explained by the fact that reduced-scale specimens are often tested in place of full-scale components because of the capacity and space limitations of laboratory testing facilities. To supplement this data gap, a systematic parametric study using a well-defined finite element modelling approach has been conducted and described in the following sections.

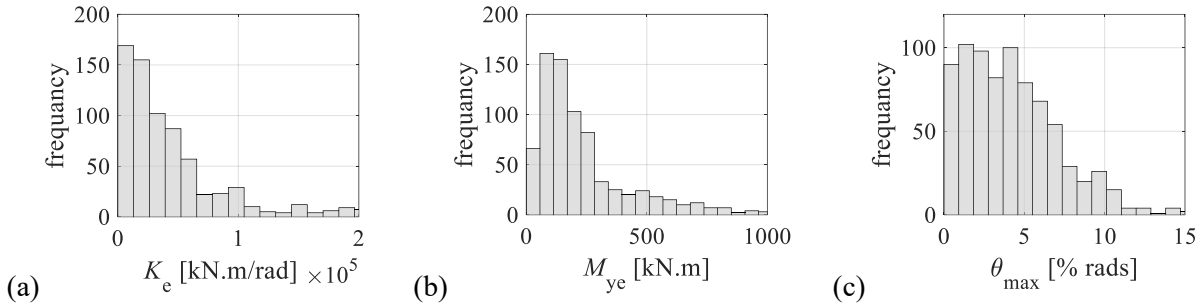

Fig. 2-20 Distribution of the deduced key response parameters: (a) K_e; (b) M_{ye}; and (c) θ_{max}.

Additionally, some specimens developed appreciable plastic deformation, however, the tests were terminated prior to the occurrence of failure (i.e., weld fracture or bolt rupture). In those cases, the capping moment (M_c) or maximum moment (M_{max}) was not attained and remained lower than expected. . For those specimens, as illustrated in Fig. 2-21, the true M_{ye} (based on complete test data) is expected to be slightly larger than the deduced one (based on incomplete test data), while the true K_s is expected to be somewhat smaller than the deduced one.

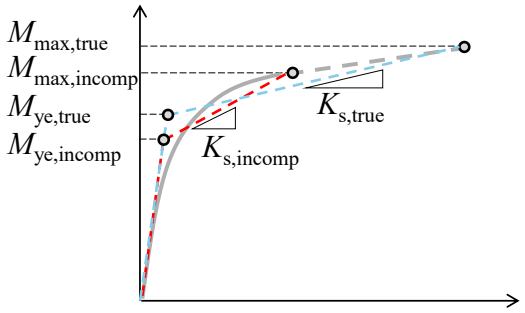

Fig. 2-21 Illustration of incomplete test data on deduced M_{ye} and K_s values.

To quantify how this may affect the deduced parameter values, some specimens (that reached their M_{max}) are re-fitted assuming they only reached 2% radians. Fig. 2-22(a) and (b) show the ratio of M_{ye} and K_s values based on complete and incomplete data, respectively. For the connection strength (M_{ye}), the incomplete data results in a strength that is 17% less than the actual strength data. For the post-yield stiffness (K_s), the actual value of K_s is an average of 50% of the incomplete data, which is more easily affected by the connection rotation. The ratio of M_{ye} and K_s can serve as a reference in further research, providing a reasonable assumption for incomplete specimens.

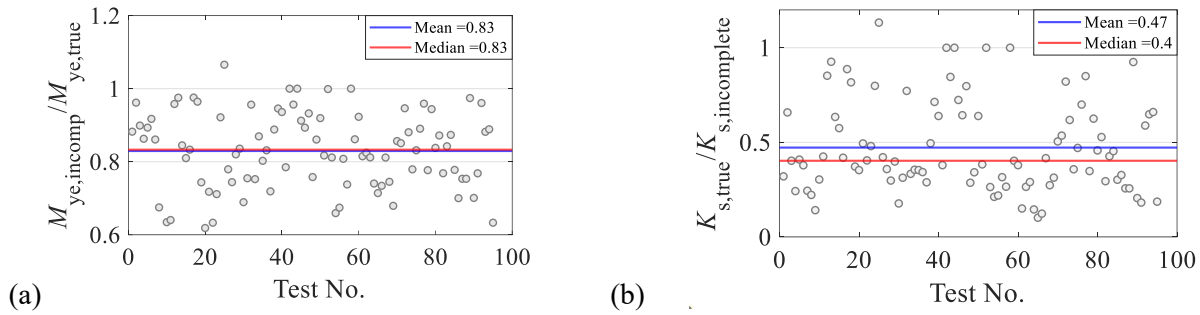

Fig. 2-22 The ratio of M_{ye} and K_s values based on complete (true maximum strength) and incomplete test data: (a) M_{ye} (θ_{max} > 2%); (b) K_s (θ_{max} > 2%).

2.6. Database organisation and accessibility

The database was stored in the format of Microsoft Excel (Database_EEPC.xls) and MATLAB R2021a (*Database_EEPC.mat*). The Excel database is used for modifying/updating existing specimens and adding new specimens. The MATLAB database is used for data tabulation, academic research, and analysis, including data fitting, processing, and plotting. The *M–θ* response data were digitised and stored using the folder hierarchy shown in Fig. 2-23. Table. 2-3 shows the naming convention used for the digitised data under monotonic and cyclic loading. The naming of digitised data considers the load type and the connection configuration. For the monotonic curves, the naming only includes the load type. For both the monotonic and cyclic envelopes, the negative and positive envelopes are all digitised. This is shown by [_Load direction]. For some interior connections, the *M-θ* curves for two beams were recorded, and the left (L) and right (R) beams are shown by [_Beam]. Therefore, the *M-θ* curves of the average of these two beams were stored. Photos were extracted from the different experimental research publications and stored in the database (under the "Photos" folder, see Fig. 2-23). These include photos of the test setup, instrumentation, connection geometric details, connection damage, *etc*. These photos were named based on the order ([Number][Category][Specimen ID][Note]). The database is made available through an interactive Graphical User Interface (GUI), which is now available to visualise each specimen, see Fig. 2-24. The GUI is publicly available for downloading at GitHub [61].

Table. 2-3 Description of naming and organising digitised data

Digitised data name	Curve type
Monotonic. mat	Monotonic curve data
Monotonic_Env[_Beam][_Load direction]. mat	Monotonic envelope
Cyclic_Env[_Beam][_Load direction]. mat	Cyclic curve data

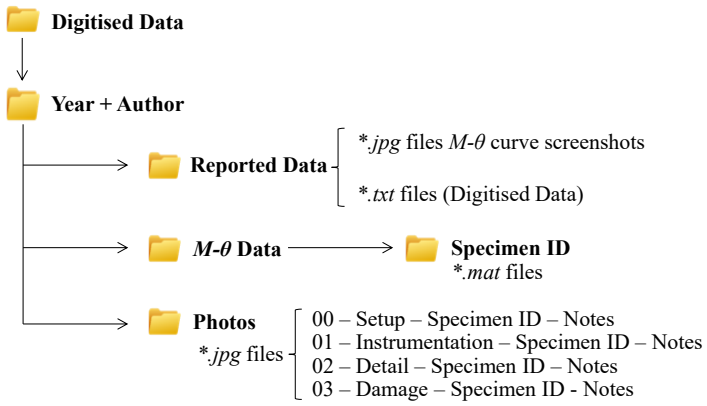

Fig. 2-23 Experimental database structure.

Fig. 2-24 Experimental database GUI: (a) digitised *M-θ* data and bilinear fitting; (b) reported photo of damage and failure mode(s).

2.7. Summary remarks

A digital experimental database of 843 bare-steel and composite EEPC specimens has been compiled from 148 publications dating to the 1960s. This database includes multi-attribute tabulated parameters, digitised *M-θ* curves, deduced response parameters, and reported photographs. A systematic framework was established for data curation, parameter tabulation to characterise each specimen's research origin, geometric and material properties, and observed damage modes. The *M-θ* curves were carefully digitised from original plots, and key response parameters for stiffness, strength, and ductility were subsequently deduced using a consistent numerical method. Furthermore, published photographs detailing experimental setups, instrumentation, and failure modes were extracted and catalogued. To facilitate users' interactions with this database, a downloadable GUI tool has been developed. This tool also integrates code-based and existing empirical models, allowing the users to directly compare theoretical predictions against the experimental *M-θ* data. This database serves multiple purposes: 1) it provides a benchmark for evaluating

the advantages and shortcomings of existing models; and 2) it can be used as the data source for developing more robust predictive models in the subsequent chapters.

3

ASSESSMENT OF EXISTING PREDICTIVE MODELS

3.1. Literature review

The nonlinear response arises from the simultaneous plastic deformations occurring in the various connections' components, including the endplate, the bolts, the column flange, the column web panel zone, and the beam. Due to the multitude of deforming components, predicting the response of SR connections can be challenging. In the literature, several researchers proposed numerical models to predict the connection response. These models can be categorised as analytical, mechanical or empirical models. In analytical approaches, the connection response parameters (mainly the elastic stiffness and the plastic moment capacity) are computed using analytical expressions that rely on the principles of solid mechanics and material behaviour. Examples of such models are the yield line method [62, 63] and the T-stub method [64]; the former is demonstrated in Fig. 3-1(a). In mechanical models, the connection components are idealised using a mechanical assembly of uniaxial springs and rigid elements; each of which represents the elasto-plastic response of the corresponding component. Note that the springs' elastic response is generally deduced from analytical methods. This method is demonstrated in Fig. 3-1(b). The most popular application of this method is the Eurocode3 component method [65].

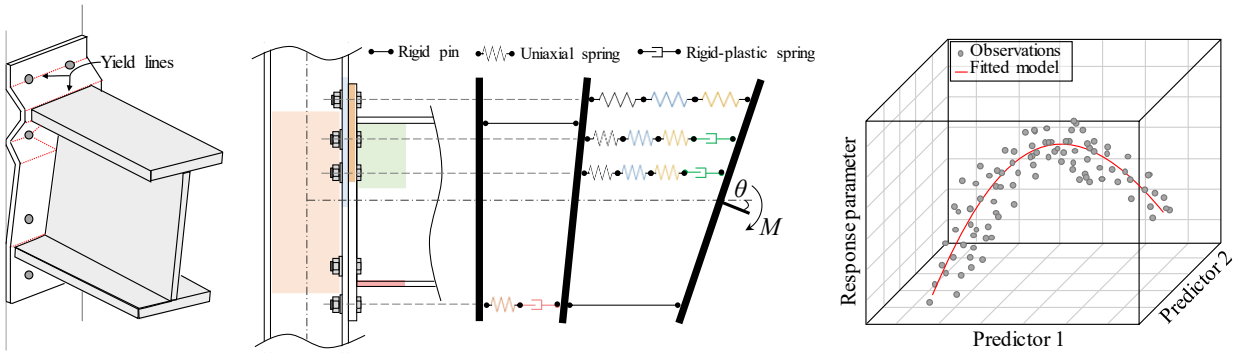

Fig. 3-1 Illustration of main numerical model types: (a) analytical [yield line method adapted from Eatherton et al [66]], (b) mechanical, and (c) empirical.

Lastly, in empirical models, regression analysis is conducted against experimental and/or simulation data to fit an empirical expression including several significant predictors, as illustrated in Fig. 3-1(c). These models are developed (and benchmarked) based on test/simulation data for a limited range of testing parameters (e.g., joint configuration, boundary conditions, applied load history, etc.) and connection configurations (e.g., connection geometry, materials, bolt pretension level, etc.). Consequently, model extrapolation beyond the validation data set design space may result in significant errors. Consequently, these models may still fall short of reliably predicting key response parameters. Moreover, analytical/mechanical models use simplified assumptions to idealise component deformation, while empirical models employ a limited number of predictors to simplify the regression procedure and the resulting empirical expression. As such, not all sources of deformation, as well as loading, material and geometric parameters influencing the response are accounted for. In fact, past brief assessments

demonstrated that the error in some of these models can exceed 100% in predicting the connection of the most fundamental response parameters, the elastic stiffness and plastic strength [49, 67].

Within the past two decades, there has been a stronger push towards the development of robust numerical models and acceptance criteria for different structural components [68, 69]. This is driven by the growing adoption of PBD approaches and the rise in computational capabilities. With that in mind, the objective of this section is to provide a summary review of existing numerical models (their type, development procedure, scope and limitations). Emphasis is placed on bare steel EEPCs with I-shaped columns, and existing models for connections with composite concrete slabs are ignored herein because they ultimately depend on predicting the response of the bare steel connection. The compiled comprehensive experimental database of more than 800 specimens compiled in Chapter 2 is utilised to consistently assess the robustness of these models in predicting the connection response. This assessment will highlight the strong aspects of existing models and their drawbacks to help inform future studies aiming to develop more robust numerical models.

3.2. Model types

The connection's M-θ response is represented by different models in the literature. This includes simple linear elastic models, bilinear and multilinear models, and continuous nonlinear models, as shown in Fig. 3-2. In linear models, only the K_e is predicted. In bilinear models, K_e as well as the M_{ye} or the M_u are predicted. In multilinear and continuous nonlinear models, the full moment-rotation response of the connection is predicted. Common nonlinear models include the three-parameter [70] and four-parameter [71] power models, as well as the Ramberg-Osgood model [72] as illustrated in Fig. 3-3. The three-parameter power model requires prior knowledge of K_e and M_u. The four-parameter power model additionally requires the post-yield stiffness K_s. The Ramberg-Osgood model requires prior knowledge of the anchor point coordinates (θ_0, M_0). All these nonlinear models require a model shape parameter η that describes the transition between the elastic and plastic branches. An elaborate summary of analytical models used to represent the M-θ curve can be found in the literature [48, 73-75].

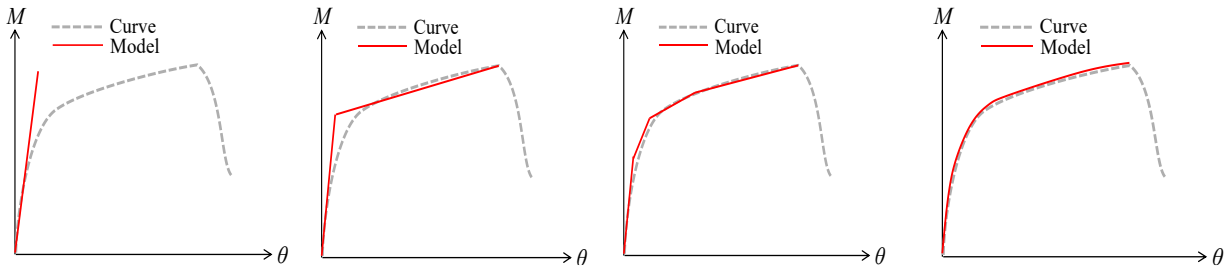

Fig. 3-2 Different analytical moment-rotation curves used in existing numerical models: (a) linear, (b) bilinear,(c) multilinear, and (d) nonlinear.

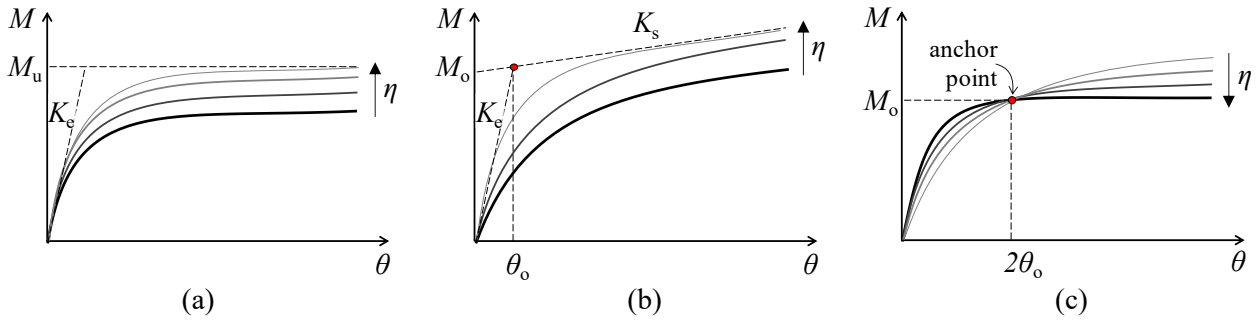

Fig. 3-3 Common nonlinear models: (a) Modified three-parameter power model, (b) Modified four-parameter power model, and (c) Ramberg-Osgood model.

Numerous studies and national standards provide equations to predict the aforementioned response parameters. These models are either based on the connection kinematics and principles of solid mechanics (i.e., analytical or mechanical models) or empirically derived through curve fitting, as discussed earlier. Analytical and mechanical models are generally robust as long as the underlying assumptions of the derivation are valid. However, they can be particularly laborious and usually too complex for application by practising engineers and researchers. This is due to the intrinsically complex elastic/inelastic behaviour of SR connections, which results from the multitude of deformable components within the connection (i.e., bolts, angles, plates, etc.) and the interaction between them. Empirical models, on the other hand, are advantageously simpler, making them favourable among engineers. In such models, regression analysis is conducted against a given experimental or simulation data set. The nonlinear equation, given by Eq. 3-1, is widely used in literature. This equation has an exponential form where RP is the predicted response parameter, X_i is the predictor i, which is generally a geometric or material parameter, and a_i is the exponent for predictor i. On the downside, these models may lack a physical basis, which can sometimes lead to unrealistic numerical responses. Plus, these models are generally as good as the number of significant predictors considered in the regression and the size/range of the dataset.

$$RP = a_0 \, (X_1)^{a_1} \, (X_2)^{a_2} \, \ldots \, (X_n)^{a_n} \qquad 3\text{-}1$$

3.3. Model assessment metric

The robustness of each model is assessed, and possible reasons behind the observations are discussed in this chapter. To evaluate a model's robustness in predicting a given response parameter X, the simple relative error metric, $\varepsilon(X)$, is computed using Eq. 3-2, where X_{test} and X_{model} are the values of the response parameter X as deduced from test data and predicted by the model, respectively. Accordingly, a negative error value implies a conservative model prediction and vice versa. For models that predict the M-θ curve directly, data fitting, as previously described, is conducted to deduce the relevant response parameters for comparison. In the next section, the error metric will be presented in scatter plots along with the values of the associated

median (μ). The rest of the error metrics, including the mean and median errors, standard deviation (σ) and max/min values, are summarised. The median represents the error tendency for the majority of the predictions, the mean reflects all errors, including the outliers, and the standard deviation can be used to evaluate the error variability.

$$\epsilon(X) = \frac{X_{\text{model}} - X_{\text{test}}}{X_{\text{test}}} \times 100\% \quad 3\text{-}2$$

3.4. Eurocode 3 Component Method

The component method is implemented in CEN [7]. This is a general method that can be used to evaluate the initial stiffness and flexural strength of different steel connections. The procedure of applying this method is 1) identify the relevant connection components; 2) evaluate the plastic resistance and stiffness of each component; 3) mechanically assemble all components to evaluate the initial stiffness and flexural strength for the whole joint. Fig. 3-4 illustrates the components in EEPCs. Above the beam's neutral axis, components are tensile bolts (*bt*), endplate in bending (*epb*), column flange in bending (*cfb*), column web in tension (*cwt*), and beam web in tension (*bwt*). Below the beam's neutral axis, components are the beam flange and web in compression (*bfc*) and column web in compression (*cwc*). Apart from all of those, the panel zone in shear (*cws*) is also considered. In this method, components are classified as elastic-plastic and rigid-plastic. The elastic-plastic component can impact both the initial stiffness and flexural strength, which are *cwt*, *cfb*, *epb*, *bt*, *cwt*, *cws*, and *cwc*. Note that the flexural strength and initial stiffness of the components under tension (i.e., *epb* and *cfb*) are computed using the analytical equivalent T-stub model, as illustrated in Fig. 3-4 and Fig. 3-5. The joint's flexural moment ($M_{j,Rd}$) and initial stiffness ($S_{j,ini}$) are computed by Eq. 3-3 and Eq. 3-4, respectively, h_r is the distance from the centre of each bolt row to the centre line of beam compressive flange, $F_{t,Rd}$ is the total design resistance, E is the Young's modulus, z is the equivalent lever arm, k is the stiffness factor, r is the bolt row number, and μ is the stiffness ratio.

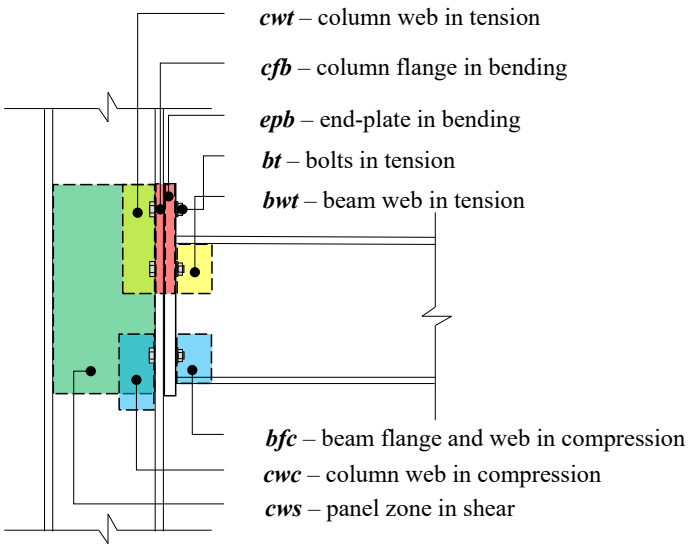

Fig. 3-4 Components of EEPCs.

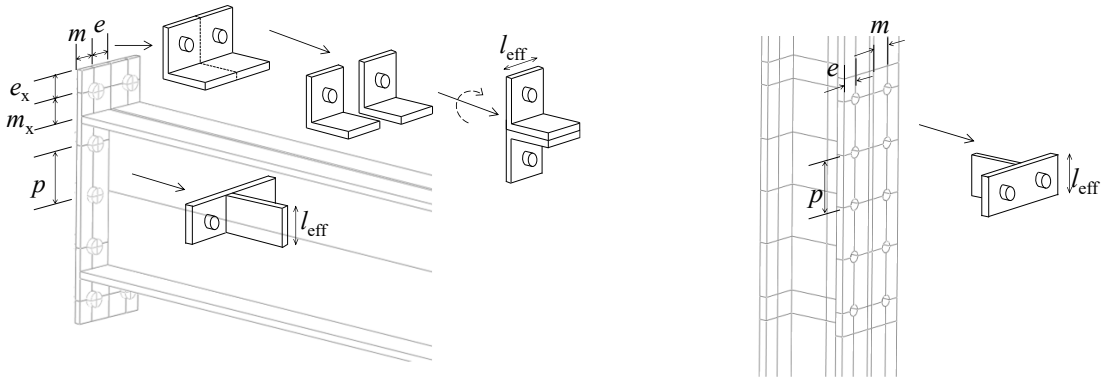

Fig. 3-5 T-stub components in EEPCs: (a) endplate side; (b) column side.

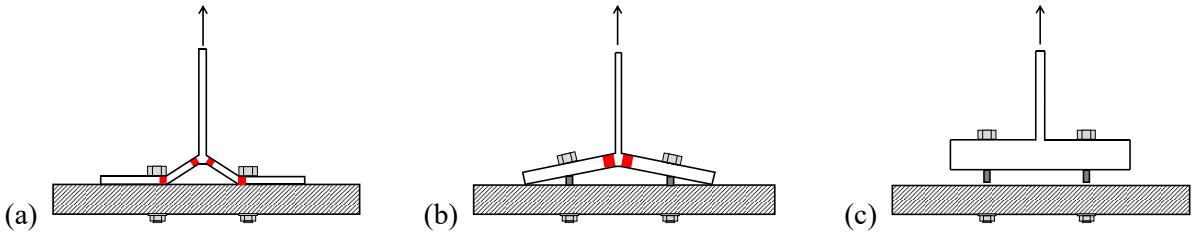

Fig. 3-6 T-stub failure modes: (a) mode 1; (b) mode 2; and (3) mode 3.

$$M_{\mathrm{j,Rd}} = \sum_{\mathrm{r}} z_{\mathrm{r}}\, F_{\mathrm{t,Rd}} \qquad 3\text{-}3$$

$$S_{\mathrm{j,ini}} = \frac{E\, z_{\mathrm{r}}^2}{\mu \cdot \sum_{\mathrm{r}} \frac{1}{k_{\mathrm{r}}}} \qquad 3\text{-}4$$

3.4.1. Assessment of $M_{j,Rd}$ and $S_{j,ini}$

A total of 409 beam-to-beam and beam-to-column specimens with I-shaped sections at the major axis are selected. Note that unit values are assumed for all partial safety factors. This is because the measured material properties are used. Besides, for specimens with four bolts per row, the method proposed by Demonceau et al [76] was employed. Fig. 3-7 shows the error of $M_{p,Rd}$ and $S_{j,ini}$. It is noticed that the mean and median errors are around -30% in Fig. 3-7(a). This means the component method underestimates the $M_{p,Rd}$. Several specimens are out of the range of ±50%. The inaccurate predictions for those specimens may be attributed to several factors. Firstly, the lack of reported measured material properties or geometric parameters in the literature may affect the l_{eff} of the equivalent T-stub. Besides, the assumptions of the component methods may also affect. Three discrete T-stub deformation modes are assumed based on predefined and idealised yield line patterns, which may not be accurate in some cases. This method also assumes the centre of the beam compression flange as the connection's rotation centre for different bolt rows. This is a major assumption, as the rotation centre is highly dependent on endplate thickness and bolt layouts. Relatively larger errors are observed in specimens with uncommon configurations, such as two-bolt rows above beam tensile flange, stiffened plates, and deep beams (h_b>700mm). The component method also ignores strain hardening and the membrane effect.

Referring to the prediction error of $S_{j,ini}$ in Fig. 3-7(b). The median error is close to 10%, which means the component method overestimates the $S_{j,ini}$. There is no observed correlation between the $S_{j,ini}$ error and geometric parameters, such as the ratio of t_{ep} to t_{cf}. Compared to $M_{p,Rd}$, $S_{j,ini}$ is a more sensitive and easily affected response parameter. Note that some specimens may be predicted with an error over 200%. This can be attributed to several aspects. It is noticed that several parameters are not considered in the component method, such as bolt pretension level and the load applied at either the beam or column. The data digitisation and deduction (see Chapter 2.5) may also affect the K_e assessment. Apart from all those potential reasons, the imperfections in the initial components may also affect the K_e, such as the small gaps between the rough surfaces of the column flange and endplate. Besides, test errors due to human factors may also affect the K_e.

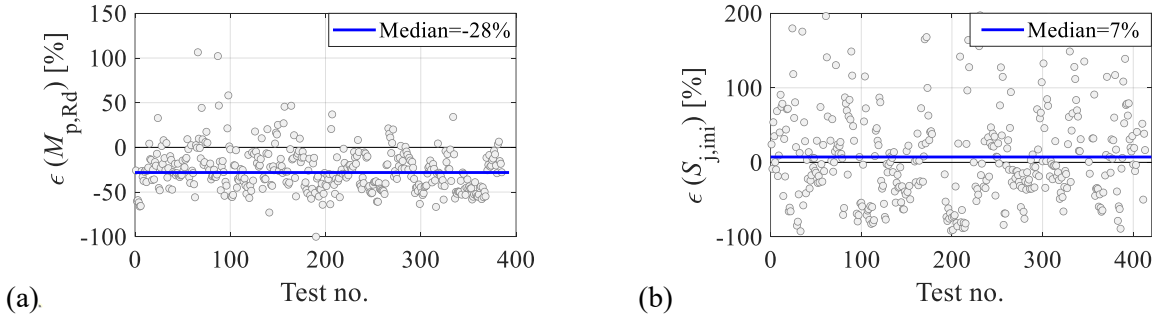

Fig. 3-7 Eurocode 3 component method: (a) $M_{p,Rd}$ error; (b) $S_{j,ini}$ error.

3.5. Yield Line Method

3.5.1. Code-based yield line pattern

The yield line method is a typical analytical method used for FR connection design in AISC Design Guide 4 [77] and AISC 358-16 [2]. In detail, the yield line analysis is based on the assumed plastic deformation. The assumed plastic deformation includes the facets and the yield line. Those analytical formulas for the yield line parameters (Y_p and Y_c) are based on the equilibrium of internal work and external work. The internal work is calculated by the plastic hinges along each yield line. The external work is calculated by the bending moment and axial force acting on the beam rotation. In Fig. 3-8, the yield line patterns of the unstiffened endplate and column flange with standard configuration are illustrated, as it is the most typical configuration used in practice. Due to the different bolt configurations and presence of stiffeners (i.e., plate rib stiffener or column flange stiffener), Eatherton et al [24] summarised the yield line patterns and formulas of yield line parameters for seven endplate and six column flange configurations. For example, the yield line parameter of the unstiffened 4-bolts endplate and column flange is computed by Eq. 3-5 and Eq. 3-6, respectively.

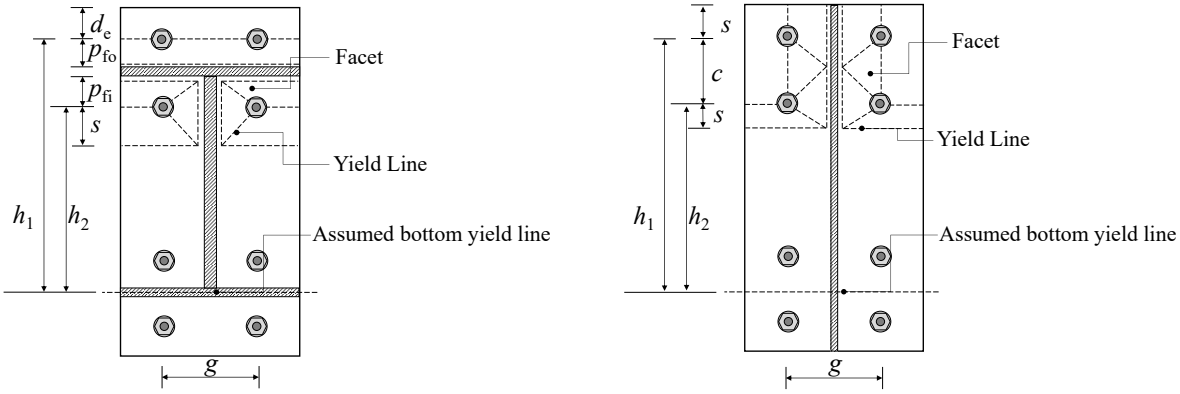

Fig. 3-8 Illustration of typical yield line patterns: (a) Unstiffened endplate; (b) Unstiffened column flange.

$$Y_p = \frac{b_{ep}}{2}\left[h_1\left(\frac{1}{p_{fo}}\right) + h_2\left(\frac{1}{p_{fi}} + \frac{1}{s}\right) - \frac{1}{2}\right] + \frac{2}{g}\left[h_2(p_{fi} + s)\right] \quad 3\text{-}5$$

$$Y_c = \frac{b_{cf}}{2}\left[h_1\left(\frac{1}{s}\right) + h_2\left(\frac{1}{s}\right)\right] + \frac{2}{g}\left[h_1\left(s + \frac{3\,c}{4}\right) + h_2\left(s + \frac{3}{4}\right)\right] + \frac{g}{2} \quad 3\text{-}6$$

Using the computed yield line parameters, the plastic moment resistances (M_p) of the endplate and column flange can be computed by Eq. 3-7. and Eq. 3-8. The SR/PS connection's M_p is then taken as the smaller value of $M_{pl,p}$ and $M_{pl,c}$. Note that the full-strength connections are also considered in this assessment. In detail, the smaller value of $M_{pl,p}$, $M_{pl,c}$, and $M_{pl,b}$ is taken as the plastic moment resistance.

$$M_{pl,p} = f_{yB}\, t_{ep}^2\, Y_p \quad 3\text{-}7$$

$$M_{\mathrm{pl,c}} = f_{\mathrm{yC}}\, t_{\mathrm{cf}}^2\, Y_{\mathrm{c}} \qquad 3\text{-}8$$

The yield line method is assessed here using beam-to-column specimens with I-shaped or rigid columns. This method considers the endplate and column flange dimensions, the bolt layout and the presence of stiffeners. Before assessing the model, the first step is to analyse the applicability and the potential shortcomings of the equations. One of the shortcomings of the yield line method is the assumed yield line patterns. Multiple yield line patterns can be assumed for a specific endplate or column flange configuration. Referring to Eatherton et al [24], there are, for example, three yield line patterns proposed for the endplate of a standard stiffened 4-bolts configuration. Ideally, the pattern that produces the least yield parameter value will control the design. However, this is always known in advance as it is dependent on different geometric parameters, such as the distance from the outermost bolt row to the endplate edge (d_e), as shown in Fig. 3-9. Eatherton observed that Pattern B is the least one once the d_e is smaller than 160mm, and Pattern A is the largest one once the d_e is less than 40mm. This indicates that, to apply the yield line parameter, it is necessary to select the appropriate yield line pattern so that the plastic moment can be closer to the real value. For simplicity, however, the proposed yield line parameter expressions used here are based on a single pattern (which controls for most but not all geometric ranges), potentially causing a relatively high error in the plastic moment for some specimens.

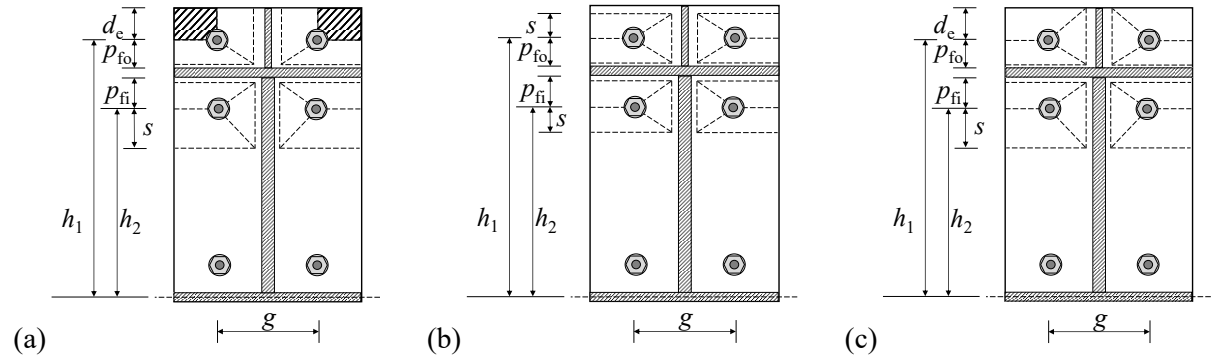

Fig. 3-9 Yield line patterns for standard 4-bolts stiffened endplate configuration: (a) Pattern A: Alternative in Eatherton et al [24]; (b) Pattern B: AISC 358-16 (when $d_e > s$, set $d_e = s$); (c) Pattern C: AISC 358-16 (when $d_e < s$).

The other potential issue with the yield line method is the lack of consideration of bolts. The d_b and bolt's material strength are frequently included in the prediction models for SR/PS connections. As the yield line method is typically used for designing FR connections, therefore, bolts are assumed and designed to be strong enough to resist plastic elongation. However, for the design of SR/PS connections, the bolt can be designed to develop the plastic elongation along with the excessive plastic deformation at the endplate and column flange. In this case, the yield line method may overestimate the connection's strength.

Fig. 3-10(a) and (b) show the error in M_p, prediction for the deduced M_{ye}, and the distribution of M_p error. The median error is -1%. For this method, the error is right-skewed distributed with a standard deviation of

±60%. Some specimens are scattered with errors exceeding 100% or falling below -50%. This means the yield line method cannot predict the connection strength very well in most cases. However, it is still noticed that several specimens are predicted with a substantial error.

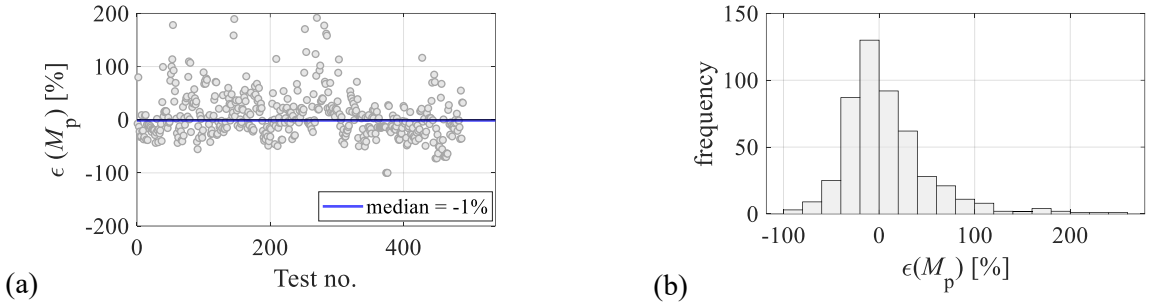

Fig. 3-10 Yield line method: (a) M_p error, (b) distribution of M_p error.

Component deformation or special design criteria may also significantly affect connection strength, such as brittle failure of bolts, premature weld failure, or unreasonable component size. Therefore, the error distribution against different damage modes is plotted and shown in Fig. 3-11(a). Weld failure means only those specimens fail at the weld. Bolt failure means the specimens only fail by bolt rupture or stripping. Endplate bending means the specimens develop visible plate plastic deformation. Column flange bending means the specimens only excessively deform at the column flange. Beam local buckling means the specimens buckled at the beam flange or web.

It is observed that the mean and median errors of specimens failed by weld or bolt failure are close to those damaged by endplate or column flange bending. It is found that the plastic strength of specimens that failed prematurely is, on average, 5% less than that of specimens with excessive plastic deformation. However, a specimen that failed due to weld failure shows an M_p error exceeding 100%. This is a specimen tested by Shi et al [78], which was stiffened by column and rib plate stiffeners. This specimen was supposed to develop excessive plastic deformation in the panel zone in shear. However, a weld crack occurred at the endplate and rapidly expanded to the rib plate stiffener when the panel zone showed a sign of plastic rotation. Therefore, the overestimated prediction is caused by premature weld failure and a deformation mode different from the assumption of the yield line method.

Although the mean and median of the prediction for specimens damaged by endplate and column flange bending are close to 0%, some specimens are either significantly overestimated or underestimated. Fig. 3-11(b) shows the correlation between the ratio of p_t to t_{ep} and the error of specimens damaged by EPB. It is observed that the prediction error shows a negative trend as the ratio of p_t to t_{ep} increases. Note that the yield line method easily overestimates the specimens controlled by EPB once the ratio of p_t to t_{ep} is less than 10. In detail, a total of 18 specimens are overestimated by over 50% and five specimens are overestimated by over 100%. The smaller value of p_t/t_{ep} means a smaller capacity of the endplate to develop excessive

plastic deformation. It is observed that those overestimated specimens developed a limited endplate bending and an excessive bolt elongation (i.e., Mode 2 in Eurocode 3). However, the yield line method did not consider the bolt material and mechanical properties, which are necessary for designing FR connections. Therefore, the plastic strength of those specimens is reduced due to the bolt elongation. Once the ratio of p_t to t_{ep} is larger than 10, the yield line method underestimates the plastic strength of all specimens. A total of 11 specimens is underestimated. All those specimens have an endplate thickness of less than 10mm and developed an excessive endplate bending (i.e., Mode 1 in Eurocode3). Most of those specimens are tested by Özkılıç [79], and the author also observed a similar underestimation by this yield method. Therefore, a total of 156 specimens were numerically simulated by Özkılıç [79]. It was found that the actual yield line patterns differ from those assumed by the yield line method. The difference in yield line pattern is mainly caused by the lack of consideration of bolt washer diameter and weld thickness. It is found that increasing the bolt diameter and weld thickness will enhance the plastic moment capacity, which means the p_{fo} and p_{fi} are reduced.

By using the same geometric parameters, the ratio of p_t to t_{ep}, it is observed that the error of M_p shows a positive correlation to the p_t/t_{ep} for specimens deforming by column flange bending, as shown in Fig. 3-11(c). Note that the yield line method easily underestimates the specimens with p_t/t_{ep} less than 5. The smaller value of p_t/t_{ep} indicates a larger capacity of the column flange to develop excessive plastic deformation. All those specimens were damaged by column flange bending, while bolts and endplates remained elastic during the test. However, it is found that the yield line patterns of those specimens do not fit the yield line pattern assumption. Those differences between the assumed and actual yield line patterns may be attributed to those specimens stiffened by a doubler plate or with four bolts per row. When p_t/t_{ep} is larger than 5, the yield line method easily overestimates the M_p. A total of 10 specimens is overestimated. All those specimens are damaged not only by column flange bending but also by slight endplate bending and bolt elongation. Therefore, the plastic strength of those specimens is less than the expected value. Besides, some specimens also developed a slight panel zone in shear or column web compression. However, the yield line method did not consider the effect of column web or panel zone deformation, so the M_p is easily overestimated once a specimen develops a slight plastic deformation.

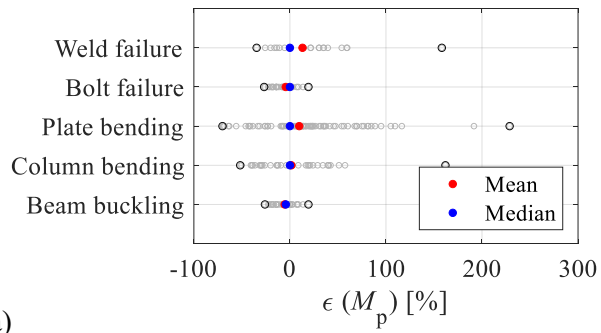

(a)

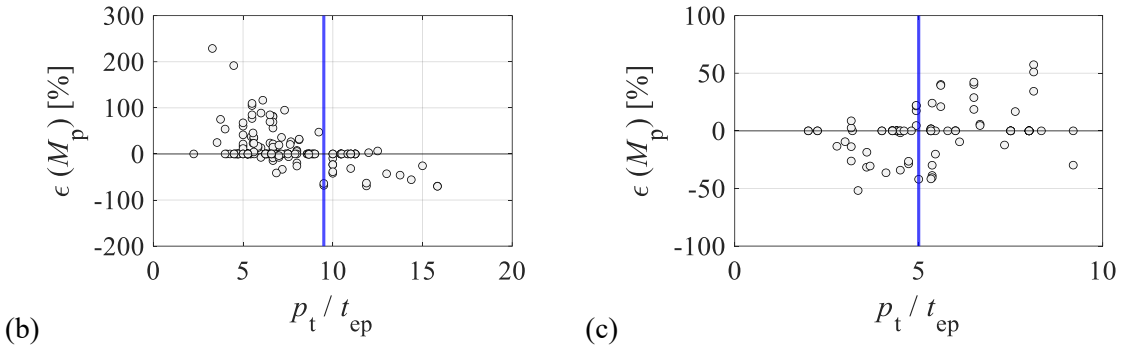

Fig. 3-11 Yield line method: (a) M_p error per damage mode, and M_p error versus p_t/t_{ep} for specimens controlled by (b) EPB; (c) CFB.

3.5.2. Proposed yield line pattern for thin endplate and large bolt diameter by Ozkilic

As mentioned in the previous section, the yield line method underestimates the M_p of specimens with thin endplates. Therefore, Özkılıç [79] proposed a new yield line pattern for a thin endplate and a large bolt diameter, which is shown in Fig. 3-12 and computed by Eq. 3-9, where d_w is the bolt washer diameter. This new yield line pattern was proposed by the CFE simulations of 156 specimens. The applicable range of those specimens follows as 1) beam section (IPE300 and IPE500); 2) column section (HEA 300 and HEA 500); 3) t_{ep} (6, 8 and 10mm); 4) d_b (24, 27, and 30mm); 5) g (90 or 160mm). Özkılıç [79] validated that the new yield line pattern average overestimates the M_p for specimens with a thin endplate by 17% error on average. To assess whether this new yield line pattern can accurately predict the M_p for other collected specimens with a thin endplate, several specimens are selected from the database, and this pattern is applied.

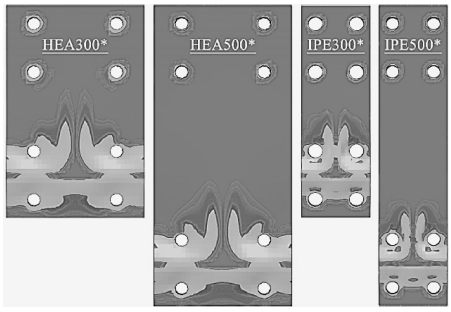

Fig. 3-12 Observed yield line patterns in Özkılıç [79]

$$Y_p = h_o\left[\frac{\frac{b_{ep}}{2}}{p_{fo}-0.5\cdot d_w-0.8\cdot t_{weld}}\right] + h_1\left[\frac{2\cdot s}{g-d_w-t_{cw}-0.8\cdot t_{weld}} + \frac{\frac{(b_{ep}-g)}{2}}{p_{fi}-0.5\cdot d_w-0.8\cdot t_{weld}} + \frac{\pi}{2}\right] \quad 3\text{-}9$$

Specimens tested by Özkılıç [79] are selected to assess the new yield line patterns, as shown in Fig. 3-13(a). The median error for all specimens is 22%. This matches the observation by Özkılıç [79]. Note that several specimens are predicted with an error over 50%. Therefore, several geometric parameters are selected to investigate how this new yield line pattern is affected. Fig. 3-13(b) shows the correlation between the M_p and p_t/t_{ep}. It is observed that the M_p shows a negative linear-trend correlation to the p_t/t_{ep}. Note that this new

yield line pattern easily overestimates M_p once the p_t/t_{ep} is smaller than 10. This is reasonable because this new yield line was proposed based on the specimens that failed by endplate fracture while bolts remained elastic (Mode1 in Eurocode 3). However, the smaller p_t/t_{ep} means a specimen may develop an excessive bolt elongation (i.e., Mode2 in Eurocode 3), so that the plastic strength is reduced.

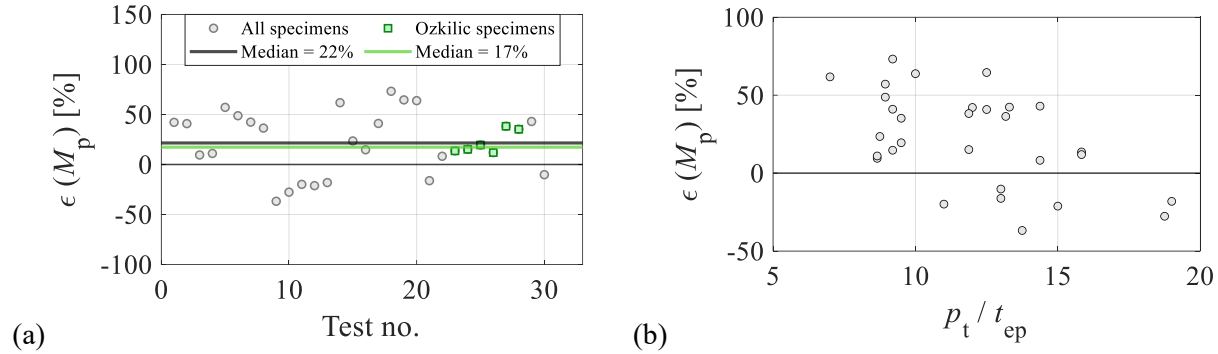

Fig. 3-13 Özkılıç [79] model: (a) M_p error, and (b) M_p error versus p_t/t_{ep}.

3.6. Kozlowski et al (2008)

Kozlowski et al [80] proposed an empirical model for K_e and M_p with four geometric parameters – t_{ep}, h_c, h_b, and d_b. This model is for the specimen with four bolts with a square layout at the beam tensile flange. The equation is different for three specimen setups: interior connections, exterior unstiffened connections, and exterior stiffened connections, as shown in Eq. 3-10(a) and (b). The applicability of this model is in the following range: t_{ep} = 12-30 mm, h_c = 140~400 mm (HEB sections), h_b = 160~400 mm (IPE sections), and d_b = 16~24 mm. This model considers different connection configurations, which is a good aspect. However, in terms of K_e, the column web is not considered in this model. The panel zone deformation generally decreases the K_e, especially for exterior unstiffened connections and interior connections under anti-symmetrical loading. Besides, bolt pretension is not included for K_e because a larger bolt pretension leads to a larger K_e. In terms of M_p, material properties are not included explicitly. This model assumes that the steel and bolt grades are S235 and 10.9, respectively. The bolt grade for most specimens is limited to 8.8 or 10.9, which is similar to the model assumption. However, the f_{ym} varies from 200 MPa to 800 MPa, which is beyond the model material's applicability. Besides, the g is assumed to be 3.5 times the d_b, the vertical bolt distance to the tensile beam flange (m_x) is considered to be 1.5 times the d_b, and the b_{ep} is assumed to be the average value of the b_{cf} and b_{bf}. Due to these model assumptions, there may be outliers for some specimens in model K_e or M_p perdition.

$$K_e = \begin{cases} 0.44\, h_c^{-0.22}\ h_b^{2.1}\ t_{ep}^{0.5}\ d_b^{-0.1} - 4896 & \text{interior} \\ 1.5\, h_c^{0.44}\, h_b^{1.2}\, t_{ep}^{0.35}\, d_b^{0.005} - 19211 & \text{exterior unstiffened} \\ 0.0563\, h_c^{-0.54}\, h_b^{2.49}\ t_{ep}^{0.99}\ d_b^{0.09} + 12714 & \text{exterior stiffened} \end{cases} \quad \text{3-10 (a)}$$

$$M_{\mathrm{p}}=\begin{cases}4.8\times10^{-4}\,h_{\mathrm{c}}^{0.24}\,h_{\mathrm{b}}^{1.31}\,t_{\mathrm{ep}}^{0.32}\,d_{\mathrm{b}}^{0.9}-21 & \text{interior}\\ 7.4\times10^{-5}\,h_{\mathrm{c}}^{0.62}\,h_{\mathrm{b}}^{1.2}\,t_{\mathrm{ep}}^{0.4}\,d_{\mathrm{b}}^{0.85} & \text{exterior unstiffened}\\ 5\times10^{-5}\,h_{\mathrm{c}}^{0.16}\,h_{\mathrm{b}}^{1.6}\,t_{\mathrm{ep}}^{0.36}\,d_{\mathrm{b}}^{1.1} & \text{exterior stiffened}\end{cases} \quad \text{3-10 (b)}$$

To assess this model, a subset of 419 specimens is used to evaluate K_{e}. These specimens are mild steel or stainless steel, with a single row above the beam tensile flange and two vertical bolt columns. All specimens are tested along the major axis. For those specimens with total rotation, the K_{e} is computed by eliminating the beam flexural stiffness. For those specimens where the beam is welded at the column top, the K_{e} is computed by removing either the beam or column flexural stiffness. The relative error of K_{e} is shown in Fig. 3-14. The median error is 98%. This means the model cannot predict the K_{e} accurately. Note that 222 specimens within the applicable range (i.e., red markers in Fig. 3-14) show a similar prediction. However, some specimens are still predicted with an error over 200%. No visible correlation between the K_{e} error and geometric parameters such as t_{ep}, p_{t}, d_{b}, and g is observed. This may be attributed to the complexity of predicting K_{e}. The equation of this model to predict K_{e} only explicitly includes four geometric parameters. Besides, the K_{e} equation was proposed using regression analysis for the results calculated by the component method in Eurocode3, indicating that the calculated K_{e} value for each specimen contains an error by Eurocode3. The average value of the K_{e} error by Eurocode3 can reach 80% for EEPCs. Therefore, several potential aspects may lead to an inaccurate prediction of K_{e}.

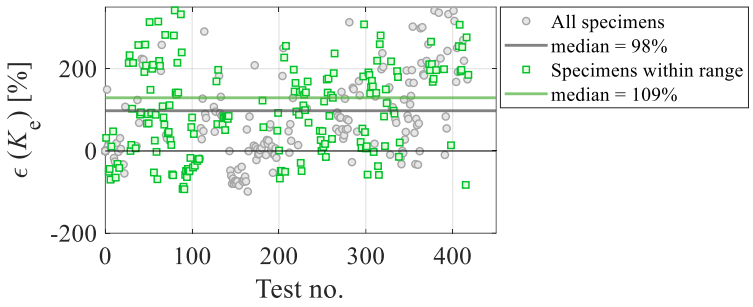

Fig. 3-14 Kozlowski et al [80]: K_{e} error.

There are 439 specimens used for assessing M_{p}. The M_{p} used for the assessment is consistent with the M_{ye}. Based on Fig. 3-15(a), the median error is -42%. Compared to the K_{e} prediction, this model shows a better performance in predicting M_{p}. However, it is still larger than the acceptable range of error (i.e., general ±20%). Those specimens within the applicable range are also assessed. No significant differences are observed between all specimen predictions and specimens in the applicable range. The median M_{p} error is similar to the average M_{p} error predicted by Eurocode3. Similar to the K_{e}, the equation for predicting M_{p} was also proposed using regression analysis for the results calculated by the component method in Eurocode3. This means inappropriate assumptions, such as the value of partial safety factors and effective T-stub length, may lead to underestimated predictions. Note that this model assumes all steels are grade S235. Therefore, the measured f_{yP} is used to investigate the potential correlation to M_{p}, which is shown in

Fig. 3-15 (c). It is observed that this model underestimates the M_p once the f_{yP} is larger than 355MPa, which is expected. This is because the larger steel grade will enable the connection to achieve both higher yielding and plastic strength.

In summary, the Kozlowski model is not good at predicting the K_e and M_p. In the K_e equations for all cases, column geometric parameters (e.g., t_{cf} and t_{cw}) are not considered. However, the deformation on the column flange and web easily and negatively affects the connection stiffness for both exterior and interior connections under anti-symmetric loading. Compared to the K_e prediction, the Kozlowski model performs better in predicting M_p. However, the mean of error is still larger than 30%. One of the key investigations is that the M_p prediction is affected by the measured f_{yP}.

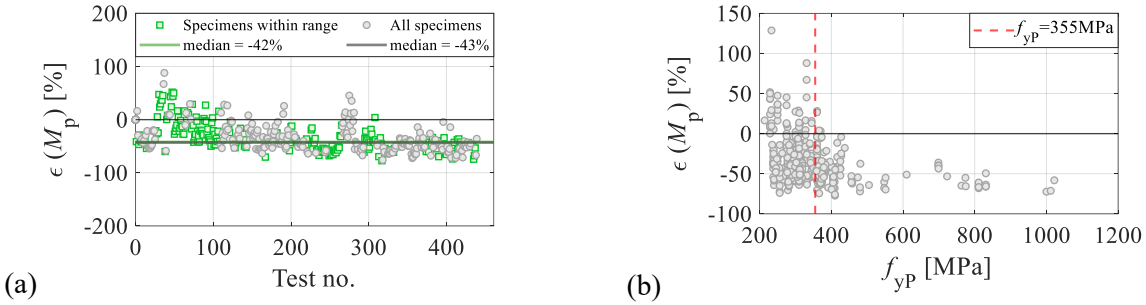

(a) (b)

Fig. 3-15 Kozlowski et al [80] model: (a) M_p error, (b) M_p error versus f_{yP}.

3.7. Terracciano and Della Corte (2018)

Terracciano et al [81] proposed a model for predicting K_e and M_p. It is an empirical model based on regression analysis and a self-proposed design chart for 52 specimens, which are combined by European I-shaped beams (IPE200 to IPE 750) and I-shaped columns (HEM120 to HEM 400). Those 52 specimens are the standard 8-bolt configuration (i.e., single bolt row above and below beam flanges). The K_e and M_p are computed by normalised stiffness (k_b) and normalised moment resistance (m_b), as given by 3-11 and 3-13. The k_b and m_b correspond to the strength coefficient (α) and stiffness coefficient (β). The k_b and m_b computations are defined using four geometric parameters: d_b, h_b, t_{cf}, and h_c. A cubic function is proposed for the k_b, as given by Eq. 3-12(a) to (d). Depending on the h_c, the m_b is calculated by two bilinear functions, as given by Eq. 3-14 (a) to (d). The model is applicable for the following ranges: d_b/t_{cf} = 0.5~1.5, h_b = 200~750mm, h_c = 140~430mm.

$$K_e = k_b \frac{E_b \cdot I_b}{L_b} \quad \text{3-11}$$

$$k_b = \left[8.343 \left(\frac{d_b}{t_{cf}}\right)^3 + 33.3 \left(\frac{d_b}{t_{cf}}\right)^2 + 47.32 \left(\frac{d_b}{t_{cf}}\right) + 0.865 \right] \frac{k_{b,1.5}}{25} \quad \text{3-12(a)}$$

$$k_{b,1.5} = \alpha_k h_b + \beta_k \quad \text{3-12(b)}$$

$$\alpha_{\mathrm{k}} = -1.35 \times 10^{-6}\, h_{\mathrm{c}}^2 + 10^{-3}\, h_{\mathrm{c}} - 0.188 \quad \text{3-12(c)}$$

$$\beta_{\mathrm{k}} = 2.39 \times 10^{-4}\, h_c^2 - 0.19\, h_{\mathrm{c}} + 53.12 \quad \text{3-12(d)}$$

$$M_{\mathrm{p}} = m_b\, f_{\mathrm{ymb}}\, Z_{\mathrm{x,b}} \quad \text{3-13}$$

$$m_{\mathrm{b}} = \begin{cases} \left[\, 2.205 \left(\frac{d_{\mathrm{b}}}{t_{\mathrm{cf}}}\right) - 0.524 \,\right] m_{\mathrm{b,1.5}} & \left(\, m_{\mathrm{b}} \le m_{\mathrm{b,1.5}} \text{ and HEM120}\sim\text{HEM140}\right) \\ \left[\, 1.690 \left(\frac{d_{\mathrm{b}}}{t_{\mathrm{cf}}}\right) - 0.371 \,\right] m_{\mathrm{b,1.5}} & \left(\, m_{\mathrm{b}} \le m_{\mathrm{b,15}} \text{ and HEM160}\sim\text{HEM400}\right) \end{cases} \quad \text{3-14(a)}$$

$$m_{\mathrm{b,1.5}} = \alpha_{\mathrm{m}} \cdot h_{\mathrm{b}} + \beta_m \quad \text{3-14(b)}$$

$$\alpha_{\mathrm{m}} = \begin{cases} -1.4 \times 10^{-7}\, h_{\mathrm{c}}^2 + 9.5 \times 10^{-5}\, h_{\mathrm{c}} - 0.0169 & (\text{HEM120}\sim\text{HEM280}) \\ 9.3 \times 10^{-4} & (\text{HEM300}\sim\text{HEM400}) \end{cases} \quad \text{3-14(c)}$$

$$\beta_{\mathrm{m}} = \begin{cases} -5.8 \times 10^{-3}\, h_c + 3.142 & (\text{HEM120}\sim\text{HEM280}) \\ 3.0 \times 10^{-3}\, h_{\mathrm{c}} + 0.344 & (\text{HEM300}\sim\text{HEM400}) \end{cases} \quad \text{3-14(d)}$$

Before the model assessment, there are some potential shortcomings in the model based on qualitative analysis of these given equations. In terms of K_e prediction, the endplate geometric parameter is not considered explicitly in the model. This may lead to some large errors because the endplate bending is one of the main deformations. Besides, this model does not categorise the specimen configurations. For instance, the panel zone shear deformation affects the K_e for these unstiffened exterior specimens and interior specimens under anti-symmetrical loading. In terms of M_p, material properties such as measured yield stress and Young's modulus are not covered in this model. This is one of the key parameters missed in the model. This is because each component's yield stress directly determines the specimen's overall yield moment resistance, while plastic moment resistance depends on the specimen's yield condition. On the other hand, the ratio of d_b to t_{cf} is used for K_e and M_p equations, which is not a common variable in prediction equations. Back to the parametric studies in this model, the endplate thickness (t_{ep}) and bolt diameter (d_b) are defined as the unknown design variables. Assuming t_{ep}/t_{cf} and d_b/t_{cf} varying from 0.5 to 1.5, normalised stiffness (k_b) and moment resistance (m_b) design charts (t_{ep}/t_{cf} as X-axis and d_b/t_{cf} as Y-axis) are computed by the given beam sections (IPE200 ~ IPE750). To involve all variables in a single equation, the ratio of d_b to t_{cf} is taken as the primary variable. The normalised stiffness (k_b) and moment resistance (m_b) are eventually computed based on the equation with d_b/t_{cf} and other shift factors (given by Eq. 3-12 and 3-14), which involved beam height (h_b) or column height (h_c).

To assess this model, a subset of 417 specimens is used, which involves exterior and interior connections with I-shaped columns fabricated from carbon and stainless steel. These specimens are all tested about the major axis. Note that model assumptions 1) column flange stiffener at both sides and 2) t_{ep}=t_{cf} are not considered. The K_e is computed from k_b using Eq. 3-11, where the length of the beam (L_b) is taken as 7.5m, which is similar to what is assumed in the model. Based on Fig. 3-16(a), the median of K_e error is 68%. This

means the model overestimates K_e. This is mainly attributed to the lack of critical geometric parameters, such as p_t. To investigate the effect of p_t on the prediction, the ratio of p_t to t_{ep} is selected, and the correlation between this ratio and absolute K_e error for specimens in the range is shown in Fig. 3-16(b). It is observed that the absolute error becomes larger with the increase of p_t/t_{ep}. This indicates that the model cannot accurately predict the K_e when specimens develop excessive endplate bending as the p_t is not considered.

The M_p is computed from m_b by Eq. 3-13 and Eq. 3-14. Fig. 3-17(a) shows the error of M_p. The median error is 41%, which means the M_p is overestimated. This reflects that the model also cannot predict the M_p accurately. Based on Eq. 3-14, h_b and h_c are the main variables in M_p computation. Therefore, the correlation between absolute M_p error and $h_b/(t_{ep}\, d_b)$ for specimens in the range is investigated, as shown in Fig. 3-17(b). With the increase of $h_b/(t_{ep}\, d_b)$, the M_p prediction becomes larger. The specimens with large $h_b/(t_{ep}\, d_b)$ have relatively thin endplates and large bolts. Therefore, the connections may easily develop excessive endplate yielding, which affects the M_p. In future research, p_t shall be considered as one of critical geometric predictors for both the K_e and M_p.

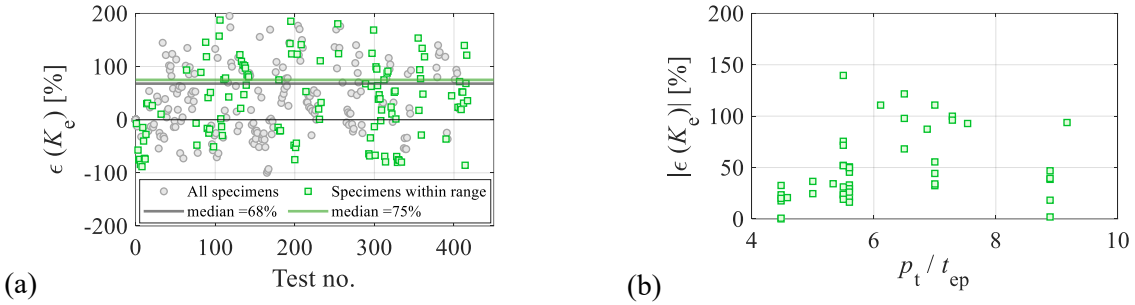

Fig. 3-16 Terracciano et al [81] model: (a) K_e errors; (b) correlation between the absolute K_e error versus p_t/t_{ep} for specimens in the range.

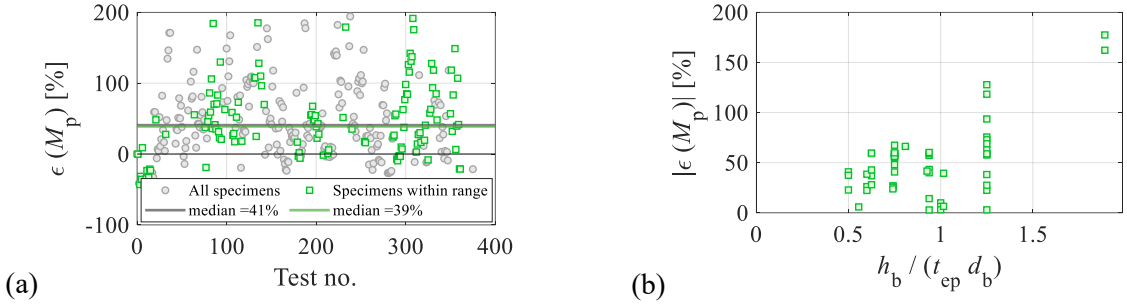

Fig. 3-17 Terracciano et al [81] model: (a) M_p errors; (b) correlation between the absolute M_p error versus $h_b/t_{ep}/d_b$ for specimens in the range.

3.8. Eladly and Schafer (2021)

Eladly and Schafer [20] proposed a model for predicting the M-θ curve for stainless steel connections. It is a non-linear empirical model developed through regression analysis of data from 180 finite element

simulations. Those 180 specimens have a typical 8-bolt configuration (i.e., single bolt row above and below the beam flanges) with stiffened columns. The model is based on the *M-θ* curve by Richard and Abbott [71], as shown in Fig. 3-3. This model is defined using five parameters: K_e, $K_{s,tan}$, M_o, η, and θ_u. These empirical equations were developed (using MVLR model) to compute these parameters for connections with stiffened and unstiffened endplates, as given by Eq. 3-15 to Eq. 3-18. These equations consider the geometric parameters of t_{ep}, t_{cf}, g, h_b, Z_1 (i.e., distance from the first bolt row to the bottom beam flange), Z_2 (i.e., distance from the second row to the bottom beam flange), $t_{stiff,P}$, and d_b, as well as the material properties of f_{yp}, f_{uP}, and E_p. The applicability of this model is valid for the following ranges: t_{ep} = 8 to 12 mm, d_b = 12 to 16 mm, h_b = 240 to 300 mm. In terms of qualitative analysis, there are several good aspects in this model: 1) The equations are separated into groups based on the presence of plate stiffener, and 2) apart from typical geometric parameters, material properties are also considered, which is important for predicting M_o, $K_{s,tan}$, and θ_u.

$$K_e = \begin{cases} 1.24 \times 10^{-5}\ t_{ep}^{0.81}\ t_{cf}^{0.31} g^{-0.24} (h_b - Z_2)^{-0.13}\ (Z_1 - h_b)^{-0.15}\ h_b^{2.67}\ d_b^{0.96}\ f_{yP}^{0.06}\ E_P^{0.17} \\ 1.06 \times 10^{-6}\ t_{ep}^{0.51}\ t_{cf}^{0.15}\ g^{-0.2}\ (h_b - Z_2)^{-0.19}\ (Z_1 - h_b)^{-0.02}\ h_b^{1.90}\ d_b^{0.77}\ f_{yP}^{0.22}\ E_P^{0.77}\ t_{stiff,P}^{0.11} \end{cases} \quad 3\text{-}15$$

$$M_o = \begin{cases} 2.97 \times 10^{-4}\ t_{ep}^{1.02}\ g^{-0.11}\ (h_b - Z_2)^{-0.13}\ (Z_1 - h_b)^{-0.18}\ h_b^{1.05}\ d_b^{1.17}\ f_{yP}^{0.42} \\ 2.83 \times 10^{-3}\ t_{ep}^{0.55}\ g^{-0.04}\ h_b^{0.71}\ d_b^{1.31}\ f_{yP}^{0.26}\ t_{stiff,P}^{0.03} \end{cases} \quad 3\text{-}16$$

$$K_{s,tan} = \begin{cases} 1.22 \times 10^{-5}\ t_{ep}^{0.39}\ t_{cf}^{0.23}\ g^{-0.25}\ (h_b - Z_2)^{-0.1}\ (Z_1 - h_b)^{-0.13}\ h_b^{2.85}\ d_b^{0.64}\ f_{yP}^{0.07}\ f_{uP}^{0.02} \\ 1.01 \times 10^{-4}\ t_{ep}^{0.85}\ t_{cf}^{0.27}\ g^{-0.31}\ (h_b - Z_2)^{-0.19}\ (Z_1 - h_b)^{-0.16}\ h_b^{2.43}\ d_b^{0.32}\ f_{yP}^{0.1}\ f_{uP}^{0.03}\ t_{stiff,P}^{0.38} \end{cases} \quad 3\text{-}17$$

$$\eta = \begin{cases} 2.6\ \times 10^{-3}\ t_{ep}^{0.9}\ t_{cf}^{0.38}\ g^{-0.21}\ (h_b - Z_2)^{-0.24}\ (Z_1 - h_b)^{-0.21}\ h_b^{0.49}\ d_b^{-0.59}\ f_{yP}^{0.95} \\ 8.5\ \times 10^{-4}\ t_{ep}^{0.8}\ t_{cf}^{0.12}\ g^{-0.30}\ (h_b - Z_2)^{-0.16}\ (Z_1 - h_b)^{-0.05}\ h_b^{0.52}\ d_b^{-5.65}\ f_{yP}^{1.05}\ t_{stiff,P}^{0.33} \end{cases} \quad 3\text{-}18$$

$$\theta_u = \begin{cases} 0.61\ t_{ep}^{-1.00}\ t_{cf}^{-0.30}\ g^{0.25}\ (h_b - Z_2)^{0.56}\ (Z_1 - h_b)^{0.13}\ h_b^{-1.03}\ d_b^{1.21}\ f_{yP}^{-0.10} \\ 1.82\ t_{ep}^{-1.03}\ t_{cf}^{-0.32}\ g^{0.19}\ (h_b - Z_2)^{0.59}\ (Z_1 - h_b)^{0.10}\ h_b^{-1.12}\ d_b^{1.42}\ f_{yP}^{-0.17}\ t_{stiff,P}^{-0.25} \end{cases} \quad 3\text{-}19$$

To assess the model, a subset of 432 specimens is used, involving exterior beam-to-column connections with I-shaped columns fabricated from either conventional carbon steel (401 specimens) or stainless steel (31 specimens). Carbon steel specimens are included in the model assessment since carbon steel and stainless-steel show similar behaviour in the elastic range. Also, the model considers the endplate Young's modulus as a predictor for K_e. All these specimens' columns are stiffened at both beam flange levels. The endplate measured yield stress for stainless steel specimens at 0.2% offset strain, $f_{y,0.2}$, is used as defined in the model. For carbon steel specimens, the endplate-measured yield stress is used for the same parameter. The K_e and M_o are validated using the same parameters derived from the collected specimens. Fig. 3-18(a) and Fig. 3-18(b) show the error for K_e and M_o, respectively. Based on Fig. 3-18(a), the median K_e error is equal to -9%. This model cannot predict the K_e accurately as the median of error is still larger than the acceptable error (typically, 0% ~ ±30%). For most specimens, the error is negative, with a standard deviation of ±116%. This means the model underestimates K_e. This is in part because the model only considers the d_b

and ignores the P_t, which can significantly influence K_e. In the model, no pretension load is applied to bolts. However, the higher P_t, the higher K_e [31, 82]. On the other hand, the column panel zone deformation is not considered in this model. This can be explained by the fact that the model is based on connections controlled by endplate bending, which results in no obvious panel zone deformation in CFE models. However, the interior stiffened specimens easily develop the panel zone shear deformation under anti-symmetrical loading. There are four specimens with the large errors (>3σ). Those specimens are from the test by Ryan [83] in which slender beams and columns (class 4 as per CEN [7]) are used. These beams are beyond the model applicability range. This is demonstrated in Fig. 3-19(a), which shows the correlation between the absolute value of errors and the beam depth. Note that in the database, there is a lack of test data for beams deeper than 610mm. Therefore, more specimens with the beam (h_b >610mm) may need to be collected to investigate the model's robustness further and confirm this observation.

The error for M_o is shown in Fig. 3-18(b). There are 425 specimens available. Based on Fig. 3-18(b), the median error is equal to -15%. Similar to the K_e, the model underestimates M_o for most specimens. Most errors are negative and right skewed, with a standard deviation of ± 35%. Based on Fig. 3-19(b), it is observed that the error is correlated with the h_b/t_{ep}. For deep beams with relatively thin endplates (h_b/t_{ep} > 18), the model tends to underestimate M_o. For these specimens, the controlling deformation is endplate excessive bending. This may lead the connections to yield quickly. While for shallow beams with relatively thick endplates (h_b/t_{ep} < 12), the model overestimates M_o. The controlling deformation is the column web local buckling. Due to the shear deformation in the column panel zone, M_o decreases. However, in the model, the web of the utilised column section was relatively stocky (h_c = 240mm and t_{cw} = 10mm) and did not undergo excessive deformation. This leads to an overestimated prediction in the model. In future research, the prediction equations of M_o may be separated into groups based on h_b/t_{ep} due to the different controlling deformation modes.

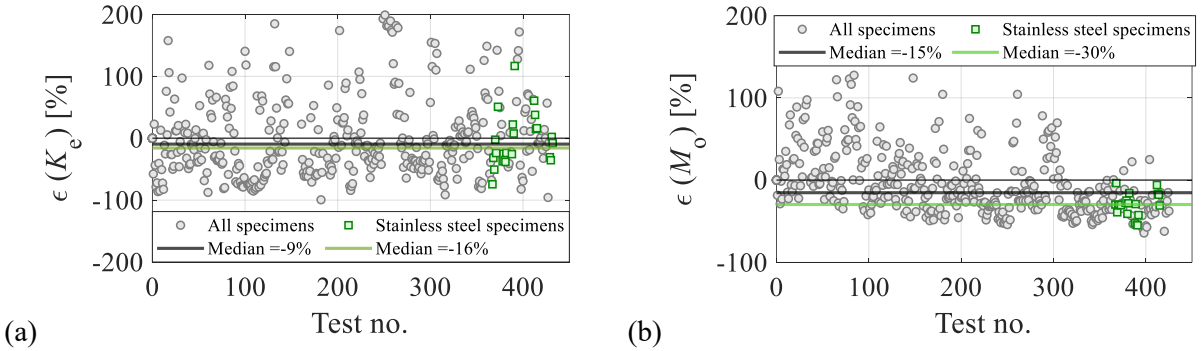

Fig. 3-18 Eladly and Schafer [20]: (a) K_e error; (b) M_o error.

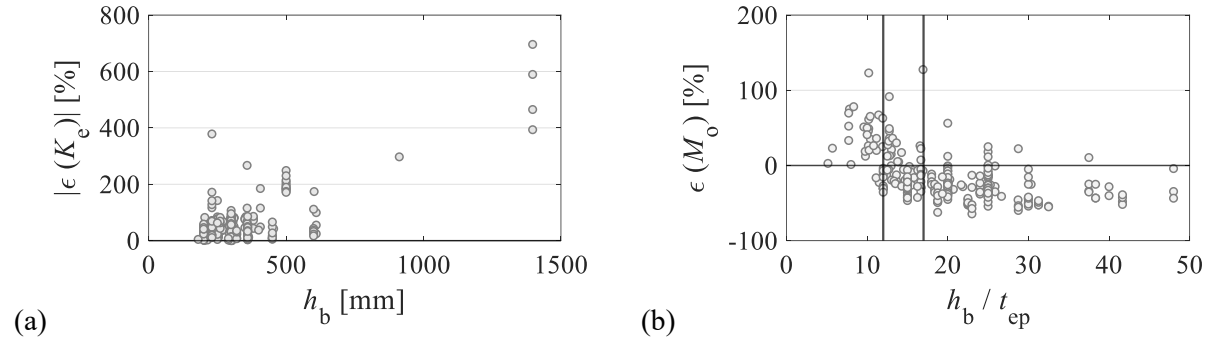

Fig. 3-19 Eladly and Schafer [20]: correlation between model errors and geometric parameters for all specimens: (a) absolute K_e error versus h_b; (b) M_o error versus h_b/t_{ep}.

The error for the ultimate rotation (θ_u) for 131 specimens is shown in Fig. 3-20. Note that θ_u corresponds to θ_C as deduced from test data. This model easily overestimates θ_u for carbon steel specimens. Based on the prediction of these 16 stainless-steel specimens, this model predicts the results accurately, with the median error within ±6%. Therefore, the failure mode and material properties shall be considered in future research for θ_u prediction, regardless of whether the material is carbon or stainless steel. However, due to the limited number of stainless-steel specimens, the performance of this model with a larger number of specimens remains uncertain. Therefore, more data collection on stainless-steel specimens shall be carried out.

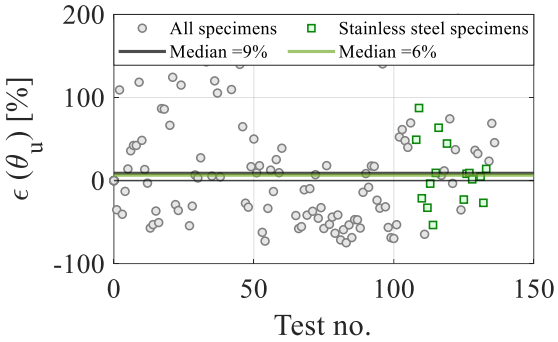

Fig. 3-20 Eladly and Schafer [20] model: θ_u error.

3.9. Tartaglia et al (2021)

Tartaglia et al [84] proposed a compliant design procedure for SR/PS EEPCs based on AISC [85]. In this design method, the required connection parameters (i.e., t_{ep}, t_{cf}, and d_b) are determined using the yield line theory (see Eatherton et al [24] and Section 3.5 for details). This procedure, as illustrated in the flowchart shown in Fig. 3-21, is employed herein to determine the classification of the connections (i.e., where the connection is FR, SR with brittle behaviour or SR with ductile behaviour). The procedure is as follows:

(1) Input connection parameters: Specific geometrical parameters and material properties are extracted from the database for each specimen. This includes bolt configuration, bolt pitch, component thickness, component size, and nominal material yield strength.

(2) Compute the yield line parameters (i.e., Y_p and Y_c) based on the yield line parameters formulas summarised by Eatherton et al [24]. The endplate yield line parameter is based on the bolt configuration and the presence of plate rib stiffeners. The column flange yield line parameter is based on bolt configuration and the presence of column flange stiffeners.

(3) Overstrength factor (C_{pr}): In AISC [85], the EEPC is designed as FR. Therefore, the C_{pr} is assigned as 1.1 to ensure the plastic hinge is at the beam. The overstrength coefficient proposed by Tartaglia et al [84] is calculated based on the endplate nominal yield and ultimate strength.

(4) Compute the bending moment at the column face (M_{cf}): M_{cf} is equal to the sum of the expected moment at the beam plastic hinge (M_{pr}) and additional shear resistance moment, as shown in Eq.3-20 and Eq.3-21. The dead load and live load on the slab (w_g) are assigned as 4KN/m^2 and 1KN/m^2, and the structure bay width is 6m, based on the structural design by Flores et al [86]. Therefore, the w_g along the beam is assumed as 30KN/m. The distance from the column face to the plastic hinge (S_h) depends on the presence of a plate rib stiffener. For the unstiffened connections, S_h is the minimum value of h_b /2 or 3 b_{bf}. For the stiffened connections, S_h is the distance from the column face to the edge of rib stiffener (i.e., $t_{ep} + L_{rib}$).

$$M_{cf} = M_{pr} + \left(\frac{2\,M_{pr}}{L_b} + V_{gravity}\right) s_h \qquad 3\text{-}20$$

$$V_{gravity} = \frac{w_g\ L_b}{2} \qquad 3\text{-}21$$

(5) Compute the required bolt diameter ($d_{b,req}$): The minimum bolt diameter depends on the M_{cf}, resistance factor (ϕ_n), and the number of tension bolt rows, as computed by using Eq. 3-22. In the procedure by Tartaglia et al [84], the ϕ_n is assigned as 0.9. This is to force the bolts to generate non-ductile behaviour. There are three conditions of bolt rows: two, three, and four. The distance (h_i) is from the centreline of each bolt row to the centreline of the compressive beam flange.

$$d_b = \sqrt{\frac{2\,M_{cf}}{\pi\ \phi_n \sum_{i=1}^{i=n} h_i}} \qquad 3\text{-}22$$

(6) Compute the required endplate thickness ($t_{ep,req}$) and column flange thickness ($t_{cf,req}$): The summarised yield line parameters are used to compute the required thickness. In the procedure by Tartaglia et al [84], the ϕ_d is assigned as 1. The material properties are all nominal endplate and column yield strength.

(7) Design check for t_{ep}, t_{cf}, and d_b: After computing all key parameters, the specimen's t_{ep}, t_{cf}, and d_b are compared with the required ones to check the connection classification. If all three geometric parameters are larger than the required values, this means the specimen is an ES connection (i.e., damage is expected to occur in the beam) at least. If one of the three geometric parameters is less

than the required value, it indicates that the specimen is a PS connection. Therefore, there is a need to conduct an additional check to determine if this SR connection is ductile.

(8) Check the ductility of PS connections: If a specimen is classified as a PS connection, the required bolt diameter is recalculated by using a C_{pr} value of 0.8 to satisfy the PS requirement by Eq. 3-23. This is to ensure the bolts are strong enough for the endplate to develop visible plastic deformation. If the computed bolt diameter based on C_{pr} equal to 1 is smaller than the bolt diameter in the test, this means the specimen is ductile and partial strength. Otherwise, the specimen is classified as brittle and SR.

$$d_{b,req\_ductile} = C_{pr}\, t_{ep} \sqrt{R_y} \sqrt{\frac{\phi_d\, f_{ynP}\, Y_p\, 2}{\phi_n f_{ynb} \sum_{i=1}^{i=n} h_n 1.11\pi}} \quad \text{3-23}$$

(9) Re-design for ES connections with other C_{pr}: For those with at least ES connections, the C_{pr} is changed from 1 to 1.2 (C_{pr} = 1.2 based on Tartaglia et al [87]) to classify if the connection is FR or ES. If all computed geometric parameters are smaller than the specimen's, this means the specimen is FR.

(10) Specimen classification: Through computing all those parameters, there are three types of connection classified, which are FR, ES, ductile SR, and brittle SR.

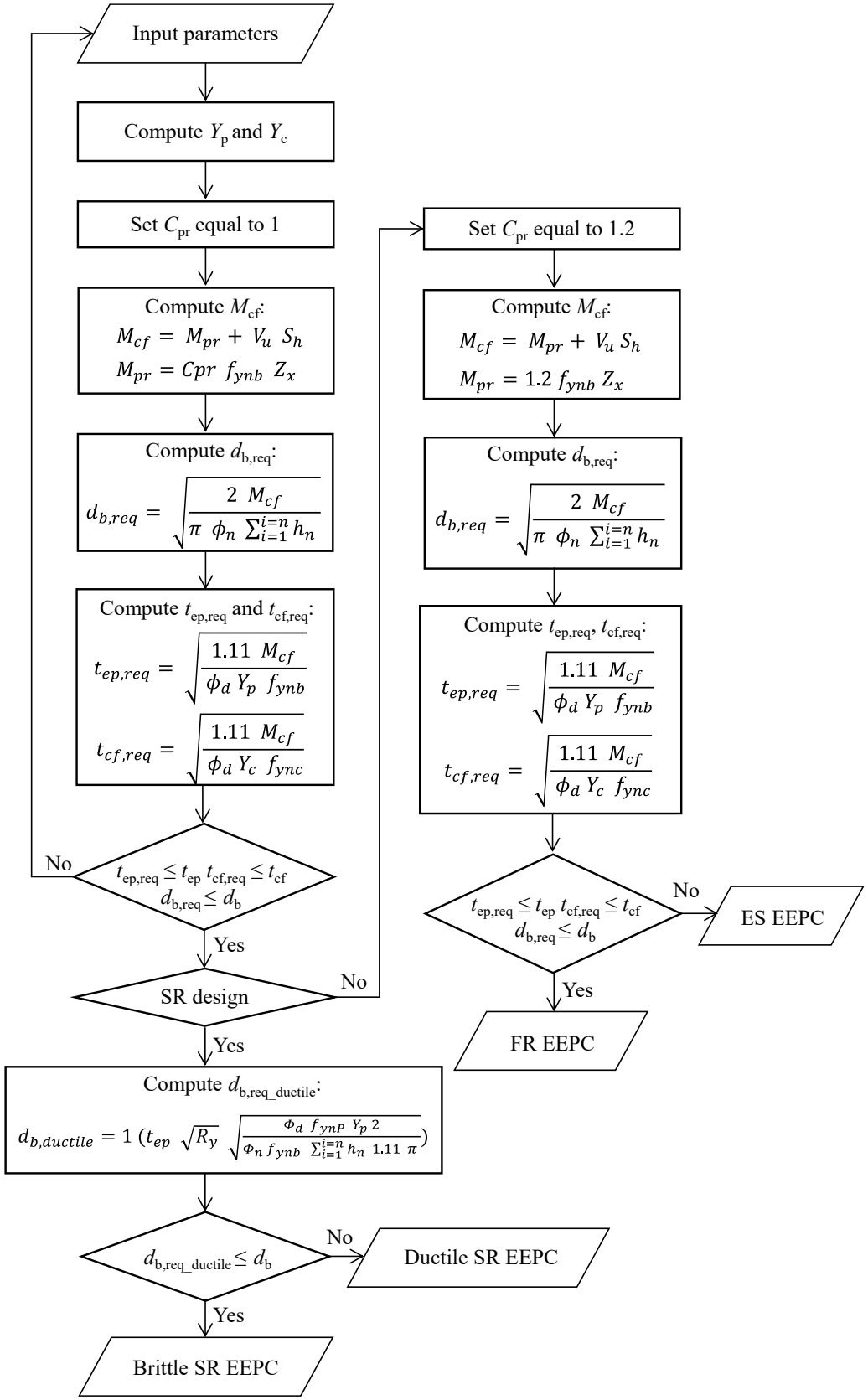

Fig. 3-21 Flowchart of the EEPC classification procedure as per AISC [85] and Tartaglia et al [84].

Before assessing this design procedure, several potential issues may affect the accuracy of this method. Firstly, the weld failure is not considered. This means that some specimens that failed at the weld cannot develop their true strength and ductility, which may not fit this procedure. Secondly, the bolt diameter for ductile criteria is computed based on a specific overstrength factor (C_{pr}=1) and $M_{pl,p}$. The d_b is calculated to ensure the endplate can develop full plastic strength before the bolt failure. However, for the unstiffened PS specimens (t_{ep}>>t_{cf}), the column flange or web may develop an excessive deformation as the weakest component. Therefore, the bolt diameter for ductile criteria, when computed based on endplate thickness, may not be reliable.

To assess this procedure, the connections are categorised as follows:

(1) FR connection: Specimen only deformed at the beam, and C_{pr} is larger than 1.

(2) ES connection: Specimen deformed both at the connection and the beam, and C_{pr} is between 0.8 to 1.

(3) Ductile (D) SR connection: Specimen only deformed at the connection (i.e., endplate or column), and C_{pr} is less than 0.8.

(4) Brittle (B) SR connection: Specimen failed by bolt rupture or weld fracture with no significant prior deformation, and C_{pr} is less than 0.8.

Based on this category, a total of 441 specimens are compared to the procedure by Tartaglia et al [84], as shown in Fig. 3-22. Overall, the numbers of 474 specimens (i.e., 58% of all specimens) is accurately predicted. However, several specimens are mistakenly predicted. Therefore, in Table. 3-1, the main reasons are listed and explained in the following sections.

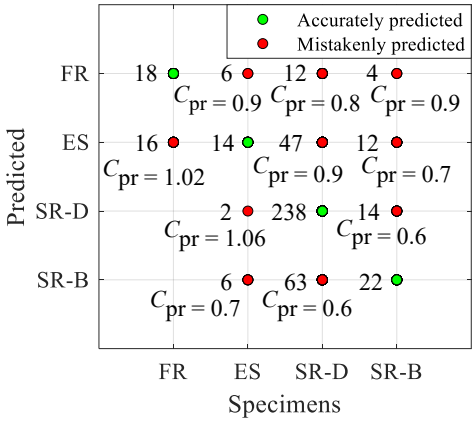

Fig. 3-22 Predictive matrix of beam-to-column specimens and design procedure by Tartaglia et al [84].

Table. 3-1 Reason for incorrect predictions for beam-to-column specimens

		Observed			
		FR	ES	SR-D	SR-B
Predicted	FR	-	Material uncertainty	Column web not considered	premature weld failure
	ES	Material uncertainty	-	Column web not considered	premature weld failure
	SR-D	-	Column flange not considered	-	premature weld failure
	SR-B	-	Column flange not considered	Column flange not considered	-

For FR specimens, the main issue is associated with the material properties. The mistakenly predicted specimens failed only due to beam buckling, with α is around 1. Additionally, some specimens measured yield stress closely match the nominal yield stress. Therefore, those specimens are classified as FR. However, in the design procedure, the material yield stress is assumed as 1.25 f_y. This may cause a slight reduction in the connection strength. The difference in material leads to a mistaken prediction.

For ES specimens, some are predicted to be FR. This is due to a similar issue of material properties. However, six ES specimens (C_{pr} is around 0.85) are predicted as brittle SR specimens. Those specimens were all tested by Sherbourne [25] with a relatively thick endplate (t_{ep}/t_{cf}>1.5). The controlled damages include column web and beam buckling, and specimens failed due to bolt rupture. However, in the design procedure, the required bolt diameter is extremely large due to the thick endplate (see Fig. 3-21). Therefore, those specimens are predicted as brittle and SR. Note that two ES specimens are predicted as ductile SR. It is found that both specimens' bolts are stronger than the requirement. However, one specimen's endplate thickness is less than the procedure requirement, and the other specimen's column flange thickness is less than the procedure requirement. Therefore, both specimens failed at the beam, which is their weakest component.

For ductile SR specimens, it is observed that this procedure easily predicts those with excessive column deformation as brittle and SR. This is because those specimens were mainly damaged at the column flange and the thick endplate (t_{ep}>>t_{cf}). This procedure determines if the SR specimen is ductile by using the principle – bolt strength stronger than endplate plastic moment (see Fig. 3-21), and all columns are stiffened at both flanges. Therefore, the required bolt diameter for those specimens becomes extremely large. However, the required bolt diameter does not need to be that large, as the column is a weak component and easily deforms. Some ductile SR specimens are predicted as FR or ES. This is due to the lack of consideration for the column web. In this procedure, all CFE-verified specimens by Tartaglia et al. (2019) are assigned two doubler plates at the column web. However, for unstiffened specimens with slender column webs, even if all parameters exceed the requirements, column web bending or panel zone shear as the controlled damage will significantly reduce connection strength, causing the specimen to behave as ductile and PS.

For brittle SR specimens, it is observed that some specimens are predicted as FR, ES, or ductile SR. Those brittle SR specimens failed by premature weld failure or bolt rupture. This means that those specimens can develop their full capacity if the weld failure is prevented. Therefore, for those specimens, this procedure may make an accurate prediction if those specimens can fully develop their capacity.

A total of 85 splice specimens are compared to the procedure by Tartaglia et al [84], as shown in Fig. 3-23. Note that most splice specimens are SR, and only one specimen is FR. Overall, 75 specimens (i.e., 88% of all specimens) are accurately predicted. However, several specimens are mistakenly predicted. Therefore, in Table. 3-2, the main reasons are listed and explained in the following sections.

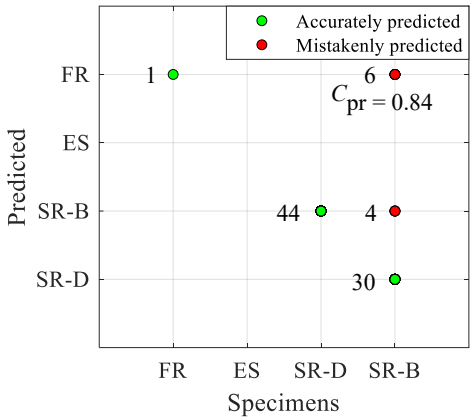

Fig. 3-23 Predictive matrix of splice specimens and design procedure by Tartaglia et al [84].

Table. 3-2 Reason for incorrect predictions for splice specimens

		Observed			
		FR	ES	SR-D	SR-B
Predicted	FR	-	-	-	Bolt stripping or premature bolt rupture
	ES	-	-	-	-
	SR-D	-	-	-	Bolt stripping or premature bolt rupture
	SR-B	-	-	-	-

It is observed that only the brittle splice specimens may be mistakenly predicted. Six specimens are predicted to be FR, yet they are all brittle. This is associated with premature bolt stripping. It is found that the average C_{pr} of all those specimens is around 0.84. This means those specimens may develop their full capacity without the bolt stripping. The bolt stripping may also cause those ductile specimens to behave in a brittle manner. Four specimens are predicted as ductile. However, those specimens failed due to premature bolt stripping before the endplate non-linear deformation.

Compared Fig. 3-22 with Fig. 3-23, it is noticed that this procedure can effectively predict the ductile SR specimens. For all splice specimens, as they can be regarded as beam-to-column specimens with the thick column (i.e., $t_{cf} >> t_{ep}$), this procedure accurately predicted all ductile SR splice ones. Therefore, this proves

that those ductile SR beam-to-column specimens mistakenly predicted are caused by the lack of consideration of column deformation in this procedure.

3.10. Summary remarks

Seven existing predictive models were assessed, which includes six for EEPCs' mechanical responses and one for rigidity-ductility classification. The assessment revealed critical issues that are essential to consider for the further development of more robust models, which follow as:

- Fig. 3-24 summaries the performance of the mechanical response models. Regardless of the model types (i.e., mechanical, analytical, and empirical) and their complexity, all assessed models fail to yield an accurate prediction, especially for K_e with errors easily exceeding 100%. This is not only because that K_e is a sensitive parameter but also the assessed model's simplified assumptions that do not account for all critical geometric and material parameters as well as limited range of testing parameters and connection configurations so that model extrapolation to other cases can yield high errors.
- The assessed mechanical response models generally yield consistent predictions of M_p. For specimens within their applicability domain, the majority of prediction errors fall within ±40%.
- The classification model for rigidity-ductility achieves an overall accuracy of approximately 60% across all specimens. Primary sources of error include material uncertainty, which hinders the model's ability to differentiate between ES and SR EEPCs, and the neglect of column web and panel zone contributions, which affects ductility prediction accuracy.

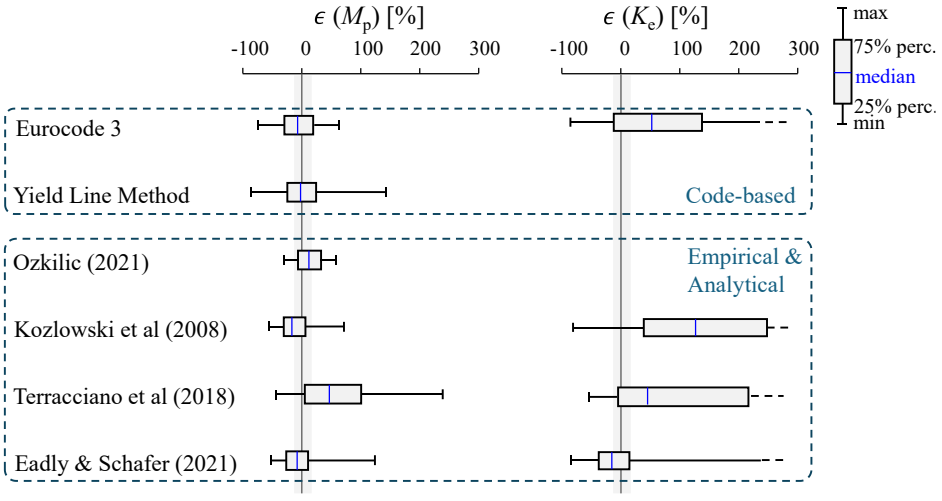

Fig. 3-24 Statistic summary of the existing code-based and empirical models.

4

CONTINUUM FINITE ELEMENT MODELLING

4.1. Overview

A systematic continuum finite element (CFE) modelling approach has been proposed for simulating the EEPCs' behaviour up to failure. The following sub-sections describe the approach specifics: 1) analysis solver, 2) mesh element size/type, 3) contact and constraint settings, 4) loading and boundary conditions, 5) constitutive nonlinear material models, and 6) ductile damage model. This is followed by a thorough validation of the modelling approach against available experimental data.

4.1.1. Analysis solvers

There are two main solvers used in ABAQUS/CAE: the standard implicit solver and the dynamic explicit solver. The main difference between those two solvers is the algorithm used to solve for each time increment. The implicit solver (i.e., *Static step*) is generally used to solve linear or nonlinear static problems. It involves automatic incrementation based on the full Newton iterative method, which establishes a static equilibrium, with displacements computed at the end of each time increment. For nonlinear problems, each increment needs several iterations to compute a solution. The more iterations at each time increment will lead to a smaller the relative error. Implicit solver is efficient for solving smooth nonlinear problems. However, in some highly discontinuous processes, such as material entering softening (i.e., damage and fracture) and abrupt changes in contact area, many iterations may be needed. Therefore, the time increment becomes very small to satisfy the equilibrium, potentially causing some convergence issues that are not expected.

To avoid the non-convergence issues in the implicit solver, the explicit solver (i.e., *dynamic explicit step*) can be used. Explicit solver can be used for solving high-speed dynamic, quasi-static, and large nonlinear problems with the central difference algorithm. For solving quasi-static problems, explicit solver requires a minimal loading rate, typically less than 5mm/s, and a time increment to ensure the kinetic energy is significantly smaller than the internal energy, as shown in Fig. 4-1. When the time increment is very small after setting a small loading rate, mass scaling modification needs to be considered. For quasi-static problems, mass scaling is used to increase the computational efficiency. This is because the material behaviour is not rate-independent, which is not important for scaling the time. Therefore, the mass of the whole model can be artificially modified to achieve a stable time increment and reduce the computation time. In this CFE approach, mass scaling is applied by setting the time increment to 10^{-5}, which is based on the ratio of the smallest mesh element characteristic length (L_c) to material wave speed (c_d), where L_c ranges from 5 to 10mm for solid hexahedral elements, and c_d is around 5000m/s for steel material.

Both implicit and explicit solvers are suitable for simulating the full-scale EEPC's M-θ behaviour to failure, as each offers distinct advantages. With respect to the implicit solver, it is used for the large-scale parametric simulations in Chapter 6 and validation of the EEPCs' hysteretic response under cyclic loading, offering

both efficient computational cost and accurate performance. When it comes to the explicit solver, it is powerful for investigating the full-scale EEPCs' post-capping behaviour without convergence issues in Chapter 5. The validation of implementing these two solvers is fully provided in the next section.

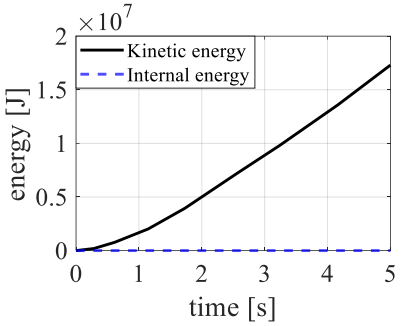

Fig. 4-1 Comparison between kinetic and internal energy for quasi-static problems in the explicit solver.

4.1.2. Mesh and element type

4.1.2.1. Mesh in implicit solver

Two types of solid hexahedral elements are used in the implicit solver, which are *C3D8I* and *C3D20R*, see Fig. 4-2. C3D8I is a linear solid element with eight nodes and eight integration points, using the incompatible mode. This type of element is used for non-excessive bending components such as stiffeners, bolts, beams, and columns [88]. Compared with other linear solid elements (i.e., *C3D8* and *C3D8R*), shear locking and hourglass effects can be effectively avoided. Shear locking in Fig. 4-3 (a) is a typical numerical error, where the shear strain is overestimated as the linear element develops unrealistically stiffer deformation under excessive bending. *C3D8I* elements have incompatible mode formulations, which enrich the displacement field with additional internal degrees of freedom. This ensures *C3D8I* elements behave more closely to quadratic elements in terms of accuracy, with a lower computational cost. Hourglass effect in Fig. 4-3 (b) is another common numerical error, especially for linear elements with reduced integration points. This is mainly because the integration point in the middle of the linear element may capture zero stress and strain from each node. To prevent this, *C3D8I* elements with full integration points can effectively capture the deformation of each node. In terms of capturing component's excessive bending deformations (i.e., endplate) with an efficient computational cost, quadratic elements with reduced integration points (i.e., *C3D20R*) are used. Note that this type of element is safe from unexpected shear locking and hour-glassing due to a greater number of nodes and integration points. However, it requires a larger computational cost.

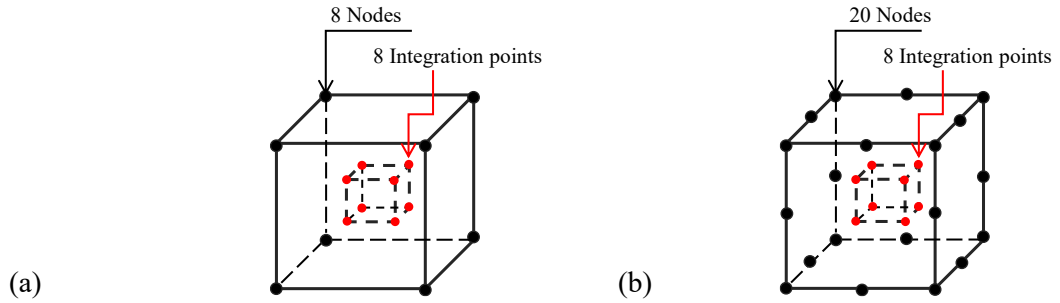

Fig. 4-2 Mesh elements used in implicit solver: (a) *C3D8I* linear solid element; (b) *C3D20R* quadratic solid element.

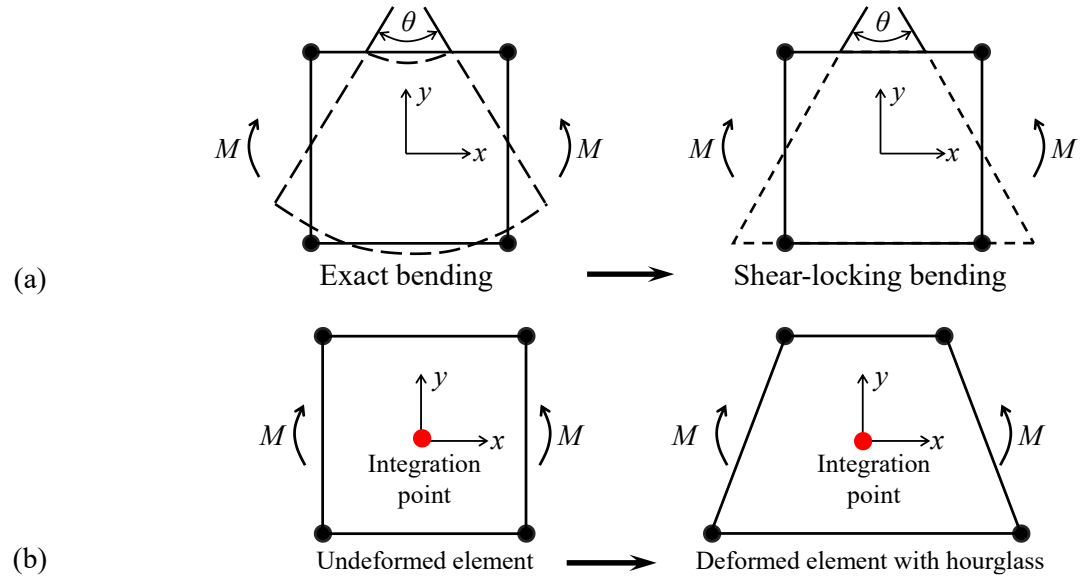

Fig. 4-3 Numerical errors: (a) shear locking; (b) hourglass effect.

Apart from the mesh types, the mesh shape/size also influences the simulation accuracy and computation time. To assist the meshing algorithm, each component is first partitioned as shown in Fig. 4-4. Partitioning is mainly done around the bolt holes. Next, the endplate, beam, and column mesh sizes are set, with at least two layers of mesh present along the endplate thickness, beam flange thickness, and column flange thickness, respectively, using local mesh seeding. The mesh size, assigned to the width of those components, generally ranged from 10 to 20 elements. For the bolts, the mesh size ranged from 2mm to 5mm. The bolts are meshed using 15 to 20 elements, employing the *"Sweep"* mesh control technique and the "*Medial Axis*" algorithm to ensure mesh symmetry. Fig. 4-4 shows an example of component partition and mesh mapping used in the implicit solver.

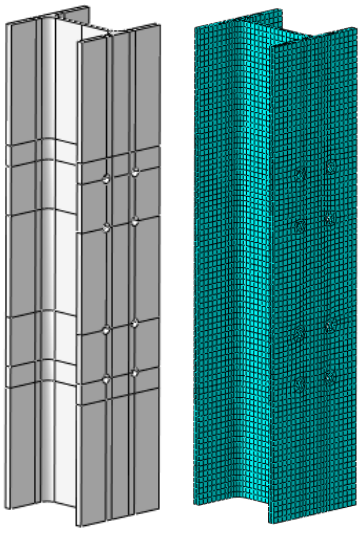

(a) column (global mesh size 15)

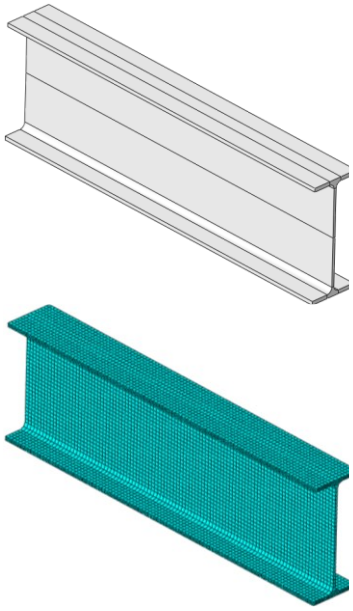

(b) beam (global mesh size 15)

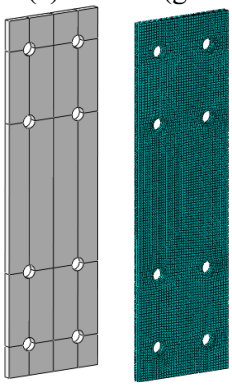

(c) endplate (global mesh size 5)

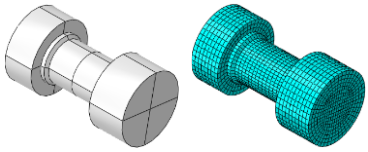

(d) bolt (global mesh size 2)

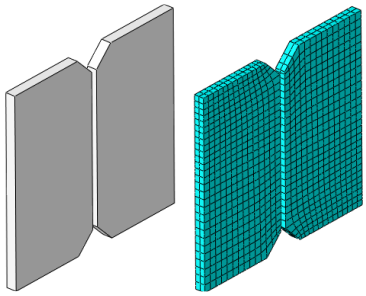

(e) stiffeners (global mesh size 6)

Fig. 4-4 Partition and mesh mapping in implicit solver: (a) column; (b) beam; (c) endplate; (d) bolt; (e) stiffeners.

4.1.2.2. Mesh in explicit solver

The quadratic brick elements are not available within the explicit solver. Instead, the modified quadratic 10-node tetrahedral mesh (*C3D10M*) is used (see Fig. 4-5) is assigned to components (i.e., beam, column, endplate, and stiffener). The *C3D10M* element performs well in capturing the geometries of complex components and excessive plastic deformation, with control over shear locking and hourglass effects. Note that the *C3D8I* solid linear element is still assigned to the bolts. This is mainly attributed to: 1) saving substantial computation time as bolts have the smallest mesh size of other components; and 2) bolts mainly develop axial elongation rather than excessive bending deformation. Fig. 4-6 shows an example of component partition and mesh mapping used in the explicit solver.

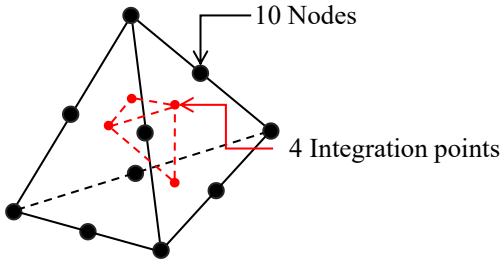

Fig. 4-5 Mesh elements used in explicit solver – C3D10M quadratic solid element

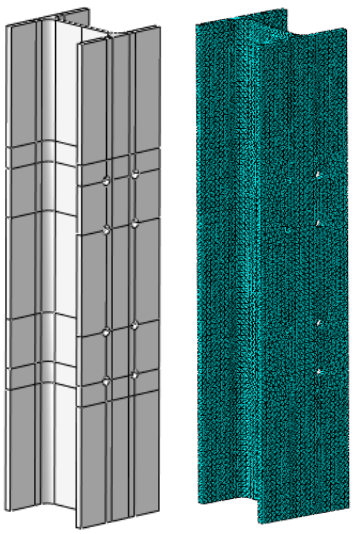

(a) column (global mesh size 15)

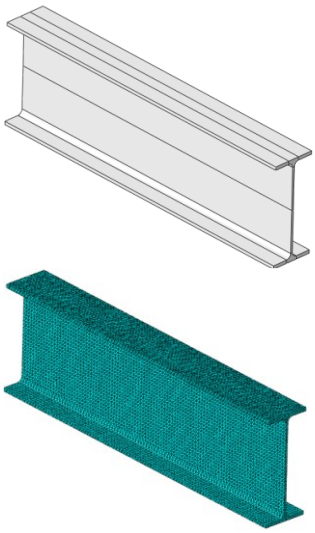

(b) beam (global mesh size 15)

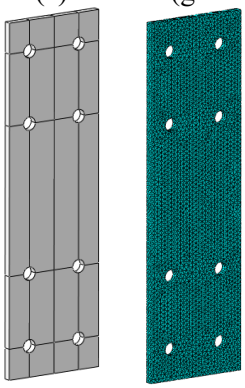

(c) endplate (global mesh size 5)

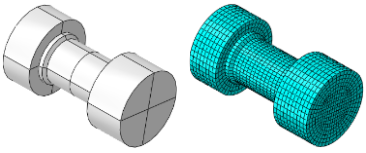

(d) bolt (global mesh size 2)

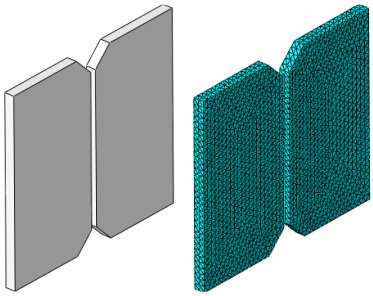

(e) stiffeners (global mesh size 6)

Fig. 4-6 Partition and mesh mapping in explicit solver: (a) column, (b) beam, (c) endplate, (d) bolt.

4.1.3. Interactions between components

A general interaction property is defined for the entire model, involving hard normal contact with allowable separation and tangential behaviour with a static friction coefficient of 0.35. The weld between the beam and endplate or the stiffeners and the column was not modelled explicitly to reduce computational time and modelling effort. Instead, a "*surface-to-surface*" contact is applied between the welded surfaces with a "*Tie*" constraint, as shown in Fig. 4-7. This means that two surfaces (i.e., primary and secondary surfaces) are not allowed to develop any relative motion between them. The primary surface belongs to the primary

components (beam or column), while the secondary surface belongs to the attached components (endplate or stiffener). Note that the secondary surface was finely meshed compared to the primary components to reduce surface penetration between meshes.

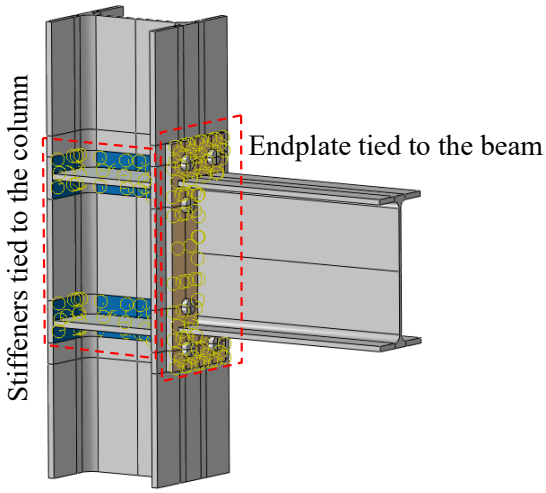

Fig. 4-7 "Tie" constraints for modelling welds – endplate to the beam and stiffeners to the column.

4.1.4. Boundary conditions and loading

The boundary condition depends on the restraint at the end of the components. The boundary condition includes three degrees of displacement (i.e., δ_x, δ_y, and δ_z) and three degrees of rotation (i.e., R_x, R_y, and R_z). Fig. 4-8 illustrates an example of an exterior connection with a column axial load at the top. For the column base, only the in-plane rotation (i.e., R_x) is free. For the column top, the in-plane rotation (i.e., R_x) and vertical displacement (i.e., δ_y) are free. As all components are solid bodies, reference points can be used for applying the load and boundary conditions. A reference point on a solid body can represent all instances of the solid body, simplifying the assignment of load and boundary conditions.

The load can be applied using the displacement control method by transferring the load as the beam tip displacement, which is the product of the beam length and the reported maximum rotation. To ensure the CFE model's quality, the beam tip displacement can be set at a value of 10% to 15% larger than the true/targeted beam tip displacement. The bolt pretension load is assigned at each bolt shank by using the "Fix at the current length" method. This method can ensure the bolt length remains unchanged, allowing the bolt pretension force at each bolt shank to change.

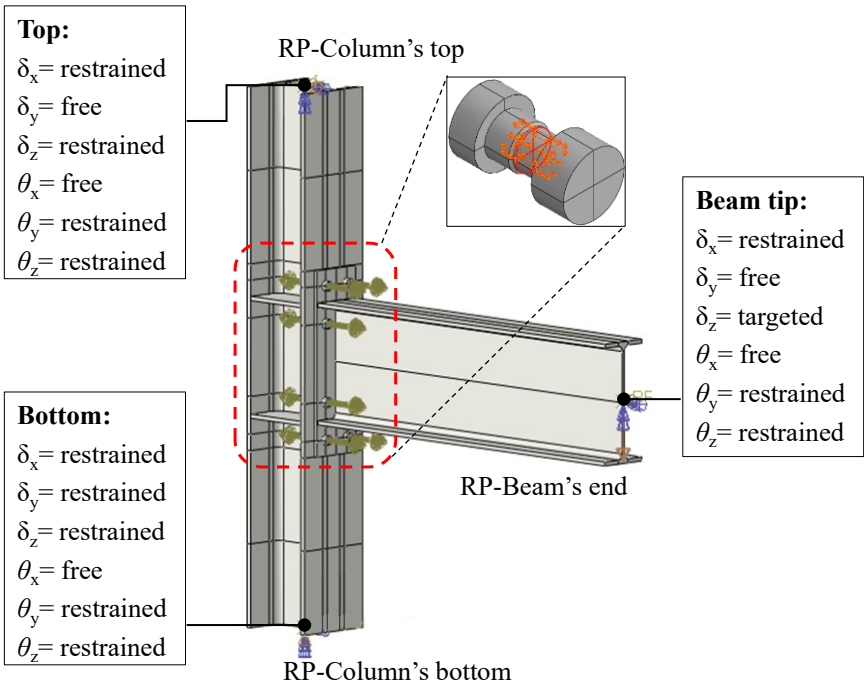

Fig. 4-8 The illustration of typical forces and boundary conditions.

4.1.5. Extraction of force and component deformations

The EEPCs' *M*-θ behaviour and rotational contribution of each component can be obtained by using a systematic numerical method. Fig. 4-9 illustrates the distribution of several critical targeted points. Point A is at the middle web of the beam end. Point B is at the middle of the endplate edge at the same level as the top beam flange. Point C is at the middle of the bottom endplate edge at the same level as the bottom beam flange. Point D is at the middle of the column flange at the same level as the top beam flange. Point E is at the middle of the column flange at the same level as the bottom beam flange. Point F is in the middle of the top panel zone at the same level as the top beam flange. Point G is in the middle of the bottom panel zone at the same level as the bottom beam flange. The total connection rotation (θ_{total}), joint rotation (θ_{total}), and rotational contribution of each component (e.g., θ_{ep}, θ_{cf}, and θ_{pz}) can be deduced based on the equations in Fig. 4-9. Note that δ_A refers to the vertical displacement at the beam end, and δ_B to δ_F refers to the horizontal displacement of each point. The moment (*M*) can be directly computed as the product of the vertical force at Point A and the distance from Point A to the face of the column flange.

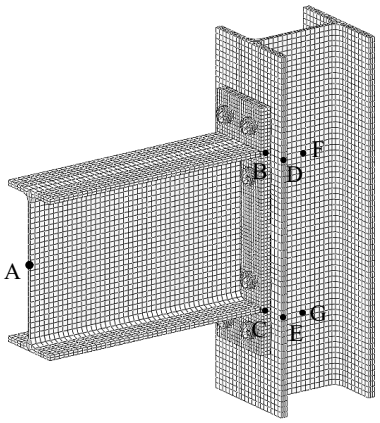

$$\theta_{\text{total}} = \frac{\delta_{\text{A}}}{L_{\text{b}}}$$

$$\theta_{\text{pz}} = \frac{\delta_{\text{F}} - \delta_{\text{G}}}{h_{\text{b}}}$$

$$\theta_{\text{cf}} = \frac{(\delta_{\text{D}} - \delta_{\text{E}}) - (\delta_{\text{F}} - \delta_{\text{G}})}{h_{\text{b}}}$$

$$\theta_{\text{ep}} = \frac{(\delta_{\text{B}} - \delta_{\text{C}}) - (\delta_{\text{D}} - \delta_{\text{E}}) - (\delta_{\text{F}} - \delta_{\text{G}})}{h_{\text{b}}}$$

$$\theta_{\text{b}} = \theta_{\text{total}} - \theta_{\text{pz}} - \theta_{\text{cf}} - \theta_{\text{ep}}$$

Fig. 4-9 Target points distribution.

4.2. Constitutive nonlinear material model

A material modelling approach is introduced herein, which includes the true stress-strain material properties, yield criterion, material hardening, and nonlinear material model. Firstly, the von Mises yield criterion is determined. The isotropic and kinematic hardenings are determined for monotonic and cyclic loading simulations, respectively. Nonlinear material model is appropriately defined by converting the engineering stress-strain response to the true stress-strain response, see Fig. 4-10. The elastic behaviour is simply defined using the elastic modulus (E) and Poisson's ratio (μ). Note that the value of Poisson's ratio is defined as 0.3. With respect to the plastic behaviour from the yield point to the ultimate point, the engineering stress-strain response is converted to the true stress-strain response by using Eq. 4-1 and Eq. 4-2. Eventually, for the post-necking behaviour, several models or assumptions can be used. This includes 1) assuming a conservative post-necking flat behaviour (i.e., bilinear model); 2) establishing a linear line based on a single point at fracture by Eq. 4-3 and Eq. 4-4; or 3) employing a more accurate nonlinear curve based on available empirical or analytical expressions [89-92].

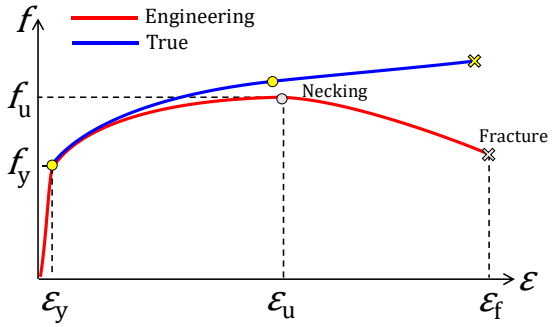

Fig. 4-10 True curve vs Engineering curve.

$$\varepsilon_{\text{true,hardening}} = \ln(1 + \varepsilon_{\text{engineering}}) \quad \text{4-1}$$

$$\sigma_{\text{true,hardening}} = \sigma_{\text{engineering}} \cdot (1 + \varepsilon_{\text{engineering}}) \quad \text{4-2}$$

$$\varepsilon_{\text{true,fracture}} = \ln\left(1 + \varepsilon_{\text{engineering,fracture}}\right) \quad 4\text{-}3$$

$$\sigma_{\text{true,fracture}} = \frac{F_{\text{fracture}}}{A_{\text{fracture}}} \quad 4\text{-}4$$

4.3. Calibration of phenomenological ductile damage model for high-strength bolts

Bolt rupture should be explicitly simulated to capture the ductility of EEPCs controlled by bolt failure, as it is the main source of the strength loss. Softening response can be simulated by using solid mesh elements in ABAQUS/CAE. This requires the appropriately defined true stress-strain response before necking and the calibrated damage parameters from the post-necking stage to rupture. Note that the definition of true stress-strain response before necking is fully defined and explained in Section 4.1.5. To calibrate the softening response leading to damage, a damage model needs to be first defined. Damage models can be classified as either coupled or uncoupled. Coupled models can explicitly simulate fracture by void propagation, while the uncoupled models implicitly simulate fracture by predefining a critical stress/strain corresponding to the onset of damage. The coupled model is chosen here because it is simple and computationally efficient. The coupled damage model, demonstrated in Fig. 4-11, is divided into two phases: the *damage initiation* and *damage evolution*. Several phenomenological *damage initiation* criteria are available for different practical applications. The ductile criterion is used to predict the onset of damage due to nucleation, growth, and coalescence of voids, as in the case of bolt tensile rupture. This criterion is based on a pre-defined equivalent plastic strain ($\varepsilon_{\text{pl},0}$) at a given stress triaxiality (η), and strain rate ($\dot{\varepsilon}_{\text{pl}}$), at the initiation of damage. Essentially, the material will follow the undamaged plastic response until the damage criterion is met in a given finite element (Point "b" in Fig. 4-11). After which, the *damage evolution* phase begins, where the undamaged true stress-strain curve progressively degrades based on the damage parameter (D), and the strain starts to localise in a particular region of the CFE model. The stress will continue to degrade until the plastic strain reaches the fracture plastic strain $\varepsilon_{\text{pl,}}$ at which D=1.0; i.e., complete failure (Point "c" in Fig. 4-11). The evolution of the parameter D with respect to the plastic strain, following damage initiation, is defined based on 1) the extent of plastic deformation beyond the damage initiation point (u_{pl}) before reaching complete fracture $\varepsilon_{\text{pl,f}}$, and 2) the shape of the D-u_{pl} relation (e.g., linear, exponential, etc.). Since $\varepsilon_{\text{pl,f}}$ is dependent on the characteristic length of the mesh element, L_{c}, the extent of deformation is alternatively described using the equivalent plastic displacement at fracture u_{f}, to reduce the mesh-dependency following strain localisation. This is calculated using Eq. 4-5. If u_{f} is set equal to zero, then instantaneous failure will occur right after damage initiation. In theory, and by default, D will keep increasing until reaching a maximum value of D_{max}=1.0 coincident with complete fracture. However, in reality, a complete fracture occurs earlier, at a lower D value (e.g., D_{max}=0.32), as shown in Fig. 5-11 (a). This maximum degradation can be pre-defined based on calibrations against test data in Section 5.3.1.4.

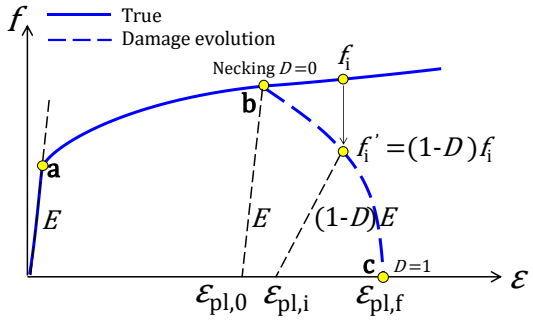

Fig. 4-11 Illustration of ductile damage parameters in the coupled damage model.

$$u_f = L_c\,(\varepsilon_{pl,f} - \varepsilon_{pl,0}) \qquad 4\text{-}5$$

4.3.1.1. Fracture locus models

As stated earlier, the damage initiation criterion is defined based on the equivalent plastic strain at damage initiation ($\varepsilon_{pl,0}$), the corresponding stress triaxiality (η), and strain rate ($\dot{\varepsilon}_{pl}$). In quasi-static simulations, the strain rate parameter is irrelevant; hence, the criterion is defined based on $\varepsilon_{pl,0}$ and η. Since $\varepsilon_{pl,0}$ is dependent on η, a damage initiation curve ($\varepsilon_{pl,0}$ versus η) must be defined. This curve is also known as the fracture locus. Several models are available to characterise the $\varepsilon_{pl,0}$-η relation, and the latest empirical model proposed by Bao and Wierzbicki [93] provides the best match with test data. The model was validated against a series of tests, including tension, shear, and compression on aluminium alloy coupons. Graphically, the model is shown Fig. 4-12. The model discretises the damage initiation curve into three stages, as expressed by Eq. 4-6, where C_1 and C_2 are model parameters that correspond to the critical plastic strain $\varepsilon_{pl,0}$ under pure shear (η=0.0) and tension (η=1/3), respectively.

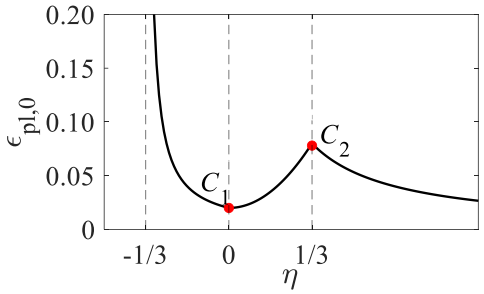

Fig. 4-12 Fracture locus model proposed by Bao and Wierzbicki [93].

$$\varepsilon_{pl,0} = \begin{cases} \infty & \eta \le -\frac{1}{3} \\ \frac{C_1}{(1+3\,\eta)} & -\frac{1}{3} < \eta \le 0 \\ C_1 + (C_2 - C_1)\,(3\,\eta)^2 & 0 < \eta \le \frac{1}{3} \\ \frac{C_2}{3\,\eta} & \eta > \frac{1}{3} \end{cases} \qquad 4\text{-}6$$

4.3.1.2. Calibration of fracture locus and ductile damage parameters

Fig. 4-13 shows the layout, boundary conditions, and mesh for a typical bolt. In this model, only the bolt is simulated without the clamping and loading setup. Instead, reference points are defined at the centre of the internal surfaces of the bolt's head and nut. These reference points are tied to these surfaces using a "*Tie*" constraint. One reference point is fixed while a monotonically increasing displacement is applied to the other. The C3D8I mesh elements are used with a global mesh size of 2mm. This is mainly enforced for the mesh element's length in the shank's longitudinal direction, see Fig. 4-14. In this case, L_c is the length of the diagonal line across the mesh element. Moreover, the 2 mm mesh size ensures at least 10 elements across the bolt shank for bolt sizes ranging from M16 to M24, which are typically used in endplate connections. The calibration process follows as:

- The true stress-strain response is generated up to the necking point, and a perfect flat behaviour is assumed from the necking point to the rupture point.
- Implementing the trial-and-error approach, C_2 in the BW model governing damage initiation is determined as the average *PEEQ* at the bolt necking cross-section when the difference between the simulated and reported bolt ultimate displacements is within 5%. Subsequently, C_1 ($\varepsilon_{pl,u}$ under shear) is qualitatively set as $C_2/4$. This is as per past experimental observations [94-96].
- For damage evolution, D_{max} is calibrated as $1–(F_f/F_u)$ based on the reported experimental data. Subsequently, $\varepsilon_{pl,f}$ is calibrated as the average *PEEQ* at the bolt fractured cross-section when the different between the simulated and reported bolt fracture displacements is within 5%. The corresponding fracture displacement, u_f, is then computed as L_c ($\varepsilon_{pl,f}$-C_2).

A total of 25 Gr8.8 and 30 Gr10.9 bolt assemblies collected from the literature were calibrated, with full geometric and material details provided in Table. 5-1. Note that the calibrated parameters ($\underline{C_2}$, $\varepsilon_{pl,f}$, and D_{max}) exhibit variability due to unavoidable inherent material uncertainties. Therefore, the average calibrated parameters incorporating uncertainty bounds (i.e., minimum and maximum) are presented in Table. 4-1.

Table. 4-1 Calibrated parameters for the ductile damage model incorporating uncertainty bounds

Gr8.8		Gr10.9		All bolts
C_2	$\varepsilon_{pl,f}$	C_2	$\varepsilon_{pl,f}$	D_{max}
0.08±0.025	0.31±0.09	0.066±0.018	0.26±0.06	0.3±0.05

The explicit solver was used here to trace the bolt behaviour until complete failure. Note that the strain-rate field can be set to zero or a very small value (e.g., 0.05) representative of the loading rate being applied within quasi-static conditions. The grade and geometric details of the validation bolt specimens are summarised in Table. 4-2. Note that in this table, and throughout the manuscript, L_t refers to the threaded length within the bolt grip length (i.e., the thread length within and beyond the nut is excluded). Fig. 4-15

shows comparisons of the force-displacement curves predicted by the CFE model and the measured ones for all the validated bolt specimens. To quantify the influence of inherent material uncertainty, the minimum and maximum calibrated parameter values were adopted in the same plot. The results indicate that this uncertainty produces a variation of approximately 15% in bolt ductility.

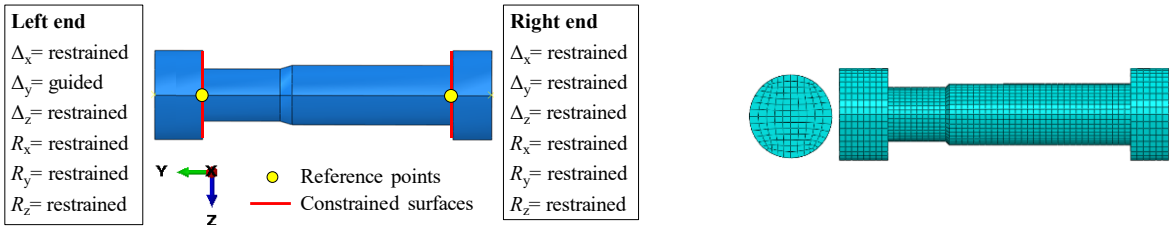

(a) boundary conditions (b) mesh layout (2mm)

Fig. 4-13 Finite element equivalent-shank model of a typical bolt.

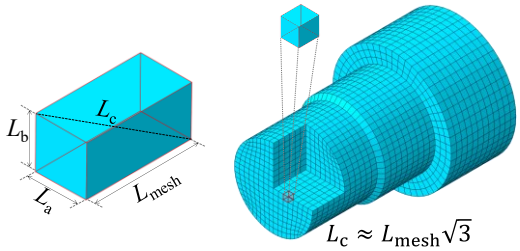

Fig. 4-14 Demonstration of the relation between the mesh element size and characteristic length.

Table. 4-2 Summary of the validation bolt assemblies and their basic dimensions [unit: mm]

Reference	Bolt	Grade	f_y	f_u	L_s	L_t	$d_{b,shank}$	$d_{b,thread}$	d_{head}
[97]	M24	10.9	900	1100	57.3	22.7	24.0	21.0	36
[98]	M20	8.8	785	981	54.0	30.0	20.0	17.6	30

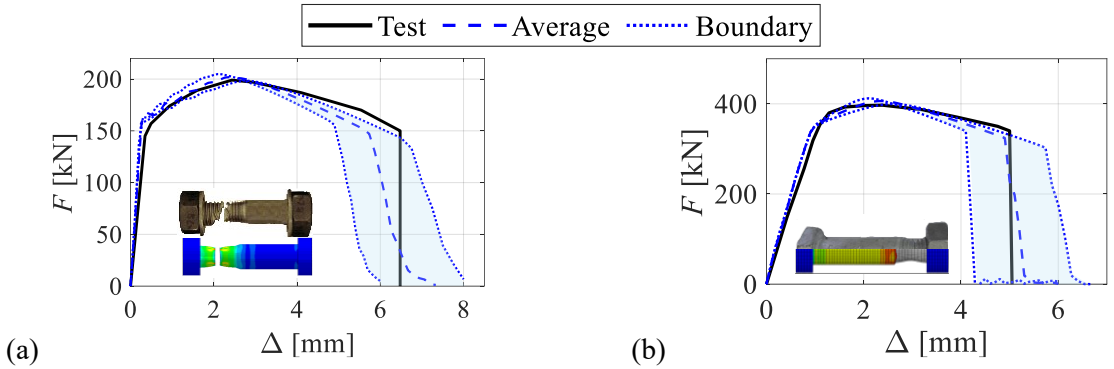

Fig. 4-15 Comparison of F-Δ response: (a) M20 Gr 8.8 [98]; and (b) M24 Gr 10.9 [97].

4.4. Validation of the CFE modelling approach

4.4.1. Validation under monotonic loading

Selected specimens were simulated to investigate the individual component's *M-θ* response and deformation, effect of mesh sensitivity and analysis solvers. Table. 4-3 summarises the main attributes and material properties of the selected joint specimens. Fig. 4-16 shows the CFE validation against specimen J-11 *M-θ* response as well as the deformation contributions of the endplate and panel zone. The results demonstrate that the simulation effectively captures both the deformation modes and the corresponding *M-θ* responses of the components. Fig. 4-17(a) shows the *M-θ* response comparisons between the test data (J-11) and three different mesh densities, from one element across the flange/web thickness to three elements. It is observed that all simulations with varying mesh densities show good agreement with the test specimen. Moreover, a higher mesh density yields simulation results that correlate more closely with the test data. Additionally, the effect of analysis solvers (i.e., implicit and explicit) was investigated, as shown in Fig. 4-17 (b). It is noticed that both the implicit and explicit solvers can show a good agreement against the test specimen (EEP1). It should be noted that the explicit solver led to a computational cost roughly twice that of its implicit counterpart.

Table. 4-3 Summary of the validated full-scale joint specimens' main attributes [unit: MPa]

Reference	ID	Joint	Column	Beam	t_{ep}	Bolt
			HEA 320 (S355)	IPE 360 (S355)	18 (S355)	M24 (10.9)
[99]	J-11	Exterior	E: 206000 f_y: 450 f_u: 553	E: 210000 f_y: 448 f_u: 537	E: 209000 f_y: 405 f_u: 534	E: 206000 f_y: 995 f_u: 1161
			BU 294x302 (S275)	BU 506x201 (S275)	12 (S275)	M20 (8.8)
[100]	EEP1	Exterior	E: 198000 f_y: 365 f_u: 513	E: 204000 f_y: 307 f_u: 476	E: 204000 f_y: 307 f_u: 476	E: 200000 f_y: 700 f_u: 940

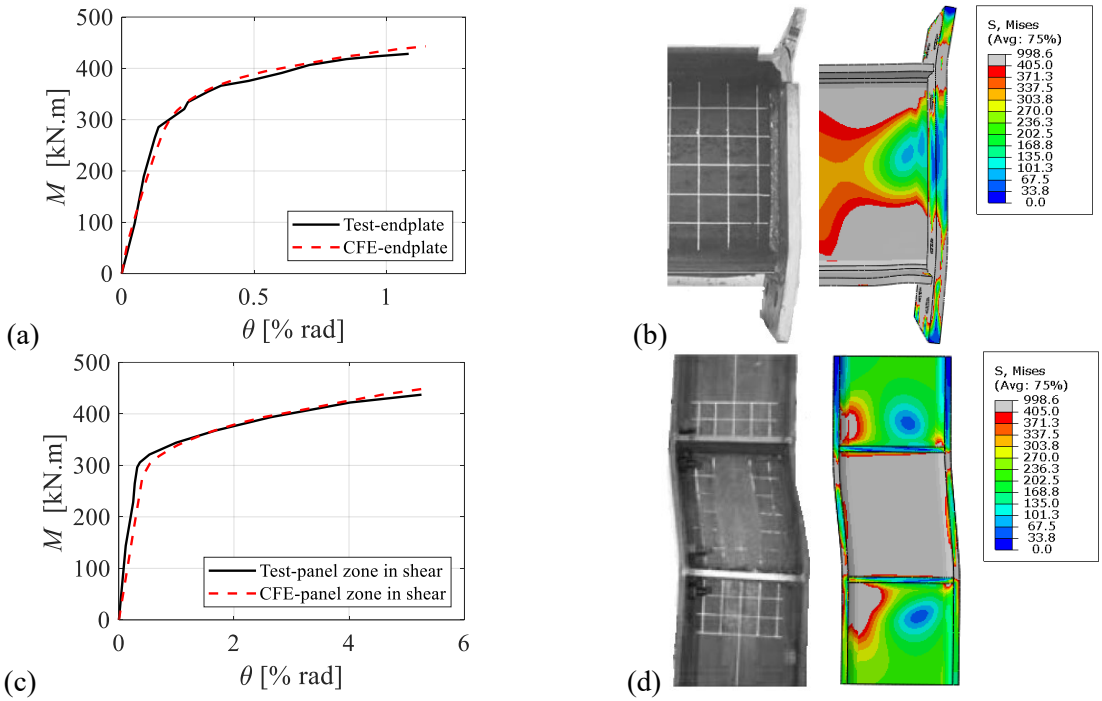

Fig. 4-16 Validation of the CFE modelling approach against specimen J-11 [99]: (a-b) endpalte *M-θ* response and deformation mode; and (c-d) panel zone *M-θ* response and deformation mode.

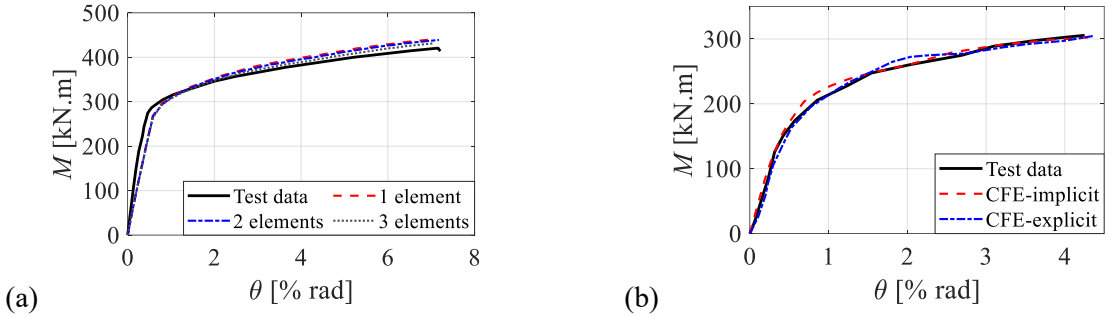

Fig. 4-17 Validation of the CFE modelling approach: (a) mesh sensitivity: specimen J-11 [99]; (b) analysis solver: specimen EEP1 [100].

4.4.2. Validation under cyclic loading

Selected specimens were simulated under ramped symmetric cyclic drifts using implicit solver. The damage parameters of bolts are not considered to avoid the non-convergence issues and save the computation cost.

Table. 4-4 summarises the main attributes and material properties of the selected validation joint specimens, respectively. Note that the nonlinear material model with kinematic hardening, which is based on the Von Mises yield criterion, was considered to capture the Bauschinger effect and ratcheting. Fig. 4-18 shows sample validations against test specimens undergoing cyclic loading. The proposed CFE modelling approach can effectively capture the strength, stiffness, and pinching behaviour of carbon and stainless steel EEPCs.

Table. 4-4 Summary of the validated full-scale joint specimens' main attributes [unit: mm and MPa]

Reference	ID	Joint	Column	Beam	t_{ep}	Bolt
			BU 300x250 (Q345)	BU 300x200 (Q345)	20 (Q345)	M20 (10.9)
[78]	JD3-C	Exterior	E = 192000 f_y = 409 f_u = 537	E = 195000 f_y = 409 f_u = 537	E = 188000 f_y = 450 f_u = 553	E = 206000 f_y = 995 f_u = 1161
			BU 300x180 (EN14301)	BU 250x150 (EN14301)	10 (EN14301)	M16 (A4-80)
[101]	ESC	Exterior	E = 179000 f_y = 282 f_u = 755	E = 194000 f_y = 290 f_u = 630	E = 194000 f_y = 286 f_u = 692	E = 178000 f_y = 574 f_u = 747
			BU 300x200 (S30408)	BU 300x150 (S30408)	12 (S30408)	M20 (TEI)
[102]	SE1	Exterior	E = 200000 f_y = 286 f_u = 703	E = 204000 f_y = 288 f_u = 723	E = 198000 f_y = 299 f_u = 661	E = 202000 f_y = 966 f_u = 1002

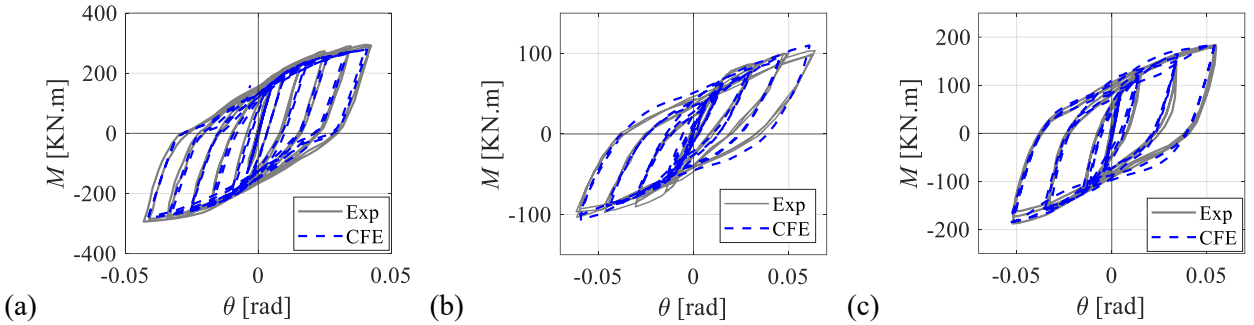

Fig. 4-18 Validation of the CFE model against cyclic data: (a) specimen JD3-C [78]; (b) specimen ESC [101]; (c) specimen SE1 [102].

4.4.3. Validation under monotonic loading and bolt failure

To validate the calibrated phenomenological damage model for bolts, five full-scale joint specimens with endplate connections are validated using the explicit solver. These specimens have different configurations (exterior/interior/splice and extended/flush), geometry, bolt sizes, and material properties. Note that one specimen is fabricated from high-strength steel (S690). Additionally, two flush endplate connections (i.e., S6 and 2-3A) are also considered in the validation, since the bolts undergo elongation and rupture under dominant tensile loading, a behaviour that is also observed in SR EEPCs.

A relatively large number of specimens is included to demonstrate the general applicability of the proposed methodology. All specimens were subjected to ramped monotonic loading and ultimately failed due to bolt rupture. The specimens had varying ductility, with the failure rotation ranging from 3% to 12% rads. Bolt rupture was preceded by visible plastic deformations in the various connection components (CFB, CWB, BB, EPB, BE, etc.). Table. 4-5 summarises the main attributes and material properties of the selected

validation joint specimens, respectively. Note that details of the bolt's ductile damage parameters are mentioned in Table. 4-1.

Table. 4-5 Summary of the validated full-scale joint specimens' main attributes [unit: E and f (MPa)]

Reference	ID	Type	Column	Beam	t_{ep}	Bolt
[103]	Test 2	Splice Extended	None E = 200000 f_y = 300 f_u = 450	IPE 400 (Fe360) E = 200000 f_y = 214 f_u = 350	12 (Fe360) E = 200000 f_y = 730 f_u = 940	M20 (8.8) E = 200000 f_y = 995 f_u = 1161
[78]	JD3-M	Exterior Extended	BU 300x250* (Q345) E = 192000 f_y = 409 f_u = 537	BU 300x200 (Q345) E = 195000 f_y = 409 f_u = 537	20 (Q345) E = 188000 f_y = 450 f_u = 553	M20 (10.9) E = 206000 f_y = 995 f_u = 1161
[99]	J-41	Exterior Extended	HEA 320* (S355) E = 206000 f_y = 450 f_u = 553	IPE 360 (S355) E = 210000 f_y = 448 f_u = 537	18 (S355) E = 209000 f_y = 405 f_u = 534	M24 (10.9) E = 206000 f_y = 995 f_u = 1161
[104]	S6	Interior Flush	HEB 300 (S355) E = 200000 f_y = 461 f_u = 580	IPE 500 (S355) E = 200000 f_y = 461 f_u = 580	12 (S355) E = 200000 f_y = 461 f_u = 580	M20 (10.9) E = 200000 f_y = 990 f_u = 1133
[105]	2-3A	Exterior Flush	HW 400x400 (Q345) E = 186000 f_y = 356 f_u = 550	HW 300x300 (Q345) E = 186000 f_y = 356 f_u = 550	15 (S690) E = 186000 f_y = 789 f_u = 820	M27 (8.8) E = 199000 f_y = 700 f_u = 950

*Stiffened column flange

Fig. 4-19 shows comparisons of the moment-rotation response between the test data and CFE simulations. In this figure, the CFE simulation results are shown up to the point of the first bolt rupture occurrence (noted here as the failure rotation, θ_f); subsequent bolt failures, which would reduce the moment capacity to zero, are omitted. The CFE simulation shows a good agreement with the test data. Some differences in the initial stiffness and maximum strength of the connection are observed in some joints; however, this difference does not exceed 15%. The priority of the current simulation is to examine the validity of the proposed methodology in reasonably predicting the failure rotation of actual joints. As such, tuning the CFE model parameters to achieve a perfect fit with the moment-rotation test data was not a priority. Note that several specimens show a divergence up to 1.5% rads with respect to the θ_f using the average calibrated damage parameters, as expected. Similar divergence was also observed in past studies [95, 106, 107] due to unavoidable uncertainty associated with the variability of material properties and the fracture phenomenon. In reality, even for bolts from the same batch with exact class and specifications, the fracture point

(displacement) can vary by up to 20% [98, 108, 109]. Despite the discrepancies between the average calibrated parameters and the test data, the failure rotations of all specimens fell within the calibrated bounds, with a maximum deviation of approximately ±25%. This demonstrates the capability of the calibrated model, incorporating inherent uncertainty, to accurately capture bolt failure under realistic conditions where bolts are subjected to combined actions (i.e., stress states that deviate from pure uniaxial tension). This is particularly notable given that the CFE models could be applied blindly, without any model tuning. However, the number of calibrated specimens is limited, which may not fully capture the extent of uncertainty. In addition, the use of 2 mm C3D8I meshes and an explicit solver can reduce computational efficiency, which is critical for large-scale parametric CFE simulations. This necessitates a simplified bolt damage model that incorporates uncertainty, allowing efficient large-scale parametric CFE simulations while maintaining acceptable accuracy.

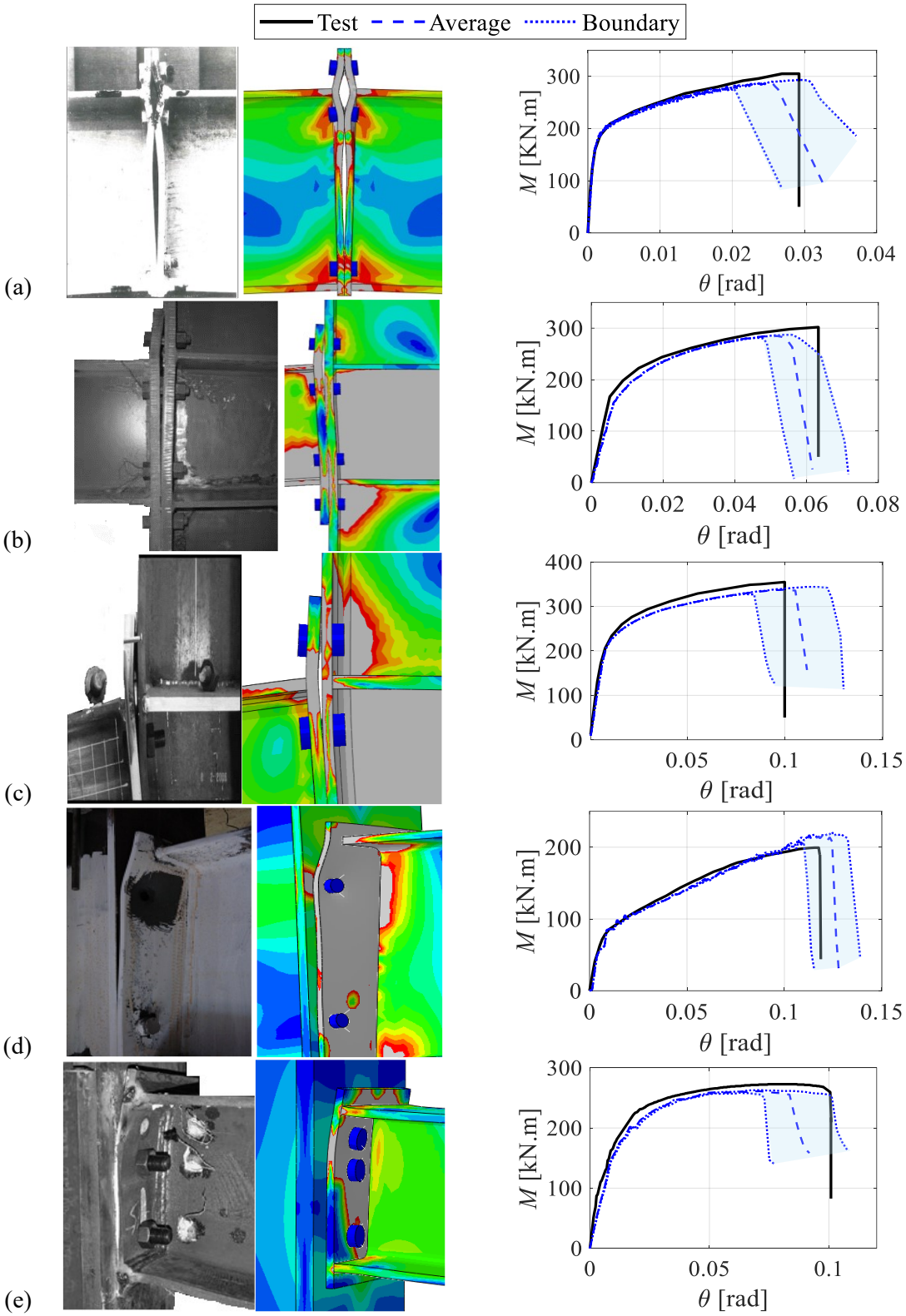

Fig. 4-19 CFE model validation against full-scale joint tests: (a) specimen *Test2* by [103]; (b) specimen *JD3-M* by [78]; (c) specimen *J4-1* by [99]; (d) specimen *S6* by [104]; (e) specimen *2-3A* by [105].

4.5. Summary remarks

A systematic CFE modelling approach, designed to simulate endplate connections governed by bolt rupture, has been developed, calibrated, and validated. The model's technical specifications are detailed, including the analysis solvers, nonlinear material model, element types, component interactions, boundary conditions, and loading protocol. Additionally, a numerical method is defined to extract the force and displacement contributions for the connection and each component. The rupture behaviour for Gr8.8 and 10.9 bolts (i.e., mostly used in EEPCs) was simulated by calibrating the critical damage parameters within the existing fracture locus model (i.e., BW model). Several validations were conducted, which are summarised as:

- A preliminary study was conducted to evaluate the influence of analysis solvers and mesh sensitivity. Both implicit and explicit solvers were found to be viable for quasi-static simulations. Furthermore, convergence studies on various mesh densities indicated the suggested mesh assignment can reach a balance between efficiency and accuracy. This is critical for enabling the large-scale parametric studies in the following chapter.
- The validation of several SR EEPCs under cyclic loading demonstrates that the developed CFE approach effectively captures different levels of pinching behaviour.
- Using the calibrated bolt ductile damage models, a key validation was performed against five SR endplate connections under monotonic loading. The results showed divergences of up to 1.5% rads at the rupture point in some cases, reflecting unavoidable uncertainties in material properties and the inherent complexity of fracture. The failure rotations of all specimens fell within the calibrated bounds, with a maximum deviation of approximately ±25%. However, the CFE approach using a fine solid mesh and explicit solver results in computationally expensive simulations. These findings directly motivate the development of simplified bolt fracture models with explicit uncertainty quantification for large-scale parametric CFE simulations, as detailed in the following chapters.

5

HIGH-STRENGTH BOLT DATABASE AND FORCE-ELONGATION MODEL

5.1. Overview

The critical parameters in the ductile damage model for Gr 8.8 and 10.9 bolts have been calibrated to capture the rupture effectively. However, over-fitting through trial-and-error procedures and model parameter tuning can introduce bias, making the model's accuracy questionable when extrapolated to other cases. In detail, an error of up to 20% of the rotation was observed in the joint-level validation due to the unavoidable uncertainty associated with the variability of material properties and the fracture phenomenon, see Fig. 4-19. On the other hand, the calibrated solid model has a very fine mesh density (i.e., L_{mesh}=2mm), which requires a high computational cost. This is a drawback for large studies involving system-level or parametric joint-level CFE simulations. To solve these problems, axial connector can be an alternative model to simulate the bolt's behaviour up to failure, as illustrated in Fig. 5-1(a). Compared with solid mesh models, the axial connector approach requires only the bolt's full-scale force–displacement (F-Δ) response and uses a single spring element, as shown in Fig. 5-1(b). Moreover, this spring element can be incorporated into mechanical models to enhance the accuracy of existing code-based approaches, such as the component method in Eurocode 3 [7].

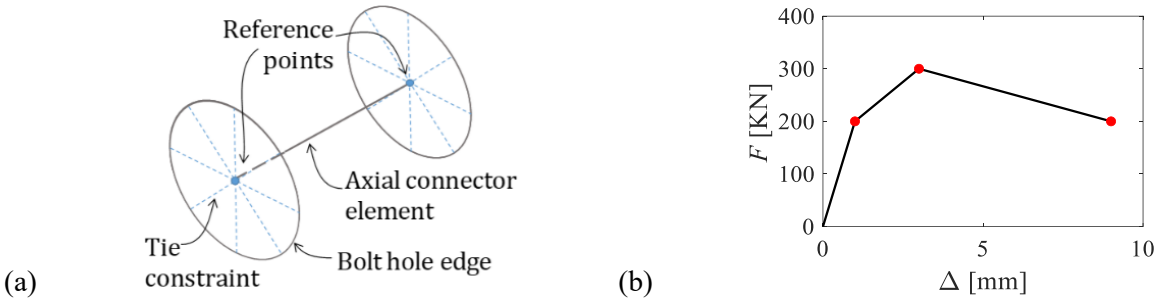

Fig. 5-1 Axial connector model: (a) assembly; and (b) typical trilinear F-Δ response.

In this Chapter, a hybrid empirical-analytical bolt model is proposed to simulate bolt rupture as part of CFE models, using the axial connector approach. This approach is meant to be practical by being 1) computationally efficient (does not need prior calibration, biased model tuning, sophisticated modelling, or significant simulation time), 2) simple to apply for a wide range of bolt geometries and grades, and 3) able to provide consistently accurate results across scales with quantifiable prediction intervals. Firstly, 200 high-strength bolts of different grades and geometric parameters were tested up to failure under varying loading speeds. Next, the experimental data are combined with those collected from the literature to create a multi-attribute dataset. Empirical expressions are developed using the compiled dataset to define the bolt's full-scale trilinear response, including the uncertainty boundaries. These expressions address the limitations of current research with respect to generalization and accuracy. Thorough validations are presented with respect to individual bolt assemblies and full-scale joint tests, highlighting the model's accuracy and the

potential implications of bolt response uncertainty. Finally, the effect of the loading speed (i.e., strain rate) on the bolt response parameters is quantified.

5.2. High-strength bolt database

5.2.1. Experimental study

A total of 200 European HV high-strength bolts were tested. The bolts were either bright zinc-plated (BZP) or galvanised (GLV) with partial-thread (PT) or full-thread (FT). Both grade 8.8 and 10.9 are considered, as well as bolt sizes ranging from M12 to M24. Different bolt lengths were considered, ranging from 75 mm to 100 mm. This is meant to vary the gripped thread length to investigate its effect on bolt ductility.

The bolts were tested in the Testing and Structural Research Laboratory (TSRL) at the University of Southampton using the 630 kN Schenck servo-hydraulic machine shown in Fig. 5-2(a). The bolt assembly is pulled in tension using two identical rigid bolt rigs, each with a plate thickness of 30 mm. Hardened adaptor washers, inserted within the rigs' groove holes, are used to adapt the rig for different bolt sizes, as illustrated in Fig. 5-2(b). Those are 10 mm thick washers, fabricated from Grade EN24 steel and have a +1 mm larger hole diameter than that of the bolt. In addition to the machine-recorded displacement, Digital Image Correlation (DIC) and a linear displacement potentiometer (LVDT) were used to measure the separation distance between the rigid test rigs and to detect any slippage or elastic deformations in the setup. Note that slippage between the machine grips and the test rigs was not observed in any test, and the true bolt's axial elongation was recorded, see Fig. 5-2(c). The bolts were tightened to a snug-tight condition (bolt torque of 80 N.m). Two grade 10.9 nuts were generally used in each test to eliminate the chance of thread stripping in the HV-type bolts. This was not possible, however, for the 75 mm long bolts, where only one nut is used. Standard flat washers were sometimes used at the bolt head and/or the nut to generate variations in the grip length. The bolts were subjected to a monotonic tensile axial displacement at a constant loading speed of 0.05, 10, or 80 mm/s. For a given bolt size and length, three identical tests were conducted to quantify response variability.

Fig. 5-3 shows sample F-Δ responses of bolts with different grades and geometric parameters. The displacement Δ in these plots represents the bolt's elongation, excluding the setup's elastic deformations (refer to Fig. 5-2(c)). For the short 75 mm bolts with one nut (Fig. 5-3(a)), thread stripping is observed as expected. The 100 mm long M16 bolts (Fig. 5-3(b)) developed limited elongation with thread rupture occurring close to the shank due to the short thread length within the gripped length (L_t less than 10% of L_s). Fig. 5-3(c) shows that bolts with lower grade and larger L_t develop larger elongation, as expected. These sample plots demonstrate the uncertainties in elastic stiffness, strength, and ductility even when the bolts

have the same geometric/material parameters and are produced by the same manufacturer. Those uncertainties would be discussed and investigated in the following sections.

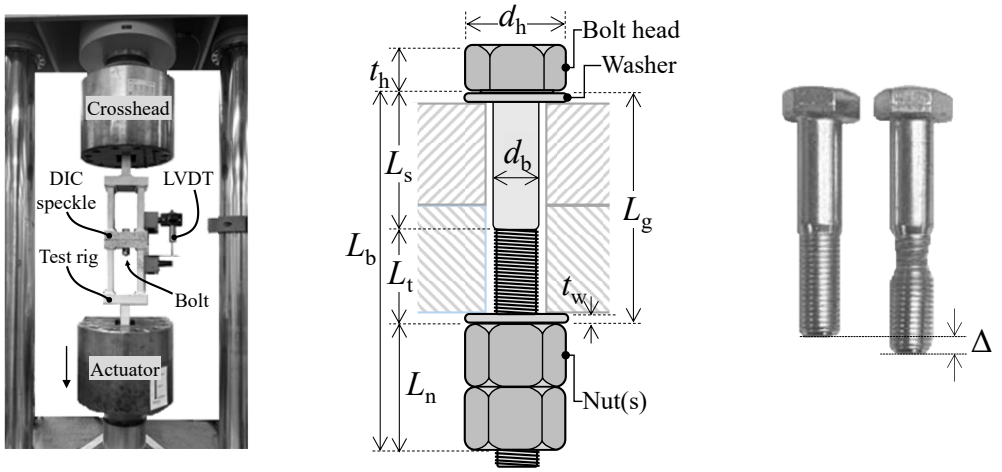

Fig. 5-2 Tensile bolt testing: (a) test machine and setup, (b) test rig cross-section and bolt assembly, and (c) true bolt axial elongation.

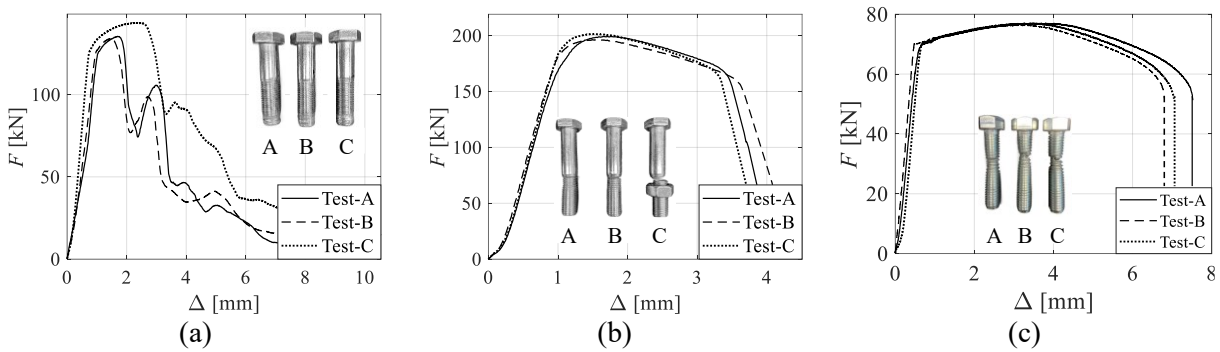

Fig. 5-3 Examples of bolt failure modes and F-Δ responses: (a) M16 Gr. 8.8 L_b=75, (b) M16 Gr. 10.9 L_b=100, and (c) M12 Gr. 8.8 L_b=90.

5.2.2. Multi-attributed experimental database for high-strength bolts under quasi-static loading

Following the same strategy of establishing the experimental database in Chapter 2, a multi-attribute database with 31 parameters was assembled. In addition to the 108 specimens tested under quasi-static tension, 76 additional ones were collected from ten different research programs within the literature, resulting in a dataset of 184 bolt specimens under quasi-static tensile loading. Table. 5-1 summarises the main parameters for this dataset, and Fig. 5-4 shows a breakdown of the dataset's basic parameters. The majority of specimens are partially threaded Gr 8.8 M16/M20 bolts that failed by tensile rupture.

Fig. 5-5 illustrates the key response parameters deduced from a typical F-Δ response. The response parameters are the measured elastic stiffness (K_e), the measured strengths (i.e., F_y, F_u, and F_f), the measured critical plastic displacements (i.e., $\Delta_{u,p}$ and $\Delta_{u,f}$), and the failure mode type (i.e., stripping or rupture). Note

that the measured K_e was deduced from the digitised test curves based on the secant slope joining the points at the 20 kN and 70% F_u. Note that, before data deduction, the initial slight movement before contact (labelled as *'s'*) was removed (if present).

Table. 5-1 Summary of collected tests on high-strength bolt assemblies under quasi-static loading [unit: mm]

Reference	No.	Grade	d_b	L_b	L_t	L_s	L_g
Author's tests	108	8.8; 10.9	12;16;20;24	75-150	2.5-100	0-56	60-100
[98]	4	8.8	16	100	22.5	54	78
[97]	18	10.9	16;20;24	100-120	7-24	56-73	80
[110]	4	12.9	16;20;24	140	6-100	0-94	100
[111]	4	10.9	16;20;24	140	5-100	0-95	100
[112]	13	8.8; 10.9	16;20	105-161	4-99	0-109	84-144
[113]	4	8.8	16	153	11-118	0-113	118-130
[114]	4	10.9	10	-	5-60	0-55	60
[115]	2	A490	22	-	3; 14	89	92; 103
[116]	8	A325	22;25;29	-	51-102	0-115	102-171
[117]	2	A325	22	-	3; 19	89; 105	108

-: not reported

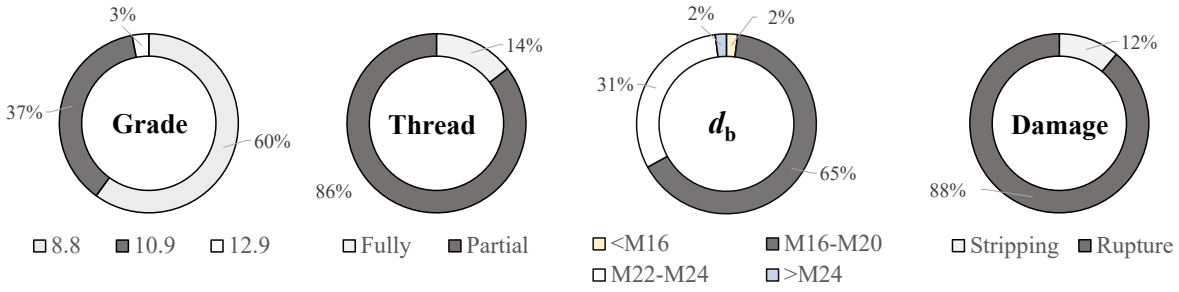

Fig. 5-4 Breakdown of the high-strength bolt database basic parameters.

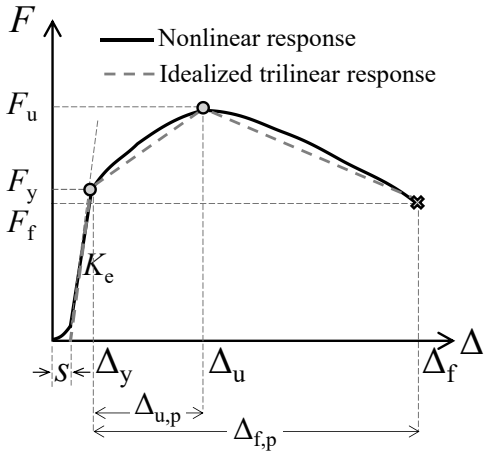

Fig. 5-5 Key response parameters in the F-Δ curve and the deduction method.

5.3. High-strength bolt rupture models and CFE validation

5.3.1. Proposed bolt's force-displacement model

5.3.1.1. Initial elastic stiffness, K_e

Computing the axial stiffness (K_e) of a bolt assembly can be challenging due to the changing cross-section and interaction between the nut and the bolt's thread [118]. Few researchers provided analytical or hybrid analytical-empirical expressions for K_e. Agerskov [119] proposed an expression for computing the elastic deformation of a non-preloaded bolt as given by Eq. 5-1, where n_w is the number of washers, t_w is the washer thickness, and A_{nom} is the bolt's nominal area. This expression considers the contributions of the shank, threads, washer, and nut. It was analytically driven and further modified by empirical coefficients. It was shown in the literature that this expression overestimates K_e by 9% to 20% [120].

$$K_e = \frac{E\,A_{nom}}{(L_s+1.43\,L_t+0.71\,L_n)+2(0.2\,L_n+0.2\,n_w\,t_w)} \quad 5\text{-}1$$

Similarly, Swanson and Leon [121] proposed Eq. 5-2, where β is a correction factor that was recommended to be taken equal to 0.55. Note, however, that earlier research [122, 123] noted that β is not constant but somewhat varies from 0.3 to 2.86, indicating the large uncertainty for K_e computation. Consequently, it was observed that K_e predicted by this expression can be overestimated by 74% on average [124].

$$\frac{1}{K_e} = \frac{\beta\,d_b}{E\,A_{nom}} + \frac{L_s}{E\,A_{nom}} + \frac{L_t}{E\,A_s} + \frac{\beta\,d_b}{E\,A_s} \quad 5\text{-}2$$

The German standard VDI2230 [125] provides a code-based K_e model that considers the shank, threads, head, nut, and washer, as given in Eq. 5-3, where d_h is the bolt head diameter, d_{w1} is the inner washer diameter, and d_{w2} is the external washer diameter. Similarly, Eurocode 3 Part 1-8 [7] provides Eq. 5-4 to compute K_e for a single bolt row, as part of the component-based method, which considers the bolt head, shank, washer, and nuts.

$$\frac{1}{K_e} = \frac{L_s + 0.4\,d_b}{E\,A_{nom}} + \frac{L_t + 0.85\,d_b}{E\,A_s} + \frac{n_w\,t_w}{E\,A_p} \qquad 5\text{-}3$$

$$where,\ A_p = \frac{\pi}{4}\left(d_h^2 - d_{w1}^2\right) + \frac{1}{2}\left(d_{w2}^2 - d_h^2\right) tan^{-1}\left[\frac{0.75\,d_h\,(n_w\,t_w - d_h)}{(d_{w2}^2 - d_{w1}^2)}\right]$$

$$K_e = \frac{1.6\,E\,A_s}{L_g + 0.5\,t_h + 0.5\,L_n} \qquad 5\text{-}4$$

Fig. 5-6 shows the comparisons between the measured K_e and those predicted by the existing expressions. Note that the expressions are evaluated assuming E=200 GPa. It is observed that existing expressions do not provide consistently accurate estimates of the stiffness. All expressions, except for Eurocode 3, overestimate K_e by 50% to 70%, which is consistent with past observations in the literature [120, 124]. The expression by Swanson et al [121] can provide reasonable estimates if the β factor is taken equal to 2.5 (see Fig. 5-6(b)). The Eurocode 3 expression mostly underestimates the bolt's stiffness by up to 50%. Note that this expression does not consider the threaded region length.

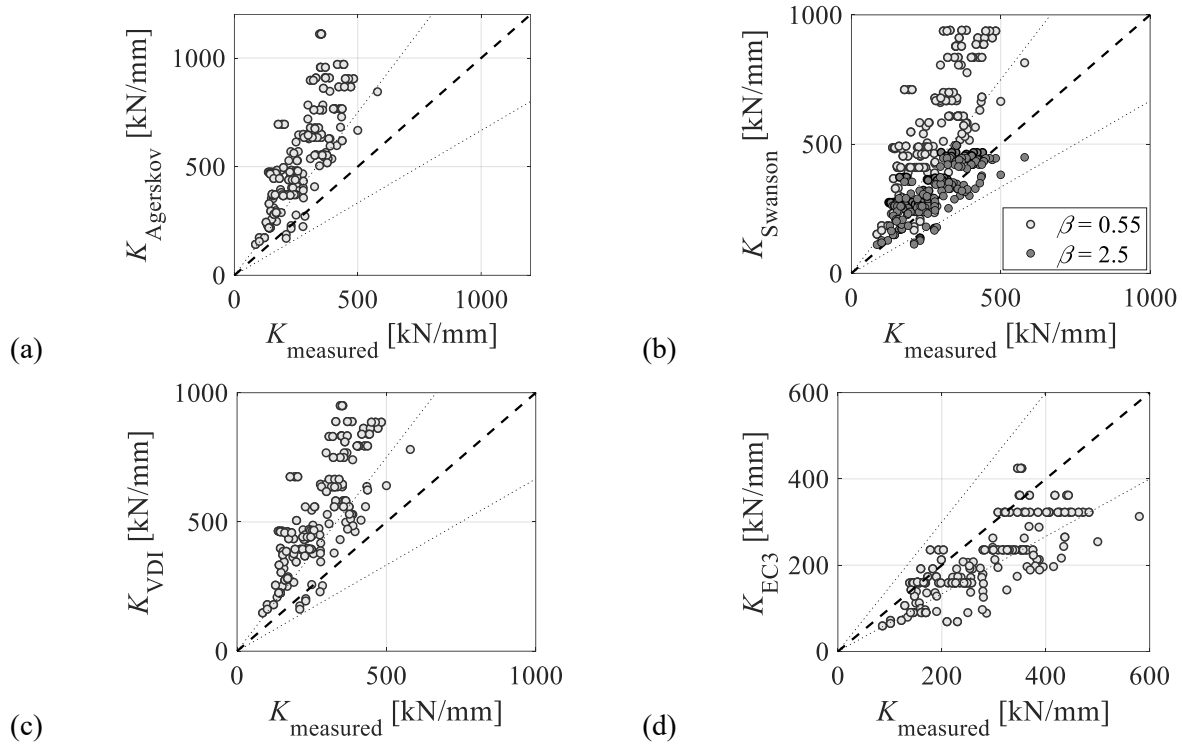

Fig. 5-6 Comparison between the measured K_e and existing predictive expressions: (a) Agerskov, (b) Swanson et al, (c) VDI 2230, and (d) Eurocode 3.

To address the limitations of existing expressions, a more accurate one is developed herein. It is proposed to compute K_e using a basic/simple analytical expression that is modified with a correction factor, as given by Eq. 5-5. The analytical stiffness ($K_{e,\,analytical}$) is based on the equivalent axial stiffness of the shank and the threaded portions within the griped region. The stiffness correction factor (β) is then computed as a function of d_b, L_g, L_t, and L_n, using the nonlinear power expression given in Eq. 5-6. The regression

coefficients are regressed against the measured K_e to $K_{e,\,analytical}$ ratios. The regression values corresponding to the best fit (mean) as well as those based on the LB and UB bounds of the 68% and 95% prediction intervals (PI) are tabulated in Table 2. The fitted expression has an R^2 of 0.70. As shown in Fig. 9, the new expression provides K_e reasonable estimates where 61% and 95% of the specimens are predicted with an error less than 20% and 50%, respectively

$$K_{\mathrm{e}} = \beta\, K_{\mathrm{e,analytical}} = \beta \left(\frac{1}{\frac{1}{\frac{E\,A_{\mathrm{s}}}{L_{\mathrm{t}}}} + \frac{1}{\frac{E\,A_{\mathrm{nom}}}{L_{\mathrm{s}}}}} \right) \tag{5-5}$$

$$\beta = c_0\, d_b^{c_1}\, L_t^{c_2}\, L_g^{c_3}\, L_c^{c_4} \tag{5-6}$$

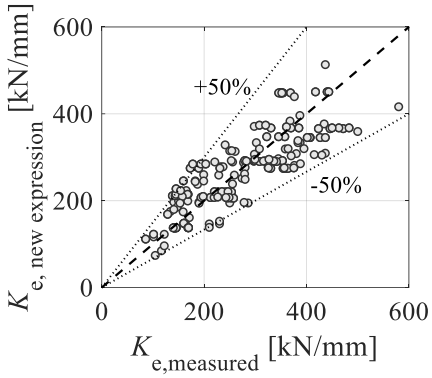

Fig. 5-7 Performance of the propsoed K_e expression.

Table. 5-2 Regression coefficients for β based on data fitting and uncertainty bounds

Coefficients	Best fit (mean)	68% PI		95% PI	
		LB	UB	LB	UB
c_0	0.362	0.338	0.387	0.316	0.415
c_1	-0.440	-0.430	-0.450	-0.420	-0.46
c_2	0.087	0.087	0.087	0.087	0.087
c_3	0.490	0.484	0.500	0.477	0.500
c_4	-0.320	-0.311	-0.330	-0.302	-0.340

The previous K_e expression is intended for use with the axial spring approach. However, the need for the correction factor β to match bolt test data highlights an important issue that relates as well to continuum finite element models that employ the equivalent shank solid model, as illustrated earlier in Fig. 4-13. In this model, only the shank and the threaded portions (within the gripped length) are represented. Therefore, the resulting axial stiffness is expected to be equivalent to $K_{e,\,analytical}$ (which diverges from the true stiffness value). This is demonstrated in where the results of a CFE simulation are compared with test data for a sample specimen resourced from D'Aniello et al [97]. The CFE simulation results in overly conservative

stiffness. This issue was noted by D'Aniello et al [118] where it was recommended to reduce the modulus of elasticity E by 50% on average. A similar approach is employed here by modifying the modulus of elasticity E_{mod} using the β factor, which considers the bolt's geometry, i.e., $E_{mod} = \beta \cdot E$. When the bolt model is analysed with the modified E, the stiffness matches the test data, as shown in Fig. 5-8. It should be noted that for connections controlled by the deformations of other components, such as an endplate or an angle, this issue will have an insignificant impact on the joint stiffness. However, for other connections where the bolt is the weaker component, ignoring the E modification can result in erroneous global stiffness.

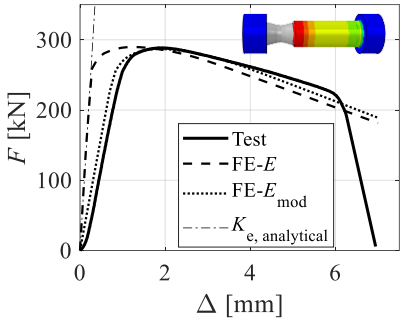

Fig. 5-8 Comparison between the equivalent shank solid model and test data considering the modified modulus of elasticity [test data by [97]].

5.3.1.2. Yield and ultimate strengths, F_y and F_u

The bolt's yield and ultimate forces (F_y and F_u) can be computed as the product of the bolt's tensile stress area (A_s) and engineering yield and ultimate stresses (f_y and f_u), respectively. For this purpose, the strength parameters (i.e., F_y and F_u) are deduced from F-Δ curves. Specifically, the yield strength (F_y) is determined as the force at which the elastic slope diverges from the F-Δ curve, beyond 10% (0.3mm for most cases) [126].The ultimate strength (F_u) is directly determined when the F-Δ curve reaches the maximum point. Subsequently, the strength parameters are converted to the yield and ultimate stresses (i.e., f_y and f_u). Fig. 5-9 shows the histogram for the measured f_y and f_u/f_y values for different bolt grades. The variability in the measured material stresses is evident in these distributions. Assuming they follow a normal distribution, the inherent material uncertainty is quantified using the 68% prediction intervals (i.e., ±1 standard deviation, σ) and superimposed in Fig. 5-9. In summary, coefficient of variations of 6.5% and 3% are observed on average for f_y and f_u/f_y, respectively, which is consistent with past observations [127].

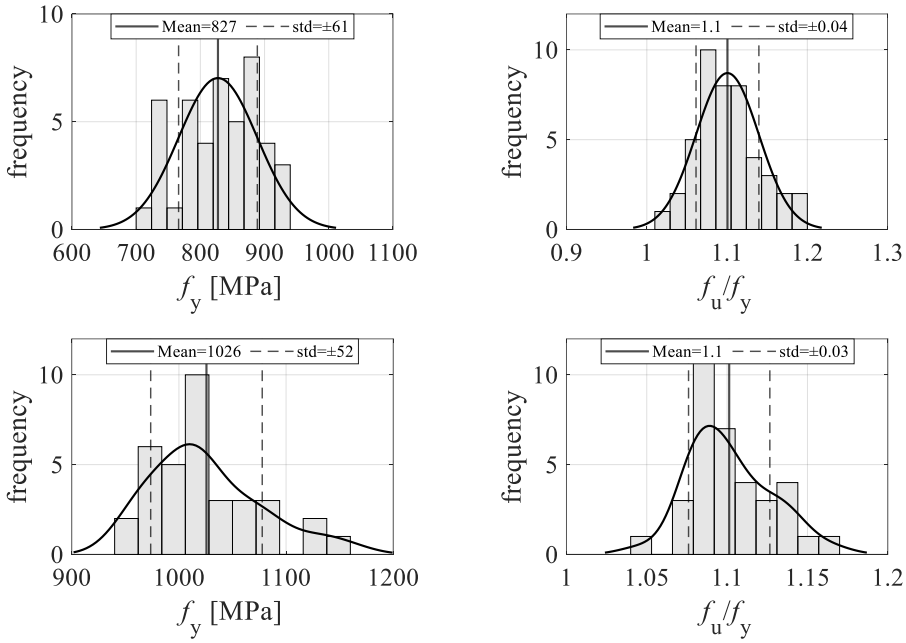

(a) Gr 8.8/A325

(b) Gr 10.9/A490

Fig. 5-9 Distribution of the bolt's measured engineering stress parameters based on the collected dataset.

5.3.1.3. Plastic ultimate and fracture displacements, $\Delta_{u,p}$ *and* $\Delta_{u,f}$

The critical plastic elongations, $\Delta_{u,p}$ and $\Delta_{f,p}$, are key to capturing the bolt's ductility. The critical elongations (i.e., Δ_u and Δ_f) are deduced from the data and then transformed into the plastic elongations after subtracting the yield elongation (i.e., K_e/F_y). The relation between the plastic elongations and the gripped thread length (L_t) is investigated in Fig. 5-10 , while differentiating bolts by their grade (i.e., Gr 8.8/A325 and Gr 10.9/A490). It is observed that the critical plastic elongations linearly increase with L_t, as expected. The fitted linear functions are given by Eqs. 5-7 and 5-8. Note that for a bolt with a given grade and L_t, the critical plastic elongation may vary because of the inherent uncertainty associated with the material and the fracture phenomena. Therefore, the 68% ($\pm\sigma$) PIs are superimposed in the plots and summarised in Table. 5-3. Those intervals can be used in sensitivity and reliability analysis or when a conservative design is sought.

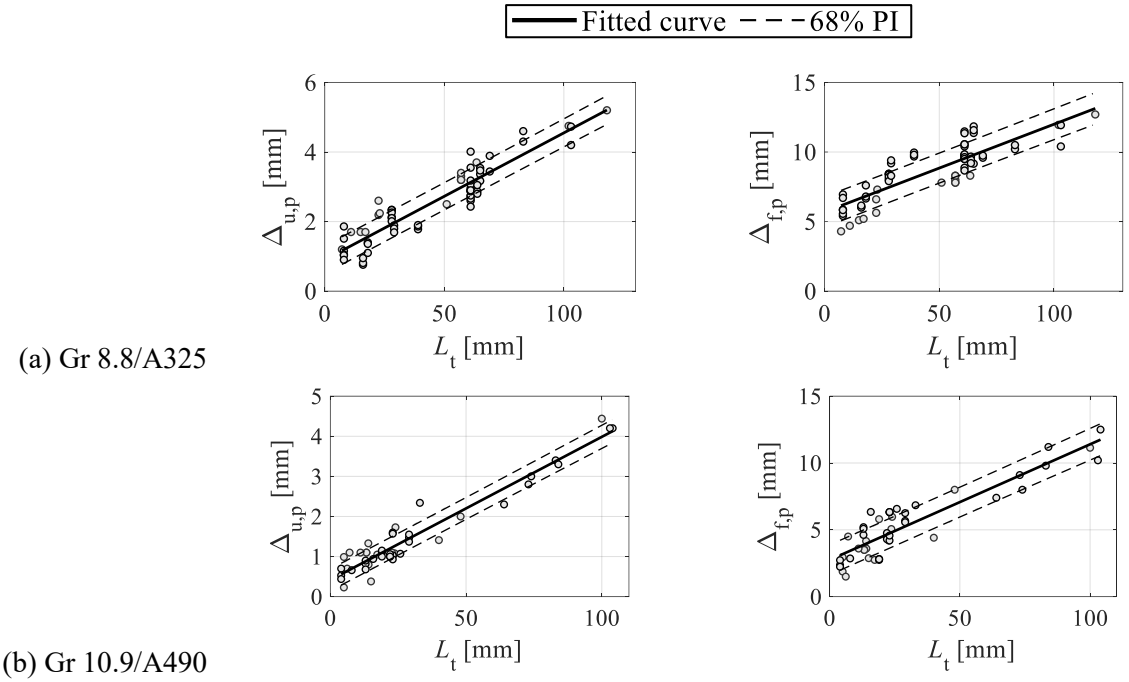

(a) Gr 8.8/A325

(b) Gr 10.9/A490

Fig. 5-10 Established relations between the ultimate and fracture plastic elongations and the gripped thread length.

$$\Delta_{u,p} = \begin{cases} 0.89 + 0.0360\, L_t & \text{Gr 8.8} \\ 0.41 + 0.0357\, L_t & \text{Gr 10.9} \end{cases} \quad 5\text{-}7$$

$$\Delta_{f,p} = \begin{cases} 5.82 + 0.0644\, L_t & \text{Gr 8.8} \\ 2.87 + 0.0847\, L_t & \text{Gr 10.9} \end{cases} \quad 5\text{-}8$$

Table. 5-3 Uncertainty bounds for carbon steel bolts' critical plastic elongations [units: mm]

Grade	68% PI		95% PI	
	$\Delta_{u,p}$	$\Delta_{f,p}$	$\Delta_{u,p}$	$\Delta_{f,p}$
8.8	Eq. 5-7 ± 0.43	Eq. 5-8 ± 1.1	Eq. 5-7 ± 0.85	Eq. 5-8 ± 2.2
10.9	Eq. 5-7 ± 0.30	Eq. 5-8 ± 1.2	Eq. 5-7 ± 0.60	Eq. 5-8 ± 2.4

5.3.1.4. Maximum damage parameter

The post-ultimate drop in strength to F_f can be represented using the maximum damage parameter (D_{max}), which is defined as $1\text{-}F_f/F_u$. Based on the collected data, Fig. 5-11 (a) shows the distribution of D_{max}, which has an average value of 0.32 and a standard deviation of 0.05. Fig. 5-11 (b) shows the QQ-plot of the D_{max} distribution with a linear correlation. Note that the p-value is computed as 0.39, which indicates the D_{max} is normally distributed regardless of the material and geometric parameters

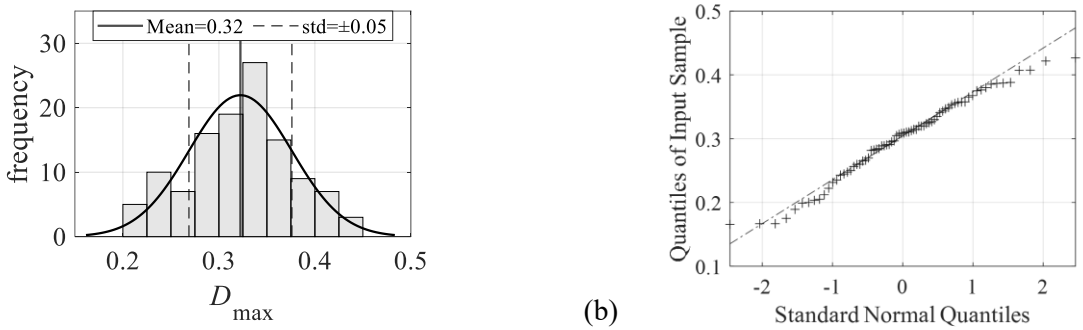

Fig. 5-11 Maximum damage parameter D_{max}: (a) histogram with fitted normal distribution; (b) QQ plot.

5.3.1.5. Procedures for constructing a bolt spring model

1) Using the bolt's geometric parameters (d_b, L_g, L_t, and L_c), compute the elastic stiffness (K_e) using Eq. 5-5.
2) Modify K_e using the correction factor (β) as per Eq. 5-6.
3) Compute the plastic ultimate and failure elongations ($\Delta_{u,p}$ and $\Delta_{f,p}$) using Eqs. 5-7 and 5-8, respectively.
4) Compute the bolt's plastic and ultimate forces (F_p and F_u) as the product of the bolt's tensile stress area (A_s) and yield and ultimate stresses (f_y and f_u), respectively. The stress values can be assumed as the nominal or the expected ones based on the statistical metrics summarised in Fig. 5-9. Alternatively, other material variability factors from the literature can be used [127].
5) Lastly, assume a value for D_{max} based on the distribution in Fig. 13 and use it to compute the failure force ($F_f = D_{max} F_u$).

Additionally, a GUI (see Fig. 5-12) has been publicly available and downloadable at Elkady [128].

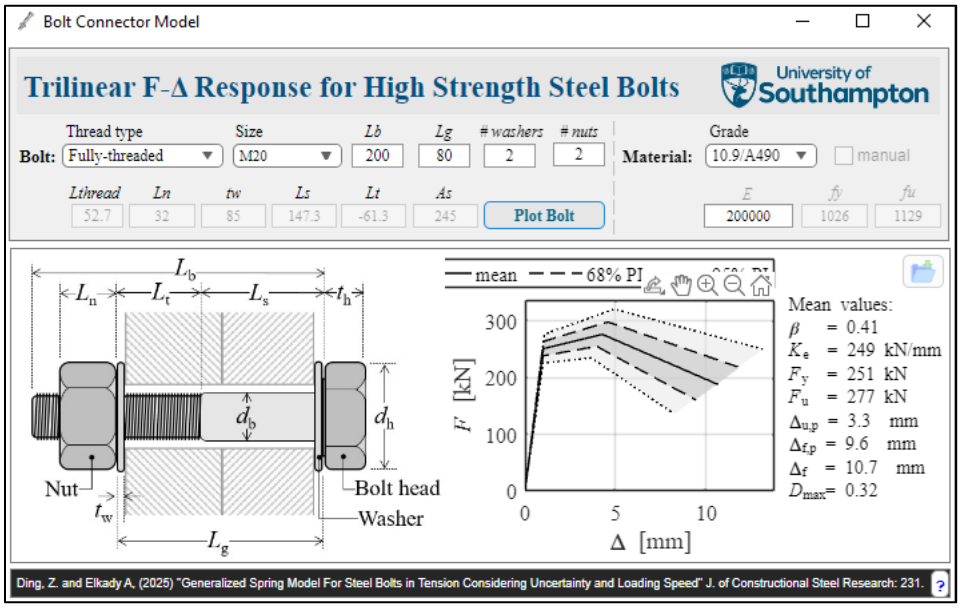

Fig. 5-12 Proposed bolt model GUI – Example of a Gr 10.9 M20 fully-thread specimen.

5.3.2. Validation of the proposed empirical bolt spring model at the joint level

In this section, the accuracy of the proposed methodology for simulating bolt fracture is examined in comparison with several past test specimens. The section is divided into two subsections. First, the methodology is validated against isolated bolt assemblies in tension. Second, the methodology is validated against full-scale beam-to-column joints with endplate connections under monotonic joint rotation.

5.3.2.1. Bolt assembly tests

In this section, validation is conducted against four carbon steel bolt assemblies from four different experimental studies [97, 98, 111, 113]. The grade and geometric details of the validation bolt specimens are summarised in Table. 5-4. All the specimens experienced necking followed by rupture within the threaded area. Fig. 5-13 shows comparisons of the F-Δ test curves and those predicted by the empirical connector model. In these plots, the predicted responses are based on the mean and 68% upper and lower PI bounds. The shaded area between the 68% PI lines represents the uncertainty range for the prediction. For all cases, damage initiation (at F_u) is well predicted, the damage evolution (post-peak degrading – negative- slope) is in good agreement with the test data, and the observed bolt failure displacement Δ_f (at complete loss of force) falls within the 68% PI bounds. Apart from the ductility, the equivalent elastic stiffnesses computed by Eq. 5-5, as well as the strength values, for all assemblies also show a good agreement with the test data.

Table. 5-4 Summary of the validated bolt assemblies, their geometry, and the calculated mean response parameters [unit: mm and kN/mm]

Reference	Bolt*	Grade	L_g	L_t	$\Delta_{u,p}$	$\Delta_{f,p}$	K_e
[113]	M16 PT	8.8	130	17	1.5	6.9	196
[97]	M24 PT	10.9	80	23	1.2	4.8	413
[111]	M20 FT	10.9	100	100	4.0	11.3	292
[98]	M20 PT	8.8	77.5	22.5	1.7	6.3	337

*PT: partially threaded; FT: fully threaded

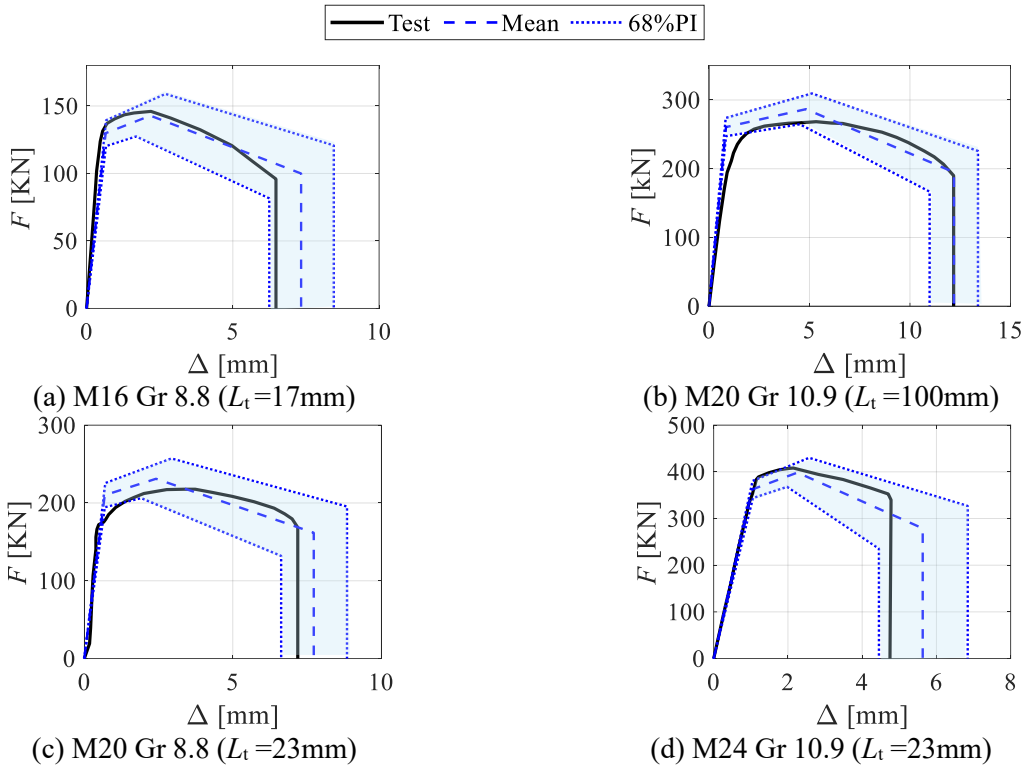

(a) M16 Gr 8.8 (L_t=17mm) (b) M20 Gr 10.9 (L_t=100mm)

(c) M20 Gr 8.8 (L_t=23mm) (d) M24 Gr 10.9 (L_t=23mm)

Fig. 5-13 Comparison of F-Δ response for different bolt assemblies demonstrating uncertainty range.

5.3.2.2. Joint tests

Five full-scale joint specimens with extended and flush endplate connections are selected from five different research studies [53, 78, 129-131] for validation. Note that the geometry and material properties of those specimens are fully reported in Table. 4-5. Details of the CFE modelling approach are fully provided in Chapter 4. Note that the dynamic *Explicit* solver is used while maintaining a slow loading rate, consistent with the validated quasi-static tests, with insignificant inertia forces and low kinetic energy maintained. All components, except for the bolt, are meshed with quadratic tetrahedron elements (*C3D10M*) with a mesh size ranging between 10mm and 20mm. The trilinear bolt models are summarised in Table. 5-5. Note that the axial connector detail is shown in Fig. 5-14 (a) where two reference points were applied to couple the internal surfaces of the bolt head and nut. It is recommended that the bolt head and nut are modelled using solid elements (i.e., *C3D8I*) such that yield line patterns in the connected elements can be correctly captured. The connector stiffness and ductility parameters were computed. The connector is assigned an axial property where elastic, plastic (post-yield branch), and damage (post-ultimate branch) properties are defined blindly based on the previously outlined procedure.

Table. 5-5 Computed damage parameters for the bolt components in the connector [unit: mm]

Reference	Specimen	Bolt	L_t	$\Delta_{u,p,mean}$	$\Delta_{f,p,mean}$
[129]	Test2	M20 (FT)	28	1.40	5.20
[130]	2-3A	M27 (FT)	50	2.70	9.00
[131]	S6	M20 (PT)	16	0.98	4.20
[78]	JD3-M	M20 (PT)	10	0.77	3.70
[53]	J4-1	M24 (PT)	10	0.77	3.70

Fig. 5-14 (b-f) shows comparisons of the moment-rotation response between the test data and computational simulations. In these plots, the CFE simulation results are shown up to the point of the first bolt rupture occurrence (noted here as the failure rotation, θ_f); subsequent bolt failures, that would drop the moment capacity to zero, are omitted. The computational simulation shows a good agreement with the test data. Some differences in the initial stiffness and maximum strength of the connection are observed in the joint specimens; however, this difference does not exceed 15%. The priority of the current study is to examine the validity of the proposed methodology in reasonably predicting the failure rotation of actual joints. As such, tuning the computational model parameters to achieve a perfect fit with the moment-rotation test data was not a priority. Note that the error in the mean predicted failure rotation of all specimens (i.e., based on the bolt's mean critical elongations as per Eqs. 5-7 and 5-8 is within ±10%, as summarised in Table. 5-6, which is acceptable from the perspective of engineering practice. Most importantly, the predicted failure rotation of all specimens fell within the 68% PI bounds with a maximum error range of about ±20%. Referring to Table. 5-6, the 68% PI uncertainty in bolt ductility can result in up to ±1.3% rads variation in the joint's rotational ductility. Note that a larger variation would be observed if the 95% PI bounds are employed. In summary, these validations demonstrate the ability of the proposed model to capture bolt failure within a real scenario where the bolt is subjected to combined actions (i.e., the stress state deviates from pure uniaxial tension). This is particularly notable considering that the computational models involved blind application of the methodology without any material calibration or model tuning.

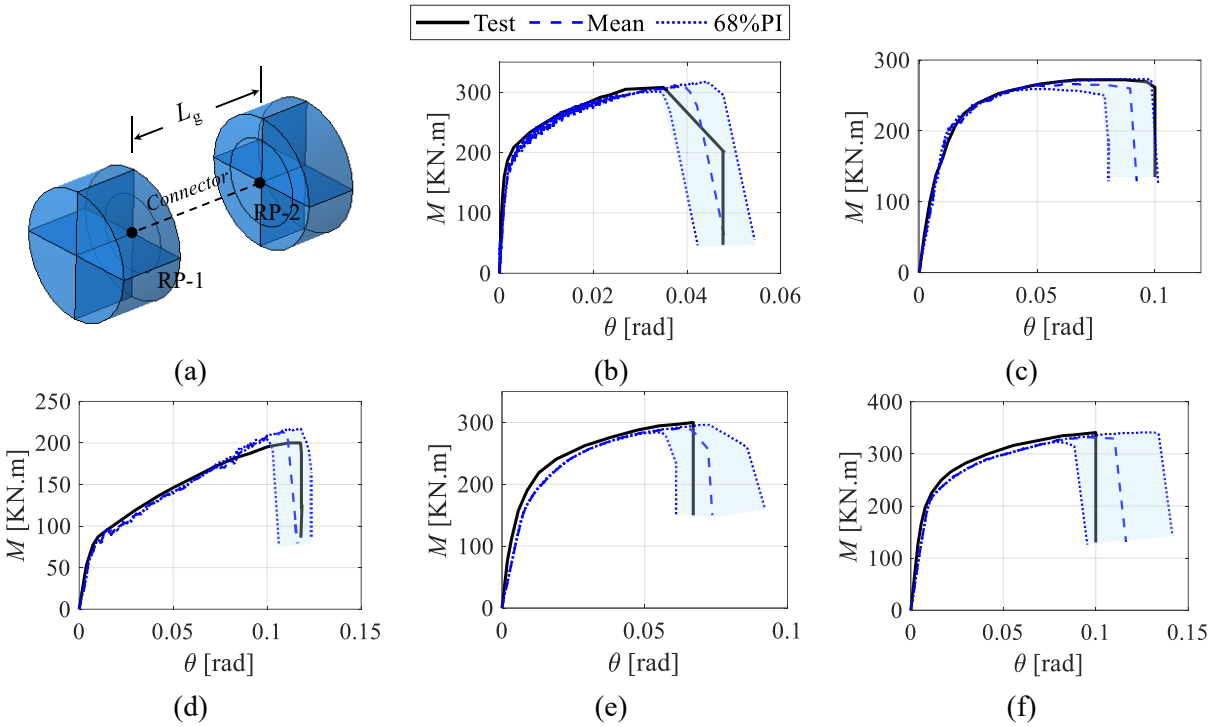

Fig. 5-14 Validation of the proposed methodology against full-scale bolted endplate joints.

Table. 5-6 Range of observed errors in predicted failure rotation based on full-scale joint tests [unit: % rad]

Reference	Specimen	$\theta_{f,test}$	$\theta_{f,CFE}$			Relative error [%]		
			LB	M	UB	LB	M	UB
[129]	Test2	3.5	3.2	3.8	4.4	-8.6	8.6	25
[130]	2-3A	10.0	7.9	9.0	10.0	-20	-10	0
[131]	S6	11.8	10.0	11.0	12.0	-15	-7	1.6
[78]	JD3-M	6.7	5.6	6.5	7.6	-16	-3	13
[53]	J4-1	10.0	8.9	10.3	11.6	-11	3	16

*Lower boundary (LB), mean value (M), and upper boundary (UB)

5.4. Implications of the loading speed on bolt response

Actual hazards (e.g., earthquake, explosion, or sudden column loss) induce faster loading speeds on the joint components including the bolts. Past tests mostly investigated the strain-rate-dependent properties of the bolt material using round (i.e., turned-down) coupon specimens. Grimsmo et al [132] tested Gr 8.8 coupons under different strain rates (i.e., from 10^{-3} to 10^{2} s^{-1}). It was observed that the ultimate stress (f_u) can increase by up to 15%, while the fracture strain showed no explicit dependency. Similarly, Kendall et al [133] observed that the ultimate strain was slightly increased, whereas the fracture strain remained constant for Gr 8.8 material under a loading speed of 0.05 to 10mm/s. Yang et al [134] tested Gr 8.8 and 12.9 coupons with strain rates ranging from 0.00025 to 100 s^{-1} and observed that the strength increased by up to 15%, the

ultimate strains increased by 35%, and the fracture strain was non-correlated to strain rates. Studies on bolt assembly behaviour under high-speed loading are still limited. Therefore, a series of tests was conducted as part of this experimental campaign to investigate this issue further.

Out of the 200 specimens, 92 were tested under high-speed loading: 56 bolts were tested at 10 mm/s and 35 bolts at 80 mm/s. Those two speeds are equivalent to strain rates of about 0.5 to 8 s^{-1} (assuming a gauge length of 10 mm). Fig. 5-15 (a) shows a sample plot of a bolt assembly under different loading speeds. Note that for 10 mm/s tests, the actual speed reached the target speed before the yield point, as demonstrated in Fig. 5-15 (b), while for the 80mm/s tests, the speed at the yield point was slightly less (~ 76 mm/s).

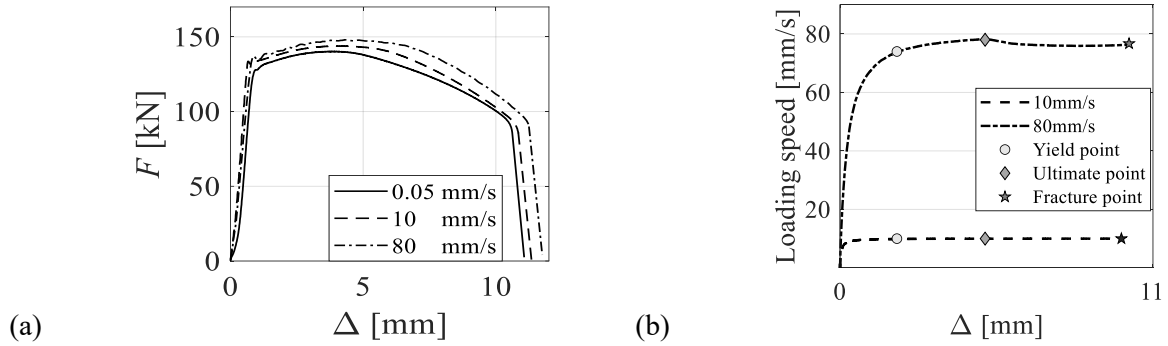

Fig. 5-15 Bolt responses under high-speed loading: (a) force-elongation responses; (b) speed evolution as a function of bolt elongation

The bolt response parameters are deduced from the dynamic (i.e., 10 and 80 mm/s) force-elongation curves and normalised by the corresponding values of the quasi-static tests (i.e., 0.05 mm/s). Fig. 5-16 shows the average normalised dynamic responses for strength and ductility. Overall, the strength (f_y and f_u) and plastic ultimate displacement ($\Delta_{u,p}$) visually show an increase with the increase in loading speed. In contrast, no explicit dependency is observed in the plastic fracture displacement ($\Delta_{u,f}$). Those observations are consistent with the previous tests [132, 134]. To quantify the effect of load-rate dependency, Table. 5-7 summarises the factors of the normalised responses. Concerning strength (f_y and f_u), both Gr 8.8 and 10.9 bolts develop a 1% increase for f_y at 10mm/s. Larger increases are observed at 80mm/s, with 6% and 4% increases for Gr 8.8 and 10.9 bolts, respectively. Similar dependency is observed in f_u, a 2% increase is observed for both Gr 8.8 and 10.9 bolts at 10mm/s. When it comes to 80mm/s, Gr 8.8 and 10.9 bolts develop an increase of around 4%. For ductility ($\Delta_{u,p}$ and $\Delta_{u,f}$), both Gr 8.8 and 10.9 bolts show an increase with the increase of loading rate for $\Delta_{u,p}$. Specifically, an increase of up to 10% was observed at 80mm/s regardless of bolt grades. When it comes to 10mm/s, Gr 8.8 and 10.9 bolts show an increase of 4% and 8%, respectively. Finally, Gr 8.8 and 10.9 bolts show an over 5% decrease in $\Delta_{u,f}$ at 10mm/s, whereas the $\Delta_{u,f}$ at 80mm/s is slightly decreased by 3% and increased by 1% for Gr 8.8 and 10.9 bolts, respectively.

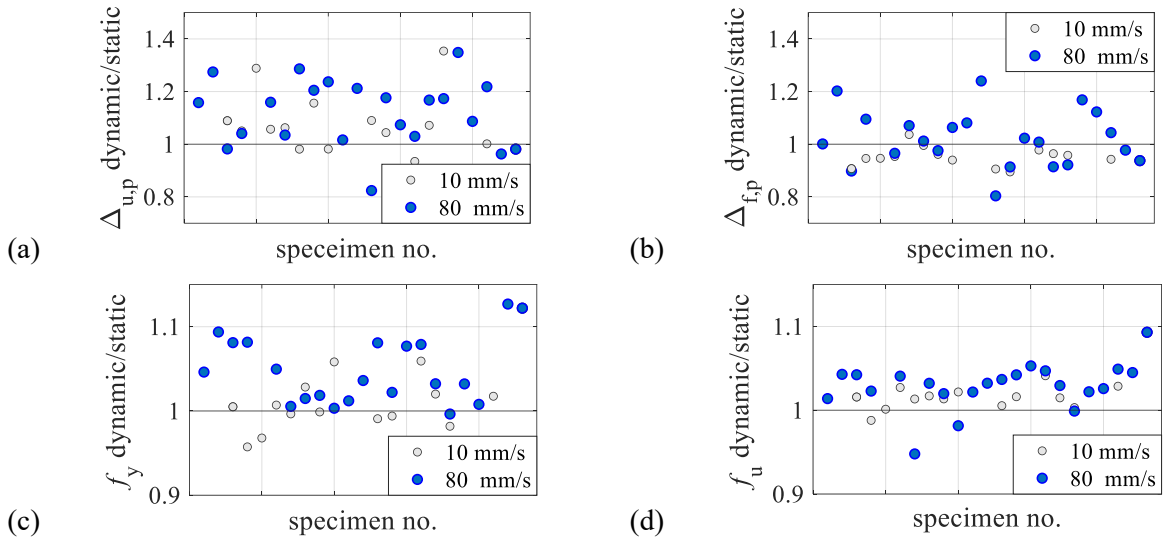

Fig. 5-16 Dynamic-to-static response ratios for bolt assemblies under different loading speeds.

Table. 5-7 Summary of average dynamic-to-static ratios for the plastic elongation and stress parameters

Grade	Loading speed [mm/s]	Average dynamic-to-static ratio			
		$\Delta_{u,p}$	$\Delta_{f,p}$	f_y	f_u
8.8	10	1.04	0.92	1.01	1.02
	80	1.10	0.97	1.06	1.03
10.9	10	1.08	0.94	1.01	1.02
	80	1.10	1.01	1.04	1.04

5.5. Additional guidance on bolt stripping simulation

A total of 19 bolts in the compiled database failed by thread stripping, primarily due to incompatibilities in bolt-nut material strength, geometric mismatches between the bolt shank and the nut threads, and or the use of a single nut in HV bolts. Fig. 5-17(a) shows the comparison of the force-displacement response between the ruptured and stripped bolts. Bolts that undergo thread stripping exhibit the same linear elastic behaviour as ruptured bolts up to yielding. Beyond yield, however, they can only develop limited plastic elongation (typically around 1 mm), reaching approximately 0.90 to 0.95 F_u, followed by a limited post-capping deformation with a rapid loss of strength (generally 0.5–1.5 mm). Fig. 5-17(b) shows comparisons between test data and simulation using this qualitative guidance. In these simulations, the residual strength stage due to thread re-engagement is ignored from a conservative point. Fig. 5-17(c) shows comparisons between test data and CFE simulation results for a joint-level specimen. The figure shows good agreement between the test and simulation, indicating that the developed bolt model, along with the qualitative guidance, can effectively capture bolt stripping with acceptable accuracy.

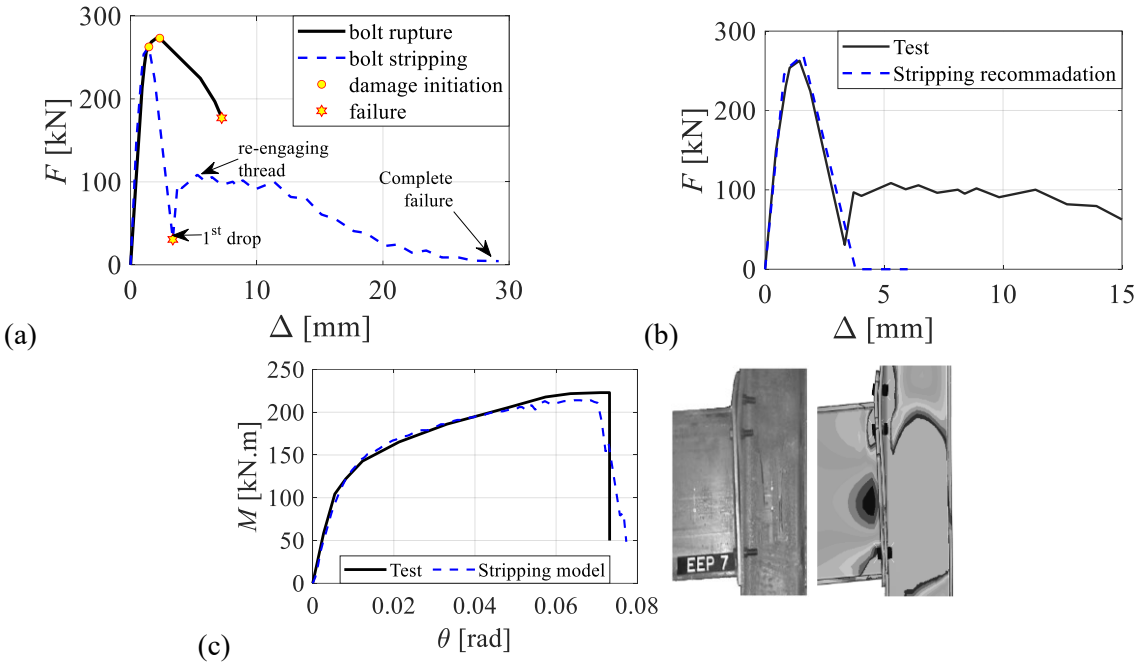

Fig. 5-17 (a) Force-dispalcement responses of the ruptured and stripped bolts; (b) Recommadation for modelling stripping bolts; (c) joint-level simulation: specimen *EEP7* by Tahir and Hussein [100]

5.6. Model limitation

The developed model and empirical expressions are valid for partial- and full-threaded bolts of grade 8.8, A325, 10.9, or A490 with a nominal diameter between 12 and 30 mm and a grip length between 60 and 170 mm. Those ranges cover the ones allowed in construction practice EN-15048 [135]. The model can be potentially extrapolated to long structural rods/bolts (L_g > 200 mm). Note that for steel rods that are cold-forged (not heat-treated), the post-ultimate plastic elongation may be omitted [136].

In joints undergoing rotational demands, the bolts are subjected to combined tension and shear. The bolt's shear to tension force ratio depends on several factors, such as the number of bolts, the beam depth, gravity loads, catenary action, and level of rotation. Based on the compiled database for full-scale joint tests (see Chapter 2), when the connection reaches its capacity, the ratio of shear to tension force in bolts as part of EEPCs varies between 0.01 and 0.2 with an average value of 0.07, as shown in Fig. 5-18. This level of shear force is not detrimental to the bolt behaviour [95, 110, 111, 137]. Accordingly, the proposed model is valid for such cases. Conversely, for connections where the bolts are under dominant shear or bearing stresses, such as shear-tab connections or double web angle connections, the model is not appropriate.

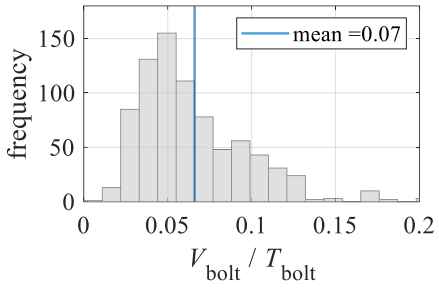

Fig. 5-18 The ratio of shear to tension force in bolts as part of EEPCs.

The strain rate effect is assessed herein based on 92 tests at two loading speeds. Accordingly, the assessment is conducted qualitatively to evaluate the average change in the bolt's response quantities under higher loading speeds. Considering the observed relatively strong variability in the test results at high loading speeds, much more data is needed (across a wider range of varying loading speeds) to capture the underlying response correlations/dependencies and to develop explicit expressions that account for the loading speed. Until then, the connection response can be potentially evaluated at high loading speeds using the developed quasi-static expressions, after being modified using the quantified dynamic-to-static ratios.

A bolt assembly can be coated at the shank, threads, and nut surface with more than 20 alloys and metals. High-strength carbon steel bolts are generally covered by either zinc-plated, black oxidation, or galvanised layers. An appropriate coating can effectively improve the mechanical performance of bolts and protect against corrosion. Different coatings may affect the bolt behaviour and consequently that of the connections [122]. For instance, Hu et al [98] found that Grade 8.8 bolts with black oxidation coating developed a 15% larger elongation than bolts with a zinc layer. The developed empirical expressions (Eqs. 5-7 and 5-8) include bolts with different coatings (i.e., BZP and GLV). Those constitute part of the uncertainty (confidence and prediction intervals) associated with these expressions.

5.7. Summary remarks

Due to the limitations of calibrated fracture locus models, a hybrid-empirical trilinear spring model that incorporates uncertainty to accurately predict bolt response up to failure is now proposed, which the details follow as:

- A comprehensive database was firstly compiled from 200 original tests on high-strength bolts under varying geometries and loading speeds, supplemented by 76 additional specimens from the literature.
- Utilising the experimental database, an analytical expression modified by a correction factor was proposed to compute the bolt's elastic stiffness, which explicitly account for the elastic interaction between the nut and bolt threads. Subsequently, empirical expressions relating to thread length and

grade were developed to compute the bolt's plastic ultimate and fracture displacements. Critically, the inherent material uncertainty in these parameters was quantified by implementing 68% prediction interval bounds.

- The proposed spring model can be assigned to the axial connector as part of CFE simulation. Several bolt assemblies and joint specimens were validated, and the predicted failure rotations of all specimens fell within the uncertainty bounds with a maximum error range of about ±20%. Most importantly, the implementation of axial connectors for bolts significantly enhances the computational efficiency of the joint-level simulations without compromising accuracy. This is critical for a large-scale parametric CFE simulation in the subsequent chapter. Moreover, the spring model can also be incorporated into mechanical models to enhance the performance of existing code-based approaches, such as the component method in Eurocode 3.
- The effect of faster loading rates was also qualitatively investigated. While no clear tendency was observed for elastic stiffness or fracture elongation from 0.05mm/s to 80mm/s, but it showed an average increase of 5% in yield and ultimate strengths, and 8% in plastic ultimate elongation.

6

PARAMETRIC CFE STUDY

6.1. Past studies on parametric simulations for EEPCs

Several parametric simulations have been conducted in the literature to study the behaviour of EEPCs. Table. 6-1 summarises the investigated primary parameters in past studies and their respective ranges.

Rölle [131] conducted a parametric study to investigate the EEPCs' ductility. All specimens are unstiffened connections with S355 structural steel and HV Gr10.9 bolts under monotonic loading. Seven geometric parameters were considered. All specimens were designed as SR.

Augusto et al [138] conducted a parametric study for 56 exterior carbon steel EEPCs under monotonic and cyclic loading. Components are constant with S355 steel and Gr 10.9 bolts. Six geometric parameters were considered. All investigated parameters satisfied the design requirement in Eurocode 3. All specimens were designed to be damaged by EPB or CWS.

Elflah et al [139] conducted a parametric study for 32 exterior stainless steel EEPCs under monotonic loading. The beam section is constant for all specimens. Two grades of stainless steel were applied: austenitic and lean duplex. All investigated parameters satisfied the design requirement in Eurocode 3 [7]. All those 32 specimens were designed to be damaged by EPB or CFB.

Eladly and Schafer [20] conducted a parametric study for 180 exterior stainless-steel EEPCs under monotonic loading. Two grades of stainless steel and seven geometric parameters were considered, while the column depth, column flange width, and column web thickness were constant. The bolt preload was not considered. All investigated parameters satisfied the design requirement in Eurocode 3 [7] and the recommendations by Shi et al [78]. All those 180 specimens developed excessive EPB and failed by the bolt rupture in tension (i.e., Mode 2 in Eurocode3).

Luo et al [140] conducted a parametric study for 144 exterior and interior carbon steel EEPCs under cyclic loading. Eight geometric parameters were considered. The beam section and material properties were constant. The bolt preload was considered. This parametric simulation was used to study the strength, initial elastic stiffness, and ductility. All investigated parameters satisfied the design requirement in the Code for Design of Steel Structure [141]. Specimens were designed to be damaged by EPB, CFB, or CWS.

Özkılıç [79] conducted the parametric study for 156 EEPCs to investigate five primary geometric parameters. All specimens are exterior double-extended connections with rigid columns. The materials of bolts and connection components are Gr 10.9 and S275, respectively. All bolts are pre-tightened based on AISC [142]. The parametric study focused on how the connection strength is affected by the variation of each primary parameter. It was found that larger bolt diameters and endplate width will increase the connection strength; however, larger bolt gauge and tensile bolt pitch will decrease the connection strength.

Besides, a modified yield line pattern for the unstiffened endplate was proposed, considering the weld fillet thickness.

Table. 6-1 Summary of investigated parameters in past CFE parametric studies [unit: mm]

Reference	No.	Steel type	Geometry	Ranges	Other parameters
Rölle [131]	72	Carbon	Column Beam t_{ep} d_b g p_t	HEB 300-400; HEM 300 IPE 400-600 12-20 16-27 60-220 80-220	Unstiffened column Asymmetric bolt layout S355 and Gr 10.9
Augusto et al [138]	56	Carbon	Column Beam t_{ep} d_b	HEB340; HEB500 IPE450; IPE 500 18/25 30/36	(Un)stiffened S355/Gr 10.9
Elflah et al [139]	32	Stainless	Column Beam t_{cf} t_{ep} g p_t	BU 240 BU 240 8-16 6-14 50-90 80; 110; 140; 170	Unstiffened column Asymmetric bolt layout Stainless steel
Eladly and Schafer [20]	180	Stainless	Column Beam t_{ep} g d_b p_t	BU 240 BU 240/300 8-12 50/70 12/16 92/112	Stiffened column (un)stiffened plate Stainless steel
Luo et al [140]	144	Carbon	t_{cf} and t_{cw} d_b t_{ep} h_{ep} and b_{ep}	(15,10); (12,8) 16; 20; 24 12; 16; 20 (500, 250); (450, 226)	Stiffened column Interior/exterior joint Q345/Gr 10.9
Özkılıç [79]	156	Carbon	Column Beam t_{ep} d_b g	Rigid BU 300/500 6-10 24-30 85/90/160	S235/S275/Gr 10.9

6.2. Investigated parameters

Several parameters need to be determined and appropriately designed. Those parameters are classified as primary variables, random geometric parameters for bolt layout, material parameters incorporating uncertainty and variability, and constant geometric parameters. Fig. 6-1 illustrates those investigated parameters. Note that two additional categorical parameters are also considered, which are the presence of column web stiffeners and joint configuration. The presence of column web stiffeners refers to whether the connection is unstiffened or stiffened at both the beam flanges. Additionally, the joint configuration refers to whether the connection is an exterior/interior joint under asymmetric loading or an interior joint under symmetric loading. The determination of those parameters is elaborated in the following sub-sections.

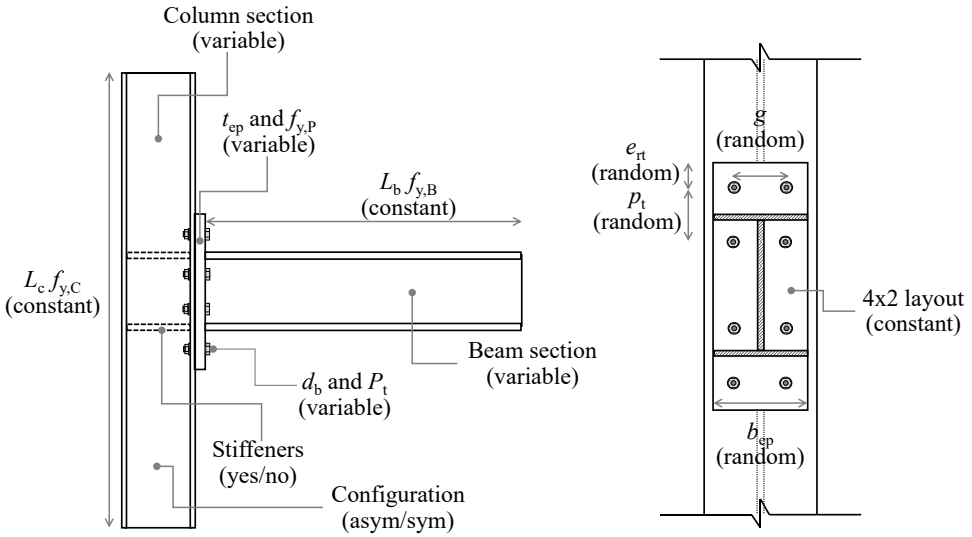

Fig. 6-1 Illustration of the investigated parameters.

6.3. Primary parameters

The behaviour of EEPCs is highly affected by the variation of geometric parameters. Therefore, several geometric parameters need to be designed and investigated. Based on the EEPC's experimental database in Chapter 2, the non-special SR I-shaped beam-to-column specimens are selected. Fig. 6-2 shows the data gaps of beam depth (h_b), column depth (h_c), endplate thickness (t_{ep}), and bolt diameters (d_b), as those are the most critical parameters for the EEPCs design. For the beam depth, a gap ranging from 500 to 600 mm is noticed. Similarly, the column depth gap, endplate thickness gap, and bolt diameter gap are observed, ranging from 240 to 400 mm, 15 to 40 mm, and 20 to 30 mm, respectively.

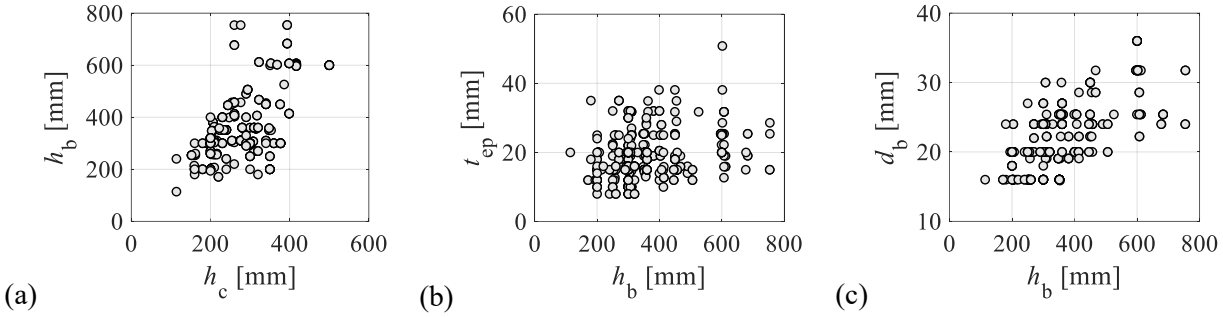

Fig. 6-2 Data gaps in the experimental database: (a) h_b versus h_c, (b) t_{ep} versus h_b; and (c) d_b versus h_b.

With respect to material parameters, either S275 or S355 steel is typically used for the endplate, see Fig. 6-3(a). Therefore, these two types of steel grades are used as one of the primary parameters, as the endplate is the main component to deform in EEPCs. For high-strength bolts, it is observed that either Gr 8.8 or Gr 10.9 bolts are typically used in EEPCs, see Fig. 6-3(b). Therefore, these two bolt grades are selected as one of the primary parameters.

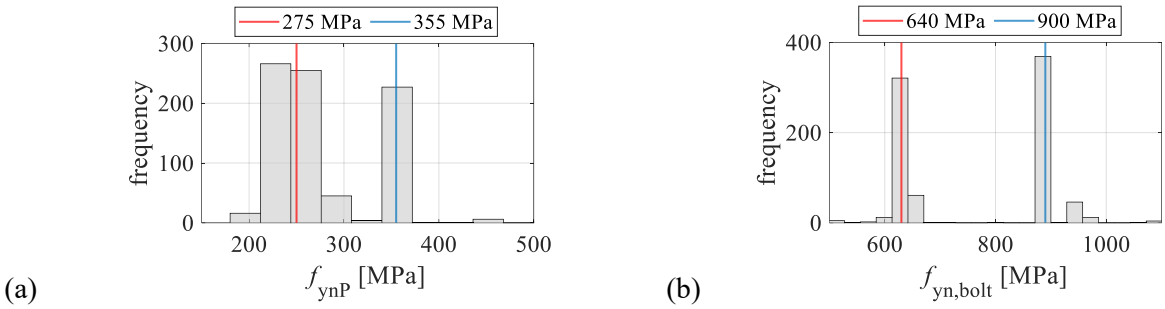

Fig. 6-3 The distribution of material properties for EEPCs: (a) endplate, and (b) bolt.

The bolt pretension level is also considered as one of the primary parameters. The bolt pretension has a significant effect on initial elastic stiffness (K_e). However, there is not much research on EEPCs' predictive models and parametric simulations focused on the impact of bolt pretension. The specimen with fully pretensioned bolts can develop up to three times the initial elastic stiffness of non-pretensioned bolts. Fig. 6-4 shows the distribution of the bolt pretension level for EEPCs. The bolt pretension level is the ratio of pretension force to the product of the bolt tensile stress area and its nominal yield stress. It is found that most specimens are either fully pretensioned (i.e., ratio ≈ 0.7) or snug-tightened (i.e., ratio ≈ 0.2). The fully pretensioned bolts are generally used for rigid connections. This is to ensure that the bolts do not bear shear force and that the friction prevents slipping between the endplate and column flange. The snug-tightened bolts are typically used for SR connections. This is because some movement or rotation is allowed at the joint. Therefore, two levels of bolt pretension are considered as the primary investigated parameters: 20% and 70% of the bolt nominal yield strength.

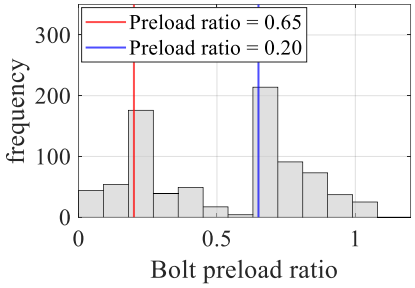

Fig. 6-4 The distribution of the level of bolt pretension for EEPCs.

Table. 6-2 summarises all primary parameters: the beam section, column section, endplate thickness, bolt diameter, bolt grade, endplate grade, and level of bolt pretension. A total of 1984 specimens are permutated. The presence of column stiffeners (i.e., no stiffener or stiffeners at both beam flanges) and variability of loading direction (i.e., external/interior joints under asymmetric loading and interior joint under symmetric loading) are also considered. This aims to capture the behaviour of the column flange and web panel zone. Fig. 6-5 shows how to name a specific investigated specimen. Note that the "E" means the exterior or interior ones under asymmetric loading, and the "U" means the unstiffened column flange. Note that the range of

primary parameters also covers some redundant data which overlaps the observation in Fig. 6-2, such as the shallow beam and column (i.e., $h_b < 400$ mm and $h_c < 300$ mm) and thin endplate (i.e., $t_{ep} < 15$ mm). This aims to capture the variability by randomly sampling the geometric and material parameters, which is critical to the development of predictive models in the next section.

Table. 6-2 Ranges of primary connection parameters

h_b [mm]	h_c [mm]	t_{ep} [mm]	Bolt	Bolt grade	Plate grade	P_t [% of $f_{yn,b}$]
IPE 300 to 600	HEA 200 to 280	10 to 40	M18 to 30	8.8 (A325)	S235	20
W 310x33 to 360x634	HEB 200 to 400		7/8" to 1-1/2"	10.9 (A490)	S275	70
	W 310x74 to 920x238				S355	

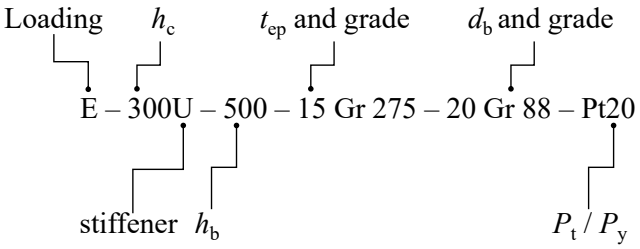

Fig. 6-5 Naming convention for the investigated specimens.

6.4. Secondary parameters

Several secondary parameters shall be appropriately designed for specimen's geometric characteristics and material properties. Note that all these secondary parameters are dependent on the primary parameters. Fig. 6-6 shows the flowchart of designing each secondary parameter. The secondary parameters include the constant parameters (i.e., L_b, L_c, and bolt layout), random geometric parameters (i.e., b_{ep}, e_{rt}, p_t, and g), and material properties incorporating uncertainty. The details of designing each secondary parameter are fully explained in the following sections.

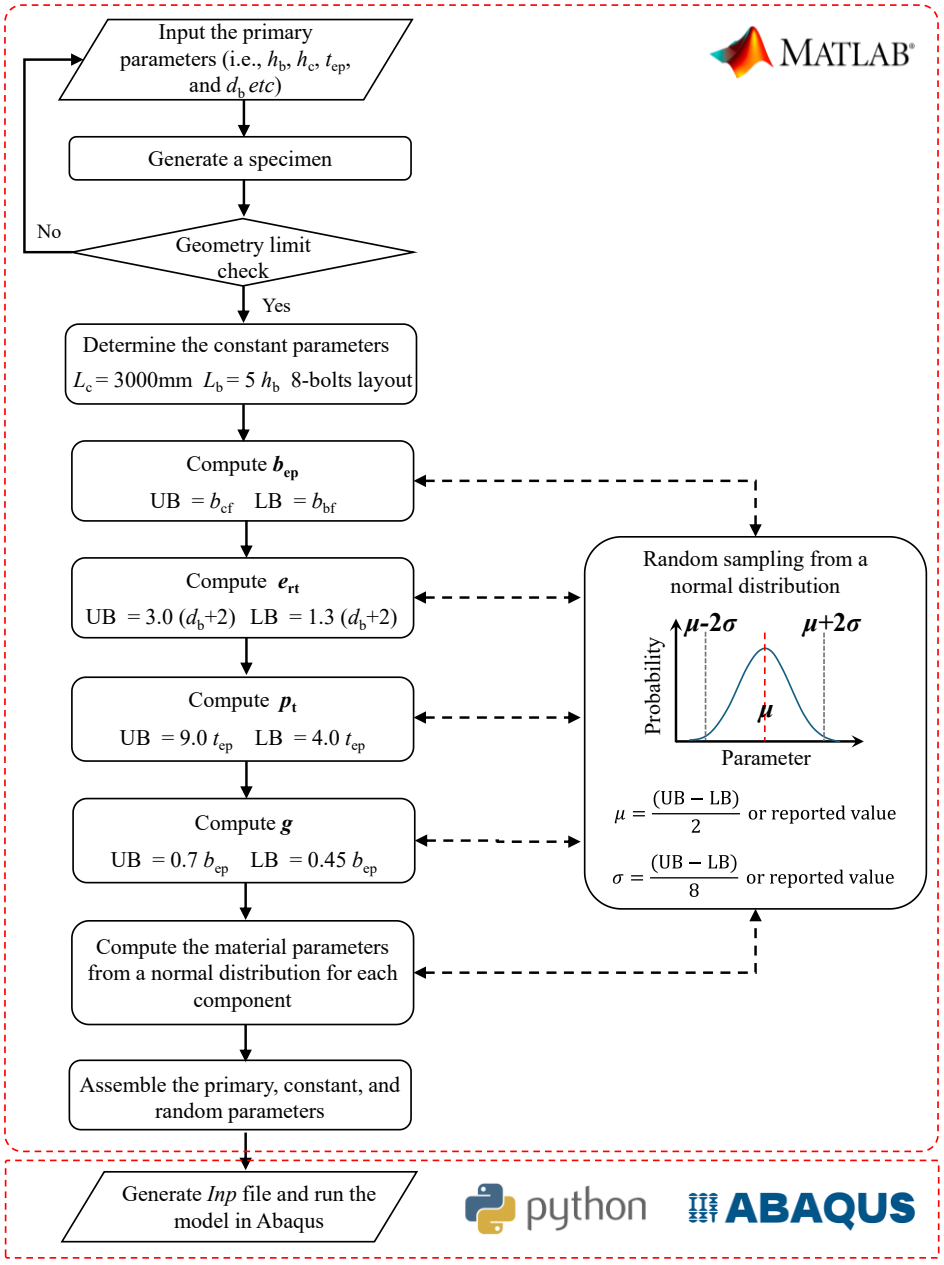

Fig. 6-6 Flowchart of the parametric specimen's geoemtric and material parameters.

6.4.1. Constant parameters

All parametric specimens are double-sided connections with standard eight-bolt layout as this type of connection is widely used in practice, especially for seismic design. The column length (L_c) is kept constant at 3000 mm which is the typical story height. With respect to the beam length (L_b), Fig. 6-7 shows the distribution of the mean's length-to-depth ratio for SR EEPCs based on the database. It is noticed that the L_b of most specimens is four to five times their h_b. For simplicity and consistency, the value of 5 is herein determined for the ratio of L_b to h_b in this parametric simulation.

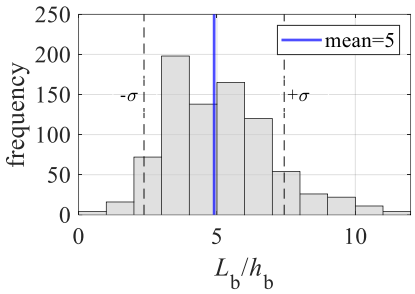

Fig. 6-7 Distribution of the ratio of L_b to h_b.

6.4.2. Random geometric parameters for bolt layout design

The upper boundary (UB) and lower boundary (LB) values of bolt pitch (p_t), bolt gauge (g), bolt edge distance (e_{rt}), and endplate width (b_{ep}) computed based on the statistics in the experimental database, see Fig. 6-6. For each specimen, the values of random geometric parameters are determined based on a random sampling from a normal distribution. Note that this normal distribution is generated with the computed mean value (μ) and standard deviation (σ) based on the UB and LB. Additionally, the requirements of AISC [142] and CEN [7] are also considered to ensure each specimen has a realistic bolt layout.

6.4.3. Material variability

The variability of material is also considered to better simulate the CFE model. This is because the uncertainty of material has a significant effect on the connection behaviour. For high-strength bolts, two grades are studied: Gr 8.8 and Gr 10.9. Note that the material variability of high-strength bolts have been fully described in Chapter 5. For structural steels, three grades are studied: S235, S275, and S355. Table. 6-3 shows the average (μ), standard deviation (σ), and numbers of different section steels based on the experimental database. Random sampling from a normal distribution is used to determine the actual yield stress, ultimate stress, and Young's modulus.

Table. 6-3 Stress and Young's modulus variability for structural steels in the EEPC database

Steel grade	Statistical metric	f_y [MPa]	f_u [MPa]	E [MPa]
S235	μ	301	440	197482
	σ	45	45	10346
	Number	129	112	37
S275	μ	324	477	206468
	σ	29	39	10228
	Number	70	64	22
S355	μ	395	529	205674
	σ	28	34	7405
	Number	38	39	23

Apart from the EEPC database, several studies also focused on the statistics of material properties. Mak and Elkady [50] established an experimental database for flush endplate connections (FEPCs). Table. 6-4 shows the statistical data for S235, S275, S355, Gr 8.8, and Gr 10.9 steels in the FEPC database. Additionally, Table. 6-5 shows the statistical data for S235, S275, and S355 steels in past studies. Note that the material variability with respect to strength observed in the EEPCs experimental database is consistent with the literatures.

Table. 6-4 Stress and Young's modulus variability based on the FEPC database by Mak and Elkady [50]

Steel grade	Statistical metric	f_y [MPa]	f_u [MPa]	E [MPa]
S235	μ	285	424	201118
	σ	35	37	7707
	Number	45	34	11
S275	μ	316	478	198681
	σ	33	50	18644
	Number	43	42	27
S355	μ	393	537	205912
	σ	35	47	14738
	Number	26	25	8

Table. 6-5 Stress and Young's modulus variability for structural steels in past studies

Reference	Steel grade	Statistical metric	f_y [MPa]	f_u [MPa]	E [MPa]
Melcher et al [143]	S235	μ	285	422	-
		σ	22	20	-
		Number	5493	5493	-
	S355	μ	394	566	-
		σ	25	25	-
		Number	1089	1089	-
Sadowski et al [144]	S355 JR	μ	410	465	208000
		σ	53	52	27456
		Number	120	120	174
	S355 J2+N	μ	406	540	208000
		σ	69	29	27456
		Number	31	31	174
	S550 MC	μ	631	678	208000
		σ	34	37	27456
		Number	23	23	174

The strain variability of structural steels is also studied. Three grades are considered: S235, S275, and S355. However, no available data was collected from the experimental database. Therefore, Table. 6-6 shows the statistical data of ultimate and failure strains for each grade in several past studies. The mean (μ) and standard deviation (σ) values for each grade are computed based on the average values from all past studies.

Table. 6-6 Strain properties of structural steel in the experimental database

Steel grade	Reference	ε_u	ε_f
S235 (and equivalent)	Coelho [145]	0.14	0.25
	Melcher et al [143]	-	0.38
	Braconi et al [57]	-	0.33
	Kossakowski [146]	0.16	0.27
	Wang and Chen [147]	-	0.22
	Lacalle et al [148]	0.15	-
	Prinz et al [149]	-	0.32
	Li and Wang [150]	-	0.34
	Shi et al [151]	0.11	0.37
	Kozłowski and Kukla [152]	0.18	0.34
		$\mu = 0.15$ $\sigma = 0.03$	$\mu = 0.31$ $\sigma = 0.06$
S275 (and equivalent)	Ali [153]	-	0.33
	Torić et al [154]	0.20	0.26
	Aldeeb and Abduelmula [155]	0.18	0.32
	Kozłowski and Kukla [152]	0.20	0.32
	Alrubaidi et al [156]	0.14	0.21
	Ho et al [157]	0.19	0.34
		$\mu = 0.18$ $\sigma = 0.03$	$\mu = 0.3$ $\sigma = 0.05$
S355 (and equivalent)	Melcher et al [143]	-	0.31
	Braconi et al [57]	-	0.26
	Prinz et al [149]	-	0.28
	Foster et al [158]	0.16	0.29
	Shi et al [159]	0.15	0.20
	Costa et al [160]	0.13	-
	Gao et al [101]	0.16	0.32
	Ho et al [157]	0.15	0.27
		$\mu = 0.15$ $\sigma = 0.01$	$\mu = 0.28$ $\sigma = 0.04$

6.5. Summary of the parametric simulated specimens

A total of 1980 CFE simulations were conducted for EEPCs with an 8-bolt layout. Fig. 6-8 shows the design space covered by experimental and simulation data, with respect to key geometric parameters (refer to Fig. 6-2). The data uniformly covers all practical beam depths up to 900mm (see Fig. 6-8 (a)) and endplate thickness up to 40mm (see Fig. 6-8 (b)). Deeper beams with thicker endplates mostly correspond to fully rigid EEPC designs. Fig. 6-8 (a) and (b) also demonstrate the expected proportionality between the beam and column sizes as well as the endplate and column flange thicknesses. Referring to Fig. 6-8 (b), several specimens have a column flange thickness of over 40mm. Those specimens were designed to have a strong column section, with no plastic deformation. The dataset also covers a wide range of the p_t parameter (the vertical pitch of the tension bolt rows) and the endplate width (see Fig. 6-8 (c)). Finally, it is worth noting

the consistent distribution of both the experimental and simulation data across the design space and the absence of data gaps.

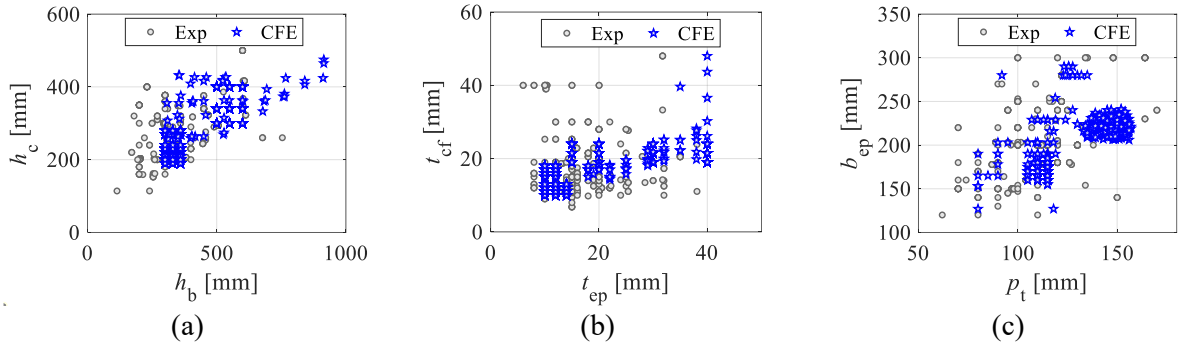

Fig. 6-8 Dataset design space distribution: (a) h_c versus h_b; (b) t_{cf} versus t_{ep}; and (c) b_{ep} versus p_t.

For all parametric simulated specimens, the proposed CFE modelling approach and bolt force-elongation model proposed in Chapter 4 and 5 are implemented. The column was 3 meters long, while the beam length was taken as five times the beam's depth. Both the column ends and the beam's free end were free to rotate (pinned) in the plane of the deformation. A monotonically increasing vertical displacement (Δ_y) is applied at the beam's free end until bolt failure occurs. The implicit solver is herein used to save the computational cost. All components were modelled using the linear solid elements with incompatible mode (C3D8I), except for the endplate with the quadratic solid elements with reduced integration (C3D20R). The mesh size was selected such that at least two mesh elements are used through a given component thickness. This resulted in a mesh size ranging from 5 to 15mm. Young's modulus as well as the values of the yield and ultimate stresses and strains were randomly sampled from normal distributions representing the intrinsic variability of the respective material. The bolt head and nut were modelled using solid hexahedral elements (C3D8I) while an axial connector was used to model the bolt shank to reduce computational time. The connector is assigned a randomised trilinear force-elongation response dependent on the bolt's grade and geometric details. The beam-to-endplate and the stiffener-to-column (when present) welded connection is modelled with a *"Tie"* constraint. A general hard contact interaction, with allowable separation after contact, was defined between the different moving parts. For the tangential behaviour, a static friction coefficient equal to 0.3 is assumed. The explicit solver was used to trace the joint behaviour up to bolt failure. Residual stresses in the hot-rolled column and beam sections were not modelled as they would not have a notable effect on the connection response [161, 162]. Geometric imperfections were not considered in the endplate or the beam. The latter is not critical when dealing with SR connections where only limited beam yielding is expected, but no beam local buckling occurs. Additionally, the data fitting and deduction of response parameters for each simulated specimen follow the procedure mentioned in Chapter 2. Fig. 6-9 presents the distribution of the key response parameters of the parametric specimens. With the careful selection of the investigated parameters and consideration of material inherent uncertainty, the parametric

specimens reveals a wide variation in their key mechanical responses. Note that some of specimens can develop a K_e, M_{ye} and θ_c over 80000 kN.m/rad, 500 kN.m, and 6% rads, respectively. Those are the gaps in the experimental database for the bare-steel beam-to-column EEPCs, see Fig. 2-20.

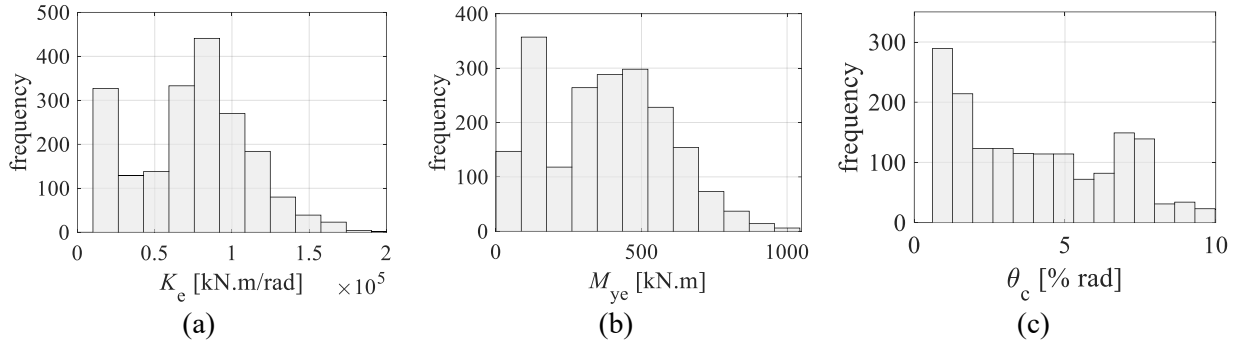

Fig. 6-9 Distribution of the key response parameters of the parametric speicmens: (a) K_e; (b) M_{ye}; (c) θ_C.

To investigate whether the parametric simulations can accurately capture the dependency of the response parameters on the EEPCs' primary parameters, Fig. 6-10 presents a comparison of M-θ responses for several parametric specimens. Note that in each case, only one parameter is varied while the others are kept constant. Fig. 6-10(a) demonstrates the effect of the column stiffeners. It is observed that the unstiffened specimen develops lower K_e and M_{ye} but a much higher θ_C. This is mainly because the unstiffened column flange is less restrained from developing more elastic and plastic deformations. Fig. 6-10(b) demonstrates the effect of t_{ep}. It is noticed that a larger t_{ep} can contribute to a larger K_e and M_{ye} but a relatively lower θ_C, as expected. Fig. 6-10(c) demonstrates the effect of d_b. It is found that a larger d_b does not make a significant difference on K_e and $M_{ye,}$ but on θ_C. This can be explained by the fact that larger bolts can effectively delay the failure after the ductile components, such as the endplate, develop excessive plastic deformations. Fig. 6-10(d) demonstrates the effect of the material properties of endplate and bolt. Note that material properties does not result in a significant difference on K_e. This is reasonable as all structural steels have the similar values of Young's modulus (E), which is one of the main factors affecting EEPC's elastic behaviour. Eventually, Fig. 6-10(e) and (f) present the effect of h_b and h_c, respectively. Clearly, specimen with deeper section will develop higher K_e and M_{ye} due to a longer lever arm from the tension to compression zones. Most importantly, all of these observations are consistent with the findings in the experimental database in Chapter 2 and past studies [20, 49]. This is a strong proof for the combination of experimental test data and parametric CFE data as a resembled large-scale data pool for the development of predictive models in the following sections.

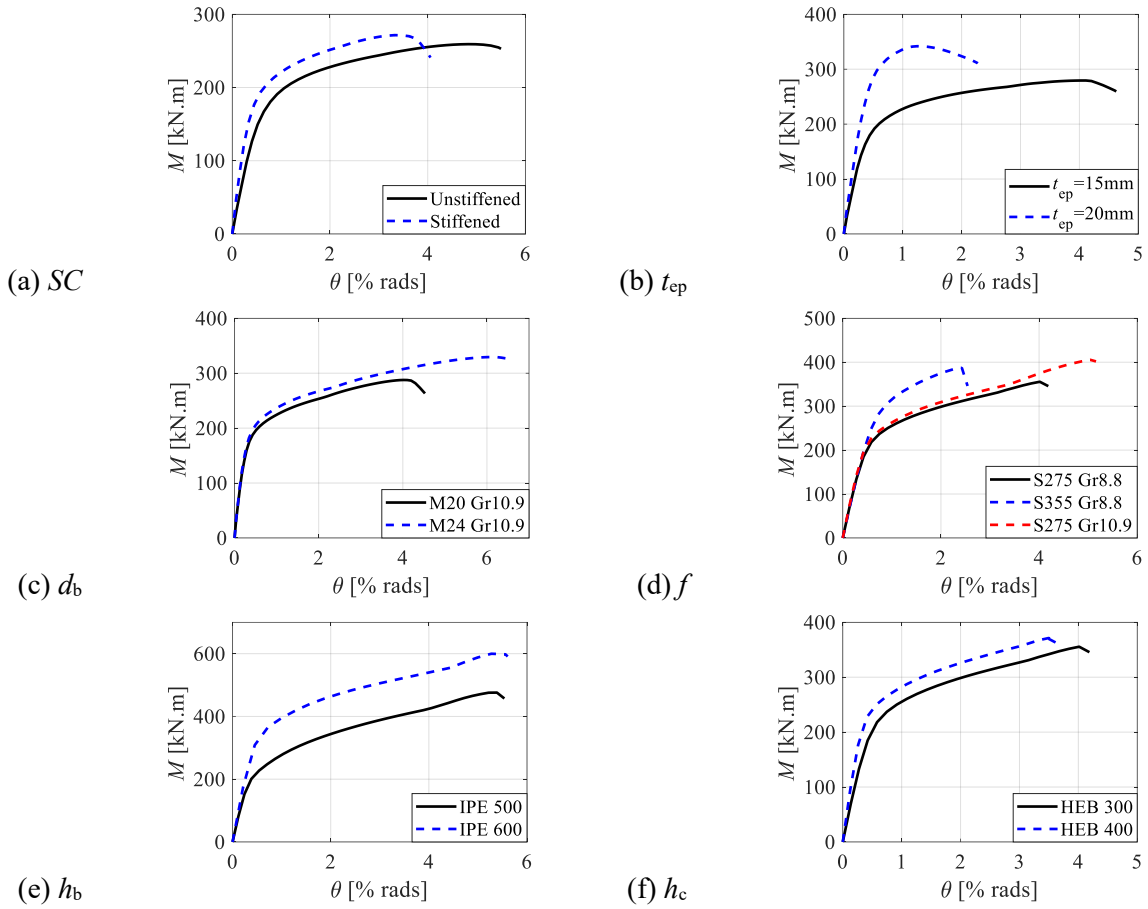

Fig. 6-10 Comparison of M-θ responses for the parametric specimens: (a) *SC* (presence of stiffeners); (b) t_{ep}; (c) d_b; (d) f (material parameters); (e) h_b; and (f) h_c.

6.6. Summary remarks

The developed CFE modelling approach was employed to simulate 1980 bare-steel beam-to-column EEPCs. A systematic procedure was proposed to design the geometric and material parameters of each specimen. The parametric simulations provide redundant data in some ranges in the experimental database. Given the randomly sampled geometric and material properties, this redundancy improves the subsequent regression analysis as it captures the variability of the predictors (i.e., geometric and material parameters). The parametric simulation also complements some geometric and material gaps in the experimental database. Furthermore, the simulated results confirmed that the influence of critical geometric and material parameters on structural response aligns with fundamental mechanical principles. Consequently, the combined experimental – numerical data pool is confirmed to be suitable for developing robust predictive models for EEPCs in the following chapter.

7

DEVELOPMENT OF ROBUST PREDICTIVE MODELS

7.1. Key parameters affecting EEPCs' *M-θ* responses

Before developing the predictive models, a literature review is presented to summarise the influence of geometric and material parameters on various connection response metrics. The distributions of the defined response metrics are then plotted to examine the overall connection behaviour, and the correlations between key parameters and each response metric are analysed.

With respect to strength (i.e., M_{ye} or M_{max}), the following parameters are found to be influential as inferred from the literature:

(1) Column flange or web thickness: In connections controlled by CFB, thinner column flanges generally result in reduced strength. This behaviour is commonly observed in connections with unstiffened and relatively slender column flanges (t_{ep}/t_{cf}>1.5), as illustrated in Fig. 7-1(a). Packer and LJ [163] observed 15% less strength when the column flange thickness is reduced from 12mm to 7mm. In exterior connections where the column web is unreinforced (i.e., without doubler plates or diagonal stiffeners), the panel zone undergoes shear and flexural deformations, further reducing connection strength. When the column flange or web is properly stiffened, its plastic deformation is effectively restrained. Under such conditions, parameters such as bolt diameter and endplate thickness become the primary factors controlling the connection strength.

(2) Endplate thickness: Endplate thickness is a highly influential parameter that controls the behaviour of SR EEPCs (i.e., 0.25 $M_{pl,b}$<M_{ye}<$M_{pl,b}$). For specimens that only deform at the endplate (see Fig. 7-1(b)), thicker endplates (0.6≤ t_{ep}/t_{cf} <1) will lead to a higher connection strength [164]. However, the thin endplate (t_{ep}/t_{cf}<0.6) may cause an excessive endplate deformation, punching through the bolts, so that the connection behaves as a simple one [165].

(3) Beam height: The beam will undergo plastic deformations, in the form of web and flange yielding and local buckling, when the connection is designed as FR or ES [39, 84], as shown in Fig. 7-1(c). In such cases, the local slenderness ratios of the beam flange and web can influence the connection strength. However, if the connection behaves as an SR/PS, the connection strength is lower than the beam's plastic moment. As a result, the beam remains in the elastic range and does not contribute to or govern the connection strength.

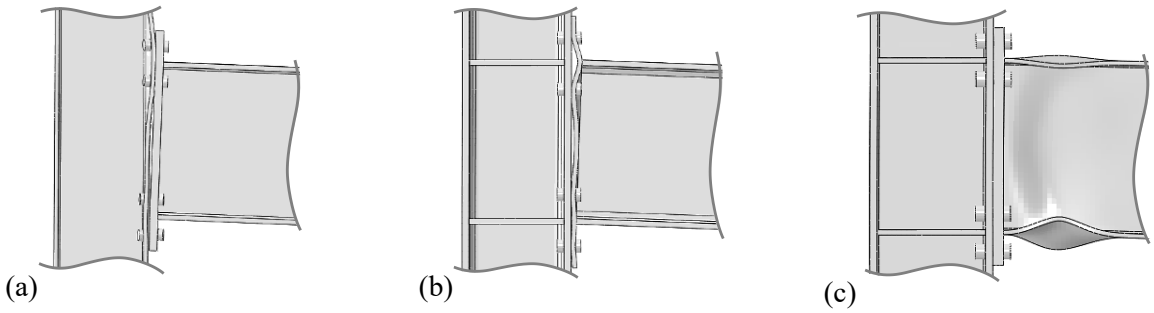

Fig. 7-1 Typical deformations that affect the connection strength: (a) column component bending (t_{ep}>>t_{cf}); (b) endpalte bending (t_{ep}<<t_{cf}); (c) beam flange and/or web buckling.

With respect to the elastic rotational stiffness (K_e), the most influential parameters are:

(1) Number of bolts in tension and vertical bolt row pitch: The connection stiffness can be enhanced by increasing the number of bolts in tension (i.e., multiple bolt rows or columns). Prinz et al [149] found that the connection stiffness of specimens with four bolts per row is about 30% larger than that of specimens with two bolts per row. Furthermore, stiffness increases as the tension bolt row is placed closer to the beam's flange at the tensile side, within the practical limits imposed by detailing constraints [34, 82].

(2) Bolt pretension level: The level of bolt pretension can significantly affect the connection stiffness. It was found that the connection elastic stiffness of fully pre-tensioned connections can be three times higher than that of non-preload connections [34, 82, 166, 167]. This is because high pre-tensioned bolts can effectively restrain the endplate inelastic deformation.

(3) Column or endplate rib stiffener: Column and plate rib stiffeners provide substantial restraint against plastic deformation on the tension side of the connection. Numerous experimental studies have shown that stiffeners can significantly enhance the elastic stiffness of EEPCs, with approximately half of the tested specimens in the experimental database incorporating either plate or column flange stiffeners. For stainless-steel connections, Gao et al [101] reported that plate stiffeners installed on both the tensile and compressive sides increased the elastic stiffness by about 10% in exterior connections and 20% in interior connections. For carbon-steel connections, Shi et al [78] found that column flange stiffeners and plate stiffeners improved the stiffness of exterior connections by approximately 10% and 13%, respectively.

With respect to ductility (i.e., θ_c), the following influential parameters are:

(1) Material properties: With respect to strength and stiffness, connections fabricated from mild carbon steel are comparable to those fabricated from stainless steel. However, with respect to ductility, Gao et al [168] and Gao et al [101] found that stainless-steel connections are capable of developing 30% to 50% larger plastic rotation than carbon steel ones. Furthermore, Coelho et al [37] found that the

plastic rotation of specimens fabricated from high-strength steel (f_{yn} = 690MPa) is 50% lower than that of specimens fabricated from mild steel (f_{yn} = 355MPa). It is worth noting that the connection components may be fabricated from different steel grades. In that case, the material properties of the component controlling the connection deformation should be considered.

(2) Component thickness: Shi et al [78] found that the thicker endplate (t_{ep} increased from 16mm to 20mm), which can reduce plastic rotation by 50% for the stiffened exterior connections. Similarly, Coelho et al [37] also found that the thicker endplate (t_{ep} increased from 10mm to 15mm) can reduce plastic rotation by 50% for the unstiffened exterior connections. In general, stronger components, such as thicker endplates and column flanges, enhance both connection strength and initial stiffness. However, ductility may decrease because the increased thickness restrains the development of plastic deformations. These relationships are examined in detail in the following sections.

(3) Bolt diameter: Shi et al [78] found that larger and stronger bolts (d_b increased from 20mm to 24mm) can transfer the plastic deformation from the bolts to ductile components (i.e., endplate, column flange, and column web panel zone), which can increase the maximum connection rotation by 30%. A similar observation was made in Munter [129], the maximum connection rotation increased from 3% to 5% as the d_b increased from 20mm to 24mm.

(4) Bolt pretension level: Nogueiro [53] found that M24 bolts with pre-tension increased from 21 kN to 83 kN can reduce plastic rotation by 60% for exterior connections.

7.2. Definition of response metrics

The following response metrics are defined and evaluated:

(1) Strength coefficient (α): The strength coefficient is used to evaluate the normalised connection strength. The α coefficient is computed using Eq. 7-1 as the ratio of the effective yield moment (M_{ye}) of the connection to the beam plastic moment ($M_{p,b}$).

$$\alpha = \frac{M_{ye}}{M_{p,b}} \qquad \text{where,} \quad M_{p,b} = Z_x f_{ymb} \tag{7-1}$$

(2) Stiffness coefficient (β): The stiffness coefficient is used to evaluate the connection's elastic stiffness. The β coefficient is computed using Eq. 7-2 as the ratio of the K_e to the beam rigidity ($E_b I_b / L_b$). Note that different L_b are used in past experimental research; although test setup limitations mainly control this length, it does not affect the connection stiffness. This is because the connected beam does not contribute to the connection stiffness. Therefore, for β computation, L_b is assumed to be 15 times the beam depth (h_b). The L_b mainly ranges from 4.6m to 5.6m, which corresponds to the length in the real structure [39].

$$\beta = \frac{K_e}{E_b\, I_b/L_b} \qquad 7\text{-}2$$

(3) Plastic rotation (θ_p): Ductility coefficient is defined as the connection plastic deformation capacity beyond the yield point and before failure. It is mainly evaluated herein by the rotation from the effective yield rotation (θ_{ye}) to the capping plastic rotation (θ_C). Connection ductility (i.e., rotational capacity) is significant in seismic design applications. This is because large inelastic deformation capacity leads to good energy dissipation under seismic loading.

7.3. Response characteristics of the experimental tests

7.3.1. Classification

The database comprises 498 specimens with I-shaped column sections (excluding specimens that are *'Special cases'*, see Section 3.2.2). The *M-θ* curves of these specimens are plotted, in Fig. 7-2. The *M-θ* curve for each specimen is normalised. This is done to support visualising and classifying the specimens. The moment is normalised by the beam's plastic moment $M_{p,b}$, while the rotation is normalised by the reference rotation θ_r, which is computed as $M_{p,b}/(E_b\, I_b/(15h_b))$. All curves are plotted up to the maximum/capping moment point (excluding and post-capping branches to aid with the visualisation). For the specimens under cyclic loading, the positive envelope is plotted rather than the negative one. The median and mean curves are superimposed in the same plot, along with the classification boundaries of Eurocode 3 [7] and AISC 360-22 [8]. From the perspective of strength and stiffness coefficients, the EEPCs can reach 0.7 $M_{p,b}$ and $11E_bI_b/L_b$, on average, respectively. This indicates the most EEPCs in the experimental database behave as PS and SR.

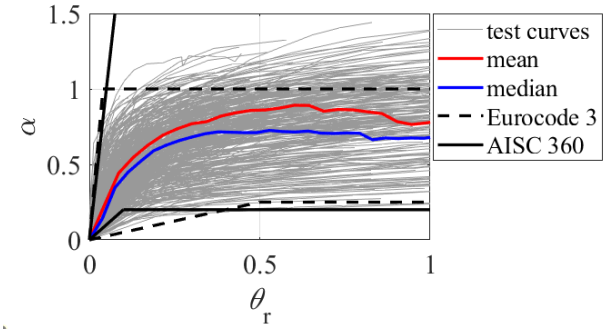

Fig. 7-2 Normalised *M-θ* curves for all specimens with I-shaped columns.

7.3.2. Strength

Distribution of the α is shown in Fig. 7-3. The figure shows that α has a normally distributed tendency, with most specimens ($\pm\sigma \approx 68\%$) developing a strength coefficient ranging from 0.4 to 0.9, and a mean/median

value of about 0.67. This indicates that EEPCs can, on average, transfer 67% of the beam's plastic moment and behave as PS.

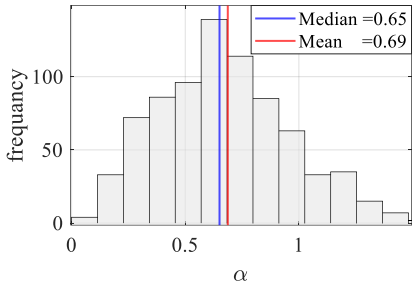

Fig. 7-3 Distribution of α for specimens with an I-shaped column section and strong-axis orientation.

For typical SR EEPCs, the strength coefficient is expected to vary between 0.25 and 1 due to the different geometric or material parameters. However, some specimens behave as simple or FR. Therefore, it is necessary to study which connection parameters lead to these extreme/boundary cases. There are seven specimens with α less than 0.25 (i.e., pinned). Table. 6-1 summarises these specimens' details. The table shows that most of these specimens were controlled by thin column flange deformation or thin endplate excessive deformation ($t_{cf}/t_{ep} > 1.7$ or < 0.6), as demonstrated earlier in Fig. 7-1(a) and (b).

There are 15 specimens with α larger than 1.1 (i.e., FR). Table. 7-1 summarises the details of these specimens. It is observed that all specimens are controlled by the beam flange or web yielding/buckling under cyclic loading (refer to Fig. 7-1(c)).

Table. 7-1 Detail of specimens with the α less than 0.25 and larger than 1.1

	Reference	Specimen	Governing mode	Stiffener	t_{ep} / t_{cf}	t_{ep} [mm]
Specimens with α < 0.25	[169]	Test 3	CFB	No	1.75	21
	[170]	CF5-U10 x 49	CFB	No	1.79	25
	[171]	EP-2-8	CFB	No	0.6	8
	[149]	2A	CFB	No	2.1	30
	[23]	C1	EPB	Column	0.42	8
	[165]	Test 5	EPB	No	0.59	10
Specimens with α > 1.1	[172]	A-5	BFY	Column/Plate	0.95	16
	[33]	Test 1-95; Test 4-95	BFB	No	0.9	25
	[1]	M-5	BFB+BWB	Plate	0.83	19
	[173]	S5 to S6	BFB+BWB	Column/Plate Column	1; 1.38	18; 25
	[54]	P1 to P4	BFB	Column	1.6	35
	[174]	TS12	BFY	Column/Plate	1.45	16

According to the parametric simulation in Chapter 6, some geometric parameters may significantly affect the connection strength. For the presence of column flange stiffener at both sides, the connection strength can be significantly affected. The average strength coefficient for stiffened and unstiffened specimens is 0.75 and 0.62, respectively. This means the column stiffener can enhance the connection strength by up to 20%. Therefore, in discussing the correlation between response characteristics and geometric parameters, specimens are differentiated based on the presence of stiffeners.

Endplate and column flange thickness are the most important geometric parameters affecting the connection strength. For the stiffened specimens shown in Fig. 7-4(a), a positive correlation was observed. For the specimens with the t_{ep}/t_{cf} smaller than 0.5, the strength can only reach up to 0.5. This is because the relatively thin endplate was assigned. The excessive plate bending (Fig. 7-1(b)) significantly decreases the connection strength. When the t_{ep}/t_{cf} is larger than 1, the specimens may develop a connection larger than the beam plastic moment.

The ratio of h_b to t_{ep} is assigned to figure out the correlation for stiffened specimens. This ratio is used because variations in beam depth can influence the connection strength by altering the lever arm of the tensile bolt rows [100]. In Fig. 7-4(b), it is observed that the α decreases with the increase of h_b/t_{ep}. The small value of h_b/t_{ep} means the relatively shallow beam and thick endplate. This can explain why the specimens can develop a strength increase by up to 50% of the beam's plastic moment.

The ratio of p_t to t_{ep} was also assigned. Fig. 7-4(c) shows a negative correlation between the p_t/t_{ep} and the α. The ratio of p_t to t_{ep} can represent the slenderness of the endplate. A larger p_t/t_{ep} means a longer p_t and thinner t_{ep}. Therefore, the connection strength can be reduced by excessive EPB.

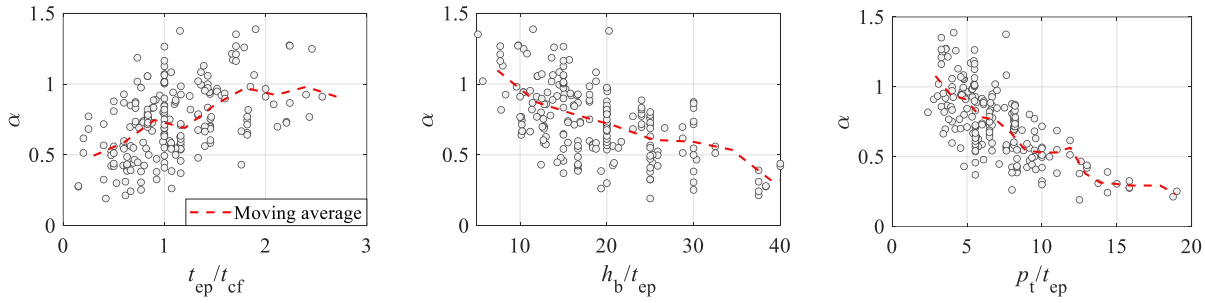

Fig. 7-4 Correlation of stregnth coefficient and geometric parameters (i.e., t_{ep}/t_{cf}, h_b/t_{ep}, and p_t/t_{ep}) for stiffened specimens.

For unstiffened specimens, the ratio of t_{ep} to t_{cf} is one of the primary geometric parameters to affect the connection behaviour. A smaller t_{ep}/t_{cf} indicates that plastic deformation may primarily occur at the endplate, so geometric parameters of the endplate affect the connection behaviour. On the contrary, a larger t_{ep}/t_{cf} indicates that plastic deformation may occur in the column component, meaning that geometric parameters

of the column flange or web could affect the connection behaviour. Therefore, the unstiffened specimens are divided based on whether the t_{ep}/t_{cf} is larger than 1.

For unstiffened specimens with the t_{ep}/t_{cf} smaller than 1, several geometric parameters are selected to investigate the connection behaviour. Fig. 7-5(a) shows a negative correlation between the α and p_t/t_{ep}. This is similar to the observation in Fig. 7-4(c), as the slender endplate may develop an excessive plastic bending so that the connection strength is reduced. Fig. 7-5(b) shows a negative correlation between the α and d_b/t_{ep}. This can be explained by deformation modes in Eurocode3. The smaller d_b/t_{ep} will lead to a connection damaged by Mode2 (see Fig. 3-6(b)), increasing strength through both BE and EPB. In contrast, the larger d_b/t_{ep} will cause a connection to be damaged by Mode1 (see Fig. 3-6(a)). Therefore, the connection strength may be reduced by only EPB.

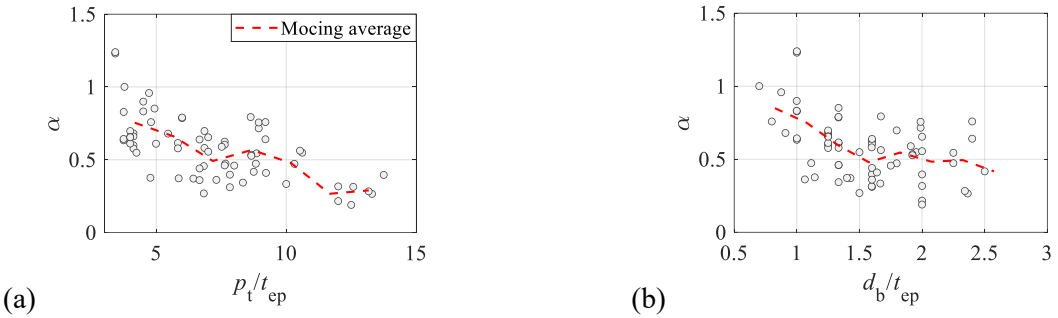

Fig. 7-5 Correlation between predictors and α for unstiffened specimens with $t_{ep}/t_{cf} < 1$.

Once the t_{ep}/t_{cf} is larger than 1, it is observed that the control damage mode is transferred from EPB to CFB or BY due to the relatively thick endplate. Therefore, a nominated ratio of h_b to t_{cf} and d_b is considered to investigate the connection strength. In Fig. 7-6, it shows that the α decreases as $h_b/(t_{cf}\, d_b)$ increases. A larger $h_b/(t_{cf}\, d_b)$ means a deeper beam, a thinner column flange, and a smaller bolt diameter, so that the connection may develop excessive CFB and the strength is reduced. In contrast, the smaller $h_b/(t_{cf}\, d_b)$ may make the connection deformed at the beam because of the shallower beam, thick column flange, and larger bolt, so that the strength is increased.

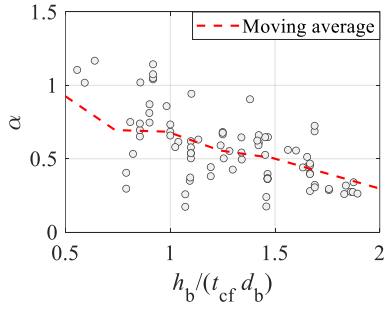

Fig. 7-6 Correlation of α against $h_b/(t_{cf}\ d_b)$ for unstiffened specimens with $t_{ep}/t_{cf} > 1$.

In summary, with respect to EEPC's strength, the main findings are as follows:

(1) Geometric parameters observation: The stiffened specimens can develop a strength 20% higher than the unstiffened specimens. The average t_{ep} for both stiffened and unstiffened specimens is around 19mm. However, the average column flange thickness for unstiffened specimens is 23mm, which is 6mm thicker than that of stiffened specimens.

(2) Correlation against α: For stiffened specimens, key geometric parameters affecting the strength are the h_b and t_{ep}. Based on the result shown in Fig. 7-4, the thick endplate and shallow beam will lead to a high connection strength. For unstiffened specimens, the column flange may develop excessive deformation without stiffeners. Therefore, the ratio of t_{ep}/t_{cf} will differentiate the connection deformation modes. When the t_{ep}/t_{cf} is less than 1 (i.e., $t_{ep}<t_{cf}$), the EPB dominates the deformation mode. It was found that the bolt layout can effectively affect the connection strength. Several geometrical parameters (i.e., p_t, m_2, g, and m_d) were investigated, and they are all negatively correlated to the α. This is mainly because a large distance of gauge or pitch can lead to excessive endplate deformation, reducing the connection strength. However, when the t_{ep}/t_{cf} is larger than 1 (i.e., $t_{cf}>t_{ep}$), the CFB, or BB, was observed as the primary deformation mode. With the increase of h_b/t_{cf}, the strength is decreased, as shown in Fig. 7-6.

(3) Primary deformation modes: For specimens with the α smaller than 0.25, the excessive endplate or column flange bending (depending on the value of t_{ep}/t_{cf}) may significantly decrease the connection strength and make it behave as a pinned one. For specimens with the α larger than 1.1, the beam flange/web buckling is the controlled deformation mode.

(4) Brittle failure: It is found that premature weld failure may affect the connection strength. Several specimens are designed as FR; however, they prematurely failed. Therefore, some outlier scatters are observed in some correlations.

(5) As several predictor parameters were proposed for the connection strength, all those predictors were tested with the α for stiffened and unstiffened specimens. Table. 7-2 shows how those parameters affect the correlation to the α.

Table. 7-2 Summary of the effect of predictor parameters for the α

Parameters	Stiffened column	Unstiffened column ($t_{ep}/t_{cf} < 1$)	Unstiffened column ($t_{ep}/t_{cf} > 1$)
t_{ep} / t_{cf}	H	-	-
h_b / t_{ep}	H	-	-
p_t / t_{ep}	H	M	-
h_b / (t_{cf} d_b)	-	-	H

Note: High (H); Medium (M); Low & None (-)

7.3.3. Ductility

Ductility is the key parameter to evaluate the energy dissipation capacity for structural safety and robustness under hazards such as earthquakes, fires, and explosions [175, 176]. In connection design, ductility corresponds to the joint rotation (θ_j). For a SR EEPC, the θ_j is larger than the connection beam rotation (θ_b), and the ductility (i.e., rotation capacity) is sourced from the ductile component plastic deformation (i.e., EPB, CFB, CWB, and CWS) [177]. Several studies and experiments demonstrate that the EEPCs have adequate rotational capacity [37, 78, 138, 164]. To evaluate the ductility, several quantitative methods are proposed. Typically, Park [178] proposed the nominated ductility index (μ) to describe the ductility, see Eq. 7-3. Eladly and Schafer [20] evaluated the ductility index for 180 SR stainless-steel specimens, and the ductility index ranges from 3 to 7. CEN [179] requires that, for seismic-resistant design, the joint rotation capacity should be at least 3.5% rad for High (H) ductility class and 2.5% rad for Medium (M) ductility class. This can be used as a reference to evaluate the plastic rotation (θ_P).

$$\mu = \frac{\theta_{\max}}{\theta_{ye}} \qquad 7\text{-}3$$

To assess the specimen's ductility, the plastic rotation (θ_P) is used to present the ductility herein. It should be noted that only specimens that reached a definitive failure mode, such as bolt rupture, bolt stripping, weld failure, or endplate fracture, were considered in the ductility analysis, as these specimens attained their full rotational capacity.

The θ_p distribution is shown in Fig. 7-7. The median and mean value are around 3.8% rad, and most specimens range from 1.5% to 7.5% rad. Besides, it shows a tendency towards a right-skewed distribution. Note that some specimens can develop an excessive deformation, where the θ_p is over 10% rad (i.e., $> 2 \cdot \sigma$), whereas some specimens can only deform less than 1% rad (i.e., $< \sigma$). It is noticed that only 17 specimens developed a plastic rotation of less than 1% rad. All those specimens failed due to premature bolt rupture or weld failure. Note that seven specimens can develop a plastic rotation larger than 10% rad. Those specimens are all exterior connections, and plastic deformation happened at the endplate (i.e., bending) or column (i.e., bending or panel zone in shear).

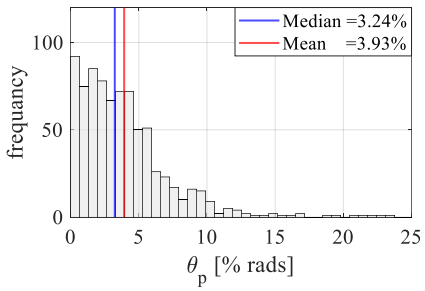

Fig. 7-7 The distribution of plastic rotation for I-shaped column specimens.

The observed θ_p distribution shows that the ductile capacity of the specimens is highly dependent on their governing deformation mode. Therefore, all specimens are classified based on the controlled damage modes: 1) EPB; 2) CFB, CWB, or CWS. Specimens that only failed by BR, BS, or WF are excluded from the data response analysis. This is because those specimens failed too early to develop their full ductile capacity. Specimens that failed by BB are also excluded. This is because those are all FR specimens.

Several studies were carried out on ductility prediction. Eladly and Schafer [20] proposed an empirical model for maximum rotation. The prediction formula mainly includes the t_{ep}, t_{cf}, d_b, h_b, and f_{yP}. Rölle [131] also proposed the ductility prediction criteria with the effect of h_b, d_b, f_{yP}, f_{ub}, p_t, and g. Shi et al [180] implicitly mentioned that the moderate endplate thickness and large d_b will lead to a higher rotational capacity. Therefore, the ductility study is based on all those published studies to investigate how those geometric parameters or material properties affect the specimen plastic rotation.

The specimens are differentiated by endplate or column component damage. For the specimens damaged by EPB, the column sections hardly show a sign of deformation; the degree of endplate deformation determines the rotational capacity. Therefore, it is observed that the endplate geometric parameters can clearly affect the plastic rotation. In Fig. 7-8(a), it is noticed that a larger ratio of t_{ep} to d_b leads to decreased plastic rotation. This is because the larger bolt and thinner endplate can promote plastic deformation of the endplate at the beam tensile flange side. Note that, once this ratio is over 1, some specimens can develop plastic rotation exceeding 4% rads. For those specimens, the ratio of t_{ep} to t_{cf} is greater than or equal to 1, causing the column flange to show signs of yield and develop plastic deformation to some extent after the endplate excessively deforms.

It is noticed that the larger beam depth will decrease the plastic rotation. Once the beam depth is over 350 mm, the specimens can only develop a plastic rotation of less than 4% rad. This is caused by multiple reasons. Some specimens failed prematurely due to weld failure, which restrained the full capacity of plastic deformation. Compared to the shallow beam, the tensile bolts for specimens with a deeper beam will develop a larger elongation at the same chord. In the design process, the deeper beams require a thicker endplate because of the larger design moment at the column face. Similar to bolt failure with a deeper beam, the rotational capacity of a thicker endplate is restrained. Therefore, the endplate is prone to fracture after reaching the yield stage, which decreases the rotational capacity.

Larger normalised bolt pitch ($p_t/(t_{ep}\, d_b)$) can promote a larger plastic rotation, see Fig. 7-8(b). For specimens with a large normalised p_t, the endplate is prone to developing plastic deformation. This can be explained by the yield line mechanism.

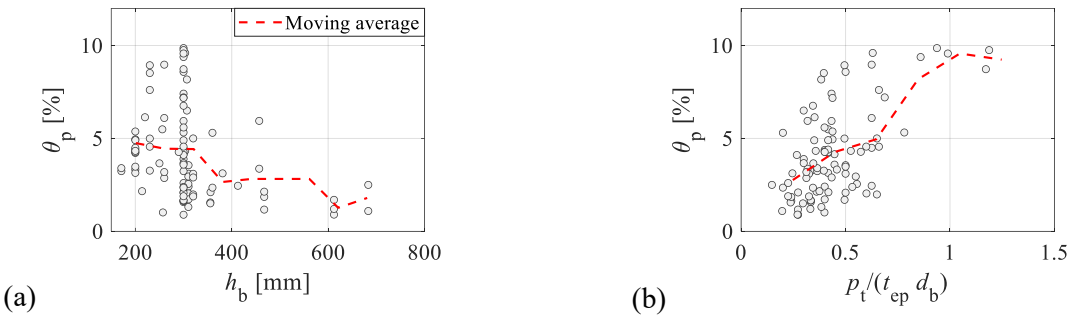

Fig. 7-8 Correlation of ductility and endplate geometric parameters for specimens failing by EPB: (a) θ_P versus h_b; (b) θ_P versus $p_t / (t_{ep}\, d_b)$.

For specimens controlled by CFB, CWB, or CWS, the endplates are not explicitly deformed or are slightly bent due to excessive column deformation. Therefore, the column geometric parameters may effectively reflect the connection ductility. Several parameters related to the column component are investigated. Geometric parameters, t_{cf}, d_b, g, and h_b are selected, and it is found that the ratio of g to the product of t_{cf} and d_b shows a positive correlation to θ_p, as shown Fig. 7-9(a), which is expected. This is because the larger g and smaller t_{cf} or d_b will lead to excessive column component bending and a larger gap between the column flange and endplate. Fig. 7-9(b) shows the correlation between the ratio of h_b to d_b. An opposite negative correlation to Fig. 7-9(a) is also observed. This can be attributed to the fact that the connection may develop plastic elongation only in the bolts rather than in other ductile components.

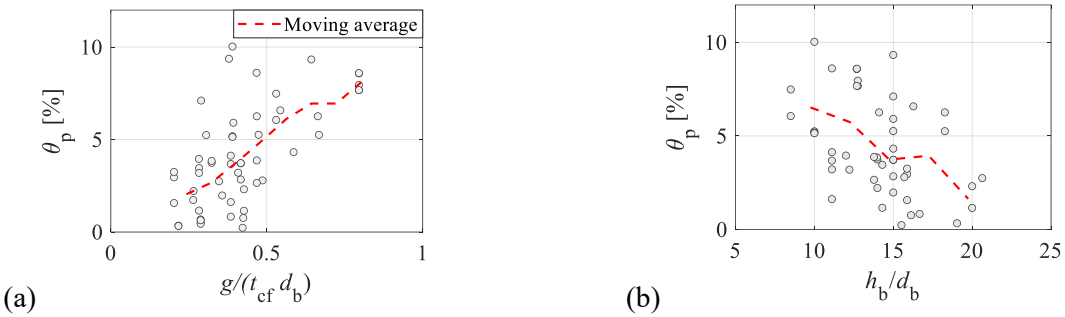

Fig. 7-9 Correlation of ductility and geometric parameters for specimens controlled by column component deformation: (a) θ_P versus $g / (t_{cf}\, d_b)$; (b) θ_P versus h_b / d_b.

In summary, with respect to ductility, the main findings are as follows:

(1) Overall specimens' ductility: The ductility is evaluated based on the θ_P. SR EEPCs can, on average, develop a plastic rotation of around 3.6% rad. Based on the ductility requirement in CEN [179], the SR EEPCs are capable of developing the plastic rotation under seismic loading.

(2) The resource of ductility: The ductility resource for SR EEPCs is mainly from the ductile components' deformation (i.e., EPB, CFB, or CWS). It is observed that the specimen exhibiting the maximum plastic rotation (θ_p>10%) experienced extensive plastic deformation across all ductile

components. This means that predicting the SR EEPCs' plastic deformation is challenging and complicated.

(3) Ductility criteria: Based on the parametric study and correlation investigation, several basic ductility criteria are concluded, as shown in Table. 7-3. Those ductility criteria are limited by the average plastic rotation of less than 5% rad for each correlation.

Table. 7-3 Basic criteria limits for high ductility

Criteria	EPB controlled	Column bending controlled
h_b	≤ 350	-
p_t / (t_{ep} d_b)	> 0.5	-
g / (t_{cf} d_b)	-	> 0.5
h_b / d_b	-	< 12

7.3.4. Stiffness

The β of most specimens ranges from 2 to 15, as shown in Fig. 7-10. However, the mean and median values are around 11 and 7, respectively, with the mean value being slightly larger than the median. This means that the data tends to have a right-skewed distribution. Due to the relatively larger second moment of inertia (I) of I-shaped beam sections, there is no specimen with β less than 0.5. This means the EEPCs with I-shaped columns have acceptable stiffness performance and behave overall as SR.

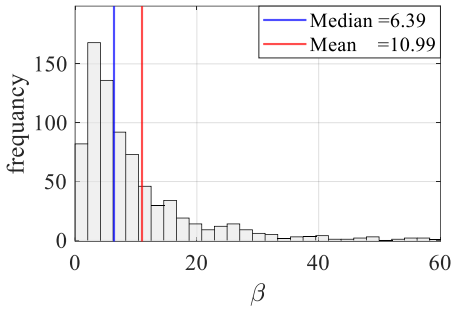

Fig. 7-10 Distribution of β for specimens with I-shaped column section.

A subset of 18 specimens exhibited connection stiffness exceeding 40 times the beam stiffness, as summarised in e.

Table. 7-4. Most of these specimens are interior column-stiffened connections under symmetric load. The shear deformation of the panel zone is restrained to increase the connection stiffness. The rigid column was used in some specimens to investigate other component behaviour; this corresponds to the stiffened column, thereby increasing stiffness. For the unstiffened specimens, most have thick column flanges (t_{cf}>20 mm) and endplates (t_{ep}>25 mm), which are larger than the mean and median values (see the geometric parameter

distribution in Chapter 2). Even if those specimens are not traditionally stiffened, the thick column flange and endplate can resist plastic deformation and develop larger stiffness. Furthermore, in most of these specimens, the high level of pretension restricts the opening between the endplate and the column flange.

Table. 7-4 Details of specimens (I-shaped column section) with the β larger than 40

Reference	Specimen	Damage mode	Configuration*	Load symmetry	Stiffener
[29]	Test 3; Test 6	CFY; CWY; BFB	C	Yes	No
[181]	EP1-3 to EP1-5 EPB1-5	EPY; BFB	T (Rigid)	No	Column
[182]	S12 x 87 S10 x 68	BE (only) WF (only)	C	Yes	Plate & Column
[1]	M-5 M-7	BFB BWB	T	No	Plate
[183]	Test5	none	T	No	No
[184]	CT1A1	EPY	C	Yes	Column

* T is cantilever; C is cruciform

Specimens are differentiated based on the presence of column stiffeners at both sides and controlled damage mode as these parameters significantly affect the β. For specimens controlled by EPB, the endplate and bolt geometric parameters are the key geometric parameters. Fig. 7-11 shows the correlation between the ratio of p_t to the product of d_b and β. A negative correlation is observed, which is expected. This is because a larger ratio can easily cause endplates and bolts to develop plastic deformations. Note that, once this ratio is larger than 0.5, most specimens can only develop an initial stiffness 10 times that of its connected beam.

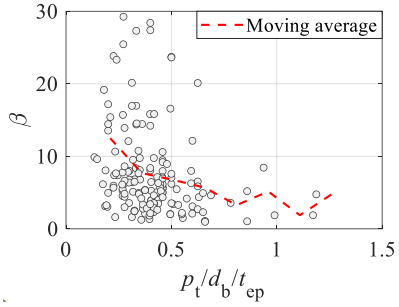

Fig. 7-11 Correlation of enplate geometric parameters and β for EPB controlled specimens.

For specimens controlled by CFB, t_{cf} is the main geometric parameter instead of the endplate parameters. It is observed that the stocky column flange can promote the specimens to develop a higher stiffness. Therefore, a ratio of p_t to the product of t_{cf} and d_b is selected. Fig. 7-12 shows a negative correlation between this ratio and β, which is expected. Similar to the EPB specimens, this larger ratio will promote the CFB specimens to develop plastic deformation. Note that, once this ratio is larger than 0.5, the CFB specimens will not develop a stiffness larger than 10 times that of their connected beams.

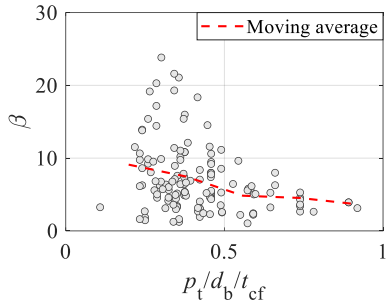

Fig. 7-12 Correlation of geometric parameters and β for CFB controlled specimens.

For specimens controlled by CWB, the column web is the weak component to develop plastic deformation. The slender column web will lead to connections developing CWB, especially for specimens under column removal scenario. Therefore, the ratio of h_b and slenderness of column web ($\lambda_{column\ web}$) is selected. Fig. 7-13 shows a negative correlation between this ratio and β, which is expected. It is observed that a specimen with a slender column web and deep beam will easily develop CWB, reducing the K_e.

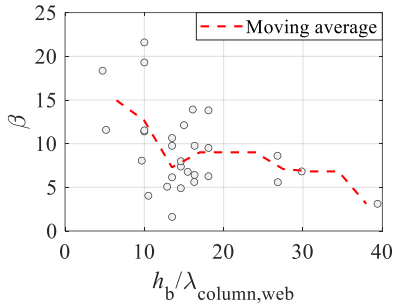

Fig. 7-13 Correlation of geometric parameters and β for CWB controlled speceimens.

In summary, with respect to stiffness, the main findings are as follows:

(1) Overall specimens' stiffness: The K_e is evaluated by using the β. The average β for EEPCs is around 7.5. This means the EEPCs typically behave as SR connections.

(2) Correlation of stiffness and geometric parameters: For specimens controlled by EPB, the endplate slenderness is the controlled geometric parameter. The slenderer endplate leads to a smaller K_e. For specimens controlled by CFB, the column flange slenderness is the controlled geometric parameter. Similar to the weak endplate, the slender column flange can significantly decrease the K_e. For specimens controlled by CWB, the slenderness of the column web is the main factor for a smaller K_e. Table. 7-5 summarises how each predictor affects the initial stiffness.

Table. 7-5 Summary of the effect of predictor parameters on the β

Parameters	EPB	CFB	CWB
p_t / t_{ep} / d_b	H	-	-
p_t / t_{cf} / d_b	-	M	-
h_b / $\lambda_{column\ web}$	-	-	H

Note: High (H); Medium (M); Low (L)

7.4. Response characteristics of the parametric simulated specimens

Using the defined response metrics, the response characteristics of the CFE parametric simulations conducted in Chapter 6 are also investigated. Fig. 7-14 shows the distribution of response characteristics. It is observed that those specimens overall behave as PS (average α is 0.44), SR (average β is 5.3), and ductile (average θ_P is 4.3%).

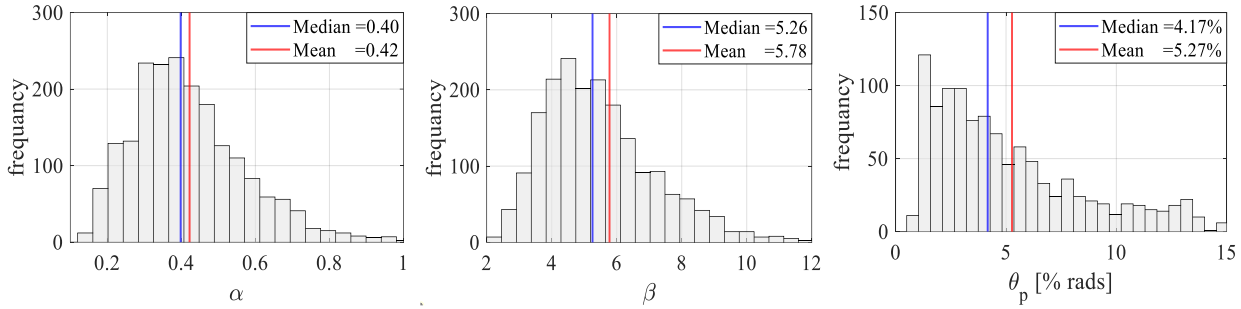

(a) (b) (c)

Fig. 7-14 Distribution of response characteristics of the parametric simulation: (a) α; (b) β; (c) θ_p.

Fig. 7-15 shows the correlation between response characteristics and key geometric parameters. It is observed that a smaller g, larger p_t, t_{ep}, and d_b will increase the α. Besides, a smaller h_b, larger p_t, t_{cf}, and d_b will increase the β. Note that a smaller t_{cf}, larger d_b, p_t, and g will increase the θ_P. Those observations are similar to the correlation for the experimental tests. However, some specimens are observed as outliers, especially in θ_P. This is mainly attributed to the unavoidable inherent material uncertainty.

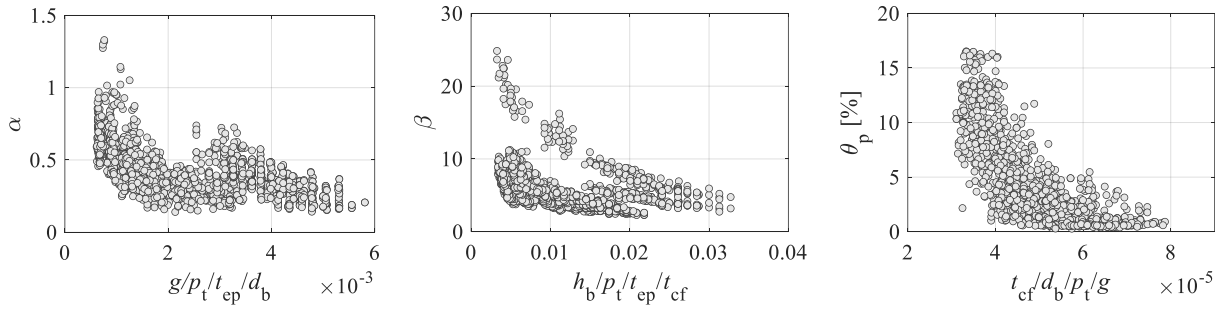

(a) (b) (c)

Fig. 7-15 Correlation between response characteristics and geometric parameters for the parametric CFE specimens: (a) α; (b) β; (c) θ_P.

7.5. Multi-variate regression model (MVLR) for PS and SR EEPCs' *M-θ* response

As mentioned earlier, this section aims to propose new and accurate models to characterise the full-range backbone *M-θ* curves of PS and ES EEPCs, including post-yielding and post-capping response. This is mainly because lumped plasticity models are common in assessing buildings within the PBD framework, as well as in nonlinear analysis procedures that are becoming more popular in engineering practice. As part of these models, zero-length rotational springs are used to represent the nonlinear response of the different structural members and connections at the expected location of the plastic zone. The springs are assigned to phenomenological mathematical models that characterize the component's monotonic/cyclic backbone response and cyclic deterioration parameters. The accuracy of such models is fundamental in acquiring accurate system-level simulations, efficient designs, and performance-based acceptance criteria. There has been significant progress in developing models for steel frame buildings, including wide-flange columns. [185], hollow-section braces [186], column web-panel zone [187], shear-tab connections [188], and fully rigid beam-to-column connections [13]. Concerning PS and ES EEPCs, accurate nonlinear models that capture the full response up to failure and their dependency on the connection's geometric and material properties remain missing (see Chapter 3). To achieve this goal, a large-scale data pool is used herein, which includes the available experimental data and supplementary data from the parametric simulations. The backbone *M-θ* response parameters of EEPCs, controlled by bolt rupture up to failure, are predicted using the traditional MVLR algorithm.

The multivariate power expression, given by Eq. 7-4, is used to develop the empirical equations for the different backbone response parameters, where Y is the dependent variable (response parameter), X_i is the i-th independent variable (geometric/material predictor), β_i is the coefficient/exponent for the i-th predictor, n is the number of predictors, and ε is the model error. This form of regression equations is widely used in the literature as part of structural modelling guidelines and standards [13, 185, 189]. This form allows for conducting linear regression in the log-log space while capturing nonlinear correlations in the original space. This model is also popular for its simple form and the ability to infer correlations between the dependent and independent variables from the equation exponents.

$$Y = \beta_0 \cdot \prod_{i=1}^{n} X_i^{\beta_i} + \varepsilon \qquad 7\text{-}4$$

7.5.1. Target response parameters and predictors

Referring to Fig. 2-14, a bilinear backbone curve is used to represent the connection's *M-θ* response. While nonlinear mathematical models, such as the Menegotto and Pinto [190] and Richard and Abbott [71] models, are better at capturing the smooth transition between the elastic and plastic branches; they fail to account for in-cycle and cyclic strength/stiffness degradation mechanisms, which are crucial for earthquake

simulation. In contrast, the bilinear backbone curve can be easily integrated with existing multilinear phenomenological cyclic degradation models, such as the *IMK* models [191], which are commonly used in system-level simulations of steel components [13, 185, 187].

Four parameters are required to construct the backbone curve. Those are the K_e, M_{ye}, post-yield strength ratio (M_c/M_{ye}), and θ_c. Additionally, the M_y is also considered. Although M_y does not affect the definition of the backbone curve, it represents a key limit state that is needed to define acceptance criteria and fragility functions as part of performance-based structural evaluations [192, 193]. Several geometric and material parameters control the response of PS/SR EEPCs (i.e., response predictors). Fig. 7-16 shows the correlation matrix of significant features. It is observed that most of the features are not correlated with each other. Note that some features (i.e., h_c and t_{cf} as well as t_{cf} and t_{cw}) have an intermediate correlation (>0.6), as expected. This is mainly because the columns are mostly hot-rolled sections with proportional dimensions in both the experimental database and the supplemented parametric simulations. To simplify the model, the predictors that most influence the behaviour are selected based on the deformation mechanics of the connections demonstrated in Table. 7-6, which are corroborated by an evaluation of the response-predictor correlations.

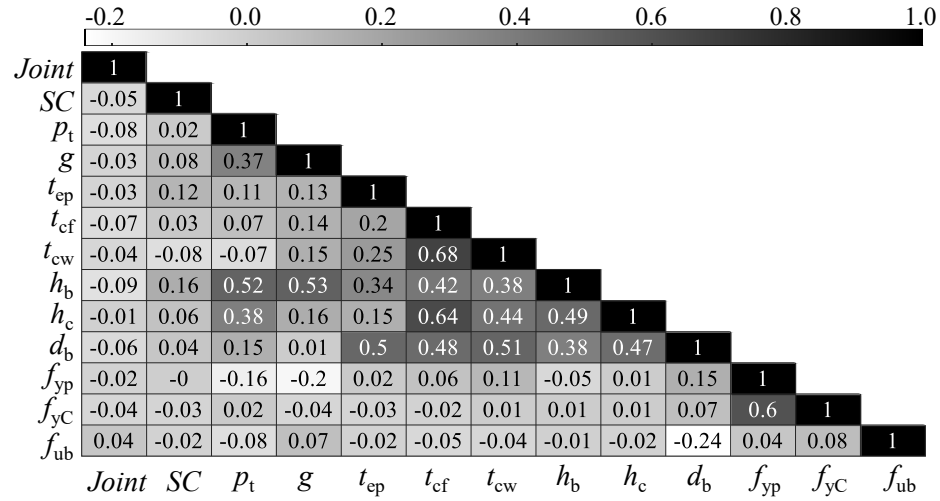

Fig. 7-16 Correlation matrix of significant features.

Table. 7-6 Selected features for each response in the developed MVLR model

Model	Significant features															
MVLR	*Joint*	*SC*	p_t	t_{ep}	t_{cf}	t_{cw}	h_b	h_c	d_b	g	f_{yP}	f_{uP}	f_{yC}	f_{uC}	f_{yb}	f_{ub}
K_e	•	•	•	•	•	•	•	•	•	•						
M_y		•	•	•	•		•		•	•	•		•			
M_{ye}		•	•	•	•		•		•	•	•		•			
M_c/M_{ye}		•	•	•			•		•		•	•	•	•		•
θ_c		•	•	•	•		•		•	•	•		•			•

7.5.2. Dataset base filters

A subset of the database, obtained by applying a base filter, was utilised for model development. Those applied filters, follow as:

- Beam-to-column connections (i.e., exterior or interior connections).
- 4E bolt configuration (i.e., two bolt rows with two bolts per row at the endplate tension side)
- Bare steel connections (no composite slab).
- Carbon steel connections (no stainless steel specimen).
- I-shaped sections (no hollow or CFST square column sections).
- No plate rib stiffeners.
- Major axis connections.
- No axial load in the beam (including specimens with catenary action).
- Non-special case specimens (see description in Chapter 2.3).
- No rigid column (i.e., over-stiffened columns and stocky columns which $t_{cf} >> t_{ep}$).
- PS or ES connections (i.e., strength coefficient $\alpha<1.1$).

In addition to the baseline filter above, additional filtering is sometimes applied for specific response parameters. For K_e, no further filtering is applied. For M_{ye} and K_s, an extra filter is used, which specimens develop a θ_c at least larger than 1.5% rads. This is to ensure that all specimens developed a significant plastic deformation at the endplate, column component, and bolt. To predict θ_c, specimens must fail due to bolt rupture.

7.5.3. Quality evaluation metric

The model performance can be evaluated by several statistical criteria. Firstly, the model cannot be overfit. This can be achieved by splitting the dataset into training sets (generally 80%) and testing sets (generally 20%). The values of statistical criteria between the training set and the testing set need to be close. There are five criteria that were implemented for the model evaluation, which follow as:

(1) *RMSE*: The root mean square error (*RMSE*) is one of the most common metrics, which calculates the normalised distance between the prediction and observed value, as shown in Eq. 7-5.

(2) *MAE*: The magnitude of the errors between the predictions and observed values can be computed by the mean absolute error (*MAE*), as shown in Eq. 7-6.

(3) *MAPE*: The mean absolute percentage error (*MAPE*) is a common metric for regression problems, which is the difference between the predictions and observed values in percentage, as shown in Eq. 7-7.

(4) R^2: The R-square value (R^2) is the most popular metric to evaluate a regression model. It represents the overall goodness of the fitting.

(5) P_{20} or P_{50}: The P value is computed as the ratio of the predictions to observed values. The P value represents the percentage of errors that fall in a prediction interval, such as ±20% or ±50%. The 20% error limit is commonly used in the literature as an upper bound for assessing acceptable predictions. The 50% error limit is used to demonstrate that the developed models do not produce largely erroneous estimates.

$$RMSE = \sqrt{\frac{1}{n} \cdot \sum_{i=1}^{n} (y_i - \hat{y}_i)^2} \quad 7\text{-}5$$

$$MAE = \frac{1}{n} \sum_{i=1}^{n} |y_i - \hat{y}_i| \quad 7\text{-}6$$

$$MAPE = \frac{1}{n} \sum_{i=1}^{n} \left| \frac{y_i - \hat{y}_i}{y_i} \right| \cdot 100\% \quad 7\text{-}7$$

$$R^2 = 1 - \frac{\sum_{i=1}^{n} (y_i - \hat{y}_i)^2}{\sum_{i=1}^{n} (y_i - \bar{y})^2} \quad 7\text{-}8$$

$$P_{20} \text{ or } P_{50} = \frac{(1/1.2) \leq \frac{y_i}{\hat{y}_i} \leq 1.2}{n} \text{ or } \frac{(1/1.5) \leq \frac{y_i}{\hat{y}_i} \leq 1.5}{n} \quad 7\text{-}9$$

Where y_i is the observed values, $\hat{y}_i$ is the predicted values, $\bar{y}$ is the mean of the observed values, and n is the number of specimens.

7.5.4. Model training and performance

MVLR is conducted using the logarithmic values of the response parameters and the predictors. A linear relationship is thus assumed between the dependent and the independent variables in the log-log space. A least-squares fit is used to regress the data and obtain the model coefficients. It is worth noting that in the regression procedures, a larger weight (proportional to the simulation-to-experimental dataset size ratio) is assigned to the experimental dataset. The larger weight is meant to reflect the confidence in the experimental data and their ability to capture real joint conditions. To check for multicollinearity, the Variance Inflation Factor (VIF) scores were quantified. As a rule of thumb, any feature achieving a VIF score larger than 5.0 was removed from the model to help reduce the model size and eliminate redundancy [194]. The VIF value of each predictor for the unstiffened specimens is summarised in Table. 7-7. Note that all selected predictors are within the threshold of 5. The model for each response parameter was also checked for overfitting through a bias-variance analysis by consistently dividing the data into a training and testing subsets (with an 80%-20% split, respectively) and ensuring that the performance fit metrics are consistent across subsets. For the final models, the entire dataset was used for inference (i.e., regression coefficient estimation). Finally, it is worth noting that conducting regression using scaled/dimensionless predictor values was also

examined, and no notable difference was observed in the model performance compared to using the absolute values. The latter approach was consequently selected, given its more straightforward mathematical form.

Table. 7-7 VIF value of each predictor in the proposed MVLR model for the unstiffened specimens

Parameters	p_t	t_{ep}	g	d_b	h_b	h_c	t_{cf}	t_{cw}	f_{yP}	f_{uP}	f_{yC}	f_{uC}	f_{ub}
K_e (Asym)	4.3	1.2	2.1	1.9	3.7	4.6	4.3	2.9					
M_y	4.4	1.4	2.1	2.0	4.1		2.1		1.1		1.2		
M_{ye}	4.5	1.46	2.2	2.7	4.7		2.6		1.1		1.28		
M_cM_{ye}	3.0	1.1		1.8	2.0				1.7	1.6	1.2	1.1	1.1
θ_c	3.5	1.1	1.2	1.7	2.5		1.2		1.0		1.2		1.1

To improve regression accuracy and model accuracy, the regression equation for each response parameter of a given connection type is separated based on the presence or absence of column flange stiffeners (noted henceforth as the *stiffened* and *unstiffened* cases, respectively). Furthermore, the joint types (noted henceforth as the external joints/interior ones with asymmetric beam loading and internal joints with symmetric beam loading) are herein used to separate the regression equations for the elastic stiffness. This is mainly because the presence of stiffeners and loading directions highly controls the panel zone shear behaviour. Specifically, under symmetric loading (i.e., joints under equal but opposing bending moments, as in the case of gravity load or column loss scenarios), the panel zone's shear distortion is restrained while under asymmetric loading (i.e., joints under equal/unequal and co-directional moments, as in the case of lateral loads), the panel zone's shear distortion is amplified.

The model performance is quantitatively assessed by several metrics defined in Chapter 7.5.3. To quantify the variability in the model prediction, the standard deviation of the residual error (σ_ε) is reported. The σ_ε, which is closely related to the *RMSE*, is expressed in the same units as the predicted response parameter. The regression metrics are summarised in Table. 7-8 for all the developed regression equations, including the mean and standard deviation of the absolute relative error ($\mu_{|\varepsilon,rel|}$ and $\sigma_{|\varepsilon,rel|}$, respectively) to assist with probabilistic simulations. In general, all regression equations achieve R^2 scores larger than 0.85. For the strength parameters (M_y, $M_{ye,}$ and M_c/M_{ye}), the model predicts more than 70% of the data points with an error of less than ±20%. For all other models, the prediction error does not exceed ±50%, except for a few cases involving sensitive K_e and θ_c parameters that experience significant variability.

Table. 7-8 Summary of performance metrics for the proposed MVLR equations

	Unstiffened						Stiffened					
	K_e		M_y	M_{ye}	θ_c	$\frac{M_c}{M_{ye}}$	K_e		M_y	M_{ye}	θ_c	$\frac{M_c}{M_{ye}}$
	Asym.	Sym.					Asym.	Sym.				
R^2	0.96	0.87	0.96	0.97	0.94	0.47	0.95	0.95	0.96	0.96	0.92	0.53
P_{20}	0.97	0.85	0.78	0.85	0.64	0.98	0.87	0.94	0.71	0.80	0.63	0.98
P_{50}	0.98	0.95	1.00	1.00	1.00	1	0.97	0.97	1.00	1.00	1.00	1.00
σ_ε	7955	9949	46	50	0.007	0.12	10518	11354	52	58	0.009	0.11
$\mu_{\lvert\varepsilon,rel\rvert}$	0.11	0.13	0.13	0.11	0.18	0.07	0.18	0.08	0.14	0.12	0.17	0.06
$\sigma_{\lvert\varepsilon,rel\rvert}$	0.08	0.12	0.09	0.09	0.11	0.06	0.13	0.12	0.09	0.09	0.11	0.06

Qualitatively, the model performance is visualised in Fig. 7-17, which shows the response parameter histogram, the predicted versus measured values, and the histogram of the residual error (predicted minus measured value) for the unstiffened EEPC models. The figure demonstrates a good match between the predicted and measured values of the regression dataset, with the scatter closely following the 1:1 reference line. This was already expected from the high P_{20} values in Table. 7-8. Larger scatter variability is observed for the K_e and θ_c parameters. These are intrinsically sensitive parameters as discussed in detail in the following sections. The spread of both the experimental and simulation datasets (differentiated by different markers in the scatter plots) around the 1:1 reference line is consistent, further confirming the soundness of the latter.

The regression quality is further checked against the Gauss-Markov theory conditions set in Chatterjee and Hadi [195]. In particular, the residual error has a mean value close to zero and is normally distributed for all response parameters. This can be inferred from the error histograms and in the sample quantile-quantile (QQ) plot shown in Fig. 7-18(a) for the M_{ye} parameter. Quantitatively, the normality of the residual error (null hypothesis) was confirmed by calculating the p-value based on the Lilliefors test [196]. The error distribution also satisfies the homoscedasticity assumption, where an even error variance is observed with respect to the predicted values. This can be visually inspected in Fig. 7-18(b) and was confirmed by the Breusch-Pagan test [197]. Accordingly, the reported σ_ε can be used in support of probabilistic simulations, structural reliability assessment, and the investigation of modelling uncertainty effects. Additionally, the mean and standard deviation of the absolute relative error (i.e., residual error divided by predicted value, ε_{rel}) are reported in Table 3. Note that $\mu_{\lvert\varepsilon,rel\rvert}$ does not exceed 20% of the expected value for all modes. This scale-invariant performance metric can also be used to quantify uncertainty.

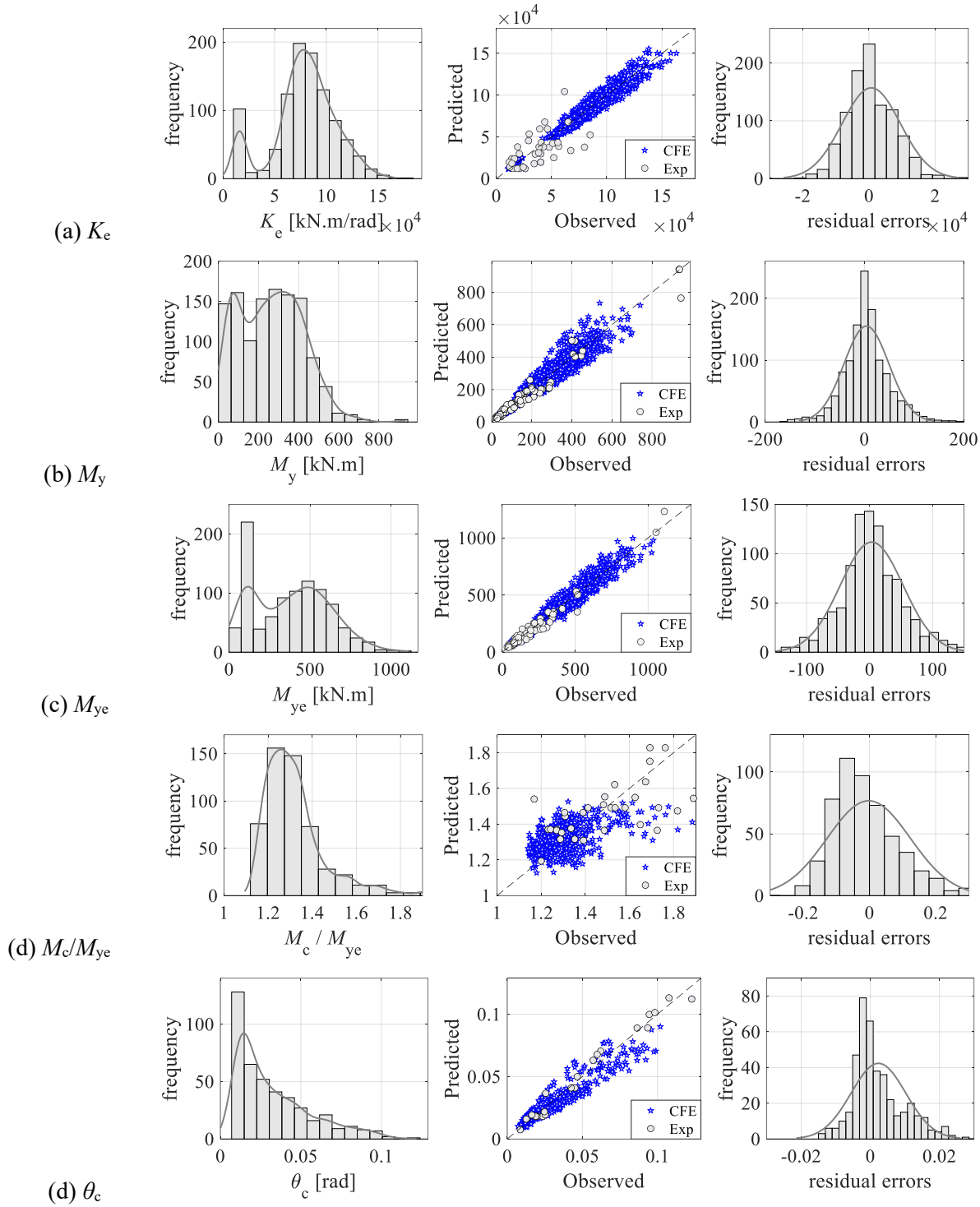

Fig. 7-17 Response parameter histogram and regression model performance for unstiffened EEPC: (a) K_e (asym.), (b) M_y, (c) M_{ye}, (d) M_c/M_{ye}, and (e) θ_c.

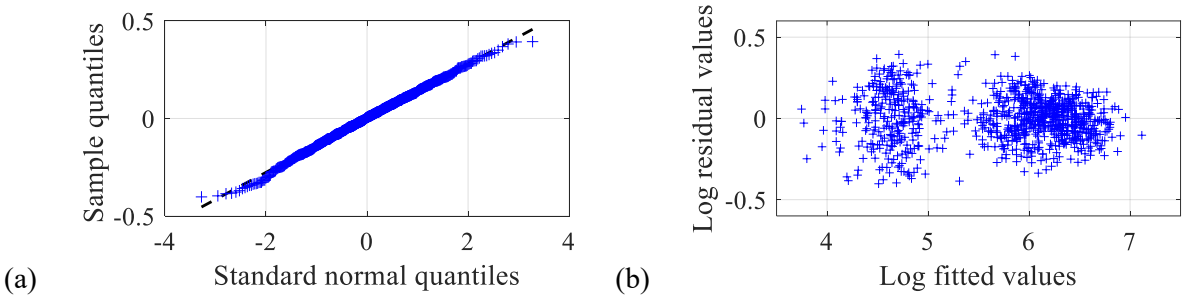

Fig. 7-18 Statistical analysis plots of the residual error for the unstiffened EEPCs M_{ye} regression model.

7.5.5. Proposed equations

The regression equations are presented in this section. The predictors in those equations are defined in mm and MPa units, while the output stiffness, strength, and rotation values are in kN.m/rad, kN.m, and radians, respectively.

7.5.5.1. Initial elastic stiffness - K_e

The K_e regression equations are given by Eq. 7-10. The elastic stiffness is a sensitive parameter that is affected by the geometry of all components and bolt layout parameters. To maintain a practical form of the equation, only eight geometric parameters were selected that are deemed the most influential in controlling the bolt elastic elongation, the column web deformation in shear, and the bending of the endplate and column flange. The negative exponents demonstrate the expected negative correlation between K_e and both g and p_t parameters for stiffened EEPCs. In contrast, the positive exponents demonstrate the positive correlation with t_{ep} and h_b.

$$K_e = \begin{cases} 4.6\text{x}10^{-1}\, p_t^{-1.60}\, g^{-0.646}\, t_{ep}^{0.514}\, t_{cf}^{0.360}\, t_{cw}^{-0.28}\, d_b^{0.40}\, h_b^{1.97}\, h_c^{1.280} & \text{stiffened; asym} \\ 5.9\quad p_t^{-1.21}\, g^{-0.453}\, t_{ep}^{1.140}\, t_{cf}^{4.380}\, t_{cw}^{-4.15}\, d_b^{0.56}\, h_b^{2.15}\, h_c^{-0.55} & \text{stiffened; sym} \\ 1.4\text{x}10^{-3}\, p_t^{0.170}\, g^{-0.460}\, t_{ep}^{0.413}\, t_{cf}^{-0.44}\, t_{cw}^{0.340}\, d_b^{0.21}\, h_b^{1.47}\, h_c^{1.470} & \text{unstiffened; asym} \\ 3.0\text{x}10^{-3}\, p_t^{0.170}\, g^{-0.720}\, t_{ep}^{0.430}\, t_{cf}^{0.470}\, t_{cw}^{1.040}\, d_b^{1.08}\, h_b^{1.64}\, h_c^{0.230} & \text{unstiffened; sym} \end{cases} \quad 7\text{-}10$$

7.5.5.2. Yielding moment – M_y

The moment at the onset of yielding in any of the connection components is predicted by Eq. 7-11. The equations incorporate six geometric parameters and two material parameters. For the latter, the yield stress of the endplate ($f_{y,P}$) and the column ($f_{y,C}$) are used. Those are the components that commonly experience plastic deformations in these types of connections. The column web panel's geometric parameters and the bolt's material properties are not considered, as they do not improve model performance and result in a high VIF score. Additionally, these components only control the onset of yielding in rare cases, such as when thick plates are used with either a small-size (weaker) bolt or column. Referring to Fig. 7-17 (b) and Table. 7-8, the proposed equations have a high performance, with a P_{20} larger than 0.7. Additional constraints shall

be applied to these equations. Specifically, for FEPC, M_y shall be between 38% and 80% of M_{ye} while for EEPCs, the value shall be within 44% and 84% of M_{ye}.

Supplementary to M_y equations, Fig. 7-19 shows the empirical cumulative distribution functions (CDFs) for the yield rotation (θ_y) along with fitted lognormal CDFs. Those are essentially the fragility curves for the yielding limit state. The statistical parameters for the fitted lognormal distribution (i.e., the mean and standard deviation of the logarithmic θ_y values) are summarised in Table. 7-9. Note that yielding occurs around 0.37% rads. At 1% rotation, the probability of reaching the yielding limit state is almost 100%.

$$M_y = \begin{cases} 3.78\text{x}10^{-7}\, p_t^{-0.37}\, g^{0.420}\, t_{ep}^{0.80}\, t_{cf}^{0.144}\, d_b^{1.12}\, h_b^{1.47}\, f_{y,P}^{0.91}\, f_{y,C}^{-0.11} & \text{stiffened} \\ 6.80\text{x}10^{-6}\, p_t^{-0.36}\, g^{-0.72}\, t_{ep}^{0.72}\, t_{cf}^{0.440}\, d_b^{0.88}\, h_b^{1.73}\, f_{y,P}^{0.61}\, f_{y,C}^{0.32} & \text{unstiffened} \end{cases} \quad 7\text{-}11$$

$$0.44\, M_{ye} \le M_y \le 0.84\, M_{ye}$$

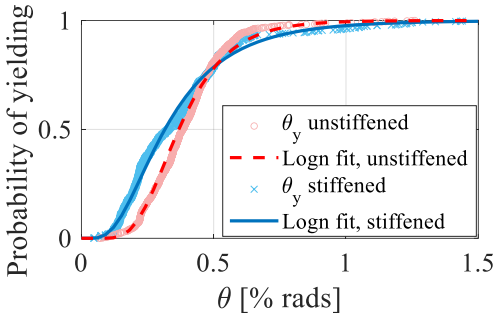

Fig. 7-19 Fragility curves for the yielding limit state for EEPCs.

Table. 7-9 Statistical parameters of the lognormal fragility curves for the yielding limit state

Presence of column stiffeners	$\mu_{\theta y}$	$\mu_{\ln \theta y}$	$\sigma_{\ln \theta y}$
unstiffened	0.40 % rads	-5.600	0.390
stiffened	0.37 % rads	-5.760	0.580

7.5.5.3. Effective yield strength - M_{ye}

The effective yield moment corresponds to the full plasticization of one of the connection's components and the initiation of the post-yield hardening phase. Using the same predictors as the yield moment, M_{ye} equations are given in Eq. 7-12. Like M_y, the M_{ye} equations have high-performance metrics. EEPCs can develop a larger 17% to 108% of $M_{p,b}$. Note that for EEPCs, M_{ye} can approach or slightly exceed $M_{p,b}$. This occurs when a balanced design is achieved, allowing the connection components (mainly the endplate) to plastically deform simultaneously with the onset of beam flange yielding/buckling.

$$M_{ye} = \begin{cases} 6.30\text{x}10^{-5}\, p_t^{-0.650}\, g^{0.090}\, t_{ep}^{0.59}\, t_{cf}^{0.28}\, d_b^{1.29}\, h_b^{1.350}\, f_{y,P}^{0.61}\, f_{y,C}^{-0.04} & \text{stiffened} \\ 3.70\text{x}10^{-5}\, p_t^{-0.136}\, g^{-0.51}\, t_{ep}^{0.56}\, t_{cf}^{0.65}\, d_b^{0.95}\, h_b^{1.365}\, f_{y,P}^{0.35}\, f_{y,C}^{0.350} & \text{unstiffened} \end{cases} \quad 7\text{-}12$$

7.5.5.4. Post-yield strength ratio - Mc/Mye

To define the connections' capping (ultimate) moment, the M_c/M_{ye} is used. Traditionally, this parameter is stable and does not experience much variability between different connection layouts and material properties. Therefore, it is recommended to define the post-yield increase in strength (i.e., strain hardening) compared to the post-yield stiffness K_s [13, 185]. Utilizing the ratio M_c/M_{ye} also resulted in a better model compared to predicting M_c directly. M_c/M_{ye} can be computed using Eq. 7-13, with a lower limit of 1.05 M_{ye} and an upper limit of 1.7 M_{ye}. The equation uses similar predictors as the moment equation, with the addition of the material ultimate stress values to capture the level of material strain hardening of the different connection components before failure.

$$\frac{M_c}{M_{ye}} = \begin{cases} 0.84\, p_t^{0.155}\, t_{ep}^{-0.15}\, d_b^{0.18}\quad h_b^{-0.08}\, f_{uP}^{0.18}\quad f_{yP}^{-0.24}\, f_{uC}^{0.19}\quad f_{yC}^{-0.31}\, f_{ub}^{0.14} & \text{stiffened} \\ 46.5\, p_t^{0.146}\, t_{ep}^{-0.12}\, d_b^{-0.12}\, h_b^{-0.10}\, f_{uP}^{-0.13}\, f_{yP}^{-0.105}\, f_{uC}^{-0.11}\, f_{yC}^{-0.21}\, f_{ub}^{0.07} & \text{unstiffened} \end{cases} \qquad 7\text{-}13$$

$$1.05 \le \frac{M_c}{M_{ye}} \le 1.7$$

7.5.5.5. Capping rotation - θc

The capping point is defined using the M_c/M_{ye} ratio and the value of the θ_c. Note that the capping point is coincident with failure in the case of SR/PS EEPCs since failure is associated herein with bolt tensile rupture. In other words, the post-capping (negative) slope can be ignored, and a sudden drop in strength can be assumed. The capping rotation can be predicted using Eq. 7-14. The equations use similar predictors as the previous ones, with the inclusion of the ultimate stress of the bolt material ($f_{u,b}$). The observed failure rotation in EEPCs is around 3.8% rads on average. EEPCs can possess an excessive ductility up to 12% rads. Unstiffened connections develop around 20% larger ductility compared to stiffened ones. This is, however, dependent on the governing deformation mode.

$$\theta_c = \begin{cases} 9.6\text{x}10^{-5} \quad p_t^{0.840}\, g^{-1.10}\, t_{ep}^{-0.300}\, t_{cf}^{-1.34} d_b^{3.90} h_b^{-0.91} f_{y,P}^{-0.17} f_{y,C}^{-0.71} f_{u,b}^{1.5} & \text{stiffened} \\ 2.7\text{x}10^{-2} \quad p_t^{-0.27}\, g^{0.740}\, t_{ep}^{-0.205}\, t_{cf}^{-1.40} d_b^{3.77} h_b^{-1.20} f_{y,P}^{-0.33} f_{y,C}^{-1.21} f_{u,b}^{1.1} & \text{unstiffened} \end{cases} \qquad 7\text{-}14$$

$$\theta_c \ge 1.5 \frac{M_{ye}}{K_e}$$

7.5.5.6. Post-capping response

The bilinear model presented earlier (see Fig. 2-14) is sufficient for design purposes. For numerical simulations, however, a sudden drop in strength (to zero) without a reasonable negative post-capping stiffness may lead to numerical instabilities once a given connection fails in a frame model. Consequently, failure progression through the frame model will not be quantifiable. For that reason, further guidelines are provided in this section for the modelling of the post-capping portion of the backbone curve. Given that

laboratory tests stop as soon as the first bolt failure takes place, the guidelines developed henceforth are based solely on the CFE simulations, where the entire backbone curve (damage progression) can be traced.

For standard 8-bolt EEPCs (see Fig. 7-20 (a)), following the failure of the top -tension- bolt row(s), the connection resistance reverts to $M_{res,c}$ which is the residual moment resistance sustained by the bottom -compression- bolt row(s). On average, $M_{res,c}$ is 20% of M_c with a coefficient of variation (COV) of 0.42. The corresponding post-capping rotation (θ_{pc}) is 0.5% rads on average with a COV of 0.44. Note here that $M_{res,c}$ can be sustained to exceedingly large rotations. For practical purposes, the ultimate rotation (θ_u) at which the resistance reaches zero can be taken as 20% rads.

For 10-bolt EEPCs (i.e., with a middle bolt row as shown in Fig. 7-20 (b)), following the failure of the top -tension- bolt row(s), the connection resistance reverts to $M_{res,m}$ which is the moment resistance sustained by the middle and bottom bolt row(s). $M_{res,m}$ can be estimated based on the expressions given in Eq. 7-15. The $M_{res,m}$ value corresponds roughly to about 65% of M_{max}. The middle bolt row will fail at a total rotation ($\theta_{c,m}$) that is about two times θ_c. Eventually, the connection reverts to $M_{res,c}$ as previously discussed.

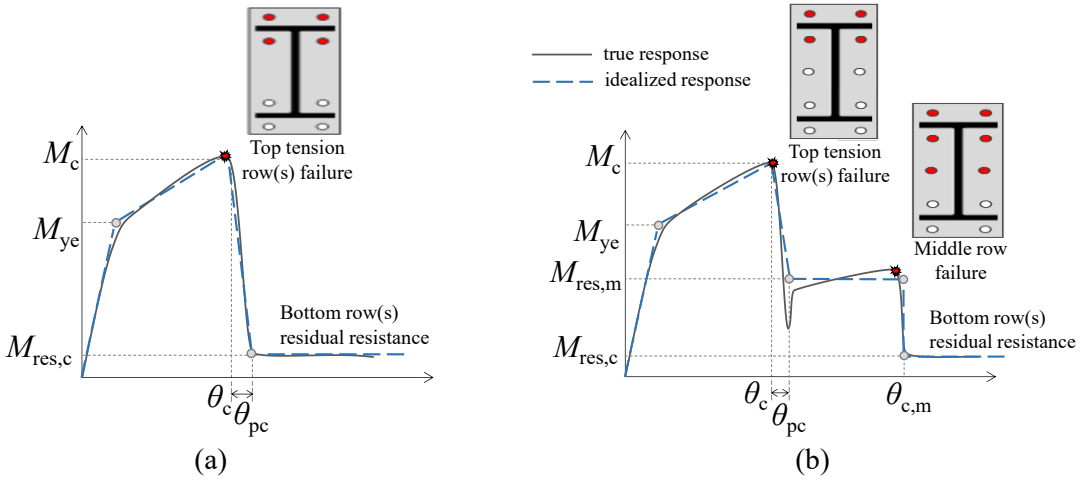

Fig. 7-20 Idealised monotonic backbone parameters in the post-capping range of EEPCs.

$$M_{res,m} = \frac{h_b - p}{h_b} \qquad (COV = 0.08) \qquad 7\text{-}15$$

7.5.5.7. *Transition stiffness* - K_{trans}

As discussed earlier in Chapter 2, the bilinear model may also fail to capture the gradual nonlinear transition between the elastic and post-yield branches. Consequently, the trilinear model with a transition stiffness parameter (K_{trans}) was introduced, as illustrated earlier in Fig. 2-14. K_{trans} can be estimated as a function of K_e. Fig. 7-21 shows the distribution of the ratio of K_{trans} to K_e, with a mean value of 0.18. K_{trans} can be estimated using the empirical power expression given by Eq. 7-16.

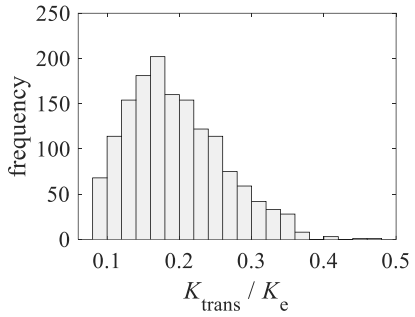

Fig. 7-21 The ratio of K_{trans} to K_e.

$$K_{\text{trans}} = 0.63\, K_{\text{e}}^{0.89}\ (\text{COV} = 0.23) \qquad 7\text{-}16$$

7.5.6. MVLR model demonstration

To visually demonstrate and validate the proposed model, the predicted backbone curves are plotted in Fig. 7-22 against the data from several representative test specimens from the literature that failed by bolt rupture. Markers are used to highlight the main backbone points including the onset of yielding. In the same plots, the code-based predictions based on the yield line method [66, 198, 199] and the mechanical component-based method of Eurocode 3 [65], are superimposed for reference. Quantitively, the ratios of the predicted response parameters to the measured ones are summarised in Table. 7-10. In general, the model reasonably captures the moment-rotation response with good prediction of the critical K_e and M_{ye} quantities. The post-yield slope and the failure points, which are not addressed by the other two models, are also well predicted across different connection layouts and material properties. The observed ± divergence from the true behaviour is a common byproduct of the data fitting process which minimizes the global error. Referring to Table. 7-10, this divergence (error ratios), with respect to any response parameter, falls within the acceptable error range. Notably, this model uncertainty can be addressed by considering either the lower or upper bounds for the backbone response, depending on the purpose. Those can be defined using the tabulated residual error metric, as discussed earlier. Additionally, a graphical user interface (GUI) is now available and downloadable at GitHub repository [200]. Fig. 7-23 shows the visualisation of the proposed MVLR model within the GUI tool.

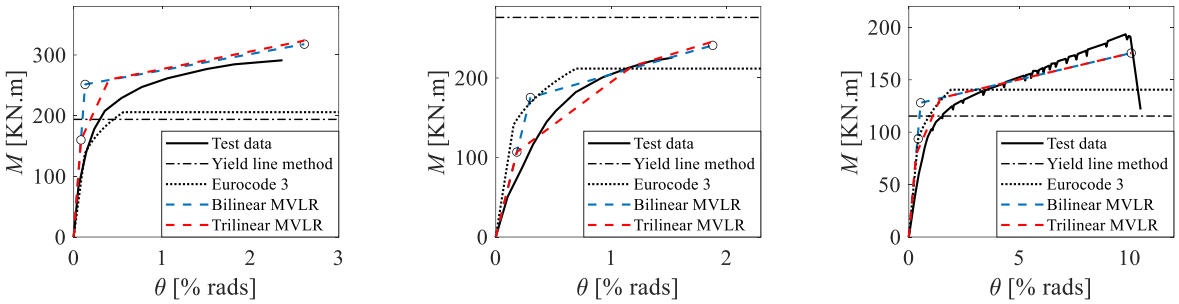

Fig. 7-22 Comparisons of the proposed backbone model, the yield line method, and the Eurocode 3 component method with representative test data: (a) stiffened EEPC [201]; (b) stiffened EEPC [202]; (c) unstiffened EEPC [149].

Table. 7-10 Summary of predicted-to-measured ratios for representative test specimens

	Yield line	**Eurocode 3**		**Proposed MVLR model**			
	M_{ye}	K_e	M_{ye}	K_e	M_{ye}	M_c	θ_c
Stiffened interior sym. [201]	0.87	1.19	0.92	1.23	1.12	1.11	1.08
Stiffened interior sym. [202]	1.80	1.98	1.39	1.15	1.14	1.08	1.20
Unstiffened exterior [149]	1.03	1.48	1.25	1.40	1.14	0.95	1.02

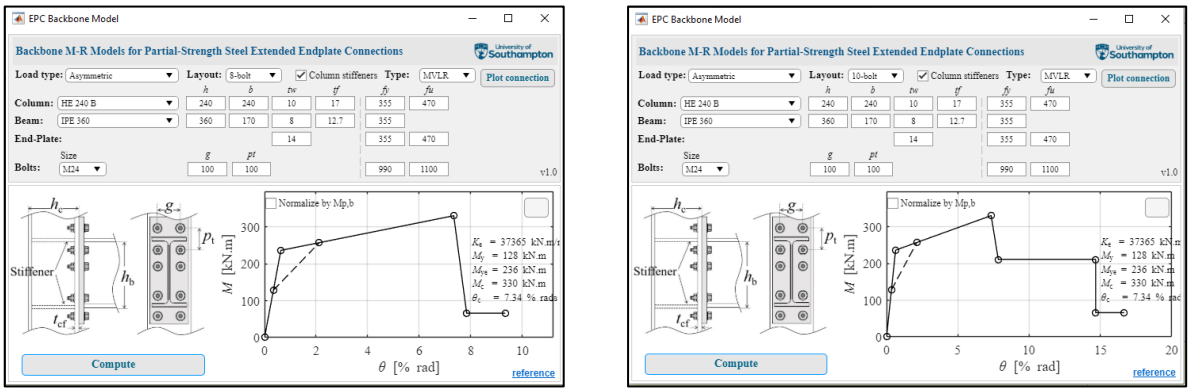

Fig. 7-23 GUI tool for the MVLR backbone model: (a) EEPC with 8-bolt layout and (b) EEPC with 10-bolt layout.

7.5.7. Model limitations and practical implementation

7.5.7.1. General applicability

The proposed models are limited to PS or ES EEPCs where the connection's plastic strength is less than or almost equal to that of the connected beam. The model applicability is valid as long as the geometric and material parameters of the connection are within the ranges of the employed dataset. Nonetheless, given that

the regression models capture the underlying effects of the different geometric/material features on the response parameters, the model could be used in concept -with caution- to extrapolate beyond its range of applicability. The model validity extends to EEPCs with more than four bolt rows (i.e., 10-bolt layout), as shown in Fig. 7-20(b). Note that the interior bolt row positioned at the beam neutral axis in these connections is primarily used to carry shear forces and does not have direct impact on the connection stiffness or strength.

7.5.7.2. Model limitations

The models predict the connection ductility considering the bolt rupture as the sole failure mode. This assumes that weld failure does not occur prior to bolt failure. Considering proper weld design and fabrication, this assumption is valid for EEPCs that do not develop large moment capacity (less than 0.7 $M_{p,b}$). For larger capacity EEPCs involving deep beams ($h_b > 400$) and stiff endplates ($p_t/t_{ep} < 9$), the larger strains induced near the weld may result in early failure. Such failure mode and others such as bolt stripping or plate tearing need to be assessed separately, perhaps using probabilistic fragility models. Additionally, under cyclic drifts, failure may occur earlier due to ultra-low-cycle fatigue. This issue requires further investigation.

The post-failure response is deduced here based only on CFE simulations, due to absence of experimental data at very large deformations. Although, the CFE modelling approach is thoroughly validated, it is only validated up to -first- failure. Therefore, it would be beneficial to have future experimental data that explores the post-failure response.

7.5.7.3. Model implementation

The models can be used to define either the monotonic backbone or cyclic envelope curve as part of existing phenomenological hysteretic component models [191]. In the case of seismic simulation, the hysteretic response parameters will need to be calibrated, specifically the parameters that control the level of pinching. In the presence of a concrete slab that is working compositely with the steel beam, the backbone parameters will need to be modified to reflect the composite action effect under hogging and sagging moments. Past recommendations for considering the composite slab effect in FR connections [203] may be applicable to PS endplate connections, However, further experimental and numerical research is needed in this area.

The models capture the total rotation of the connection, including any potential shear deformations in the column web panel zone. Accordingly, as part of lumped plasticity models, a single rotation spring shall be used to idealize the connection. This spring can be allocated at the column flange face, offset from the column centre using rigid beam elements. If a separate spring is to be used for the column web panel zone [187], the proposed backbone curves shall be modified first. This can be done by substituting larger values for the column-related predictors in the equations to implicitly remove the column impact on the stiffness and the strength of the connection.

The format of the proposed models is simple enough to be incorporated as part of numerical codes and in nonlinear modelling guidelines [189, 204]. Furthermore, a computer tool with a friendly graphical user interface is developed and made publicly and downloadable from a GitHub repository [205]. Through this tool, the user can simply define the type and parameters of the connection and visualize the generated backbone curve and response parameter values.

7.6. Artificial neural network (ANN) for PS and ES EEPCs' *M-θ* response

Artificial neural networks (ANN) has been increasingly used in structural engineering to capture the complex nonlinear response of various structural components and joints [206]. Compared to traditional MVLR models, ANNs can better model the nonlinear and highly complex interdependencies between the features and the target responses. For basic structural engineering problems that are concerned with predicting the response quantities of components, subassemblies, and systems, shallow feed forward ANN models are appropriate and sufficient. There are two main architectures for such networks: multiple-input single-output (MISO) and multiple-input multiple-output (MIMO), as demonstrated in Fig. 7-24. The MISO model is more common where separate ANNs are developed/trained independently for each response parameter. The MISO model involves a single ANN where all response parameters are predicted simultaneously. This requires that all response parameters are strongly correlated to ensure the rational feature learning in the shared hidden layer, such that the model is less likely to be overfitted by one of responses. MIMO models have the advantage of capturing the interdependence between the response parameters. While the MISO model minimizes the error for each response parameter, MIMO minimizes this for the entire backbone.

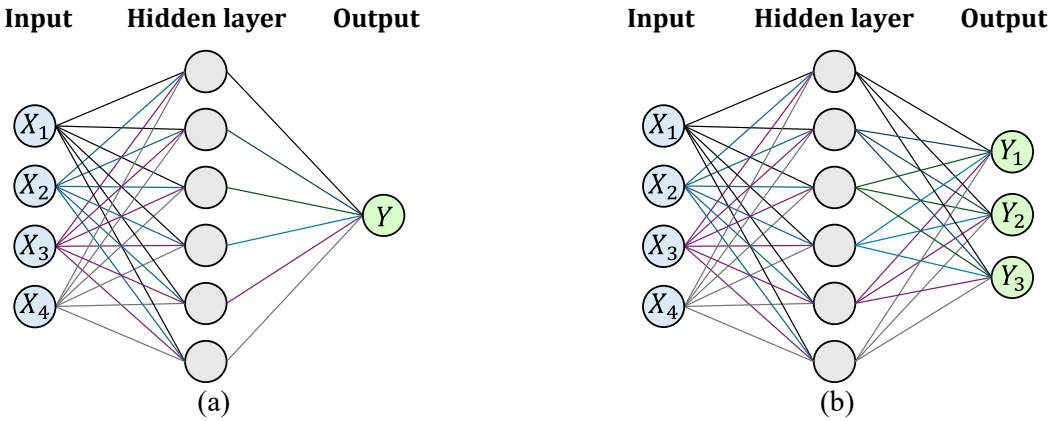

Fig. 7-24 Architecture of the shallow feed-forward ANN model: (a) MISO network; (b) MIMO network.

Several MISO models exist in the literature for steel connections. De Lima et al [207] developed an ANN using 26 test specimens for predicting the elastic stiffness and plastic strength of EEPCs, with an average prediction error of 24% and 8%, respectively. Kueh [208] trained an ANN for predicting the elastic stiffness and ultimate strength of flush endplate connections using 52 test specimens where most of prediction errors

fell within ±25%. Tran and Kim [209] developed an ANN model to predict the elasto-plastic moment-rotation response of flush endplate connections using 121 test specimens, where over 50% of specimens were predicted within ±20% error. More recently, Georgiou and Elkady [210] developed an ANN model considering the post-yield response of flush endplate connections using 198 test specimens, with over 70% of the datapoints predicted with an error less than 15%. Using 200 numerical simulations, Dharmawansha et al [211] developed a MIMO ANN for predicting the sequential moment-rotation datapoints of stainless steel SR EEPCs with a coefficient of determination larger than 0.95.

Clearly ANN models have the potential of producing more robust predictive models compared to traditional methods. This is particularly correlated with the availability of larger datasets. Given the large dataset mentioned earlier, this section develops both MISO and MIMO ANNs to characterise PS and ES EEPCs bilinear moment-rotation response up to bolt rupture. This section also focuses on the comparative performance of the ANN models with their recent MVLR counterpart. Insights on the advantages and disadvantages of the MIMO and MISO approaches are discussed to assist with future similar regression problems. Finally, the developed ANNs inner workings are interpretated and assessed with respect to mechanical understanding, and model limitation are carefully investigated and described.

7.6.1. Target Responses and Significant Features

Several geometric and material features control the EEPC's stiffness, strength and ductility. The same features identified in the proposed MVLR model for each response parameter are used. Briefly, those features include the beam and column heights (h_b and h_c), bolt diameter (d_b), endplate thickness (t_{ep}), column flange and web thicknesses (t_{cf} and t_{cw}), the vertical and horizontal bolt pitch distances (p_t and g), the endplate and column flange yield stresses (f_{yP} and f_{yC}), and the bolt ultimate stress (f_{ub}) The MVLR model also differentiated between connections with/without column stiffeners and those subjected to symmetric/asymmetric bending. Those are considered in the ANN models as categorical features and are labelled as *SC* and *Load*, respectively. The *Load* feature is encoded as 0 and 1 for the specimen under symmetric or asymmetric bending, respectively. Similarly, the *SC* feature is encoded as 0 and 1 for the unstiffened and stiffened specimens, respectively. Table. 7-11 summarises the selected features for the MISO and MIMO models of each response parameter. Note that all features are considered in the MIMO model since all parameters are predicted simultaneously.

Table. 7-11 Selected features for each response for the proposed ANN model

ANN type	Parameter	Data size	Selected critical features												
			Load	*SC*	p_t	t_{ep}	d_b	g	t_{cf}	t_{cw}	h_b	h_c	f_{yP}	f_{yC}	f_{ub}
MIMO	All	900	•	•	•	•	•	•	•	•	•	•	•	•	•
MISO	K_e	2196	•	•	•	•	•	•	•	•	•	•			
	M_{ye}	1818		•	•	•	•	•	•		•		•	•	
	K_s	1019	•	•	•	•	•	•	•	•	•	•	•	•	•
	θ_c	900	•	•	•	•	•	•	•	•	•	•	•	•	•

7.6.2. Model training and hyperparameter setting

All shallow feed-forward ANNs, see Fig. 7-24, were developed using MATLAB 2021a Machine Learning Toolbox [212]. All model hyperparameters were set as default, i.e., the target gradient set to 10^{-7}, the maximum epoch number set to 1000, and the mean square error (*MSE*) is employed as the performance metric. The Bayesian Regularisation (BR) optimisation algorithm [213] is used for network parameter (weights and biases) optimisation. The BR has several advantages such as a lower risk of overfitting and a more robust performance with sensitive and noisy data. The dataset was randomly split into 80% and 20% for the training and testing sets, respectively. Note that no additional validation set was used as the BR optimisation algorithm can automatically adjust the hyperparameters from the training set. Fig. 7-25 shows the consistent histogram distribution of the training and testing sets for each response parameters, based on the MISO dataset. This consistent data split was deliberately done to improve the training quality and reduce the risk of overfitting.

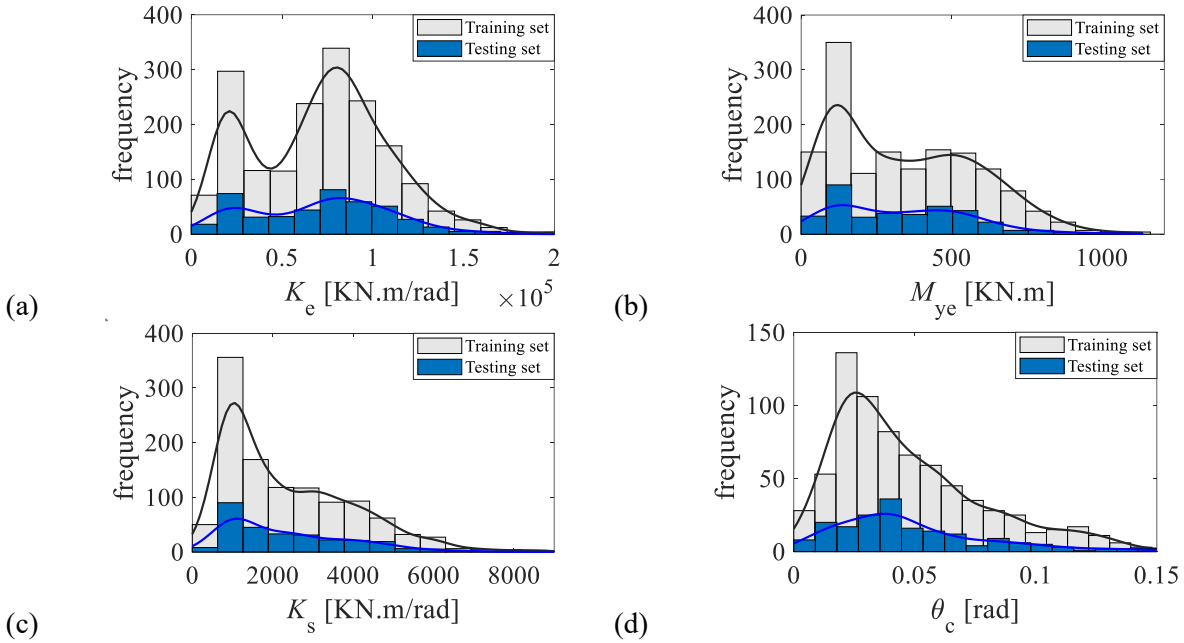

Fig. 7-25 Distributions of the training and testing set for each response for the ANN model.

Table. 7-12 summarises the ANN's parameters and training settings for the MIMO and MISO models. Several activation functions were implemented. Note that proper normalisation closing to the boundary of neuron activation functions also dominates the network's training performance. Features and response parameters can be normalised with different scaling methods as given by Eq. 7-17. The *Zscore* method normalises the input and output data (X or Y) to a distribution with a mean (μ) of 0 and a standard deviation (σ) of 1. The *LogZ* method has the same structure as the *Zscore* method but normalises the logarithmically transformed data ($X_{\log}$ or $Y_{\log}$). The *MinMax* method scales the data to a range from 0 to 1. For the MISO M_{ye} network, the *tansig* activation function bounded with -1 to 1 was utilised, which can capture the complex nonlinearity between the features and responses. Correspondingly, all input features were normalised with the *Zscore* method. For other MISO and MIMO networks, the *poslin* activation function ranging from 0 to infinity was utilised. This is mainly because that the elastic and post-yielding parameters are very sensitive to the variation of features. The *poslin* activation function can avoid unexpected negative outputs and saturation if the large-value feature is trained. Toward this, all input features were normalised with the *MinMax* method. All output responses were normalised with the *LogZ* method since their distributions are right-skewed (refer to Fig. 7-25). For the output layer, the *purelin* activation was implemented as it is widely employed in regression analysis for unbounded predictions. The number of neurons for each model was determined and optimised by the number of input features and assessing the performance across the training and test sets, as shown in Fig. 7-26. In the MISO models, the number of neurons was determined as the smallest number where the performance metrics (i.e., P_{20}, R^2, *RMSE*) of the training and testing sets remain stable and reach a minimal gap. Th same procedure was conducted to the MIMO model as well. Referring to Table. 7-12, the number of neurons varied between 11 and 16.

$$X_{\text{norm}} = \begin{cases} \frac{X-\mu}{\sigma} & (Zscore) \\ \frac{X_{\log}-\mu_{\log}}{\sigma_{\log}} & (LogZ) \\ \frac{X-X_{\min}}{X_{\max}-X_{\min}} & (MinMax) \end{cases} \quad 7\text{-}17$$

Table. 7-12 Selected features for each response for the proposed ANN model

							Activation functions	
ANN type	Parameter	N_{feature}	N_{neuron}	X_{norm}	Y_{norm}	Training algortihm	Hidden layers	Output layer
MISO	K_e	10	14	*MinMax*	*Log-Z*	*trainbr*	*poslin*	*purelin*
	M_{ye}	9	11	*Zscore*			*tansig*	
	K_s	13	16	*MinMax*			*poslin*	
	θ_c	13	14	*MinMax*			*poslin*	
MIMO	All	13	16	*MinMax*			*poslin*	

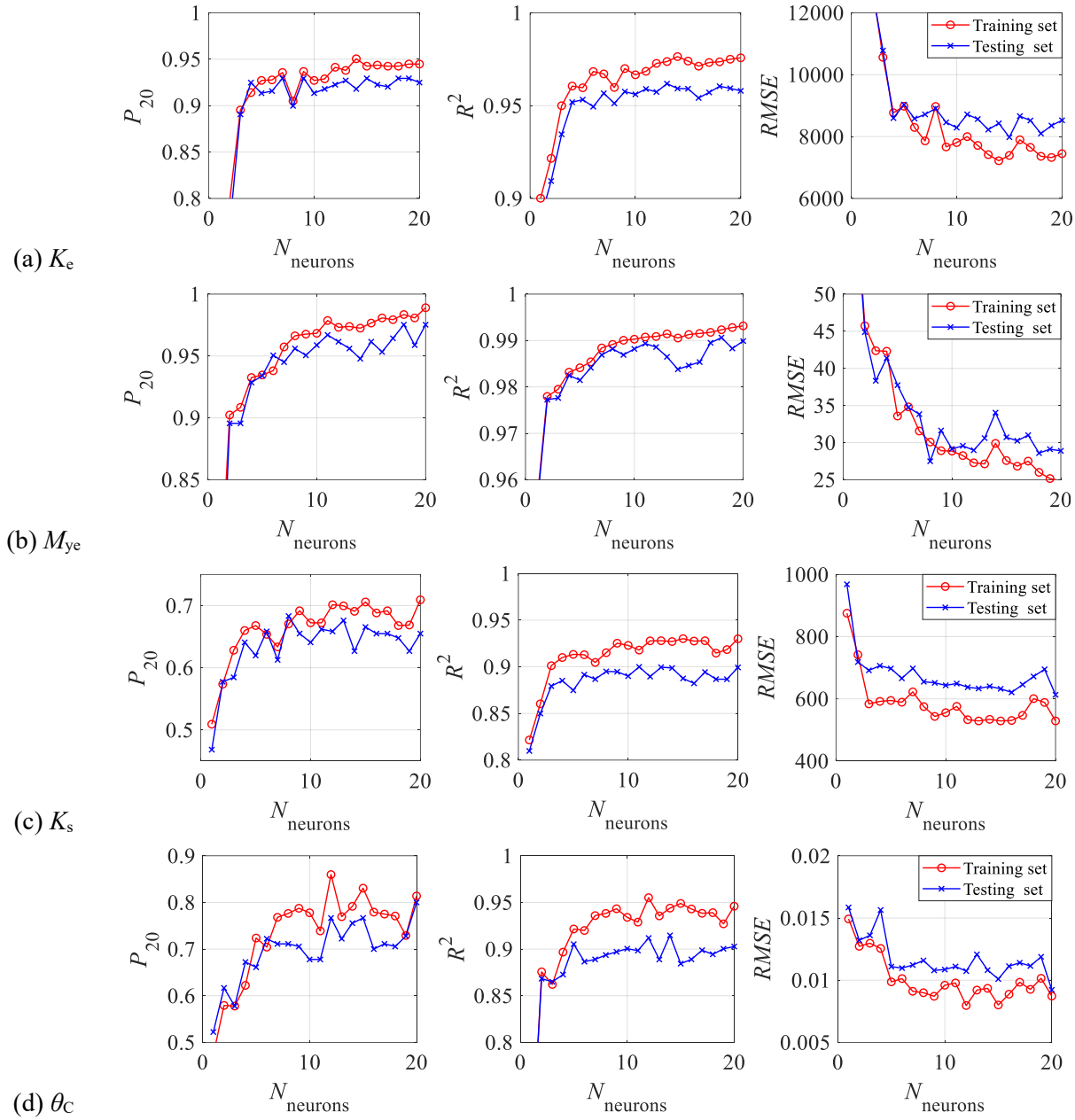

Fig. 7-26 Error plots for choosing N_{neuron} in the hidden layer for the MISO models: (a) K_e; (b) M_{ye}; (c) K_s; and (d) θ_C.

7.6.3. Model performance and interpretation

Qualitatively, Fig. 7-27 shows the predicted versus observed values of the four target responses based on the MIMO and MISO models. All plots reflect a good agreement between the model prediction and observed data, where the scatters are close to the reference 1:1 perfect-fit line, especially for M_{ye}. The plot scatter differentiates between the training and testing sets, demonstrating the consistent performance across the two sets. This implies the absence of overfitting in the models. The stiffness and rotation parameters (i.e., K_e, K_s, and θ_c) show a relatively larger divergence, as expected. For K_e, the numerical deduction from the testing

data, geometrical imperfections, and the magnitude of the bolt pretension level (which is not considered explicitly in the model) may contribute up to 30% variability, see Chapter 2.5. The K_s and θ_c are highly affected by the unavoidable inherent uncertainty in the bolt's elongation, which may lead up to 1.3% rad variability on the capping rotation (θ_c), see Chapter 5.3.2.

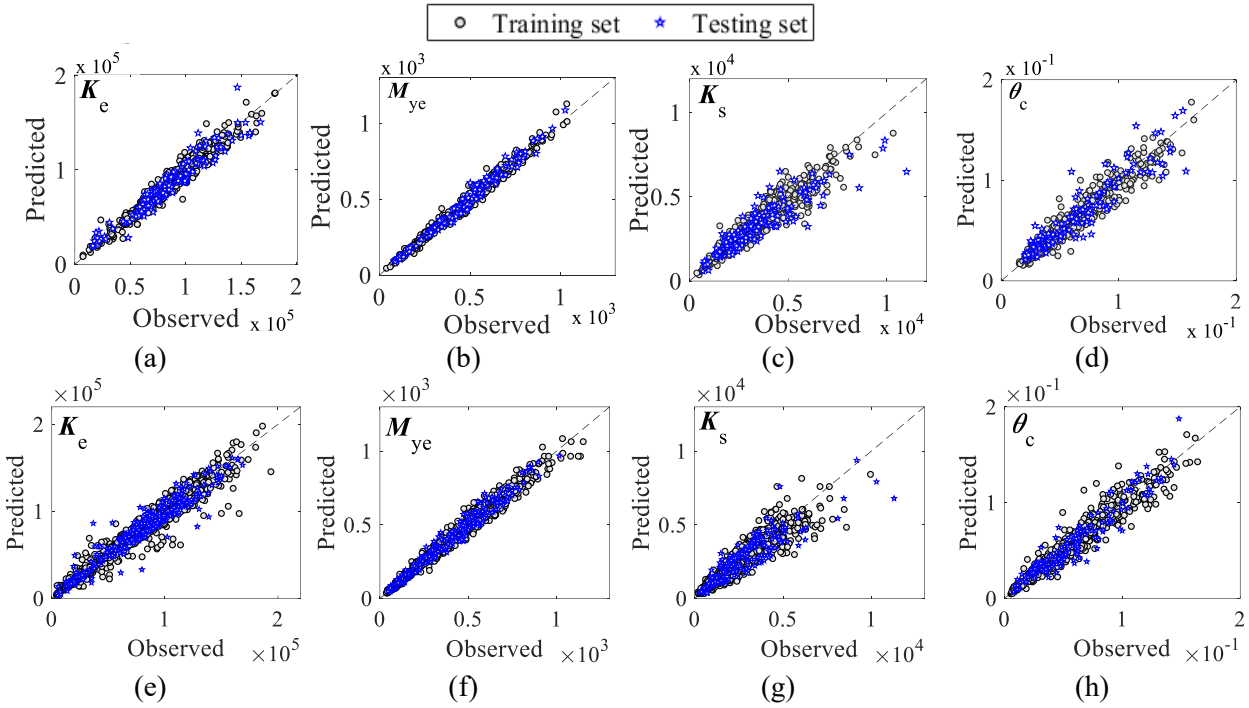

Fig. 7-27 Predicted versus measured values based on the (a-d) MIMO and (e-h) MISO models.

To quantitatively assess the models performance and absence of over-fitting, several quality-of-fit metrics are quantified and summarised in Fig. 7-28 and Table. 7-13. Both the MIMO and MISO models achieve an R^2 is larger than 0.9. Slightly larger *RMSE* values are observed in the MISO models compared to the MIMO model. This is understandable as more data noises and predictor variabilities were captured in the larger MISO model dataset, especially for K_e. Despite the unavoidable uncertainty in the datasets, all the *RMSE* values are less than 20% of the mean of their corresponding target responses. When it comes to the *P*-values, both the MIMO and MISO models developed a P_{20} and P_{50} larger than 0.65 and 0.98, respectively. This indicates that both the MIMO and MISO models can present an acceptable prediction. Most importantly, the MIMO model required almost half the dataset size of the MISO models to achieve a comparable performance. For the MISO model, the input features can be optimised based on the target response parameter, but larger data would be necessary to improve the model's performance and reduce the risk of overfitting. With a similarly sized dataset than the MIMO model, the MISO$^-$ models achieve an acceptable R^2 values larger than 0.8. Nonetheless, the MISO$^-$ models have about 30% lower performance on *RMSE* compared to the MIMO model. Unlike the MIMO approach, the MISO approach does not induce any correlations between the response parameters. Furthermore, Table. 7-14 summarises the quality metric for

the residuals and relative residuals based on the entire sets. Note that the σ_{ε} is close to the *RMSE* in Table. 7-13. This approves the developed ANN models are good fitted with low bias. Additionally, both the $\mu_{|rel,\varepsilon|}$ and $\sigma_{|rel,\varepsilon|}$ indicates that the K_e and M_{ye} models provide a prediction with an average error around 10%. With respect to the K_s and $\underline{\theta_c}$ models, slight divergences are observed but still acceptable as the average error can reach up to 18%.

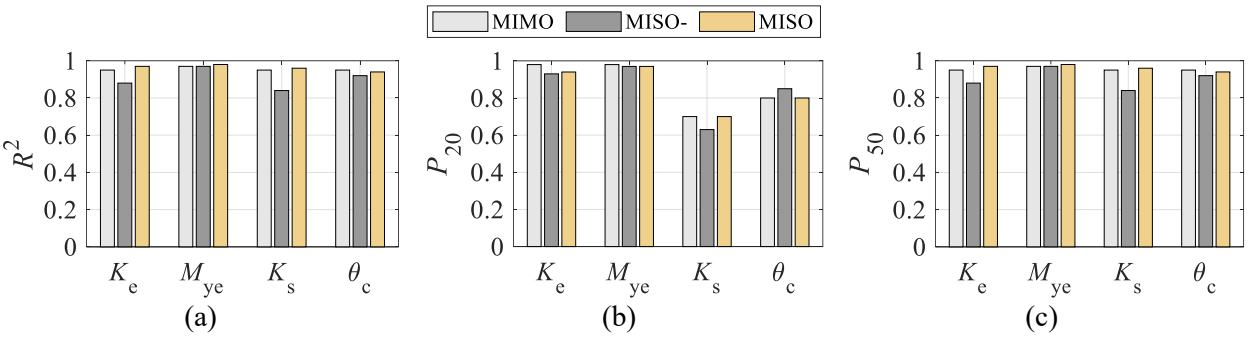

Fig. 7-28 Performance of the devleoped ANN models based on training set: (a) R^2; (b) P_{20}; (c) P_{50}.

Table. 7-13 Summary of the developed ANN models *RMSE* metrics for the training and testing sets

	Training set				Testing set			
	K_e [kN.m/rad]	M_{ye} [kN.m]	K_s [kN.m/rad]	θ_c [rad]	K_e [kN.m/rad]	M_{ye} [kN.m]	K_s [kN.m/rad]	θ_c [rad]
MIMO	6913	19	590	0.008	7804	22	714	0.010
MISO$^-$	8310	30	754	0.010	8951	33	882	0.013
MISO	7360	28	552	0.009	8064	30	719	0.011

Table. 7-14 Summary of the developed ANN models residual quality metrics for the entire set

	$\mu_{\varepsilon,rel\|}$				$\sigma_{\varepsilon,rel\|}$				σ_{ε}			
	K_e	M_{ye}	K_s	θ_c	K_e	M_{ye}	K_s	θ_c	K_e [kN.m/rad]	M_{ye} [kN.m]	K_s [kN.m/rad]	θ_c [rad]
MIMO	0.07	0.04	0.15	0.12	0.07	0.04	0.11	0.10	7431	21	685	0.009
MISO$^-$	0.08	0.04	0.17	0.13	0.11	0.06	0.15	0.12	8430	30	821	0.011
MISO	0.08	0.06	0.15	0.12	0.10	0.05	0.14	0.11	7733	28	561	0.010

In terms of model interpretation, the Shapley additive explanation algorithm (SHAP) [214] is used to explain how each predictor affects the ANN model's prediction for a given response. Fig. 7-29 shows the SHAP bee swarm plots of each predictor against the corresponding target response in MIMO and MISO models. Each point refers to a specimen and colour coded based on its feature value. The magnitude of the SHAP value indicates the positive/negative impact on the model prediction. The relatively larger variability of the SHAP value indicates that the corresponding predictor presents a more significant impact on the model's prediction, which is critical to the model optimisations.

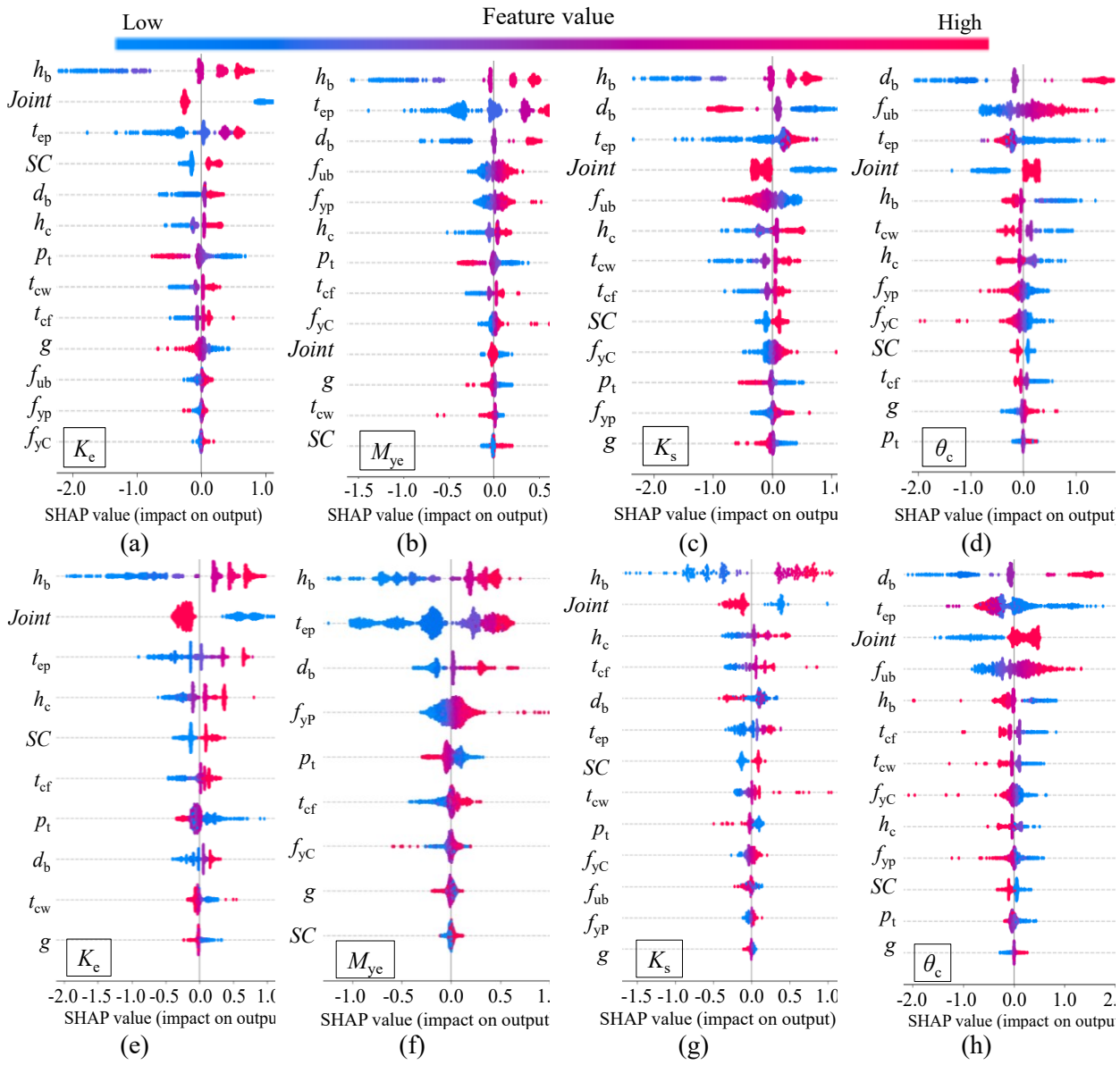

Fig. 7-29 SHAP value summary plots: (a-d) MIMO and (e-h) MISO.

With respect to K_e in Fig. 7-29 (a) and (b), the beam height (h_b), endplate thickness (t_{ep}), column height (h_c), and bolt diameter (d_b) are the top geometric features, as expected. Note that, the *Load* and *SC* also present a relatively high impact, where the stiffened EEPCs under symmetric loading will develop a higher K_e. This is because the *Load* and *SC* dominate the magnitude of the deformations of the column flange and web panel zone. The material features (i.e., f_{yP}, f_{yC}, and f_{ub}) show the least important impact on the MIMO model's prediction, see Fig. 7-29 (a). This proves the assumption made in the optimised predictor selection for the MISO model.

For M_{ye} in Fig. 7-29(c) and (d), the beam height (h_b), endplate thickness (t_{ep}), and bolt diameter (d_b) are the top three geometric features in the predictions of the MIMO and MISO models. Additionally, a larger vertical bolt pitch distance (p_t) and a smaller column flange thickness (t_{cf}) have a negative impact, as the

column flange is more likely to develop bending deformation. All material parameters (i.e., f_{yP}, f_{yC}, and f_{ub}) have a positive impact, which satisfies the mechanical point of view. Compared to K_e, the *Load* and t_{cw} present a less effect on the M_{ye} prediction in the MIMO model, as expected. This can be explained by noting that EEPC's plastic strength is mainly derived from the endplate and column flange bending. Therefore, the MISO model without those features (i.e., *Load*, t_{cw}, h_c, and f_{ub}) also has a rational SHAP distribution and reliable prediction.

In terms of the post-yielding responses (i.e., K_s and θ_c) in Fig. 7-29(e) to (h), similar observations are made. Most notably, the bolt diameter (d_b) and ultimate bolt stress (f_{ub}) are among the most critical features for the K_s and θ_c in the MIMO and MISO models. In detail, larger d_b and f_{ub} will increase the θ_c and decrease the K_s. This indicates that stronger bolts promote the plastic deformations from other ductile components, such as endplate, column flange, and web panel zone.

Beyond the SHAP bee swarm plots that demonstrate the overall features importance, the SHAP dependence plots visualise the exact correlation between a given feature and corresponding response. Fig. 7-30 shows the SHAP dependence plots between several critical features (h_b, t_{ep}, d_b) and responses (M_{ye} and θ_c) in the MISO model.

Besides, the raw correlation between those features and the corresponding responses are also superimposed in the same plot. For M_{ye} versus t_{ep} in Fig. 7-30(a), the SHAP value linearly increases with t_{ep} ranging from 8mm to 20mm. This is expected as the thicker endplate can resist higher moment with less bending. Note that a nonlinear positive correlation is observed for t_{ep} ranging from 20mm to 25mm, and the SHAP value flattens out when t_{ep} is larger than 25mm. This is understandable as t_{ep} no longer dominates M_{ye} after reaching this threshold. The plastic deformations are pushed to other components, such as CFB and CWS. Additionally, the observed raw correlation also presents a similar trend (revealed by the moving average curve). This indicates that the M_{ye} ANN model can directly capture its characteristic with limited interactions from other features. Similar observation is made for the effect of h_b on M_{ye} see Fig. 7-30(b). The M_{ye} SHAP values show a linear positive correlation against h_b, as expected. This is mainly attributed to a deeper beam leading to a larger lever arm from the tension flange to the compression zone. Correspondingly, the raw correlation between M_{ye} and h_b presents a similar pattern. This demonstrates that t_{ep} and h_b are not only the top two critical features in the M_{ye} ANN networks but also less affected by other features' interactions.

With respect to the θ_c model in Fig. 7-30(c) and (d), the SHAP values present a reasonable linear correlation against t_{ep} and d_b, which the SR EEPCs with thin endplate and strong bolt tend to develop a larger plastic deformation. However, no specific raw correlation (i.e., a flat moving average trend) is observed, which mismatches the corresponding SHAP values. This is mainly attributed to the sensitivity of θ_c and the noise and confounding from other features. The maximum ductility of SR EEPCs is resourced from all ductile components' plastic deformations, which is not relying on a primary single geometric or material feature.

Additionally, the configuration parameters, such as loading direction and column stiffener, may also significantly affect the column's plastic behaviour. The developed ANN model can effectively capture the isolated feature's contribution on a specific response, which reveals that why other pertinent models with simpler assumptions or mathematic formations (see Chapter 2.6) fail to provide a reliable prediction on post-yielding parameters.

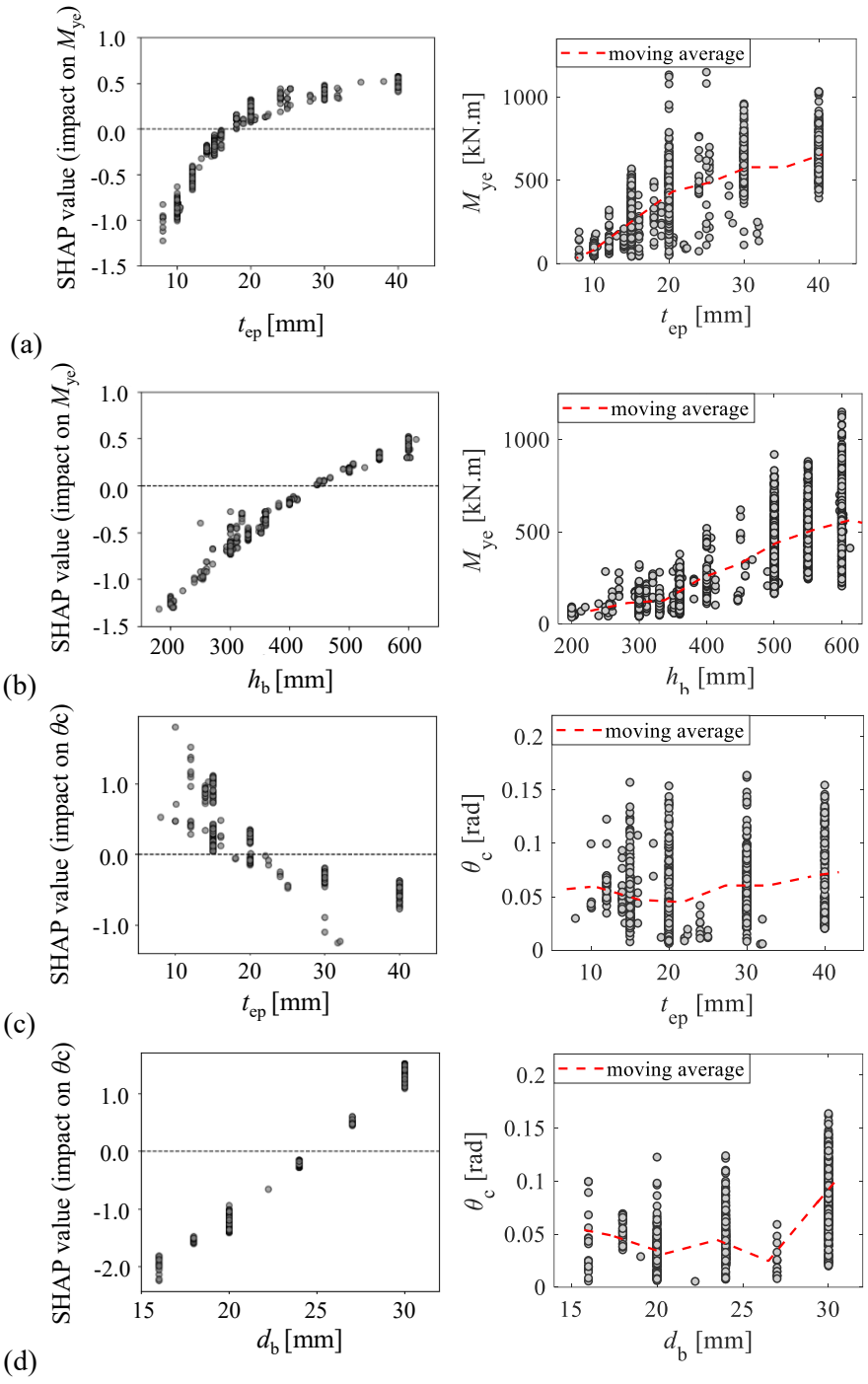

Fig. 7-30 SHAP dependence plots for the MISO models: (a) t_{ep} versus M_{ye}; (b) h_b versus M_{ye}; (c) t_{ep} versus θ_c; (d) d_b versus θ_c.

7.6.4. Model demonstration

The collated dataset is used to assess the overall performance of the developed ANN models in relation to other pertinent prediction models. Those are the code-based yield line method [24], Eurocode 3 component method [7], and the proposed MVLR model.

Fig. 7-31 shows a box-and-whiskers plot of the predicted-to-measured ratio. It is observed that the proposed ANN models present a better prediction for all target responses, except K_s. This is mainly because more feature variabilities (*Load* and *SC*) were explicitly captured and learned during the training of the ANN networks. Regarding code-based models, the yield line method fails to predict the connections controlled by the column panel zone in shear and limited endplate yielding with bolt elongation, where the prediction error can exceed 200%. This is mainly because this method only considers the yield line patterns of the endplate and column flange bending. The component method provides a relatively better prediction of M_{ye} with an average error of -30%. However, the error in K_e predicted by the component method can reach -95% and 660%. This is mainly attributed to the simple assumption of the discrete T-stub behaviour, perfect yield line pattern, and lever arm computation. Compared to the code-based models, the MVLR provides a more rational prediction of K_e and M_{ye}, owing to the large regression dataset and the explicit consideration of the effects of the load symmetry and column stiffeners. However, the predictions on θ_c can reach up to +200%, which mostly happened in the high-strength steel connections. This is mainly attributed to the model's relatively simpler formation, which struggles to capture the complex nonlinear correlations between the features and responses. With respect to the developed ANN models, over 95% of K_e and M_{ye} datapoints are predicted with an error less than 30%. For the post-yielding parameters (K_s and θ_c), a slightly larger but still acceptable error (≤50%) is guaranteed for 95% of datapoints. Note that several outliers predicted with an error of over 50% but less than 100% are observed. This is difficult to avoid due to the complex feature interaction and material uncertainties. Nevertheless, the developed ANN models still present a more accurate and robust performance towards all responses than other pertinent prediction models.

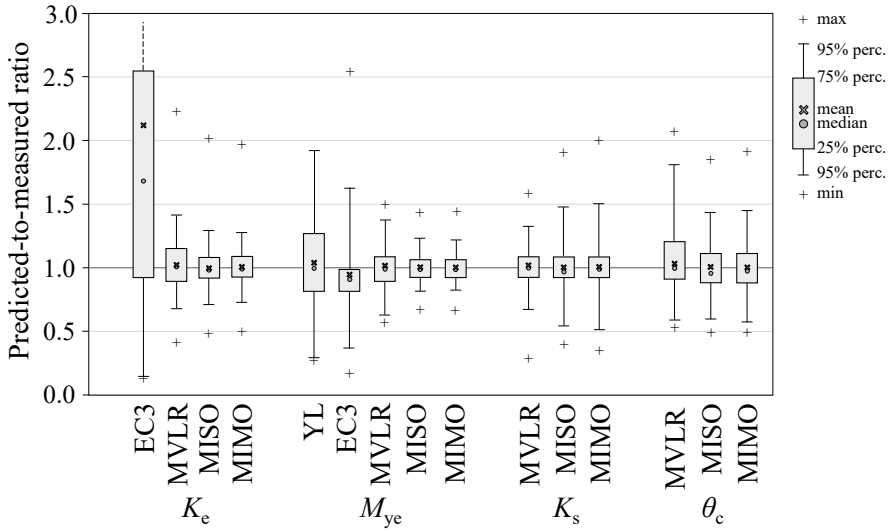

Fig. 7-31 Distribution of the prediction errors in the code-based and self-proposed models.

The performance assessment can be further inspected visually in Fig. 7-32, which shows the different models' predictions against six representative test specimens that failed by bolt rupture. Note that the response's post-capping branch is superimposed for a better visualisation based on the recommendations in Chapter 7.5.5.6. Those selected specimens have different geometric parameters, configurations (i.e., asymmetric or symmetric joint), stiffened methods (i.e., stiffened or unstiffened), and material properties (i.e., conventional structural or high-strength steel). It was observed that the proposed bilinear model can effectively capture the key response characteristics. Table. 7-15 summarises the prediction errors for each target response. Compared to the code-based models, the developed ANN models can accurately predict the K_e and M_{ye} with an average error of less than ±40%. Furthermore, the predictions of the developed ANN models for the K_s and θ_c with less divergence (i.e., average error less than ±20%) than the existing MVLR models, especially for the specimens with high-strength steels. Concerning the performance of the developed ANN models, the MISO model presents an overall better prediction with respect to all responses. This can be explained using more data in the training to capture the complex nonlinear interactions between the variables and responses, especially for the K_e and M_{ye}.

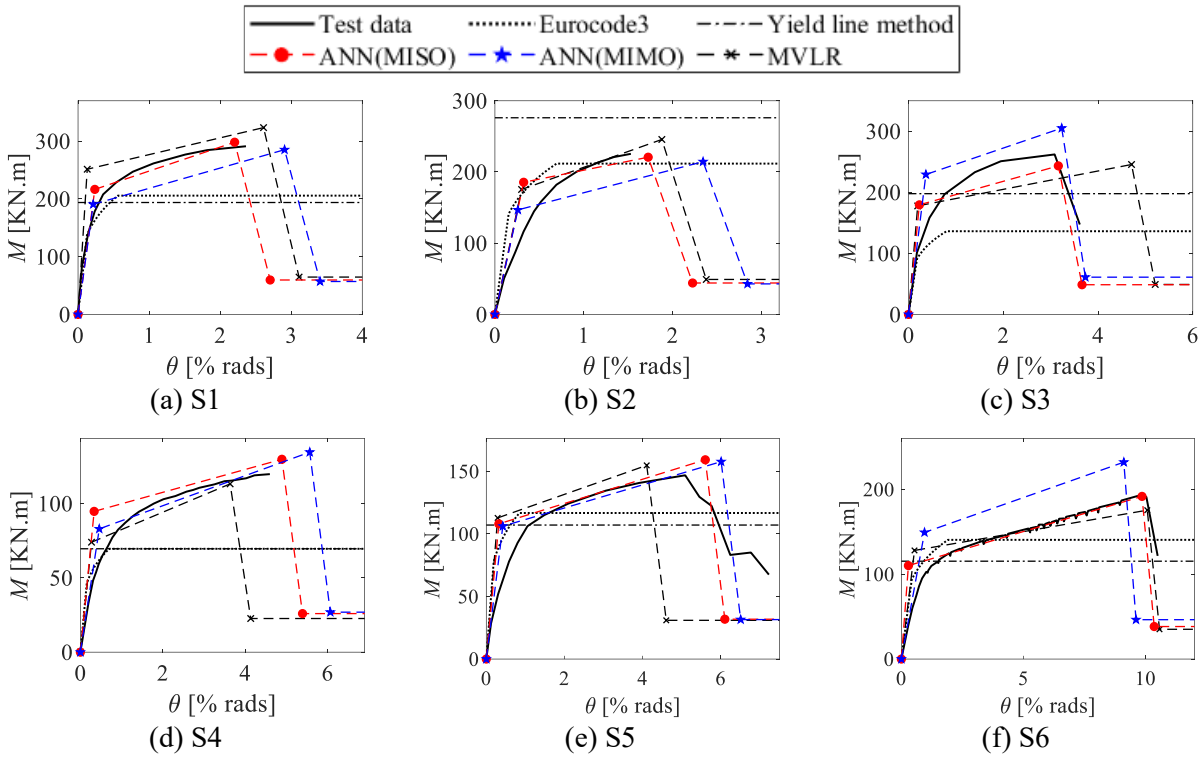

Fig. 7-32 Comparisons of the developed ANN models and key existing ones against selected experimental data: (a) stiffened by Sherbourne [25]; (b) stiffened by Tong [215]; (c) stiffened by Dubina et al [216]; (d) stiffened by Arul Jayachandran et al [171]; (e) stiffened by Yang and Tan [217]; (f) unstiffened by Prinz et al [149].

Table. 7-15 Observed error ratios in the developed ANN models and key existing ones for selected experimental specimens

ID	Yield line	Eurocode 3		MVLR				ANN MIMO				ANN MISO			
	M_{ye}	K_e	M_{ye}	K_e	M_{ye}	M_c	θ_c	K_e	M_{ye}	M_c	θ_c	K_e	M_{ye}	M_c	θ_c
S1	0.87	1.19	0.92	1.23	1.12	1.11	1.08	0.98	0.84	0.98	1.21	0.98	0.96	1.02	0.92
S2	1.80	1.98	1.39	1.35	1.14	1.08	1.20	1.35	0.96	0.95	1.30	1.35	1.20	0.97	1.13
S3	0.98	0.98	0.68	1.70	0.89	0.94	1.50	1.15	1.15	1.16	1.03	1.40	0.90	0.93	1.02
S4	0.80	1.52	0.80	1.52	0.85	0.94	0.78	1.12	0.94	1.12	1.20	1.52	1.10	1.08	1.07
S5	1.04	1.54	1.13	1.51	1.09	1.05	0.80	1.08	1.03	1.07	1.20	1.34	1.05	1.08	1.12
S6	1.03	1.48	1.25	1.40	1.14	0.95	1.02	1.14	1.23	1.19	1.08	1.70	1.00	1.03	1.00

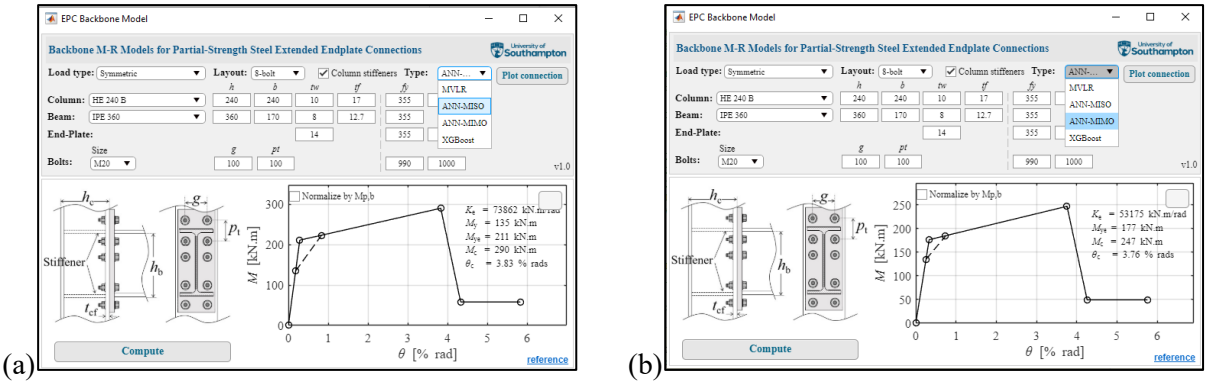

Fig. 7-33 GUI tool for the ANN backbone model: (a) MISO model; (b) MIMO model.

7.6.5. Model implementation and limitation

The developed MIMO and MISO models are made publicly available through a MATLAB script and a dedicated graphical tool [218]. The developed ANN models present high accuracy in predicting elastic stiffness, plastic strength, and post-yield response up to failure. The models are limited to SR bare steel beam-to-column joints with a major axis orientation that falls within the geometric and material applicability range of the training dataset, as given in Table. 7-16 and Table. 7-17 for the MISO and MIMO models, respectively. Extrapolating beyond these ranges may lead to erroneous results. Besides, disproportional and impractical combinations of component sizes (e.g., t_{cf}>>t_{ep}, h_c<<h_b, *etc*) may lead to an unreasonable prediction.

Table. 7-16 Statistical metrics of the MISO ANN model's features

	K_e [kN.m/rad]				M_{ye} [kN.m]				K_s [kN.m/rad]				θ_c [rad]			
Features	μ	σ	*min*	*max*	μ	σ	*min*	*max*	μ	σ	*min*	*max*	μ	σ	*min*	*max*
Load	0.75	0.44	0	1	-	-	-	-	0.66	0.47	0	1	0.78	0.41	0	1
SC	0.44	0.50	0	1	0.46	0.5	0	1	0.55	0.50	0	1	0.47	0.50	0	1
p_t	137	22	70	205	136	24	70	205	132	25	68	205	147	21	77	205
t_{ep}	21	10	8	40	20	9.4	8	40	19	9	8	51	23	9	8	40
d_b	23	4	16	36	23	4.7	16	36	23	5	16	36	25	4	16	30
g	118	15	72	180	116	15	70	180	114	16	70	180	122	11	80	180
h_c	312	66	114	500	-	-	-	-	293	68	114	500	334	49	190	400
t_{cf}	19	4.4	10	30	19	4.5	10	30	18	5	10	30	21	3	10	30
t_{cw}	11	2.4	7	20	-	-	-	-	11	3	7	20	12	2	7	20
h_b	472	114	200	607	457	116	200	754	435	119	180	607	514	89	200	754
f_{yP}	-	-	-	-	351	70	214	1022	350	73	214	1012	360	66	214	1000
f_{yC}	-	-	-	-	390	53	220	1017	389	55	229	1017	395	50	229	1000
f_{ub}	-	-	-	-	-	-	-	-	1076	124	747	1478	1041	137	740	1478

Table. 7-17 Statistical metrics of the MIMO ANN model's features [units: mm and MPa]

Features	μ	σ	*min*	*max*
Load	0.84	0.37	0	1
SC	0.44	0.50	0	1
p_t	146	20	70	205
t_{ep}	23	9	8	40
d_b	25	4	16	30
g	122	11	80	180
h_c	333	49	152	400
t_{cf}	21	3	10	30
t_{cw}	12	2	7	20
h_b	516	89	171	600
f_{yP}	362	71	229	1012
f_{yC}	396	55	229	1017
f_{ub}	1043	138	766	1478

7.7. Classification models for EEPCs' deformation mode(s)

FR EEPCs are designed by current codes [7, 8] to force the plastic deformation to occur in the beam. The backbone and hysteretic moment-rotation response of FR EEPCs can be computed and simulated using available models [13, 191]. For SR EEPCs, the full range backbone moment-rotation response can be predicted by the proposed MVLR and ANN models in the sections mentioned above. However, accurate models that predict the deformation mode(s) of SR EEPCs remain missing. SR EEPCs can develop several deformation modes as observed in past experimental and numerical studies, including EPB, CFB, and CWS. Beam yielding is also observed when the EEPC rigidity is close to the fully rigidity limit. Those deformation modes may occur individually or simultaneously, depending on the connection's geometry and the relative strength of its components. This indicates that accurately predicting the deformation modes of EEPC can be challenging. Code-based methods, including the component method [7] and the yield line analysis [8, 24] can be used to infer the deformation modes of EEPCs by identifying the weakest component. However, these models have practical limitations related to procedure complexity and prediction accuracy, particularly when dealing with multiple simultaneous deformation modes. Therefore, several non-parametric machine learning models are employed to develop a deformation mode classification model.

Four primary deformation modes are identified in EEPCs, as illustrated in Fig. 7-34. Those are EPB, CFB, CWS, and BB. Note that these modes may occur individually or simultaneously. A brief description of those modes, including their deformation characteristics and applicability in design, is provided herein.

BB (Fig. 7-34(a)) is the primary deformation mode in fully rigid EEPCs. This connection type is used in highly seismic regions, as part of pre-qualified EEPCs [39, 219]. By definition, fully rigid EEPCs with BB develop a moment capacity larger than that of the beam's plastic moment ($M_{p,b}$) and can develop a rotational capacity larger than 4% rad under cyclic loads. This mode results in excellent energy dissipation due to the rounded hysteretic response. On the other hand, the repairability of the BB mode (after earthquakes or column loss scenarios) can be challenging and costly.

In SR EEPCs, plastic deformations occur in the connection components such as EPB and/or CFB. The controlling mode is dependent on the relative thickness of those two components. EPB (Fig. 7-34(b)) occurs when a relatively thin endplate and strong bolts are implemented in design relative to the column flange (i.e., $t_{ep}<<t_{cf}$). This can be achieved by designing the endplate to be the weakest component using the component method [7] or the yield line method [24]. EPB is a favourable mode that is sought in the design of SR EEPCs as it can achieve an acceptable energy dissipation capacity and plastic rotation over 3% rad. Besides, the repairability of an endplate is simpler and more cost-effective compared to the repair of beam or column damage. On the other hand, EEPCs with an EPB mode possess a limited moment resistance (less than 80% of $M_{p,b}$).

CFB can occur in SR EEPCs (Fig. 7-34(c)). CFB is not desirable in structural design since the columns are stipulated to remain elastic for structural stability. Additionally, the repairability of column plastic deformation can be problematic [220]. Nonetheless, CFB can still be observed, particularly in unstiffened interior EEPCs undergoing column loss scenarios [152, 221]. In this case, the column flanges are subjected to combined bending and tension from the catenary action.

CWS (Fig. 7-34(d)), can occur in both FR and SR EEPCs. Current design codes only allow for limited CWS deformations to prevent excessive drift and misalignment. Recently, considering the stable hysteretic response of the CWS mode, some researchers advocated for employing a weak panel zone design while providing detailing recommendations for limiting the weld fracture probability in case of welded connections [222]. CWS can develop with a high energy dissipative capacity and strength hardening, which is critical for the seismic stability of moment resisting frames [223]. Similar to BB, the repairability of the CWS mode can be costly and challenging.

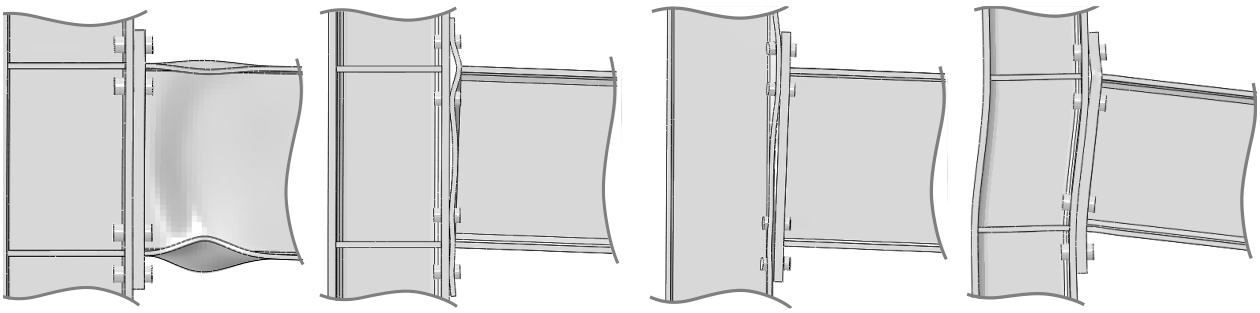

(a) BB (b) EPB (c) CFB (d) CWS

Fig. 7-34 EEPCs' primary deformation modes: (a) BB; (b) EPB; (c) CFB; (d) CWS.

The deformation mode also controls the hysteretic response of the connection. In EEPCs, the hysteretic response can vary from a rounded response to a pinched one. The former is observed in fully rigid connections where beam local buckling is dominant. In contrast, the latter is observed in SR connections controlled by plastic deformations in the connected plates (i.e., stiffness degradation and gap opening/closing between the endplate and column flange during the unloading and reloading process). A higher level of pinching reduces the seismic energy dissipation. The level of pinching depends on the deformation mode(s) and the connection geometry. Currently, there are no generalised recommendations for defining the cyclic (pinching) parameters of EEPCs within existing numerical phenomenological models. To address this issue, guidelines for capturing the cyclic response characteristics of EEPCs are provided.

Firstly, several standard machine-learning models are trained here to capture the SR EEPCs' deformation mode in this section. Those are the Decision Tree (DT), Random Forest (RF), K-Nearest Neighbour (KNN), and Support Vector Machine (SVM). Fig. 7-35 illustrates the architecture of those models. Additionally, the cyclic response of EEPCs is assessed as a function of the deformation mode. A numerical phenomenological model is then calibrated with cyclic data. Recommendations are accordingly provided for the characterization of the cyclic deterioration parameters.

The architecture of a DT, as part of a RF, is illustrated in Fig. 7-35(a). The DT includes a root node, decision nodes, and terminal leaves. The DT model starts by splitting the dataset from the root node using a defined condition (C_1) for a specific feature (X). The feature and the corresponding condition are determined based on an impurity algorithm, with Gini impurity as the default [224]. This then branches into several decision nodes with other conditions (C_2 to C_n) for each of the remaining features until the impurity quantity is no longer reduced. The terminal leaves (Y_1 to Y_n) are the final predictions (i.e., classification), which can be tracked by following a branch from the root node. RF is an ensemble of DTs (e.g., 100 DTs as the default) with a Bagging algorithm [225]. For each DT, a bootstrapped dataset is selected for the training, and a subset of features (X) is selected for C_1 to C_n. The split of each tree follows an impurity algorithm, the same as the

DT. The RF's final prediction is essentially the class with the voting majority based on the DTs' terminal leaves.

The KNN's architecture [226] is illustrated in Fig. 7-35(b) using a 2-D example. Compared to tree-based models, KNN does not build an explicit model from the training data. Instead, the Euclidean distances (by default) between a testing data point and all other training data are computed. Then, all distances are sorted in order, and the class of the nearest K points is determined as the prediction. Note that the number of K is recommended to be odd (3 by default) to avoid biased class voting.

The SVM's architecture [227] is illustrated in Fig. 7-35(c) using a 2-D example. The SVM aims to split the data based on a plane (a straight line in a 2-D model) with the maximum margin. The maximum margin is an equal distance between the nearest points (i.e., support vectors) from different classes. For high-dimensional problems, the plane is no longer a line but a hyperplane. Therefore, the kernel trick function needs to be implemented to classify a nonlinear boundary. In this section, the Radial Basis Function is selected for training.

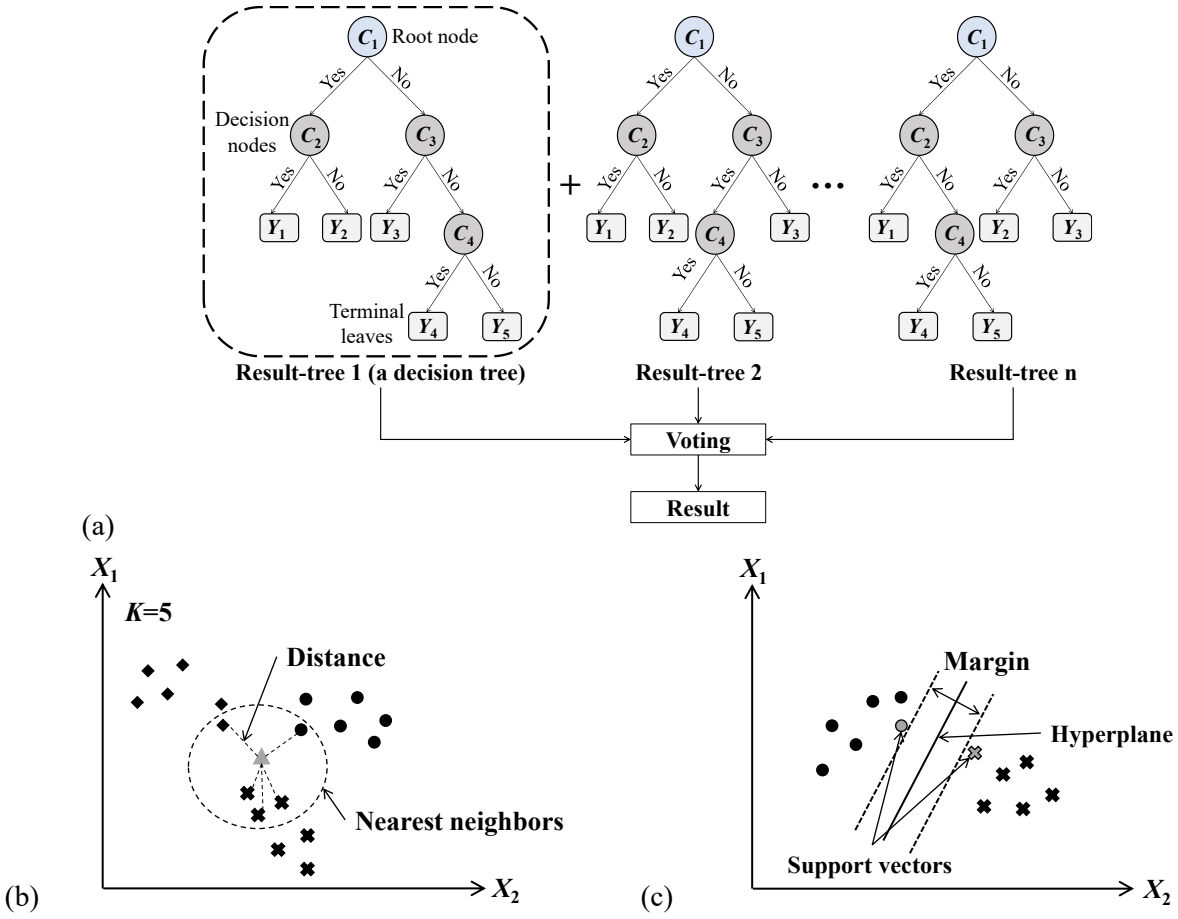

Fig. 7-35 Architecture of the classification models: (a) Tree-based; (b) KNN; (c) SVM.

7.7.1. Dataset, Target Responses, and Significant Features

The deformation mode(s) corresponding to each specimen in the dataset were deduced using a systematic method. For the experimental data, the logged deformation modes were determined manually based on the specimen test photos and/or the damage mode description as reported by the different researchers in the literature. Several experimental studies involved thorough instrumentation and provided the rotation breakdown per connection component, making it easier to identify those that yielded. As previously noted, multiple modes may occur simultaneously. In this case, all these modes are logged. For the simulation data, the deformation mode(s) are numerically deduced based on the rotational contribution of each of the connection's components, see Chapter 4.1.5. In detail, any component contributing more than 20% of the total rotation (at peak strength) is logged as a deformation mode. The 20% threshold is deemed enough to capture components undergoing appreciable plastic deformation. Fig. 7-36 shows the rotation breakdown for three sample specimens and the corresponding -logged- deformation mode(s). In Fig. 7-36 (a), the endplate (EPB) solely contributes more than 90% of the total rotation. In Fig. 7-36 (b), both the endplate (EPB) and column flange (CFB) are deforming plastically while the beam remains elastic. In Fig. 7-36 (c), EPB is the primary mode, but it is accompanied by noticeable plasticity (>20% contribution) in the beam (BB) and column web (CWS).

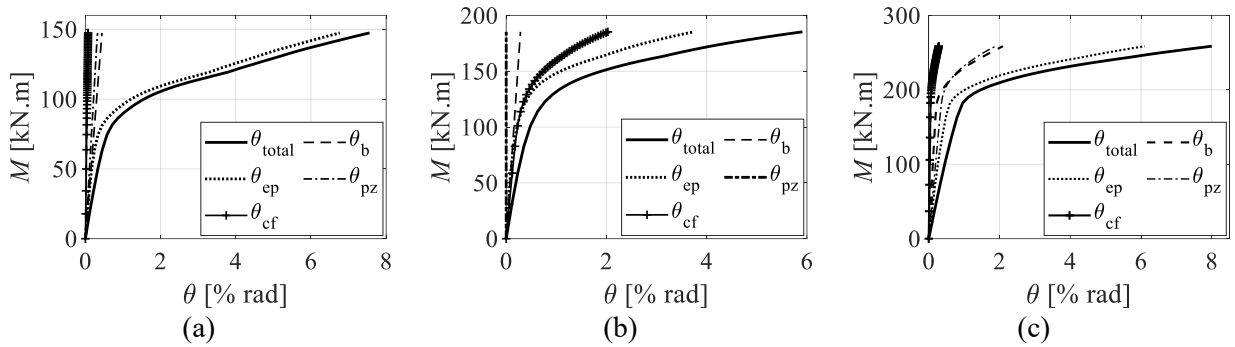

Fig. 7-36 Examples of the damage mode deduction from rotation contributions: (a) EPB; (b) EPB+CFB; (c) EPB+CWS+BB.

The same dataset trained in the proposed MVLR and ANN models is used in those classification models. Fig. 7-37 shows the distribution of the observed deformation mode classes for the entire dataset. The experimental dataset is primarily focused on SR EEPCs; hence, the EPB, CFB, and EPB+CFB classes are the most observed. A smaller number of specimens involved FR EEPCs with BB or Balanced classes. The simulation dataset also focused on SR EEPCs, given that it is more challenging to predict the deformation mode(s) for such connections. In SR EEPCs, CWS is also observed, as the column web panel zone is not necessarily designed for limited deformation in flexible framing construction for low to moderate seismicity.

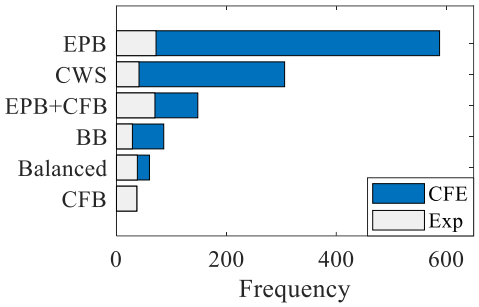

Fig. 7-37 Distribution of the observed deformation mode classes within the dataset.

The same features used in the proposed MVLR and ANN models are employed herein for the prediction of the deformation mode. A total of 11 features are used, which include geometric, material, and layout parameters. The geometric features are the endplate thickness (t_{ep}), endplate width (b_{ep}), column flange thickness (t_{cf}), vertical bolt pitch distance (p_t), beam depth (h_b), beam flange slenderness (b_{bf}/t_{bf}), and column web slenderness (h_c/t_{cw}). The latter two are known to control BB and CWS, respectively. Fig. 7-38 shows the correlation of the deformation mode classes with some of the key geometric parameters. By visually inspecting Fig. 7-38 (a), one can deduce that EEPCs mostly experience EPB when the t_{ep} is smaller than 15mm and t_{ep}/t_{cf} is less than 1.0. This mode is also expected when the endplate bending length (i.e., p_t) is large relative to its thickness (i.e., p_t/t_{ep} larger than ~7 as deduced from Fig. 7-38 (b)). Similarly, CFB is likely to occur when t_{cf} is smaller than 15mm, t_{ep}/t_{cf} is larger than 1.5, and p_t/t_{ep} is less than 7. The two modes are simultaneously observed (EPB+CFB) when the ratio of the two thicknesses is close to unity. BB occurs in fully rigid EEPCs, which coincide with thick endplates (>20mm) and a p_t/t_{ep} value around 3.5. The latter is expected, given the geometric limits specified for this type of seismically pre-qualified connections [39, 219]. For the CWS and Balanced classes, determining the classification boundary based solely on t_{ep}, t_{cf}, and p_t is complex, as the latter mode can occur in various connection layouts, and the former mode involves multiple deformation modes.

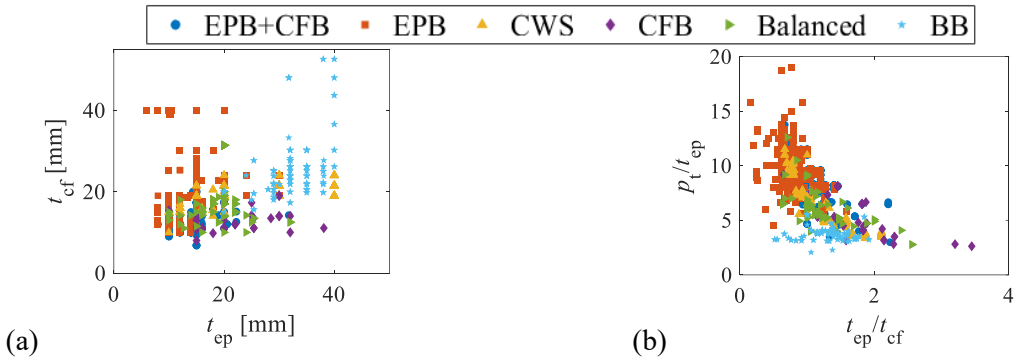

Fig. 7-38 Correlation between the deformation mode class and selected geometric features.

Two material features, endplate yield stress (f_{yP}) and column yield stress (f_{yC}), are also considered. Those control the onset of yielding and the relative strength of the endplate and column flange components. Note

that the beam's yield stress is not considered, given that it was practically equal to that of the column, for the employed dataset. Finally, two layout features are considered: *SC* which reflects the presence of column flange stiffeners (continuity plates) given their role in restraining column flange bending. This feature is encoded by 0 and 1 for unstiffened and stiffened column specimens, respectively. Finally, the *Joint* type is considered to differentiate between external joints (or interior ones with asymmetric beam loading) and internal joints with symmetric beam loading. The former reflects the joint boundary conditions and load demands under lateral loading scenarios (e.g., earthquakes) while the latter reflects those under gravity loading scenarios (e.g., column loss/progressive collapse). This is important considering that CWS would be restricted in interior joints with symmetric loading at the beam ends [168]. The *Joint* feature is encoded as 0 for exterior joints and 1 for interior joints with symmetric loading, respectively. The statistical summary of all features is shown in Table. 7-18 to describe the design space covered by the dataset. The above features, along with modern classification models, can be used to define better the multi-dimensional boundary between the different deformation mode classes. These models are discussed in the next section.

Table. 7-18 Statistical summary of the numerical features [units: mm and MPa]

Parameters	*Joint*	*SC*	p_t	t_{ep}	t_{cf}	t_{cw}	h_c	h_b	b_{bf}	t_{bf}	b_{ep}	f_{yP}	f_{yC}
μ	0.38	0.52	127	19	19	12	292	417	186	14	204	344	382
σ	0.48	0.5	24	9	7	6	68	126	36	3	37	71	57
min	0	0	205	6	7	5	114	114	100	7	120	214	220
max	1	1	62	50	50	48	475	914	305	26	330	1022	1017

7.7.2. Model training and hyperparameter setting

All four classification models were developed using the MATLAB R2021a Classification Learner Toolbox [212]. The data was randomly split into 80% and 20% for the training and testing sets, respectively, while maintaining a consistent distribution between the two sets, as demonstrated in

Fig. 7-39. For KNN and SVM, the data was normalized with the Z-score method, see Eq. 7-17. Note that data normalization is not required in tree-based models since 1) the split of each node is independently conducted, and 2) the threshold chosen for each split is consistent regardless of its scale.

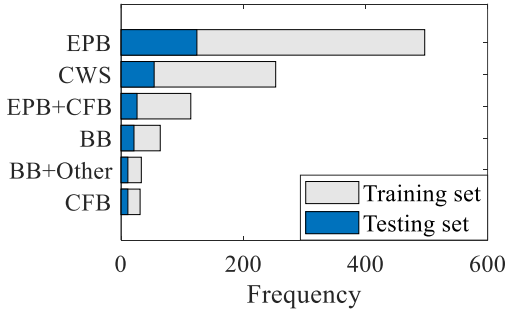

Fig. 7-39 Consistent distribution of the training and testing data sets for the classification models.

It can be observed from

Fig. 7-39, the inconsistency in the number of specimens/observations for each deformation mode class may induce bias in the classification model training algorithm and lead to poor predictive performance. In this regard, several methods can be implemented to alleviate this issue, such as the oversampling algorithm (i.e., SMOTE proposed by Chawla et al [228]) for the minority class or assigning a class weight factor [229]. A weighting factor is assigned herein, in pre-processing, for each deformation mode class within the training dataset, as summarised in Table. 7-19. The weighing factors are computed as the inverse of the ratio of a given class's number of observations to the total number of observations, divided by the number of classes [229]. This ensures the same importance level is given for each damage mode, which is a standard practice in classification model development.

Table. 7-19 Weighting factors assigned to each deformation mode class

Class	EPB	CWS	EPB+CFB	BB	Balanced	CFB
Weighting factor	0.33	0.78	1.76	1.82	2.71	6.65

7.7.3. Model performance

Fig. 7-40 shows the confusion matrices of the training and testing datasets for each of the four models. Three metrics are used to quantify the model performance: *accuracy* (A), *recall* (R), and *precision* (P). *Accuracy* measures the overall model's performance, which is the ratio of the correctly predicted specimens to the total number of specimens. *Recall* is the ratio of the correctly predicted specimens for a given class to the total number of specimens in the corresponding true class. *Precision* is the ratio of the correctly predicted specimens in a damage mode to the total specimens in the corresponding predicted class. Overall, all models achieve acceptable and consistent accuracy (> 84%) across both the training and testing datasets. The tree-based models, particularly the RF model, show the highest performance with respect to all three metrics. This is consistent with observations from similar studies in the literature [230, 231]. The RF model predicts the testing dataset with an impressive 94% accuracy. The recall and precision are over 90% for EPB, BB, and CWS. Those classes have well-defined boundaries (refer to Fig. 7-38). Lower (but still acceptable > 71%) recall and precision values are noted for the CFB, Balanced, and EPB+CFB classes. This can be attributed to the lower number of specimens, material uncertainties, and the fact that the latter two classes involve combined deformation modes. From now on, the RF model is selected for its superior performance.

To investigate the RF model's rationality from a mechanical perspective, the features' impurity-based importance indices are computed and plotted in Fig. 7-41(a). The impurity-based importance index is computed based on the feature that is used more frequently to split the data, thereby reducing impurity. The

figure shows the order of the features by their impurity-based importance. The geometric features t_{ep}, t_{cf}, and p_t are the top three features, accounting for about 50% of the overall importance. This is expected based on the earlier discussion (refer to Fig. 7-38) that demonstrated their strong correlation with the deformation mode class. The importance of h_c/t_{cw} is around 10%. This is critical for the EEPC controlled by Balanced and CWS. The importance of f_{yP} and f_{yC} is around 8% and 12%, respectively. This is expected as those parameters are critical to control the endplate and column flange bending. The importance of each feature relative to the deformation class is further investigated by computing the mean absolute SHAP values, as shown in Fig. 7-41(b) which measures how much a given feature can impact the model predictions [232]. Similar to the impurity-based importance, t_{ep}, t_{cf}, and p_t are the top three features based on the aggregated SHAP importance values. The t_{ep} feature is the most influential for all classes, except for CFB and CFB+EPB, which are more affected by t_{cf}. Note also that the feature *SC* shows a relatively higher importance, especially for EPB and EPB+CFB. This is because column stiffening is critical in determining how much a column flange can deform.

The correlation of each feature with the predicted class probability (whether positive or negative) is investigated through the SHAP summary plots in Fig. 7-42. Referring to Fig. 7-42(a), t_{ep}, t_{cf}, and f_{yP} are positively correlated with the probability of predicting BB. This reflects the fact that when the connection components (i.e., column flange and endplate) are stronger, the beam is more likely to be the weak element. Similarly, a higher-encoded *SC* value (i.e., stiffened column) will have a positive impact on BB likelihood. A smaller p_t is more likely to result in BB due to the restraint on endplate bending. This is also true for deeper beams, primarily because fully rigid joints traditionally use deep beams instead of shallow ones to control building drifts. Referring to Fig. 7-42(b), except for t_{ep}, h_c/t_{cw}, and f_{yP}, all other features (especially, t_{cf} and f_{yC}) are inversely correlated with the CFB probability of occurrence, implying that either a stronger endplate or a weaker column flange would result in CFB. Opposite correlations are observed with respect to EPB as shown in Fig. 7-42(c). Referring to Fig. 7-42(d), asymmetric specimens with larger p_t, thicker t_{ep}, and deeper h_b will be more easily to develop CWS. This is mainly because the stronger endplate and beam result in the column to be the weak component. Referring to Fig. 7-42(e), symmetric unstiffened specimens with smaller p_t and thinner t_{ep} and t_{cf} will increase the EPB+CFB probability of occurrence due to the less restraint at the column. Eventually, apart from the t_{ep}, Fig. 7-42(f) shows a similar SHAP feature than the BB, as expected. This is because the Balanced specimens have similar geometric parameters than the BB counterpart, but a weaker endplate to develop more plastic deformations. In summary, the employed model interpretation algorithms demonstrate model rationality and agreement with the established connection mechanics.

(a)

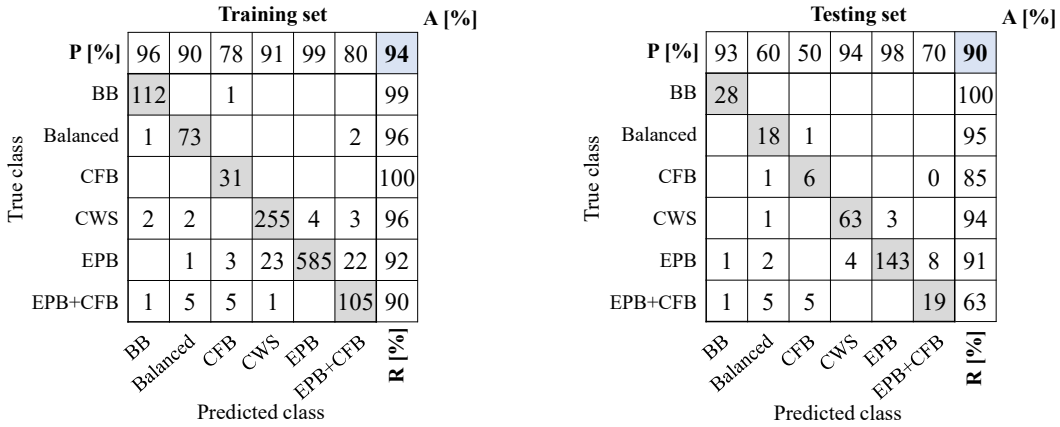

(b)

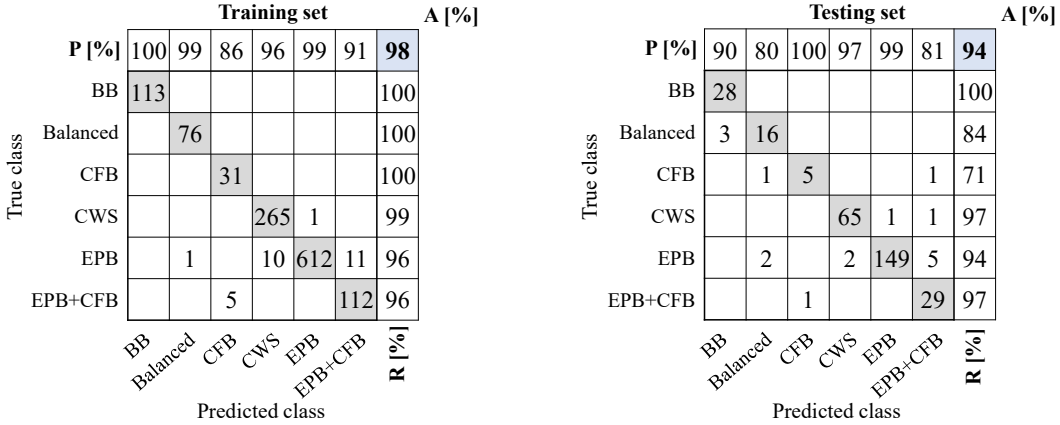

(c)

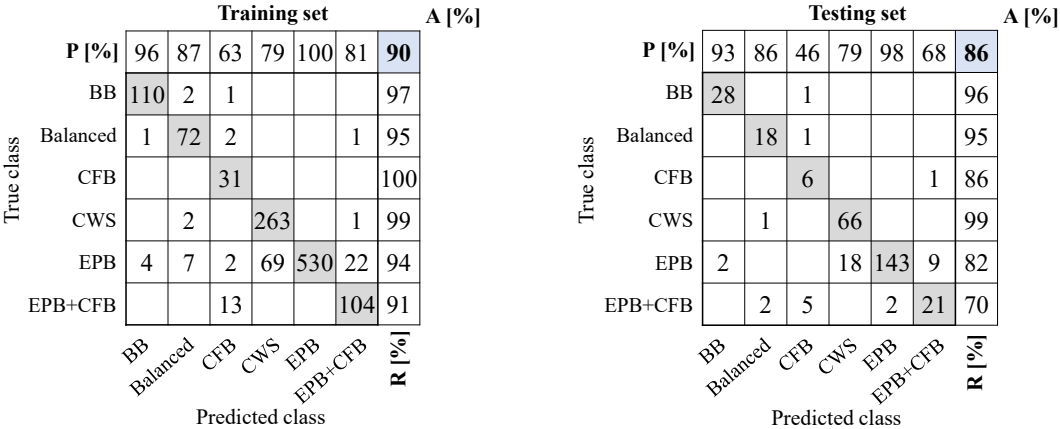

(d)

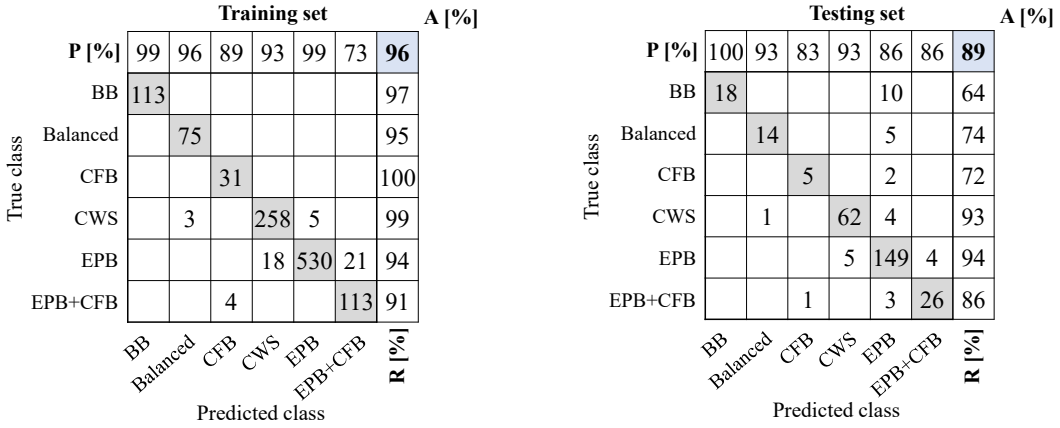

Fig. 7-40 Confusion matrices of the trained classification models: (a) DT; (b) RF; (c) KNN; (d) SVM.

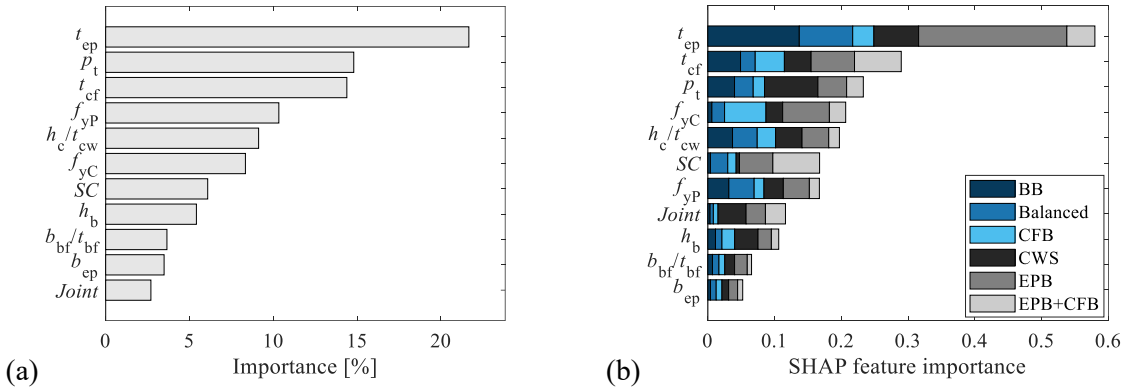

Fig. 7-41 Feature importance based on the RF model: (a) impurity-based importance, and (b) mean absolute SHAP importance.

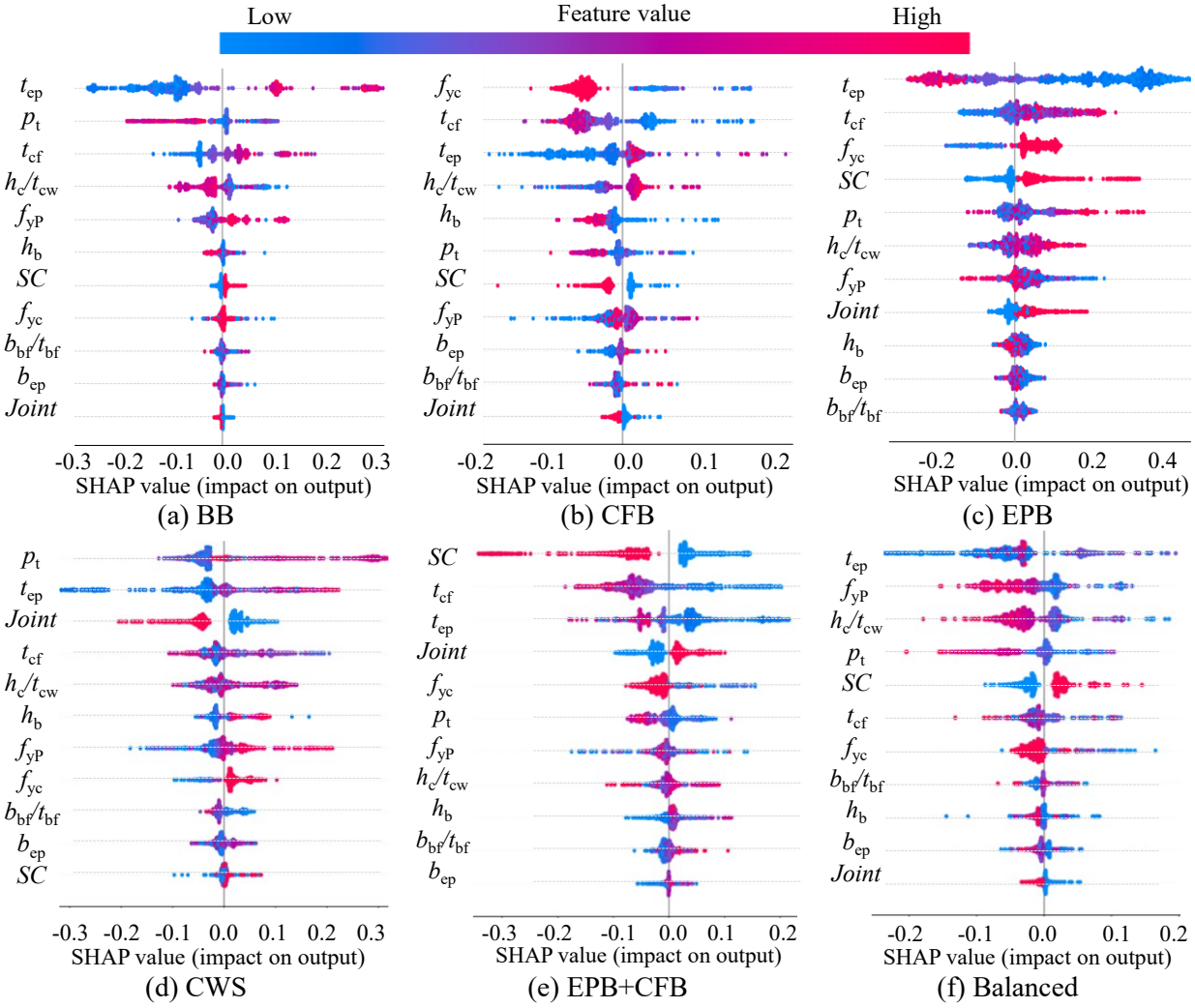

Fig. 7-42 SHAP value summary plots for the (a) BB; (b) CFB; (c) EPB; (d) CWS; (e) EPB+CFB; and (f) Balanced.

7.7.4. Implication on hysteretic response

The EEPC deformation mode affects the characteristics of its hysteretic response. Knowing the hysteretic response dependency on the deformation mode is necessary when selecting and defining numerical hysteretic models as part of system-level simulations. This section investigates this dependency and provides guidelines for the definition of the cyclic parameters of existing phenomenological deterioration models within the OpenSees framework [233].

Concerning CWS, EEPCs produce a rounded hysteretic response with excellent energy dissipation, as shown in Fig. 7-43(a). The hysteretic behaviour is stable without strength or stiffness degradation [187, 234, 235]. Similarly, EEPCs developing BB produce a rounded hysteretic response, except that stiffness and strength degradation are triggered following the onset of local buckling (see Fig. 7-43(b)). As part of system-level simulations employing the lumped plasticity approach, the *hysteretic* material model (or an equivalent model) can be used for CWS [187, 203, 236] while for BB, the *IMKBilin* phenomenological model [191] with a bilinear response can be used [13].

For EEPCs controlled by CFB, a peak-oriented hysteretic response is observed with a reduced re-loading stiffness due to the bending of the column flange (see Fig. 7-43(c)). The response can be captured by the *IMKPeakOriented* model while utilising the backbone definition per the recommendations of the proposed MVLR and ANN models. For EPB, as observed in Fig. 7-43(d-f), EEPCs undergo a pinched behaviour with reduced energy dissipation resulting from the gap opening/closing between the endplate and the column flange. The level of pinching depends on the connection's geometric parameters, particularly those controlling the endplate's bending stiffness. This is investigated herein through several parametric CFE simulations. The hysteretic responses are then calibrated against the *IMKPinching* model. Special attention is paid to the κ_f and κ_d parameters that control the onset of pinching in each cycle (i.e., pinching level) with respect to the target force and deformation, respectively, as illustrated in Fig. 7-44(a).

Fig. 7-43 (d-f) show three EPB hysteretic responses with varying pinching levels. High pinching levels are reflected by κ_f value as low as 0.7 (Figure(d)), while low pinching levels are reflected by κ_f value as high as 0.95 (Figure (f)). For κ_d, the value is almost constant as it varies between 0.95 and 1.0 (i.e., pinching starts near the zero-rotation position when the gap closes). It was observed that $\underline{\kappa}_f$ correlates with the normalized geometric parameters p_t/t_{ep} (representing the plate bending stiffness in the vertical direction) and g/b_{ep} (representing the plate bending length in the horizontal direction). This is demonstrated in Fig. 7-44(b). A longer and thinner endplate (i.e., large p_t/t_{ep}) will result in less pinching, while a higher bolt gauge with respect to the endplate width (g/bep) will result in more pinching. Using linear regression, this relation can be represented by Eq. 7-18. This, along with the backbone parameters recommended by the proposed MVLR

and ANN models, completes the definition of the phenomenological model. Fig. 7-45 shows the validation of the predicted κ_f for two EEPCs with different levels of pinching.

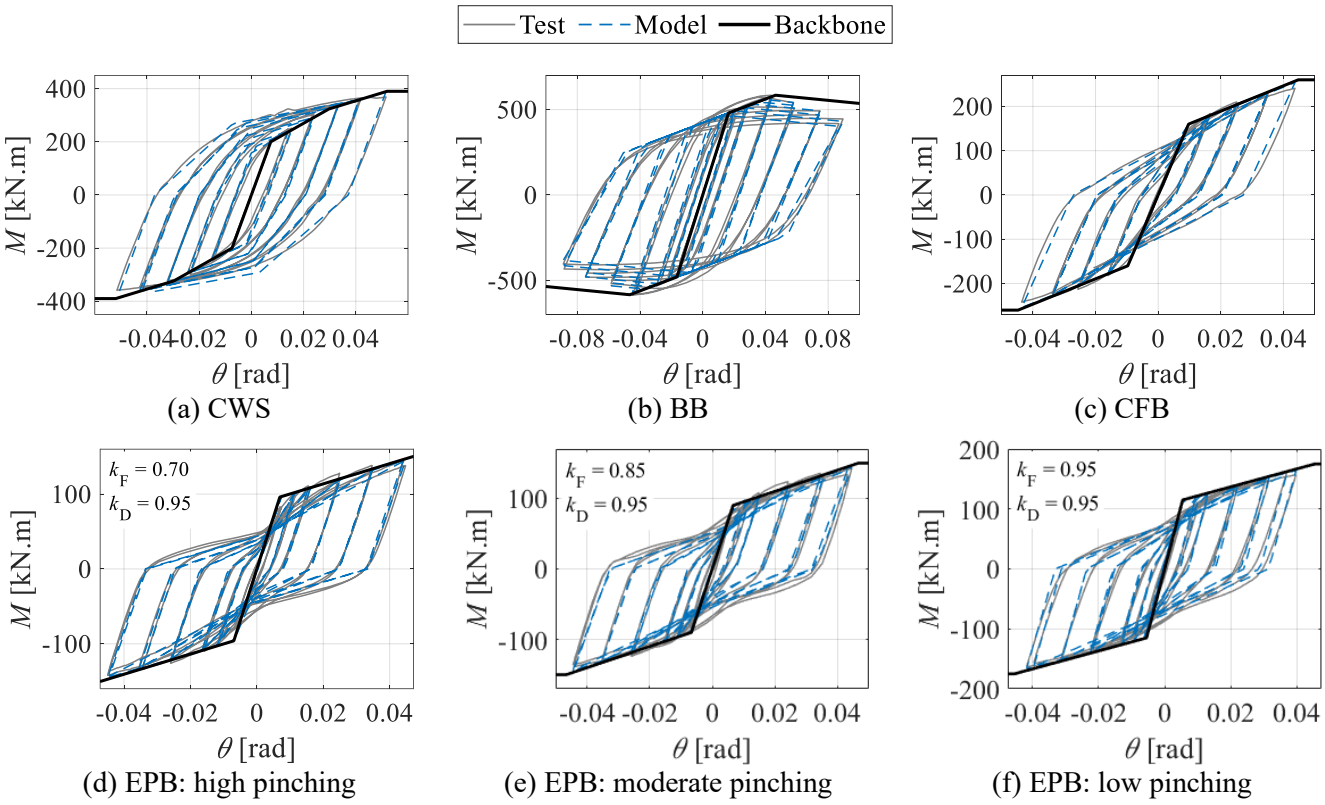

Fig. 7-43 Calibrated hysteretic responses for different deformation modes: (a) CWS; (b) BB; (c) CFB; (d) EPB: high pinching; (e) EPB: moderate pinching; (f) EPB: low pinching.

$$\kappa_f = 0.80 + 0.023\frac{p_t}{t_{ep}} - 0.34\frac{g}{b_{ep}} \qquad 7\text{-}18$$

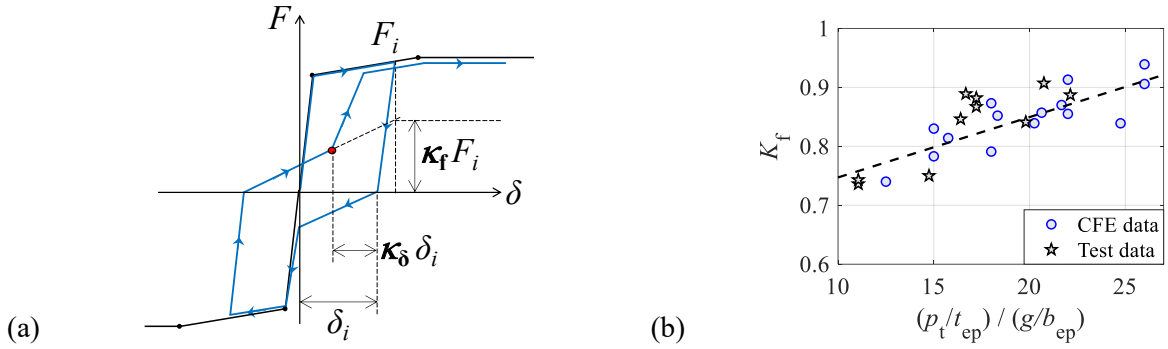

Fig. 7-44 (a) Definition of the pinching parameters; (b) correlation between κf and the endplate geometric parameters.

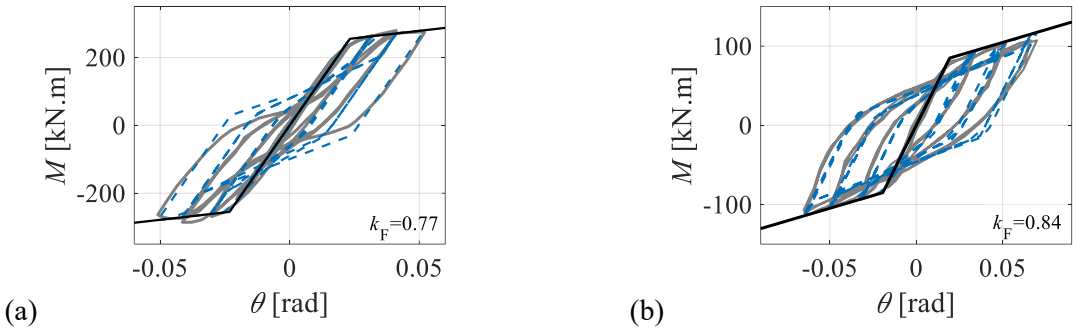

Fig. 7-45 Validation of the predicted κ_f: (a) specimen *S2* by [52]; (b) speicmen *ESC* by [43]

7.7.5. Model practical implementation

The developed classification model is made available for users to assist in structural design and analysis. Considering that tree-based models cannot be simply presented in mathematical form, the model herein is provided in the form of a MATLAB function and through a graphical user interface (GUI) tool; both of which are downloadable from GitHub [200]. In both cases, the user needs to specify the values of the *input* features (see Table. 7-18). The function (or the developed GUI) will output the predicted deformation mode class, see Fig. 7-46. Additionally, the *output* will display all six deformation mode classes and their corresponding prediction probabilities in descending order. The prediction probability is calculated as the ratio of the number of trees predicting a given class to the total number of trees. This information can help the user identify the confidence level in the predicted class and whether the prediction falls within an uncertain boundary between two or more classes.

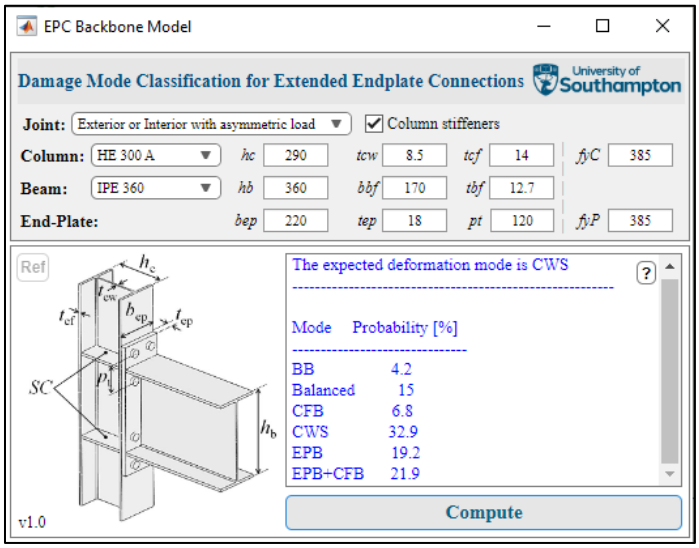

Fig. 7-46 Proposed RF classification model GUI.

Table. 7-20 shows a couple of examples of the input and outputs of the MATLAB function. Note that all bolts in those examples are assumed to be strong components. Example 1 is an unstiffened exterior joint with a shallow-depth beam (i.e., $h_b \leq 400$mm) controlled by EPB, as the thin endplate is the weak component

(i.e., $t_{ep}<t_{cf}$). By increasing the t_{ep} from 12mm to 18mm, plastic deformations extend to the column flange (i.e., EPB+CFB). By further adding column stiffeners, the column flange deformation is restrained, and plastic deformations are shifted to the column web, meaning the joint is controlled by CWS. Example 2 is a stiffened exterior joint with a medium-depth beam (i.e., 400mm$<h_b\leq$600mm) controlled by CWS. By adding doubler plates, the column web becomes stiffer, and the plastic deformations move the endplate and beam flange (i.e., Balanced). If the t_{ep} is increased to 30mm, the connected beam becomes the only weak component and the BB domains the deformation mode (i.e., fully rigid joint). Finally, Example 3 is an unstiffened interior joint with a deep beam (i.e., $h_b>$600mm) controlled by EPB+CFB as the t_{ep} and t_{cf} values are very close (i.e., $t_{ep}/t_{cf}\approx1$). By adding column stiffeners to strengthen the column flange, plastic deformations dominate in the endplate (EPB). If t_{ep} is further increased to 30mm, the joint will become rigid/full-strength, and BB controls its plastic deformations. These examples demonstrate that the proposed classification model can effectively and precisely capture the EEPCs' deformation modes with different configurations and geometric parameters.

Table. 7-20 Sample output of the classification model incorporating class probability

Example 1: Exterior joint – Beam: IPE360 – Column: HEA300											
		SC	*Joint*	p_t	b_{ep}	t_{ep}/t_{cf}	h_b	h_c/t_{cw}	b_{bf}/t_{bf}	f_{yP}	f_{yC}
Standard	Input	0	0	120	220	12/14	360	290/9	170/13	385	385
	Output	BB		Balanced		CFB		CWS	**EPB**	EPB+CFB	
		0.01		0.03		0.0		0.18	**0.44**	0.33	
increasing t_{ep}	Input	0	0	120	220	**18**/14	360	290/9	170/13	385	385
	Output	BB		Balanced		CFB		CWS	EPB	**EPB+CFB**	
		0.01		0.1		0.07		0.13	0.06	**0.64**	
increasing t_{ep} and adding stiffeners	Input	**1**	0	120	220	**18**/14	360	290/9	170/13	385	385
	Output	BB		Balanced		CFB		**CWS**	EPB	EPB+CFB	
		0.04		0.15		0.07		**0.33**	0.19	0.22	
Example 2: Exterior joint - Beam: W18x55 Column: W14x90											
		SC	*Joint*	p_t	b_{ep}	t_{ep}/t_{cf}	h_b	h_c/t_{cw}	b_{bf}/t_{bf}	f_{yP}	f_{yC}
Standard	Input	1	0	130	240	20/18	459	356/11	191/16	385	385
	Output	BB		Balanced		CFB		**CWS**	EPB	EPB+CFB	
		0.13		0.27		0.0		**0.37**	0.19	0.04	
Increasing t_{cw} by adding doubler plates	Input	1	0	130	240	20/18	459	356/**22**	191/16	385	385
	Output	BB		**Balanced**		CFB		CWS	EPB	EPB+CFB	
		0.17		**0.36**		0.02		0.21	0.21	0.03	
Increasing t_{ep}	Input	1	0	130	240	**30**/18	459	356/**22**	191/16	385	385
	Output	**BB**		Balanced		CFB		CWS	EPB	EPB+CFB	
		0.61		0.11		0.04		0.21	0.03	0.0	
Example 3: Interior joint – Beam: UB 610x229x113 Column: UC 305x305x97											
		SC	*Joint*	p_t	b_{ep}	t_{ep}/t_{cf}	h_b	h_c/t_{cw}	b_{bf}/t_{bf}	f_{yP}	f_{yC}
Standard	Input	0	1	130	240	16/15	607	306/10	228/17	385	385
	Output	BB		Balanced		CFB		CWS	EPB	**EPB+CFB**	
		0.05		0.25		0.07		0.08	0.10	**0.44**	
		SC	*Joint*	p_t	b_{ep}	t_{ep}/t_{cf}	h_b	h_c/t_{cw}	b_{bf}/t_{bf}	f_{yP}	f_{yC}
Adding stiffeners	Input	**1**	1	130	240	16/15	607	306/10	228/17	385	385
	Output	BB		**Balanced**		CFB		CWS	EPB	EPB+CFB	
		0.05		**0.39**		0.04		0.17	0.27	0.08	
		SC	*Joint*	p_t	b_{ep}	t_{ep}/t_{cf}	h_b	h_c/t_{cw}	b_{bf}/t_{bf}	f_{yP}	f_{yC}
Increasing t_{ep}	Input	**1**	1	130	240	**32**/15	607	306/10	228/17	385	385
	Output	**BB**		Balanced		CFB		CWS	EPB	EPB+CFB	
		0.43		0.19		0.07		0.20	0.08	0.03	

7.7.6. Model limitations

The proposed classification RF model has some limitations that could be further improved in the future. Those limitations are as follows:

- The developed RF model is only applicable to bare steel beam-to-column EEPCs. The applicability of the geometrical and material parameters shall be restricted to the ranges of the employed dataset (see Fig. 6-8). These ranges, however, should be sufficient to cover all practical design layouts.
- The model neglects axial load in the beam due to the limited availability of reliable data in the literature. Moreover, depending on its magnitude, beam axial force can significantly influence the

connection's deformation mode [55, 169]. Therefore, additional experimental studies considering different levels of axial load in the beam are required in the future.

- EEPCs with rib plate stiffeners are not considered in the model. However, given that rib stiffeners are typically used in fully rigid connections, the model herein can still be used to confirm the BB deformation mode. It's important to note that for other types of EEPCs, the current model may fall short, considering that rib plate stiffeners can restrain the endplate's bending mechanism and even deform on their own (Shi et al. 2007a; Bu et al. 2019). Despite this, the model is adaptable and can be used as a foundation for further research on different types of EEPCs.
- The used dataset assumes that the EEPC employs a strong bolt design. This means that the bolt is not a source of plastic deformation when the connection develops its plastic capacity. Therefore, specimens governed by bolt elongation are not captured by the classification model. However, this type of connection is not typically produced by standard design practice.
- The simulated dataset involved models that did explicitly model the beam-to-endplate weld geometry. This might result in a slightly more flexible endplate in bending (i.e., larger predicted probability of EPB occurrence) compared to reality. This is true for connections with large fillet-weld leg length and small p_t.
- The classification model assumes hot-rolled or built-up beam/column sections with non-slender flange/beam elements. The model also assumes the same material grade for the beam and the column. For the training dataset, the beam and column material grade are mostly A992 Gr. 50 or S355. Accordingly, the developed model cannot be used for joints employing slender (class 3) sections or different member steel grades.

7.8. Summary remarks

Based on an extensive data pool of experimental data and parametric simulations, several predictive models were developed and calibrated to capture the full-range M-θ response, deformation modes, and hysteretic responses of bare-steel beam-to-column EEPCs. The process began by investigating the correlations between key parameters (i.e., geometry and material) and EEPC's backbone response (i.e., stiffness, strength, and ductility). Note that the observed dependency are consistent with prior research. These

foundational insights informed the development of models. The key features of the developed models are summarised below:

- MVLR and ANN models were developed to capture the full-range M-θ responses. These models demonstrate superior performance compared to the existing models, as shown in Fig. 7-31. Note that the R^2 value in both the developed MVLR and ANN models exceeds 0.85. With respect to the strength parameters, over 70% of specimens are predicted within an error less than ±20%. For the sensitive parameters (i.e., K_e and θ_c), the model still can provide predictions with an error less than ±50% for all specimens. Statistical metrics are provided for each model to quantify the variability of residual errors. These metrics allow for the construction of LB and UB of backbone curves, which are essential for probabilistic simulations and structural reliability analysis.
- Several machine learning algorithms, including DT, RF, KNN, and SVM, were implemented to develop classification models for EEPCs' deformation modes. While all trained models yielded consistent and acceptable accuracy levels above 84%, the RF algorithm demonstrated exceptional performance, exceeding 95% accuracy on both training and test sets. Therefore, the RF model was selected for its robust predictive capability.
- Beyond a simple classification, the developed RF model outputs the probability associated with each deformation mode. Ranking these probabilities in descending order allows for an assessment of prediction confidence and the identification of uncertain predictions that lie near the boundaries between classes.
- To characterise the EEPC hysteretic response, pinching parameters κ_f and κ_d in the *IMKPinching* model were calibrated based on 25 EEPCs controlled by EPB. The calibration revealed that κ_d is essentially constant, with a value of approximately 0.95, whereas κ_f exhibits a clear correlation with the EEPC's geometric parameters. Consequently, an empirical expression was derived to predict κ_f.
- The proposed predictive models for SR EEPCs can be further extended and integrated into structural nonlinear analysis frameworks to enhance the accuracy of structural simulations. Specifically, the model can be implemented within advanced structural analysis to represent connection behaviour more accurately under nonlinear conditions, including material yielding, geometric nonlinearity, and potential failure mechanisms. By replacing simplified or idealised connection assumptions with data-driven predictive models, it becomes possible to capture the true moment-rotation responses of connections within global structural systems. This integration would allow for more reliable prediction of structural performance under extreme loading scenarios such as seismic or progressive collapse conditions, while also improving the design optimisation, assessment of system-level ductility, robustness, and load redistribution.

8

CONCLUSIONS AND PERSPECTIVES

8.1. Summary and conclusions

This thesis presents a comprehensive study on the assessment, modelling, and prediction of bare-steel beam-to-column SR EEPCs. The research program comprised four main phases:

- Establishing a multi-attribute experimental database for EEPCs and high-strength bolts.
- Evaluating the performance of existing predictive models.
- Developing a systematic finite element modelling framework incorporating a simplified bolt damage model.
- Developing robust models to predict the full-range M-θ backbone responses, deformation modes, and hysteretic response of EEPCs.

8.1.1. Experimental database for EEPCs

In Chapter 2, a total of 843 EEPC beam-to-column specimens were compiled from studies conducted since the 1960s, encompassing a wide range of configurations, geometries, material properties, and deformation modes through more than 100 tabulated parameters. In addition, the M-θ response of each specimen was digitised, and several critical response parameters were defined and derived using a consistent curve fitting method. It was observed that most bare-steel EEPCs were SR/PS connections. This comprehensive experimental database is made publicly available, and it serves as the foundation for subsequent data-driven research, including the performance assessment of existing predictive models, analysis of EEPC response characteristics, and development of more robust predictive models.

8.1.2. Assessment of the existing predictive models

In Chapter 3, seven existing predictive models were evaluated using the compiled experimental database. These models employ various mathematical formulations. The results indicated that all existing models fail to achieve consistent accuracy in predicting key response parameters, with errors often exceeding 100% for K_e and 40% for M_{ye}. This poor performance is attributed to the simplified assumptions and limited connection configurations on which most models were developed, resulting in inadequate consideration of the variability in loading types, material properties, and geometric parameters. Moreover, predictive models capable of capturing connection ductility up to failure remain limited. Several key geometric and material features that significantly influence the connection response were also identified, and these features form the basis for the self-developed predictive models presented in the subsequent sections.

8.1.3. Systematic continuum finite element modelling approach

In Chapter 4, a systematic finite element modelling approach was developed. The nonlinear material model, interaction between components, boundary condition, loading, mesh type, analysis solver, and component deformation extraction were described. Subsequently, critical strain parameters of the phenomenological fracture locus model were calibrated for high-strength bolts with different grades and a constant mesh size. Several bolted connection specimens controlled by bolt rupture were validated, showing good agreement in terms of stiffness and strength. However, the inherent uncertainty associated with bolt rupture was observed, which has a significant effect on ductility. Therefore, a hybrid analytical-empirical bolt force-elongation model was proposed to capture this effect.

In Chapter 5, a total of 200 high-strength bolts with varying material grades, geometric parameters, and loading rates were tested. A comprehensive multi-attribute database was subsequently developed using both experimental results and data compiled from previous studies. Based on this extensive dataset, a force–elongation model for bolts under quasi-static loading up to rupture was formulated. The proposed model comprises: (1) two empirical expressions for estimating the bolt's elastic axial stiffness and plastic elongation, and (2) quantification of the bolt's strength and maximum damage parameter. The inherent material uncertainty was also investigated, revealing that the bolt's elastic axial stiffness and plastic elongation can vary by up to 20%. This variability may result in a rotational ductility variation of up to ±1.3% rads at the joint level.

Experimental findings also indicate that higher loading rates significantly influence bolt behaviour, particularly in terms of strength and ductility. Specifically, the yield and ultimate stresses of Gr 8.8 and 10.9 bolts increase on average by 5% and 4%, respectively, under faster loading conditions. In terms of ductility, the ultimate plastic strength may vary by about 10% at a loading rate of 80 mm/s. However, the influence of increased loading rate on fracture plastic strength was less consistent, showing potential amplification or reduction of up to 20% at 80 mm/s. This observation highlights the need for further investigation into rate-dependent fracture behaviour.

8.1.4. Finite element parametric simulations

In Chapter 6, parametric CFE simulations for 1980 EEPCs were conducted, primarily aiming to address the design space gaps observed in the experimental database. The parametric simulations were conducted based on the developed CFE modelling approach and a bolt force-elongation model up to rupture. A systematic approach was used to define primary, random, and constant parameters, as well as material variability. The parametric simulations help produce uniform density distributions for the key geometric parameters to minimise bias. Note that geometric and material uncertainties were considered by randomly sampling the key geometric and material parameters. This aims to capture the variability of the predictors in the

subsequent development of robust predictive models for the *M-θ* response and deformation modes of EEPCs. This large-scale parametric study was used as part of the data resource for developing robust predictive models in the next section.

8.1.5. Development of robust predictive models for EEPCs

Chapter 7 fulfils the primary objective of this thesis by proposing several robust predictive models to capture the full-range *M-θ* response, deformation modes, and hysteretic responses of EEPCs. For the *M-θ* response, models based on MVLR and ANN were developed. Both models outperform existing counterparts, with most predictions falling within a ±50% error margin. The ANN model, however, demonstrated superior accuracy and robustness, predicting K_e and M_{ye} with errors within ±30%.

In terms of the EEPCs' deformation mode(s), a classification model, based on the RF algorithm, has been developed. Six deformation modes were considered, covering both primary and interactive ones that are expected to occur in both FR and SR EEPCs. The model prediction achieves a high overall accuracy (>95%) and can provide the prediction probability associated with each deformation mode. Further recommendations were provided regarding the numerical hysteretic models to be used for each deformation mode. Specifically, an empirical formula was developed to quantify the pinching parameters as part of the phenomenological *IMKPinching* model.

The practical outcomes of this research are embodied in publicly available MATLAB-based functions and computational tools. These resources are developed to support nonlinear structural analysis guidelines, optimise connection geometry for target performance levels, and construct fragility functions corresponding to yielding and failure damage states. Consequently, this work provides a direct contribution to system-level simulations and PBD frameworks for loss assessment.

8.2. Recommendations for future research

Some potential research topics are suggested, as follows:

- The developed predictive models only applies to bare steel SR EEPCs. Future work is needed to consider the presence of a concrete slab working compositely with the steel beam. The backbone parameters will need to be modified to reflect the asymmetric composite action effect under hogging and sagging moments. Past recommendations for considering the composite slab effect in FR connections [203] may be applicable to SR connections.
- The proposed models predict rotational ductility considering bolt rupture. However, weld failure may also occur individually or in conjunction with bolt rupture, particularly in SR EEPCs that approach the FR boundary. This requires further study weld ductility and weld fracture fragility.
- The loading speed effect on the bolt's force-elongation response showed substantial variability in the test results. Much more data is needed (across a wider range of varying loading speeds) to capture the underlying response correlations/dependencies and to develop explicit expressions that potentially consider the loading speed.
- Despite the developed models can provide predictions with an error less than ±20% for most of cases, the reliability analysis shall be conducted. Based on the quantified uncertainties of material properties, geometric parameters, and model's error, the partial safety factor (γ_M) can be computed for a specific target reliability index (β) using first order reliability method (FORM) [237]. The calibrated γ_M can be incorporated into design applications to enhance the robustness and reliability of the proposed models.

REFERENCES

[1] Adey BT et al. Extended end plate moment connections under cyclic loading 1997.

[2] Murray TM, Sumner EA. Extended end-plate moment connections: Seismic and wind applications, American Institute of Steel Construction; 2003.

[3] Steenhuis C. Frame design and economy. Proc of the state-of-the-art workshop Semi-rigid behaviour of Civil Engineering structural connections (Ed: A Colson), Strasbourg, France. 1992:549-59.

[4] Tahir MM. Structural and economic aspects of the use of semi-rigid joints in steel frames: University of Warwick; 1997.

[5] Weynand K et al. Economy studies of steel building frames with semi-rigid joints. Second World Conference on Constructional Steel Design. 1998.

[6] Moynihan MC, Allwood JM. Utilization of structural steel in buildings. Proceedings of the Royal Society A: Mathematical, Physical and Engineering Sciences. 2014;470:20140170. https://doi.org/10.1098/rspa.2014.0170.

[7] CEN. Eurocode 3 - Design of Steel Structures, Part 1-8: Design of Joints. Brussels, Belgium, European Committee for Standardization; 2024.

[8] AISC360-22. Specifications for structural steel buildings. . Chicago, American Institute of Steel Construction (AISC); 2022.

[9] Landolfo R. European seismic prequalification of steel beam-to-column joints: EQUALJOINTS and EQUALJOINTS-Plus projects. Journal of Constructional Steel Research. 2022;192:107238.

[10] Elkady A, Lignos DG. Full-scale testing of deep wide-flange steel columns under multi-axis cyclic loading: loading sequence, boundary effects and out-of-plane brace force demands. ASCE Journal of Structural Engineering. 2018;144:04017189. https://doi.org/10.1061/(ASCE)ST.1943-541X.0001937.

[11] Cravero J et al. Experimental evaluation and numerical modeling of wide-flange steel columns subjected to constant and variable axial load coupled with lateral drift demands. Journal of Structural Engineering. 2020;146. 10.1061/(ASCE)ST.1943-541X.0002499.

[12] Krawinkler H. Cyclic loading histories for seismic experimentation on structural components. Earthquake Spectra. 1996;12:1-12. 10.1193/1.1585865.

[13] Lignos DG, Krawinkler H. Deterioration modeling of steel components in support of collapse prediction of steel moment frames under earthquake loading. Journal of Structural Engineering. 2011;137:1291-302. https://doi.org/10.1061/(ASCE)ST.1943-541X.0000376.

[14] Allen P. Steel construction institute and British constructional steelwork association. Joints in Steel Construction, Moment Connections, London. 1996.

[15] Government. Promoting net zero carbon and sustainability in construction. In: Function GC, editor. Open Government Licence2022.

[16] Technology IEAOoE et al. Energy technology perspectives. Paris, France, International Energy Agency; 2008.

[17] Allwood JM et al. Options for achieving a 50% cut in industrial carbon emissions by 2050. 2010. https://doi.org/10.1021/es902909k.

[18] BCSA. UK structural steelwork: 2050 decarbonisation roadmap. London, UK2021.

[19] NEPC. Decarbonising construction: building a new net zero industry. London, Royal Academy of Engineering; 2021. p. 20.

[20] Eladly MM, Schafer BW. Numerical and analytical study of stainless steel beam-to-column extended end-plate connections. Engineering Structures. 2021;240:112392. https://doi.org/10.1016/j.engstruct.2021.112392.

[21] Abidelah A et al. Experimental and analytical behavior of bolted end-plate connections with or without stiffeners. Journal of Constructional Steel Research. 2012;76:13-27.

[22] Loureiro A et al. Experimental and numerical analysis of three-dimensional semi-rigid steel joints under non-proportional loading. Engineering Structures. 2012;38:68-77. https://doi.org/10.1016/j.engstruct.2011.12.048.

[23] Qin J-G et al. Initial rotational stiffness of end-plate connections based on the theory of plates and shells. Journal of Building Engineering. 2021;41:102764. 10.1016/j.jobe.2021.102764.

[24] Eatherton MR et al. Yield line patterns for end-plate moment connections. 2021. http://hdl.handle.net/10919/107459.

[25] Sherbourne A. Bolted beam-to-column connections. The Structural Engineer. 1961;39:203-10.

[26] Bailey J. Strength and rigidity of bolted beam to column connections, BISRA; 1970.

[27] Dews R. Experimental test results on experimental end-plate moment connections: Thesis presented to Vanderbilt University, at Nashville, Tenn., in partial …; 1979.

[28] Graham J. Beam to column bolted connections. Birmingham, UK: Aston University; 1981.

[29] IOANNIDES S. Column flange behavior in bolted end plate moment connections[Ph. D. Thesis]. 1978.

[30] Packer J. A limit state design method for the tension region of bolted beam-column connections. The Structural Engineer. 1977;55:446-58.

[31] Chasten CP. Theoretical modeling and testing of 8-bolt extended end-plate connections: Lehigh University; 1988.

[32] Johnstone N, Walpole W. Behaviour of steel beam-column connections, made using bolted end plates. Bulletin of the New Zealand Society for Earthquake Engineering. 1982;15:82-92.

[33] Meng RL. Design of moment end-plate connections for seismic loading, Virginia Polytechnic Institute and State University; 1996.

[34] Tong C. The elastic-plastic behaviour of semi-rigid connections in steel structures: Hatfield Polytechnic; 1985.

[35] Tsai K, Popov E. Seismic Panel Zone Design Effect on Elastic Story Drift in Steel Frames. Journal of Structural Engineering. 1990;116:3285-301. 10.1061/(ASCE)0733-9445(1990)116:12(3285).

[36] Cabrero J, Bayo E. The semi-rigid behaviour of three-dimensional steel beam-to-column joints subjected to proportional loading. Part I. Experimental evaluation. Journal of Constructional Steel Research. 2007;63:1241-53. https://doi.org/10.1016/j.jcsr.2006.11.004.

[37] Coelho AMG et al. Experimental assessment of the ductility of extended end plate connections. Engineering Structures. 2004;26:1185-206. https://doi.org/10.1016/j.engstruct.2000.09.001.

[38] Kovács N et al. Experimental and analytical studies on the cyclic behavior of end-plate joints of composite structural elements. Journal of Constructional Steel Research. 2008;64:202-13. https://doi.org/10.1016/j.jcsr.2007.07.004.

[39] Landolfo R et al. EQUALJOINTS PLUS-Volume with information borchures for 4 seimsically qualified joints. 2018.

[40] Bu Y et al. Study of stainless steel bolted extended end-plate joints under seismic loading. Thin-Walled Structures. 2019;144:106255. https://doi.org/10.1016/j.tws.2019.106255.

[41] Culache G. Assessment of steel endplate moment connections with stainless steel bolts subjected to high loading rates. Southampton, UK: University of Southampton; 2017.

[42] Elflah M et al. Behaviour of stainless steel beam-to-column joints — Part 1: Experimental investigation. Journal of Constructional Steel Research. 2019;152:183-93. 10.1016/j.jcsr.2018.02.040.

[43] Gao JD et al. Hysteretic performance of stainless steel double extended end-plate beam-to-column joints subject to cyclic loading. Thin-Walled Structures. 2021;164:107787. https://doi.org/10.1016/j.tws.2021.107787.

[44] Gao JD et al. Structural behaviour of stainless steel double extended end-plate beam-to-column joints under monotonic loading. Thin-Walled Structures. 2020;151:106743. https://doi.org/10.1016/j.tws.2020.106743.

[45] Jones S et al. Effect of semi-rigid connections on steel column strength. Journal of Constructional Steel Research. 1980;1:38-46.

[46] Goverdhan AV. A collection of experimental moment-rotation curves and evaluation of predicting equation for semi-rigid connections. Nashville, Tennessee: Vanderbilt University; 1984.

[47] Chen W-F, Kishi N. Semirigid steel beam-to-column connections: Data base and modeling. Journal of Structural Engineering. 1989;115:105-19.

[48] Abdalla KM, Chen W-F. Expanded Database of Semi-Rigid Steel Connections. Computers & Structures. 1995;56:553-64. 10.1016/0045-7949(94)00558-K.

[49] Benterkia Z. End-plate connections and analysis of semi-rigid steel frames. Coventry, UK: University of Warwick; 1991.

[50] Mak L, Elkady A. Experimental database for steel flush end-plate connections. Journal of Structural Engineering. 2021;147:04721006. https://doi.org/10.1061/(ASCE)ST.1943-541X.0003064.

[51] AISC. Seismic Provisions for Structural Steel Buildings. Chicago, IL, American Institute for Steel Construction; 2016.

[52] Lin T et al. Finite-Element Analysis of High-Strength Steel Extended End-Plate Connections under Cyclic Loading. Materials. 2022;15:2912.

[53] Nogueiro PNG. Comportamento cíclico de ligações metálicas: Instituto Politecnico de Braganca (Portugal); 2009.

[54] Akgonen AI et al. Cyclic behavior of extended end-plate connections with European steel shapes. Steel and Composite Structures. 2015;19:1185-201. 10.12989/SCS.2015.19.5.1185.

[55] Zhu C et al. Experimental Full-Range Behavior Assessment of Bolted Moment End-Plate Connections. Journal of Structural Engineering. 2019;145:04019079. https://doi.org/10.1061/(ASCE)ST.1943-541X.0002368.

[56] Thai H-T et al. Behaviour of bolted endplate composite joints to square and circular CFST columns. Journal of Constructional Steel Research. 2017;131:68-82. https://doi.org/10.1016/j.jcsr.2016.12.022.

[57] Braconi A et al. Seismic behaviour of beam-to-column partial-strength joints for steel–concrete composite frames. Journal of Constructional Steel Research. 2010;66:1431-44. 10.1016/j.jcsr.2010.05.004.

[58] Lignos D. Sidesway collapse of deteriorating structural systems under seismic excitations, Stanford university; 2008.

[59] Rohatgi A. WebPlotDigitizer. 2011. https://automeris.io

[60] NIST. Guidelines for Nonlinear Structural Analysis for Design of Buildings. NEHRP consultants Joint Venture; 2017.

[61] Elkady A. SRConED. 2025. GitHub; https://github.com/amaelkady/SRConED.

[62] Jones LL, Wood RH. Yield-line analysis of slabs. London, UK, Thames & Hudson and Chatto & Windus; 1967.

[63] Bræstrup MW. Yield-line theory and limit analysis of plates and slabs. Magazine of Concrete Research. 1970;22:99-106. 10.1680/macr.1970.22.71.99.

[64] Zoetemeijer P. A design method for the tension side of statically loaded, bolted beam-to-column connections. HERON. 1974;20.

[65] CEN. Eurocode 3 - Design of steel structures, Part 1-8: Design of joints. Brussels, Belgium, European Committee for Standardization; 2005.

[66] Eatherton MR et al. Yield line patterns for end-plate moment connections. Blacksburg, VA, USA, Virginia Polytechnic Institute and State University; 2021.

[67] Terracciano G. Yield and ultimate rotations of beam-to-column end-plate connections. Naples, Italy: University of Naples Federico II; 2013.

[68] NIST/ATC. Recommended Modeling Parameters and Acceptance Criteria for Nonlinear Analysis in Support of Seismic Evaluation, Retrofit, and Design Prepared for the U.S. Department of Commerce and the National Institute of Standards and Technology (NIST) by the Applied Technology Council (ATC); 2018.

[69] Landolfo R et al. EQUALJOINTS PLUS-Volume with pre-normative design recommendations for seismically qualified steel joints. Coimbra, Portugal2018.

[70] Goldberg JE, Richard RM. Analysis of nonlinear structures. Journal of the Structural Division. 1963;89:333-51. https://doi.org/10.1061/JSDEAG.0000948.

[71] Richard RM, Abbott BJ. Versatile elastic-plastic stress-strain formula. Journal of the Engineering Mechanics Division. 1975;101:511-5. 10.1061/JMCEA3.0002047.

[72] Ramberg W, Osgood WR. Description of Stress-Strain Curves by Three Parameters. Washington, D.C, USA, National Advisory Committee for Aeronautics; 1943.

[73] Chen WF et al. Semi-rigid Connections Handbook. Florida, USA, J. Ross Publishing Inc.; 2011.

[74] Díaz C et al. Review on the modelling of joint behaviour in steel frames. Journal of Constructional Steel Research. 2011;67:741-58. 10.1016/j.jcsr.2010.12.014.

[75] Patnana V et al. Moment–rotation response for semi-rigid connections. Recent Advances in Structural Engineering, Volume 1: Springer; 2019. p. 313-26.

[76] Demonceau J-F et al. Application of Eurocode 3 to steel connections with four bolts per horizontal row. SDSS Rio 2010 Stability and Ductility of Steel Structures. 2010.

[77] GUIDE D. 4/EXTENDED END-PLATE MOMENT CONNECTIONS—SEISMIC AND WIND APPLICATIONS, /57 58. EXTENDED END-PLATE MOMENT CONNECTIONS—SEISMIC AND WIND APPLICATIONS.

[78] Shi G et al. Behaviour of end-plate moment connections under earthquake loading. Engineering Structures. 2007;29:703-16. https://doi.org/10.1016/j.engstruct.2006.06.016.

[79] Özkılıç YO. Cyclic and monotonic performance of unstiffened extended end-plate connections having thin end-plates and large-bolts. Engineering Structures. 2023;281:115794.

[80] Kozlowski A et al. Estimation of the initial stiffness and moment resistance of steel and composite joints. CTBUH 8th World Congress, Dubai. 2008.

[81] Terracciano G et al. Design Tools for Bolted End-Plate Beam-to-Column Joints. Journal of Engineering. 2018;2018.

[82] Prescott A. The performance of end-plate connections in steel structures and their influence on overall structural behaviour: Hatfield Polytechnic; 1987.

[83] Ryan JC. Evaluation of extended end-plate moment connections under seismic loading: Virginia Tech; 1999.

[84] Tartaglia R et al. Proposal of AISC-compliant seismic design criteria for ductile partially-restrained end-plate bolted joints. Journal of Constructional Steel Research. 2019;159:364-83. https://doi.org/10.1016/j.jcsr.2019.05.006.

[85] AISC. Seismic Provisions for Structural Steel Buildings. Chicago, IL, American Institute for Steel Construction; 2010.

[86] Flores FX et al. Influence of the gravity framing system on the collapse performance of special steel moment frames. Journal of Constructional Steel Research. 2014;101:351-62.

[87] Tartaglia R et al. Full strength extended stiffened end-plate joints: AISC vs recent European design criteria. Engineering Structures. 2018;159:155-71.

[88] Song Y. Behaviour and design of stainless steel and stainless steel-concrete composite beam-to-column joints with end-plate connections: The University of Sydney; 2022.

[89] Ling Y. Uniaxial true stress-strain after necking. AMP Journal of Technology. 1996;5:37-48.

[90] Pavlović M et al. Bolted shear connectors vs. headed studs behaviour in push-out tests. Journal of Constructional Steel Research. 2013;88:134-49. 10.1016/j.jcsr.2013.05.003.

[91] Jia L-J, Kuwamura H. Ductile fracture simulation of structural steels under monotonic tension. Journal of Structural Engineering. 2014;140:04013115. 10.1061/(ASCE)ST.1943-541X.0000944.

[92] Jovanović Đ et al. Experimental and numerical investigation of the T-Stub elements with four bolts in a row until bolt fracture, Springer International Publishing; 2020.

[93] Bao Y, Wierzbicki T. On fracture locus in the equivalent strain and stress triaxiality space. International Journal of Mechanical Sciences. 2004;46:81-98. 10.1016/j.ijmecsci.2004.02.006.

[94] Yang F et al. Fracture simulation of partially threaded bolts under tensile loading. Engineering Structures. 2021;226:111373. https://doi.org/10.1016/j.engstruct.2020.111373.

[95] Song Y et al. Experimental behaviour and fracture prediction of austenitic stainless steel bolts under combined tension and shear. Journal of Constructional Steel Research. 2020;166:105916. https://doi.org/10.1016/j.jcsr.2019.105916.

[96] Li D et al. Behaviour and design of Grade 10.9 high-strength bolts under combined actions. Steel and Composite Structures. 2020;35:327-41. https://doi.org/10.12989/scs.2020.35.3.327.

[97] D'Aniello M et al. Monotonic and cyclic inelastic tensile response of European preloadable gr10. 9 bolt assemblies. Journal of Constructional Steel Research. 2016;124:77-90. https://doi.org/10.1016/j.jcsr.2016.05.017.

[98] Hu Y et al. FE simulation and experimental tests of high-strength structural bolts under tension. Journal of Constructional Steel Research. 2016;126:174-86. https://doi.org/10.1016/j.jcsr.2016.07.021.

[99] Nogueiro PNG. Cyclic behavior of steel connections (in portuguese) [Ph.D. Thesis]. Portugal: Instituto Politecnico de Braganca; 2009.

[100] Tahir MM, Hussein A. Experimental tests on extended end-plate connections with variable parameters. Steel Structures. 2008;8:369-81. http://www.kssc.or.kr/wonmun/KSSC_3_2008_8_4_369(C).pdf.

[101] Gao J et al. Hysteretic performance of stainless steel double extended end-plate beam-to-column joints subject to cyclic loading. Thin-Walled Structures. 2021;164:107787. https://doi.org/10.1016/j.tws.2021.107787.

[102] Zheng B et al. Test on seismic behaviors of stainless steel bolted extended end-plate beam-column joints. Thin-Walled Structures. 2024;196:111516. https://doi.org/10.1016/j.tws.2023.111516.

[103] Zoetemeijer P, Munter H. Proposal for the standardiation of extended end plate connections based on test results. Tests and analysis. Report 6-83-23. Delft, Netherlands, Stevin laboratory, University of Technology Delft; 1983.

[104] Rölle L. The load-bearing and deformation behavior of bolted steel and composite joints in fully plastic design and in extraordinary design situations (in german). Stuttgart, Germany: University of Stuttgart; 2013.

[105] Qiang X et al. Behaviour of beam-to-column high strength steel endplate connections under fire conditions – Part 1: Experimental study. Engineering Structures. 2014;64:23-38. 10.1016/j.engstruct.2014.01.028.

[106] Saykin VV et al. The effect of triaxiality on finite element deletion strategies for simulating collapse of full-scale steel structures. Engineering Structures. 2020;210:110364. 10.1016/j.engstruct.2020.110364.

[107] Zhao X et al. Full-range behaviour of T-stubs with various yield line patterns. Journal of Constructional Steel Research. 2021;186:106919. 10.1016/j.jcsr.2021.106919.

[108] D'Aniello M et al. Monotonic and cyclic inelastic tensile response of European preloadable Gr10.9 bolt assemblies. Journal of Constructional Steel Research. 2016;124:77-90. 10.1016/j.jcsr.2016.05.017.

[109] Moore AM et al. Evaluation of the current resistance factors for high-strength bolts. Chicago, United States, Research Council on Structural Connections; 2008.

[110] Li D et al. Behaviour and design of high-strength Grade 12.9 bolts under combined tension and shear. Journal of Constructional Steel Research. 2020;174:106305. https://doi.org/10.1016/j.jcsr.2020.106305.

[111] Li D et al. Behaviour and design of Grade 10.9 high-strength bolts under combined actions. Steel Compos Struct. 2020;35:327-41. https://doi.org/10.12989/scs.2020.35.3.327

[112] Gödrich L et al. Design finite element model of a bolted T-stub connection component. Journal of Constructional Steel Research. 2019;157:198-206. https://doi.org/10.1016/j.jcsr.2019.02.031.

[113] Grimsmo EL et al. Failure modes of bolt and nut assemblies under tensile loading. Journal of Constructional Steel Research. 2016;126:15-25. https://doi.org/10.1016/j.jcsr.2016.06.023.

[114] Schauwecker F et al. Characterization of high-strength bolts and the numerical representation method for an efficient crash analysis. Engineering Failure Analysis. 2022;137:106249. https://doi.org/10.1016/j.engfailanal.2022.106249.

[115] Christopher RJ et al. Calibration of alloy steel bolts. Journal of the Structural Division. 1966;92:19-40. https://doi.org/10.1061/JSDEAG.0001419.

[116] Bendigo RA, Rumpf JL. Calibration and Installation of High Strength Bolts, Fritz Engineering Laboratory, Department of Civil Engineering, Lehigh University; 1959.

[117] Dlugosz SE, Fisher JW. Calibration study of heavy head A325 bolts, Fritz Engineering Laboratory, Department of Civil Engineering, Lehigh University; 1962.

[118] D'Aniello M et al. Simplified criteria for finite element modelling of European preloadable bolts. Steel and Composite Structures. 2017;24:643-58. https://doi.org/10.12989/scs.2017.24.6.643.

[119] Agerskov H. High-strength bolted connections subject to prying. Journal of the Structural Division. 1976;102:161-75. https://doi.org/10.1061/JSDEAG.0004253.

[120] Wu Z et al. Simulation of tensile bolts in finite element modeling of semi-rigid beam-to-column connections. International Journal of Steel Structures. 2012;12:339-50. http://doi.org/10.1007/s13296-012-3004-8.

[121] Swanson JA, Leon RT. Stiffness modeling of bolted T-stub connection components. Journal of structural engineering. 2001;127:498-505. https://doi.org/10.1061/(ASCE)0733-9445(2001)127:5(498).

[122] Bickford J. Handbook of Bolts and bolted Joints, MarcelDekker; 1998.

[123] Swanson JA. Characterization of the strength, stiffness, and ductility behavior of T-stub connections: Georgia Institute of Technology; 1999.

[124] D'Aniello M et al. Simplified criteria for finite element modelling of European preloadable bolts. Steel Compos Struct. 2017;24:643-58. https://doi.org/10.12989/scs.2017.24.6.643.

[125] VDI. 2230-1: 2015 Systematic Calculation of Highly Stressed Bolted Joints—Joints with One Cylindrical Bolt. Diseldorf: VDI Verlag2015.

[126] Elkady A. Response characteristics of flush end-plate connections. Engineering Structures. 2022;269:114856. https://doi.org/10.1016/j.engstruct.2022.114856.

[127] Moore AM. Evaluation of the current resistance factors for high-strength bolts: University of Cincinnati; 2007.

[128] Elkady A. Bolt Connector App. 2025. United Kingdom: GitHub; https://github.com/amaelkady/Bolt-Connector-App.

[129] Munter H. Proposal for the standardiation of extended end plate connections based on test results. Tests and analysis. Stevin rapport 6-83-231983.

[130] Qiang X et al. Behaviour of beam-to-column high strength steel endplate connections under fire conditions–Part 1: Experimental study. Engineering Structures. 2014;64:23-38. https://doi.org/10.1016/j.engstruct.2014.01.028.

[131] Rölle L. The load-bearing and deformation behavior of bolted steel and composite nodes in fully plastic design and in exceptional design situations (in German): University of Stuttgart; 2013.

[132] Grimsmo EL et al. An experimental study of static and dynamic behaviour of bolted end-plate joints of steel. International Journal of Impact Engineering. 2015;85:132-45. https://doi.org/10.1016/j.ijimpeng.2015.07.001.

[133] Kendall G et al. Experimental investigation of welded steel T-stub components under high loading rates. Journal of Constructional Steel Research. 2024;220:108851. https://doi.org/10.1016/j.jcsr.2024.108851.

[134] Yang S et al. Rate-dependent behaviour of high-strength steel bolts. Journal of Constructional Steel Research. 2024;215:108560. https://doi.org/10.1016/j.jcsr.2024.108560.

[135] EN-14399-4. High-Strength Structural Bolting Assemblies for Preloading – Part 4: System HV – Hexagon Bolt and Nut Assemblies. Brussels, Belgium, European Committee for Standardization; 2015.

[136] Jankovic N et al. Behaviour and design resistance of long bolts in tension. Journal Construction Steel Research. 2025;229:109492. https://doi.org/10.1016/j.jcsr.2025.109492.

[137] Stranghöner N et al. New design approaches for tension, shear and interaction resistance of carbon steel bolts. Journal of Constructional Steel Research. 2024;212:108260. https://doi.org/10.1016/j.jcsr.2023.108260.

[138] Augusto H et al. Characterization of web panel components in double-extended bolted end-plate steel joints. Journal of Constructional Steel Research. 2016;116:271-93. https://doi.org/10.1016/j.jcsr.2015.08.022.

[139] Elflah M et al. Behaviour of stainless steel beam-to-column joints-part 2: Numerical modelling and parametric study. Journal of Constructional Steel Research. 2019;152:194-212.

[140] Luo L et al. Parametric Analysis and Stiffness Investigation of Extended End-Plate Connection. Materials. 2020;13:5133.

[141] PRC M. ChineseStandard. GB 50017-2017. Code for Design of Steel Structure. China Building Industry Press Beijing, China; 2017.

[142] AISC. Specification for Structural Steel Buildings. Chicago, IL, American Institute for Steel Construction; 2016.

[143] Melcher J et al. Design characteristics of structural steels based on statistical analysis of metallurgical products. Journal of Constructional Steel Research. 2004;60:795-808.

[144] Sadowski AJ et al. Statistical analysis of the material properties of selected structural carbon steels. Structural Safety. 2015;53:26-35.

[145] Coelho AG. Characterization of the ductility of bolted end plate beam-to-column steel connections. Coimbra: Universidade de Coimbra. 2004.

[146] Kossakowski P. Influence of initial porosity on strength properties of S235JR steel at low stress triaxiality. Archives of Civil Engineering. 2012:293-308-293-308.

[147] Wang J, Chen L. Experimental investigation of extended end plate joints to concrete-filled steel tubular columns. Journal of Constructional Steel Research. 2012;79:56-70. https://doi.org/10.1016/j.jcsr.2012.07.016.

[148] Lacalle R et al. Influence of the flame straightening process on microstructural, mechanical and fracture properties of S235 JR, S460 ML and S690 QL structural steels. Experimental Mechanics. 2013;53:893-909.

[149] Prinz GS et al. Experimental testing and simulation of bolted beam-column connections having thick extended end plates and multiple bolts per row. Engineering Structures. 2014;59:434-47. https://doi.org/10.1016/j.engstruct.2013.10.042.

[150] Li XF, Wang XW. Experimental research on anti-seismic performance of the plane steel frame beam-column joints. Applied Mechanics and Materials. 2015;777:27-33.

[151] Shi Q et al. Seismic behavior of semi-rigid steel joints—Major axis T-stub and minor axis end-plate. Journal of Constructional Steel Research. 2019;159:476-92.

[152] Kozłowski A, Kukla D. Experimental tests of steel unstiffened double side joints with flush and extended end plate. Archives of Civil Engineering. 2019:127-54. https://doi.org/10.2478/ace-2019-0051.

[153] Ali MNAS. Experimental Moment-Rotation Behavior of Semi-Rigid Beam-to-Column Connections: Eastern Mediterranean University EMU; 2015.

[154] Torić N et al. Development of a high temperature material model for grade S275JR steel. Journal of constructional steel research. 2017;137:161-8.

[155] Aldeeb T, Abduelmula M. Fatigue strength of S275 Mild Steel under cyclic loading. International Journal of Materials and Metallurgical Engineering. 2018;12:564-70.

[156] Alrubaidi M et al. Investigation of different steel intermediate moment frame connections under column-loss scenario. Thin-Walled Structures. 2020;154:106875.

[157] Ho HC et al. Non-linear necking behaviour of S275 to S960 structural steels under monotonic tension. Engineering Structures. 2022;261:114263.

[158] Foster A et al. Practical strain-hardening material properties for use in deformation-based structural steel design. Thin-walled structures. 2015;92:115-29.

[159] Shi G et al. Experimental study of ultra-large capacity end-plate joints. Journal of Constructional Steel Research. 2017;128:354-61. https://doi.org/10.1016/j.jcsr.2016.09.001.

[160] Costa R et al. Experimental behaviour of 3D end-plate beam-to-column bolted steel joints. Engineering Structures. 2019;188:277-89. https://doi.org/10.1016/j.engstruct.2019.03.017.

[161] Elkady A, Lignos DG. Analytical investigation of the cyclic behavior and plastic hinge formation in deep wide-flange steel beam-columns. Bull Earthquake Eng. 2015;13:1097-118. https://doi.org/10.1007/s10518-014-9640-y.

[162] Newell JD, Uang C-M. Cyclic behavior of steel columns with combined high axial Load and drift demand. Department of Structural Engineering, University of California, San Diego; 2006.

[163] Packer J, LJ M. A limit state design method for the tension region of bolted beam-column connections. 1977.

[164] Shi Y et al. Experimental and theoretical analysis of the moment–rotation behaviour of stiffened extended end-plate connections. Journal of Constructional Steel Research. 2007;63:1279-93. https://doi.org/10.1016/j.jcsr.2006.11.008.

[165] Bahrami M. Behaviour of beam-to-column end plate connections in structural steelwork: Dundee Institute of Technology; 1991.

[166] Driscoll GC. Top and Seat Angle Connections and End Plate Connections: Snug vs Fully Pre-Tensioned Bolts. 1989.

[167] Tarpy T, Cardinal J. Behavior of semi-rigid beam-to-column end plate connections. Joints in structural steelwork. 1981:2-3.

[168] Gao J et al. Structural behaviour of stainless steel double extended end-plate beam-to-column joints under monotonic loading. Thin-Walled Structures. 2020;151:106743. https://doi.org/10.1016/j.tws.2020.106743.

[169] Zoetemeijer P, Munter H. Influence of an Axial Load in the Column on the Behaviour of an Unstiffened Beam to Column End Plate Connection.·. Stevin Laboratory Report N° 6-84-1. Delft University of Technology. 1984. http://resolver.tudelft.nl/uuid:8e5a30d8-50f9-48f0-a4db-07617997296a.

[170] Mazroi A. Moment-rotation behavior of beam-to-column end-plate connections in multistory frames: The University of Oklahoma; 1990.

[171] Arul Jayachandran S et al. Investigations on the behaviour of semi-rigid endplate connections. Advanced Steel Construction. 2009;5:432-51.

[172] Korol R et al. Extended end-plate connections under cyclic loading: Behaviour and design. Journal of Constructional Steel Research. 1990;16:253-80. https://doi.org/10.1016/0143-974X(90)90030-K.

[173] Guo B et al. Experimental Behavior of Stiffened and Unstiffened End-Plate Connections under Cyclic Loading. Journal of Structural Engineering. 2006;132:1352-7. 10.1061/(ASCE)0733-9445(2006)132:9(1352).

[174] Chen S, Wang Z. Application of modified and improved component method in the constitutive relation research for steel connections. South China University of Technology, Guangzhou. 2015.

[175] Adegoke IO. Ductility of thin extended endplate connections: University of the Witwatersrand; 2009.

[176] Izadifard R, Maheri M. Ductility effects on the behaviour of steel structures under blast loading. 2010.

[177] Da Silva LS, Coelho AG. A ductility model for steel connections. Journal of Constructional Steel Research. 2001;57:45-70.

[178] Park R. Ductility evaluation from laboratory and analytical testing. Proceedings of the 9th world conference on earthquake engineering. 1988;8:605-16.

[179] CEN. Eurocode 8: Design of structures

for earthquake resistance. European Committee for Standardization, Brussels; 2005.

[180] Shi G et al. Monotonic loading tests on semi-rigid end-plate connections with welded I-shaped columns and beams. Advances in Structural Engineering. 2010;13:215-29. https://journals.sagepub.com/doi/abs/10.1260/1369-4332.13.2.215.

[181] Zandonini R, Zanon P. Experimental analysis of end plate connections. Elsevier Applied Science Publishers Ltd. 1988:41-51.

[182] Mazroi A. Moment-rotation behavior of beam-to-column end-plate connections in multistory frames [Ph.D. Thesis]. Ann Arbor, Oklahoma, USA: The University of Oklahoma; 1990.

[183] Abolmaali A. Nonlinear Dynamic Finite Element Analysis of Steel Frames with Semi-Rigid Joints. Norman, Oklahoma: University of Oklahoma; 1999.

[184] Maggi Y et al. Parametric analysis of steel bolted end plate connections using finite element modeling. Journal of Constructional Steel Research. 2005;61:689-708. https://doi.org/10.1016/j.jcsr.2004.12.001.

[185] Lignos DG et al. Proposed Updates to the ASCE 41 Nonlinear Modeling Parameters for Wide-Flange Steel Columns in Support of Performance-based Seismic Engineering. Journal of Structural Engineering. 2019;145:04019083. 10.1061/(ASCE)ST.1943-541X.0002353.

[186] Karamanci E, Lignos DG. Computational Approach for Collapse Assessment of Concentrically Braced Frames in Seismic Regions. Journal of Structural Engineering. 2014;140. 10.1061/(ASCE)ST.1943-541X.0001011.

[187] Skiadopoulos A et al. Proposed panel zone model for seismic design of steel moment-resisting frames. Journal of Structural Engineering. 2021;147:04021006. https://doi.org/10.1061/(ASCE)ST.1943-541X.0002935.

[188] Elkady A, Lignos DG. Effect of gravity framing on the overstrength and collapse capacity of steel frame buildings with perimeter special moment frames. Earthquake Engineering & Structural Dynamics. 2015;44:1289–307. 10.1002/eqe.2519.

[189] AISC. Seismic provisions for evaluation and retrofit of existing structural steel buildings. Chicago, IL, American Institute for Steel Construction; 2022.

[190] Menegotto M, Pinto PE. Method of analysis for cyclically loaded RC frames including changes in geometry and non-elastic behaviour of elements under combined normal Force and bending. IABSE Congress Reports of the Working Commission. 1973;13.

[191] Ibarra LF et al. Hysteretic Models that Incorporate Strength and Stiffness Deterioration. Earthquake Engineering & Structural Dynamics. 2005;34:1489-511. 10.1002/eqe.495.

[192] NIST. Guidelines for nonlinear structural analysis for design of buildings - Part IIa Steel MRFs. NEHRP consultants Joint Venture; 2017.

[193] FEMA. Seismic Performance Assessment of Buildings. Federal Emergency Management Agency, Washington, DC; 2012.

[194] Menard S. Applied logistic regression analysis. Thousand Oaks, CA, Sage; 2002.

[195] Chatterjee S, Hadi AS. Regression analysis by example. Fifth Edition ed, John Wiley & Sons; 2015.

[196] Lilliefors HW. On the Kolmogorov-Smirnov test for normality with mean and variance unknown. Journal of the American statistical Association. 1967;62:399-402. https://doi.org/10.1080/01621459.1967.10482916.

[197] Breusch TS, Pagan AR. A simple test for heteroscedasticity and random coefficient variation. Econometrica: Journal of the econometric society. 1979;47:1287-94. 10.2307/1911963.

[198] Murray TM, Shoemaker WL. Flush and extended multiple-row moment end-plate connections. Chicago, Illinois, USA, American Institute of Steel Construction; 2002.

[199] Murray TM, Sumner EA. Extended end-plate moment connections: Seismic and wind applications. 2nd Edition ed. Chicago, Illinois, USA, American Institute of Steel Construction; 2003.

[200] Elkady A. EPC Backbone App. 2025. GitHub; https://github.com/amaelkady/SRConED/tree/main/EPC%20Backbone%20Model.

[201] Sherbourne AN. Bolted beam-to-column connections. The Structural Engineer. 1961;39:203-10.

[202] Tong CS. The elastic-plastic behaviour of semi-rigid connections in steel structures. Hatfield, UK Hatfield Polytechnic; 1985.

[203] Elkady A, Lignos DG. Modeling of the Composite Action in Fully Restrained Beam-to-Column Connections: Implications in the Seismic Design and Collapse Capacity of Steel Special Moment Frames. Earthquake Engineering & Structural Dynamics. 2014;43:1935-54. https://doi.org/10.1002/eqe.2430.

[204] ASCE. Seismic evaluation and retrofit of existing buildings. Reston, VA., American Society of Civil Engineers; 2023.

[205] Elkady A. EPC backbone app. United Kingdom, GitHub; 2025.

[206] Thai H-T. Machine learning for structural engineering: A state-of-the-art review. Structures. 2022;38:448-91. https://doi.org/10.1016/j.istruc.2022.02.003.

[207] De Lima LRO et al. Neural networks assessment of beam-to-column joints. Journal of the Brazilian Society of Mechanical Sciences and Engineering. 2005;27:314-24. https://doi.org/10.1590/S1678-58782005000300015

[208] Kueh A. Artificial neural network and regressed beam-column connection explicit mathematical moment-rotation expressions. Journal of Building Engineering. 2021;43:103195. https://doi.org/10.1016/j.jobe.2021.103195.

[209] Tran V-L, Kim J-K. Revealing the nonlinear behavior of steel flush endplate connections using ANN-based hybrid models. Journal of Building Engineering. 2022;57:104878. https://doi.org/10.1016/j.jobe.2022.104878.

[210] Georgiou G, Elkady A. ANN-based model for predicting the nonlinear response of flush endplate connections. Journal of Structural Engineering. 2024;150:04024034. https://doi.org/10.1061/JSENDH.STENG-13119.

[211] Dharmawansha S et al. Predicting moment-rotation behaviour of beam to column extended endplate bolted connections: An explainable machine learning approach. Materials Today Communications. 2025;47:113086. https://doi.org/10.1016/j.mtcomm.2025.113086.

[212] MathWorks. MATLAB (Version R2025b). Natick,MA,USA, The MathWorks, Inc; 2025.

[213] Burden F, Winkler D. Bayesian regularization of neural networks. Artificial neural networks: methods and applications. 2009:23-42. https://doi.org/10.1007/978-1-60327-101-1.

[214] Lundberg SM, Lee S-I. A unified approach to interpreting model predictions. Advances in neural information processing systems. 2017;30. https://doi.org/10.48550/arXiv.1705.07874.

[215] Tong CS. The elastic-plastic behaviour of semi-rigid connections in steel structures. Hatfield, UK: Hatfield Polytechnic; 1985.

[216] Dubina D et al. Cyclic tests on bolted steel double-sided beam-to-column joints. The Paramount Role of Joints into the Reliable Response of Structures: Springer; 2000. p. 129-38.

[217] Yang B, Tan KH. Experimental tests of different types of bolted steel beam–column joints under a central column removal scenario. Engineering Structures. 2013;54:112-30. https://doi.org/10.1016/j.engstruct.2013.03.037.

[218] Elkady A. EEPC_ML_Backbone_App. 2025. GitHub; https://github.com/amaelkady/SRConED/tree/main.

[219] AISC. Seismic provisions for structural steel buildings. Chicago, American Institute of Steel Construction; 2022.

[220] Elkady A et al. Fragility curves for wide-flange steel columns and implications for building-specific earthquake-induced loss assessment. Earthquake Spectra. 2018;34:1405-29. https://doi.org/10.1193/122017EQS260M.

[221] Kukla D et al. Experimental investigation of steel beam-to-column end-plate joints under static and impact loading. Journal of Constructional Steel Research. 2024;212:108241. https://doi.org/10.1016/j.jcsr.2023.108241.

[222] Skiadopoulos A, Lignos DG. Seismic demands of steel moment resisting frames with inelastic beam-to-column web panel zones. Earthquake Engineering & Structural Dynamics. 2022;51:1591-609. https://doi.org/10.1002/eqe.3629.

[223] Krawinkler H, Mohasseb S. Effects of panel zone deformations on seismic response. Journal of Constructional Steel Research. 1987;8:233-50. https://doi.org/10.1016/0143-974X(87)90060-5.

[224] Breiman L. Classification and regression trees, Routledge; 2017.

[225] Breiman L. Bagging predictors. Machine learning. 1996;24:123-40. https://doi.org/10.1007/BF00058655.

[226] Keller JM et al. A fuzzy k-nearest neighbor algorithm. IEEE transactions on systems, man, and cybernetics. 1985:580-5. https://doi.org/10.1109/TSMC.1985.6313426.

[227] Mangasarian OL, Musicant DR. Lagrangian support vector machines. Journal of Machine Learning Research. 2001;1:161-77. https://www.jmlr.org/papers/volume1/mangasarian01a/mangasarian01a.pdf.

[228] Chawla NV et al. SMOTE: synthetic minority over-sampling technique. Journal of artificial intelligence research. 2002;16:321-57. https://doi.org/10.1613/jair.953.

[229] Bishop CM, Nasrabadi NM. Pattern recognition and machine learning, Springer; 2006.

[230] Gao X, Lin C. Prediction model of the failure mode of beam-column joints using machine learning methods. Engineering Failure Analysis. 2021;120:105072. https://doi.org/10.1016/j.engfailanal.2020.105072.

[231] Sarothi SZ et al. Machine learning-based failure mode identification of double shear bolted connections in structural steel. Engineering Failure Analysis. 2022;139:106471. https://doi.org/10.1016/j.engfailanal.2022.106471.

[232] Lundberg S, Lee S-I. An unexpected unity among methods for interpreting model predictions. arXiv preprint arXiv:161107478. 2016. https://doi.org/10.48550/arXiv.1611.07478.

[233] McKenna F. OpenSees: a Framework for Earthquake Engineering Simulation. Computing in Science & Engineering. 2011;13:58-66. http://doi.org/10.1109/MCSE.2011.66.

[234] Shin S, Engelhardt MD. Cyclic Performance of Deep Column Moment Frames with Weak Panel Zones. Advances in Structural Engineering and Mechanics. 2013.

[235] FEMA. State of the Art Report on Systems Performance of Steel Moment Frames Subject to Earthquake Ground Shaking. Federal Emergency Management Agency, Washington, DC; 2000.

[236] Gupta A, Krawinkler H. Behavior of ductile SMRFs at various seismic hazard levels. Journal of Structural Engineering. 2000;126:98-107. https://doi.org/10.1061/(ASCE)0733-9445(2000)126:1(98.

[237] Hasofer AM. An exact and invarient first order reliability format. J Eng Mech Div, Proc ASCE. 1974;100:111-21.